

ABSTRACT

Title: SPATIAL AND TEMPORAL VARIATIONS OF THE SUPRATHERMAL (3-220 KEV/E) ION COMPOSITION IN SATURN'S EQUATORIAL MAGNETOSPHERE

Robert David DiFabio, Doctor of Philosophy, 2012

Dissertation directed by: Professor Douglas C. Hamilton
Department of Physics

We have studied the composition of the suprathermal ions (3-220 keV/e) in Saturn's magnetosphere using data from the Charge-Energy-Mass Spectrometer (CHEMS) on the Cassini Saturn orbiter from 78 equatorial (Latitude = -10° to 10°) passes during the period 2004-2010. We use this data to determine how the suprathermal ion density and composition vary with time, energy, and distance from Saturn (L-shell). This information is used to study the relative importance of various sources of plasma and neutral particles and how they may vary with time. We also examine the loss and energization processes of the suprathermal ions.

In Saturn's main ring current region (L=7-16), we find that the suprathermal ion composition is 63% W^+ (O^+ , OH^+ , H_2O^+ , H_3O^+), 30% H^+ , 5.2% H_2^+ , 0.98% O^{++} , 0.55% He^+ , and 0.10% He^{++} . The C^+/W^+ and N^+/W^+ ratios are 0.0055 and 0.0078, respectively.

The high abundance of W^+ indicates that the water plumes of Enceladus are the largest source of neutrals that, after ionization, become the plasma in Saturn's magnetosphere. Saturn's atmosphere, thought to be the strongest source of neutral H , and Titan's atmosphere, thought to be the strongest source of neutral H_2 , are also important. The low abundance of He^{++} and He^+ indicates that the solar wind is a relatively minor source of plasma to Saturn's magnetosphere.

The long-term time variations of W^+ , H^+ , and H_2^+ over the period 2004-2010 are quite modest while those of He^{++} and He^+ are much larger. The small variation of the W^+ indicates that the strength of the Enceladus plumes is relatively constant on time scales of months or longer over this period.

The partial number density of all suprathermal species combined increases inward from the outer reaches of the magnetosphere, peaks between $L=8-10$, and then decreases inward. These L variations are qualitatively consistent with inward radial diffusion followed by rapid loss processes inside of $L=8-10$. Changes in composition as a function of L and energy are largely a result of differences in collision lifetimes with Saturn's neutral cloud.

SPATIAL AND TEMPORAL VARIATIONS OF THE SUPRATHERMAL
(3-220 KEV/E) ION COMPOSITION IN SATURN'S EQUATORIAL
MAGNETOSPHERE

by

Robert David DiFabio

Dissertation submitted to the Faculty of the Graduate School of the
University of Maryland, College Park in partial fulfillment
of the requirements for the degree of
Doctor of Philosophy
2012

Advisory Committee

Professor Douglas C. Hamilton, Chair
Professor Glenn Mason
Professor James Drake
Professor Michael Coplan
Professor Eun-Suk Seo

©Copyright by
Robert David DiFabio
2012

Dedication

To my wife, Mandy

Acknowledgements

There are so many people who contributed to my success, and I would like to wholeheartedly thank them. My advisor, Professor Douglas C. Hamilton, provided valuable guidance while I was pursuing my Ph.D. He helped to greatly improve my skills as a researcher and as a data analyst. Also, I appreciate the insight and helpful suggestions of Tom Krimigis, Don Mitchell, and the rest of the MIMI team at the Applied Physics Laboratory. In addition, I owe special gratitude to the members of my dissertation committee: Dr. James Drake, Dr. Glenn Mason, Dr. Michael Coplan, and Dr. Eun-Suk Seo.

God and my family have also been a constant source of strength over the years. My brothers, Bryan and Stephen, were always excited about my getting a Ph.D. My grandmothers, as well as my aunts and uncles, were all very supportive. I owe almost everything to my parents, Paul and Karen DiFabio; they always stressed the importance of education and encouraged me to pursue my goals. They loved my brothers and me more than anything in the world, and I wish they could be here to see me finally graduate. Finally, I thank my wife, Mandy. She is the best thing that has ever happened to me. I dedicate this dissertation to her.

Table of Contents

List of Tables	vi
List of Figures	vii
List of Abbreviations.....	viii
1. Introduction.....	1
1.1. Neutral Sources	8
1.1.1. Enceladus.....	8
1.1.2. Saturn's Atmosphere	11
1.1.3. Titan.....	12
1.1.4. Sputtering of Icy Moons	15
1.1.5. Saturn's Rings.....	15
1.2. Distribution of Neutral Particles.....	16
1.3. Plasma Sources.....	19
1.3.1. Ionization of Neutrals.....	20
1.3.2. Solar Wind.....	22
1.3.3. Ionosphere.....	23
1.4. Ion Transport and Acceleration.....	24
1.5. Ion Composition	25
2. CHEMS Instrument Description and Data Analysis Methods.....	29
2.1. Instrument Description.....	29
2.2. CHEMS Data Types	32
2.3. Differential Intensity from PHA Events.....	34
2.3.1. O^{++} Differential Intensity.....	37
2.3.2. PHA Species Boxes.....	38
2.3.3. Efficiencies	41
2.3.4. Transitioning to Triples Only Data	45
2.3.5. Calculating Partial Number Density	47
2.4. Data Set.....	48
3. Energy and L Variations of the Suprathermal ions: Implications for the Source Strengths	52
3.1. Data Analysis Methods.....	53
3.2. Results.....	55
3.3. Discussion	61
3.3.1. L Variations of the Partial Number Density.....	61
3.3.2. Implications for H^+ and W^+ Source.....	64
3.3.3. Implications for H_2^+ Source.....	66
3.3.4. Implications for O^{++} Source.....	67
3.3.5. Implications for He^{++} and He^+ Source.....	69
4. Energy and L Variations of the Suprathermal Ions: Loss processes in Saturn's Inner Magnetosphere	71

4.1. Results.....	71
4.2. Discussion	74
4.2.1. Lifetimes of Suprathermal Ions.....	74
4.2.2. Persistence of ~100-200 keV Ions	78
4.2.3. Energy and L Variations of H^+ and W^+ FA.....	80
4.2.4. Energy and L Variations of H_2^+ FA	80
4.2.5. Energy and L Variations of O^{++} FA.....	81
4.2.6. Energy and L Variations of He^{++} FA	83
4.2.7. Energy and L Variations of He^+ FA.....	84
5. Composition of 96 keV W^+	86
5.1. Data Analysis Methods.....	87
5.2. Results and Discussion	92
6. C^+ and N^+ in Saturn's Magnetosphere.....	100
6.1. Data Analysis Methods.....	101
6.2. Results and Discussion	103
7. Long-term Time Variations of the Suprathermal Ions	110
7.1. Data Analysis Methods.....	110
7.2. Results and Discussion	112
8. Conclusions and Future Work.....	118
8.1. L Variations.....	118
8.2. Implications for the Source Strengths.....	119
8.3. Loss Processes in Saturn's Inner Magnetosphere	122
8.4. Implications for Saturn's Neutral Cloud.....	124
8.5. Future Work	125
8.6. Concluding Remark	125
Appendix A. List of Time Ranges	127
Appendix B. Tables of Partial Number Densities.....	135
Appendix C. Lifetime Calculations.....	152
Appendix D. Fitting the 96 keV W^+ Distributions.....	173
Appendix E. C^+ and N^+ Partial Number Density Tables	187
References.....	189

List of Tables

1.1	The fields, particles, and waves instruments on Cassini.....	3
1.2	Saturn's icy moons	4
1.3	Estimates of the Enceladus source strength.....	10
2.1	E/Q (keV/e) for each CHEMS DPPS step.....	31
2.2	Data included in each PHA event.....	33
2.3	Mass and M/Q for the CHEMS Basic Rates.....	34
2.4	Mass and M/Q for each species rates box.....	34
2.5	DPPS step of transition to using only the triples data.....	47
2.6	Lower and upper E/Q bounds used to calculate PND	49
3.1	Average FA in the L=15-21 region	60
4.1	Ion-neutral collisions used to calculate lifetimes	76
4.2	Ion-neutral collision lifetimes for each energy range.....	78
4.3	Electron impact and photoionization lifetimes.....	78
5.1	O^+ , OH^+ , H_2O^+ , and H_3O^+ abundances	92
6.1	Lifetimes of 127 keV C^+ , N^+ , and W^+	109
7.1	PND of 27-220 keV/e ions for each long averaging period.....	114
7.2	The H^+/W^+ and H_2^+/W^+ ratio for each long averaging period.....	115
7.3	FA of 27-220 keV/e ions for each long averaging period.....	116

List of Figures

1.1	Diagram of Cassini spacecraft.....	2
1.2	Configuration of Saturn's magnetosphere.....	5
1.3	Tiger stripes at south-pole region of Enceladus.....	9
1.4	Lyman alpha emissions detected by Cassini UVIS.....	13
1.5	Lifetimes of water group neutrals (O, OH, H ₂ O).....	17
1.6	Equatorial water group density.....	18
1.7	Lifetimes of H ₂	19
1.8	H ₂ equatorial density.....	20
1.9	Pick-up ion source rate of O ⁺ , OH ⁺ , and H ₂ O ⁺	22
1.10	Pick-up source rate of H ₂ ⁺	23
2.1	Principles of operation of CHEMS.....	30
2.2	Mass vs. M/Q plot showing range IDs and Species Rates boxes.....	35
2.3	TOF(ch) histogram of E/Q=23.9 keV/e step.....	39
2.4	Essd(ch) versus TOF(ch) plot of E/Q=127 keV/e step.....	40
2.5	Differential Intensity Spectra of H ⁺ and W ⁺	48
2.6	Trajectories of each pass used in this study.....	51
3.1	E/Q versus L PND spectrogram of H ⁺ , W ⁺ , and H ₂ ⁺	56
3.2	E/Q versus L PND spectrogram of He ⁺⁺ , He ⁺ , and O ⁺⁺	57
3.3	(a) 3-8 keV/e H ⁺ and H ₂ ⁺ PND (b) 3-8 keV/e H ₂ ⁺ /H ⁺ ratio vs. L.....	58
3.4	(a) 9-14 keV/e PND vs. L. (b) FA vs. L.....	58
3.5	PND and FA vs. L at 36-55 keV/e, 73-110 keV/e, and 145-220 keV/e.....	59
3.6	Electron impact ionization lifetime of H and O.....	65
3.7	Thermal O ⁺⁺ source rate.....	69
4.1	Ratio of FA at L=6-7 to FA at L=15-21.....	73
4.2	Ion-neutral collision lifetimes versus E/Q.....	77
5.1	Essd(ch) versus TOF(ch) plot of 96 keV W ⁺ distribution.....	88
5.2	Fit of 96 keV O ⁺⁺ TOF(ch) distribution.....	90
5.3	Fit of 96 keV W ⁺ distribution.....	91
5.4	O ⁺ , OH ⁺ , H ₂ O ⁺ , and H ₃ O ⁺ PND and relative abundances vs. L.....	97
6.1	TOF distribution of 127 keV C ⁺ , N ⁺ , and W ⁺	102
6.2	C ⁺ , N ⁺ , and W ⁺ PND versus E/Q.....	104
6.3	(a) 118-136 keV C ⁺ , N ⁺ , and W ⁺ vs. L (b) C ⁺ /W ⁺ and N ⁺ /W ⁺ vs. L.....	105
7.1	Plot of 27-220 keV/e PND from each ring current pass vs. year.....	111
7.2	Cassini Trajectory of each ring current pass.....	112
7.3	Plot of PND and FA of each long averaging period versus year.....	113

List of Abbreviations

CAPS	Cassini Plasma Spectrometer
CHEMS	Charge-Energy-Mass Spectrometer
DPSS	Deflection Plate Power Supply
Essd(ch)	CHEMS solid state detector channel
FA	Fractional Abundance
HST	Hubble Space Telescope
INCA	Ion and Neutral Camera (INCA)
INMS	Cassini Ion Neutral and Mass Spectrometer
LEMMS	Low-Energy Magnetospheric Measurements System
MIMI	Magnetospheric Imaging Instrument
PND	Partial Number Density
SOI	Saturn Orbit Insertion
SSD	Solid State Detector
TOF(ch)	CHEMS time-of-flight channel
UVIS	Cassini Ultraviolet Imaging Spectrograph
W ⁺	Water group ions: O ⁺ , OH ⁺ , H ₂ O ⁺ , and H ₃ O ⁺

Chapter 1

Introduction

Prior to the Cassini mission, most of the information obtained about Saturn's magnetosphere was from the two Voyager spacecraft, Pioneer 11, and the Hubble Space Telescope (HST). Pioneer flew by Saturn in 1979, while the Voyager 1 and 2 flybys were in 1980 and 1981, respectively. These spacecraft were the first to detect and study Saturn's magnetosphere. The Cassini spacecraft (shown in Figure 1.1) was launched October 15, 1997 and entered Saturn's orbit on June 30, 2004. It carries 12 instruments and can observe the electromagnetic spectrum, neutral particles, and ions in Saturn's magnetosphere.

The set of instruments on Cassini can be grouped into 3 categories: optical remote sensing; fields, particles, and waves; and microwave sensing. This thesis focuses mostly on the fields, particles and waves section, particularly the Magnetospheric Imaging Instrument (MIMI). The fields, particles, and waves instruments on Cassini are listed in Table 1.1 along with references that provide a more detailed description of each instrument. Cassini is, as of this writing in 2012, orbiting Saturn and making detailed observations of Saturn's magnetosphere, atmosphere, moons, and system of rings. These observations are providing a better understanding of the various interactions and physical processes that occur in the environment around Saturn.

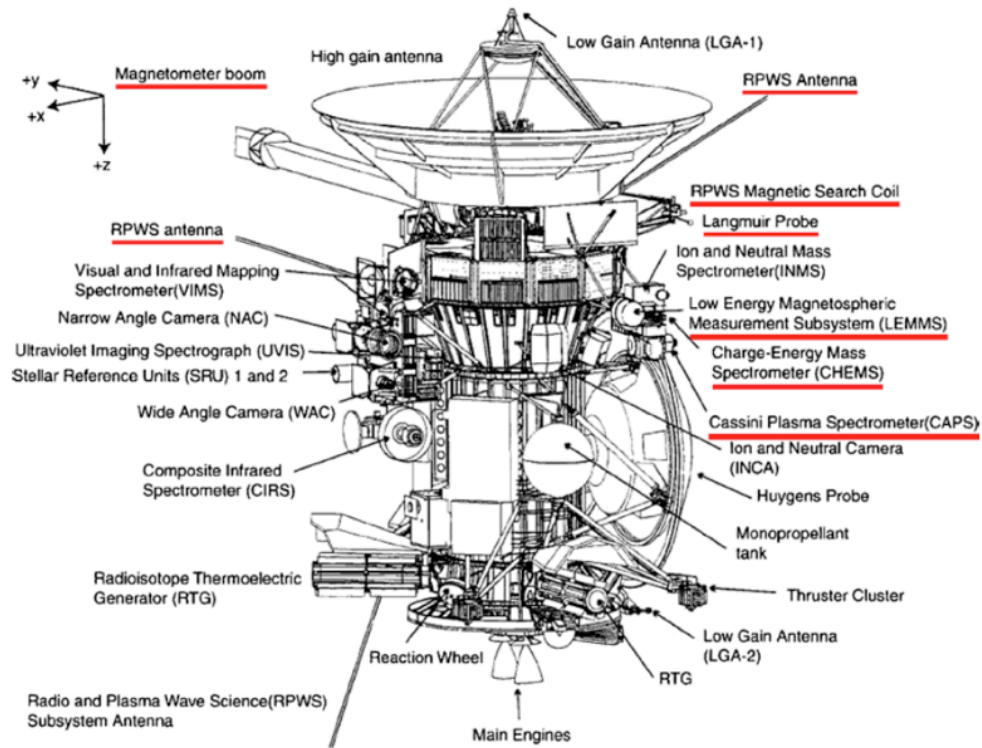


Figure 1.1: Image of the Cassini Spacecraft [Arridge *et al.*, 2012]

Saturn is the 6th planet from the Sun and, with a radius R_S of 60,330 km, is the second largest planet in the solar system. Saturn's magnetosphere was first detected in 1979 when Pioneer 11 observed that Saturn had a magnetic field strong enough to produce a large magnetosphere [Acuna and Ness, 1980; Smith *et al.* 1980]. The field strength at Saturn's surface was deduced to be 0.21 G, which is close to the field strength of Earth (0.3 G), but an order of magnitude less than that of Jupiter (4.2 G). The polarity of Saturn's magnetic field is opposite that of the Earth with the dipole axis parallel to the spin axis [Connery *et al.*, 1984]. The spin axis, however, is tilted 26.7° to the orbital plane, so Saturn has seasons during its 29.5 year orbit.

The interaction between the solar wind and Saturn's dipolar field is similar to that of Earth. Saturn's magnetic field acts as a barrier to the supersonic solar wind, and when the

Table 1.1: The fields, particles, and waves instruments on Cassini

Instrument	Function
Cassini Plasma Spectrometer (CAPS) ^a	Measures energy and ionic charge of thermal (< 30 keV) ions and electrons.
Cosmic Dust Analyzer (CDA) ^b	Detects cosmic dust ~1 millionth of a millimeter in size.
Ion Neutral Mass Spectrometer (INMS) ^c	Detects low energy (< 100 eV) positive ions and neutrals in Saturn's magnetosphere and Titan's atmosphere.
Magnetometer (MAG) ^d	Measures direction and magnitude of Saturn's magnetic field
Magnetospheric Imaging Instrument (MIMI) ^e	Measures ionic charge and energy of energetic (> 3 keV) ions and electrons. Measures composition and direction of motion of energetic neutral atoms.
Radio and Plasma Wave Science (RPWS) ^f	Measures radio waves emitted by Saturn and Titan.

^aYoung *et al.* [2004], ^bSrama *et al.* [2004], ^cWaite *et al.* [2004], ^dDougherty *et al.* [2004],

^eKrimigis *et al.* [2004], ^fGurnett *et al.* [2004]

solar wind hits this barrier, a bow shock is created. When the solar wind crosses the bow shock, it is heated and slowed to a subsonic speed. The region behind the bow shock containing the subsonic solar wind is called the magnetosheath. Since most of the plasma in the magnetosheath cannot penetrate Saturn's magnetic field, a boundary called the magnetopause is created between the magnetosheath and the magnetosphere. The magnetosphere is the region containing Saturn's magnetic field and trapped particles. The size of the magnetosphere varies with solar wind conditions. During periods of high solar wind dynamic pressure, the magnetosphere is compressed as the bow shock and magnetopause are pushed closer to Saturn. When the solar wind dynamic pressure equals its average value of 0.048 nPa [Masters *et al.*, 2008], the distance between the center of Saturn and the subsolar point of the magnetopause is estimated to be about 19 R_S [Kanani *et al.*, 2010].

Unlike the magnetospheres of Earth and Jupiter, Saturn's magnetosphere is dominated by neutral particles with the neutral mass to ion mass ratio of about 12:1 [Bagenal and

Table 1.2: Diameter and Orbiting Distance for the icy moons around Saturn (*Yoder, 1995*)

Icy Moon	Diameter (km)	Orbiting Distance (R_S)
Mimas	397	3.075
Enceladus	498	3.985
Tethys	1060	4.890
Dione	1120	6.28
Rhea	1528	8.750

Delamere 2011]. Saturn's magnetosphere contains several moons and a system of rings giving it several sources of neutral particles. The moon, Enceladus, which orbits at $4 R_S$, was discovered to have

water plumes in its south-pole region, making it the dominant H_2O source [*Waite et al., 2006; Hansen et al., 2006; Porco et al., 2006; Burger et al., 2007*]. A number of icy moons in Saturn's inner magnetosphere (See Table 1.2) are also sources of H_2O and its dissociated products via sputtering, but this source is much weaker than the Enceladus plumes [*Burger et al., 2007; Johnson et al., 2008b*]. Titan, which orbits at $20 R_S$, is usually inside the magnetosphere, but it can be outside the magnetosphere on the dayside during periods of high solar wind dynamic pressure. Titan has a dense atmosphere that is a source of several neutral species (H_2 , CH_4 , N , N_2) [*Johnson et al., 2009*]. Saturn's atmosphere is predicted to be a strong source of atomic H [*Shemansky et al., 2009*]. The ionization of the neutral particles from these sources provides the majority of the plasma to Saturn's magnetosphere.

Figure 1.2 illustrates the configuration of Saturn's magnetosphere and its plasma environment. The region within the closed magnetic field lines is called the plasma sheet. Because the plasma is tied to the field lines and the magnetic field rotates with Saturn, the plasma in this region has an eastward azimuthal velocity. This process is called corotation. Although corotation gives both the ions and electrons an eastward azimuthal velocity, gradient and curvature drifts, which are eastward for ions but westward for

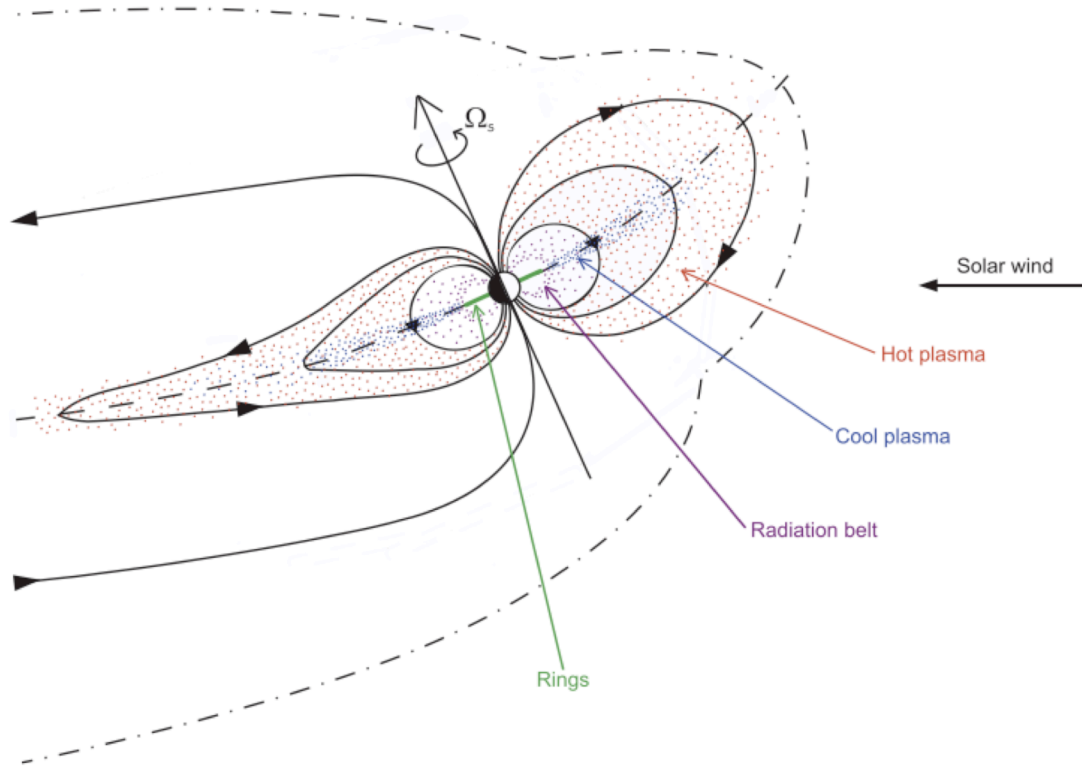


Figure 1.2: A schematic illustrating the configuration of Saturn's magnetosphere and the distribution of plasma particles [Kellett *et al.*, 2009]. The sun is to the right. The dot dashed line is the magnetopause. The dashed line indicates the bowl shape of the magnetic equator observed by Arridge *et al.* [2008a]. The blue dots represent the thermal (cold) plasma that are confined to the equatorial plane, while the red dots represent the energetic (> 3 keV) plasma that extends to higher latitudes. The purple dots in the inner magnetosphere represent the very energetic (> 1 MeV) plasma in the radiation belts.

electrons, gives the ions a larger eastward velocity. The differences in ion and electron velocities produce a current system called the ring current in Saturn's magnetosphere.

The ring current is a term that is also used for the population of particles that produces the azimuthal current. Cassini magnetometer (MAG) observations revealed that the magnetic equator is tilted northward of the dipole equatorial plane and has a bowl shape (See dashed line in Figure 1.2) [Arridge *et al.*, 2008a]. At large radial distances ($> 16.5 R_S$), the ring current distorts the dipole field and stretches it into a disc-like shape called the magnetodisc [Arridge *et al.*, 2007; 2008b].

The full corotation velocity increases linearly with radial distance and is about 200 km/s at 20 R_S , but observations revealed that the azimuthal velocity is less than full corotation [Richardson 1998; Wilson *et al.*, 2008; Thomsen *et al.*, 2010]. This sub-corotation is due to the addition of plasma to Saturn's magnetosphere via the ionization of neutral particles, momentum exchange collisions (e.g. charge exchange), and radial flows [Richardson 1998; Saur *et al.*, 2004; Mauk *et al.*, 2009; Gombosi *et al.*, 2009]. The thermal ions (this term will be used in this thesis to refer to ions with energy < 3 keV) in the plasma sheet are largely confined to the equatorial plane, as shown in Figure 1.2, as a result of the centrifugal force from Saturn's rapid rotation (rotation period = 10.8 hours) [Thomsen *et al.*, 2010].

The more energetic (> 3 keV) ions (also referred to as suprathermal ions in this thesis), however, are not so strongly confined to the equatorial plane (See red dots in Figure 1.2). The energetic ions in the night side plasma sheet extend to $\pm 5 R_S$, while the latitudinal extent of the energetic ions on the dayside can be as high as $\pm 50^\circ$ [Krimigis *et al.*, 2007; Sergis *et al.*, 2009]. The inner boundary of the plasma sheet is located at 8-9 R_S , while the outer boundary extends to the magnetopause on the dayside and beyond Titan's orbit on the night side [Krimigis *et al.*, 2007; Sergis *et al.*, 2009]. In Saturn's inner magnetosphere ($< 5 R_S$) is a region called the radiation belts where large intensities of high energy (> 1 MeV) ions and electrons are observed, but the suprathermal (3-220 keV/e) ions are significantly depleted due to ion-neutral collisions with Saturn's extensive neutral cloud [Paranicas *et al.*, 2008; Kollmann *et al.*, 2011].

Because the ionization of neutral particles is the dominant source of plasma, ion composition measurements provide insight into the strength of the neutral sources. The Cassini instruments that can make *in situ* observations of the ion composition are the Ion and Neutral Mass Spectrometer (INMS) [Waite *et al.*, 2004], Cassini Plasma Spectrometer (CAPS) [Young *et al.*, 2004], and the MIMI Charge-Energy-Mass Spectrometer (CHEMS) [Krimigis *et al.*, 2004]. The INMS instrument detects neutrals and ions at energies less than 100 eV, while the CAPS instrument detects ions with energies ranging from 1 eV to 30 keV (i.e. thermal ions).

This thesis focuses on the more energetic suprathermal (3-220 keV/e) ion composition observed by the CHEMS instrument. We examine passes from 2004-2010 that are within 10° of the equatorial plane in the dipole $L=6-21$ region. In a dipole field, the location of the magnetic field lines can be determined by $r(R_S) = L \cos^2(\lambda)$, where r is the radial distance in units of R_S , L is the L shell parameter, and λ is the latitude. L gives the radial distance in R_S between the center of Saturn and the point where the field line crosses the dipole equatorial plane. Since we only include low latitude passes in this study, the L value is approximately equal to the radial distance in R_S .

In this chapter we give an overview of the various neutral and plasma sources in Saturn's magnetosphere along with current estimates of their strengths. We describe how the neutral particles are ionized and then accelerated to the suprathermal energies where they can then be detected by CHEMS. Chapter 2 contains a detailed description of the CHEMS instrument and describes how we determine the suprathermal ion abundances

for several different ion species. In chapters 3-7, we examine the energy, radial, and time variations of the suprathermal ion composition. These observations provide constraints on the estimates of the neutral source strengths and the composition of Saturn's neutral cloud. We interpret the radial variations of the suprathermal ion partial number density and fractional abundance in terms of transport and loss time scales. Studying the temporal variations of the ion composition provides insight into whether the neutral source strengths varied with time during the period examined (2004-2010).

1.1 Neutral Sources

Saturn's magnetosphere contains multiple sources of neutral particles. The Cassini flybys of the moons Enceladus and Titan as well as remote observations of UV photons by the Cassini Ultraviolet Imaging Spectrograph (UVIS) have provided constraints on the source strengths as well as the distribution of neutral particles. These neutrals are the ultimate source of the suprathermal ions we observe and play a significant role in the depletion of the suprathermal ions inside of 8-11 R_s . Understanding the neutral sources is essential when trying to understand the ion composition and its radial variations.

1.1.1 Enceladus

The remote observation of an extensive OH cloud by the Hubble Space Telescope (HST) indicated the presence of a significant water source in Saturn's magnetosphere [Shemansky *et al.*, 1993]. Using plasma observations by Voyager and the OH observations by HST, Jurac and Richardson [2005] modeled the plasma and neutral particles in Saturn's magnetosphere and predicted that the majority of the H_2O was

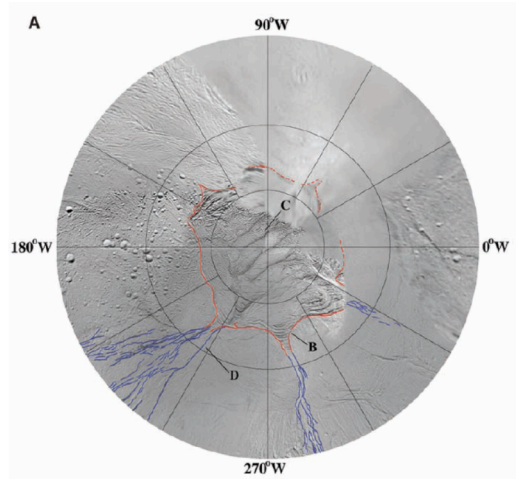


Figure 1.3: Tiger stripes at the south pole region of Enceladus [Porco *et al.*, 2006]. The water plumes in this region are the dominant source of heavy neutral particles to Saturn's magnetosphere.

coming from Enceladus at a rate of $\sim 10^{28}$ $\text{H}_2\text{O/s}$. The discovery of water plumes in the south-pole region of Enceladus by Cassini confirmed their prediction [Waite *et al.*, 2006; Hansen *et al.*, 2006; Porco *et al.*, 2006]. The Cassini Imaging Science System (ISS) observed several 130 km long fractures called “tiger stripes,” where the plume activity is located (see Figure 1.3) [Porco *et al.*, 2006]. Burger *et al.*

[2007] analyzed the INMS and UVIS observations from the E3 Enceladus fly-by and estimated a source strength consistent with the Jurac and Richardson [2005] prediction ($\sim 10^{28}$ $\text{H}_2\text{O/s}$).

The models by Saur *et al.* [2008] and Smith *et al.* [2010], however, suggest that the plume source strength varies significantly with time and can be as low as $\sim 0.6\text{--}0.7 \times 10^{28}$ $\text{H}_2\text{O/s}$. Using the magnetic field observations from the first three Enceladus fly-bys (E0, E1, E2) and the neutral measurements from the E2 fly-by, Saur *et al.* [2008] suggests that the source strength dropped nearly an order of magnitude from $\sim 5.4 \times 10^{28}$ $\text{H}_2\text{O/s}$ to 0.67×10^{28} $\text{H}_2\text{O/s}$ in the 20-day period from the Enceladus flybys E0 to E1. Smith *et al.* [2010] fit the INMS data from three Enceladus fly-bys (E2, E3, and E5) and concluded that the source strength increased by a factor of four in the seven-month period from E3 ($\sim 6.3 \times 10^{27}$ $\text{H}_2\text{O/s}$) to E5 ($\sim 2.5 \times 10^{28}$ $\text{H}_2\text{O/s}$). The models by Dong *et al.* [2011] and Jia *et*

Table 1.3: Estimates (in molecules per second) of the Enceladus source strength from models based on observations during Cassini Enceladus fly-bys.

Fly-by	<i>Saur et al.</i> [2008]	<i>Smith et al.</i> [2010]	<i>Dong et al.</i> [2011]	<i>Jia et al.</i> [2010]
E0 02/17/2005	5.4×10^{28}	-	-	3.2×10^{28}
E1 03/09/2005	0.67×10^{28}	-	-	2.2×10^{28}
E2 07/14/2005	0.67×10^{28}	0.04×10^{28} ^a	-	2.8×10^{28}
E3 03/12/2008	-	0.63×10^{28}	1.7×10^{28}	3.2×10^{28}
E4 08/11/2008	-	-	-	2.4×10^{28}
E5 10/09/2008	-	2.5×10^{28}	3.5×10^{28}	2.6×10^{28}
E6 10/31/2008	-	-	-	2.6×10^{28}
E7 11/02/2009	-	-	$1.5\text{-}1.9 \times 10^{28}$	-

^a The low E2 source rate from *Smith et al.* [2010] is likely due to the INMS data from the E2 fly-by being underestimated by a factor of $\sim 3\text{-}6$ [*Teolis et al.*, 2010].

al. [2010], however, predict far more moderate variations and estimate the source strength to only range from $\sim 1.5\text{-}3.5 \times 10^{28}$ H₂O (See Table 1.3).

Remote observations suggest that the Enceladus source is nearly constant. The Heterodyne Instrument for the Far Infrared (HIFI) on the Herschel Space Observatory observed the infrared emissions of H₂O in the Enceladus torus on 3 days: June 23, 2009; July 8, 2009; and June 24, 2010 [*Hartogh et al.*, 2011]. Based on these observations, *Hartogh et al.* [2011] estimated the source strength to be 0.85×10^{28} H₂O/s for all three days and concluded the plumes varied little with time. Analysis of Cassini UVIS observations of atomic oxygen from 2003 day 359 to 2004 day 142 indicated that the

total number of oxygen atoms within 10 R_S of Saturn only varied from $\sim 3.0\text{--}3.5 \times 10^{34}$, suggesting a nearly constant source of atomic oxygen [Melin *et al.*, 2009]. One of the main parts of this dissertation concerns the long-term (six years) variations of the suprathermal ion density and what it has to say about the variability of the Enceladus source strength.

In addition to H_2O , Cassini INMS detected several other neutral species in the Enceladus plumes. Combining the results from five Enceladus flybys, INMS observations revealed a plume composition of about 90% H_2O , 5.3% CO_2 , 0.9% CH_4 , 0.8% NH_3 , less than 0.74% HCN , and several other minor species (e.g. argon, hydrocarbons, etc) [Waite *et al.*, 2009]. A neutral species with a mass of 28 daltons was detected and estimated to make up about 4% of the plume composition [Waite *et al.*, 2006]. The mass 28 signal is most likely a combination of N_2 , CO , and C_2H_4 , but the INMS instrument did not separate these species [Waite *et al.*, 2009]. Analysis of Cassini UVIS observations of the plumes suggests that CO and N_2 make up less than 3% and 0.5% of the plume composition, respectively [Hansen *et al.*, 2008, 2011].

1.1.2 Saturn's Atmosphere

The Voyager Ultraviolet Spectrometer (UVS) and Cassini UVIS both detected an extensive neutral H cloud in Saturn's magnetosphere by observing the Lyman alpha radiation scattered by these particles [Shemansky and Hall 1992; Shemansky *et al.*, 2009; Melin *et al.*, 2009]. While it's possible that neutral H can be produced via water dissociation [Jurac and Richardson 2005], analysis of Cassini UVIS data suggested that

most of the neutral H is emitted by a plume on the sunlit side of Saturn's atmosphere at a rate of $\sim 3 \times 10^{30}$ H/s [Shemansky *et al.*, 2009]. The plume is centered at -13.5° latitude with the full width half max (FWHM) increasing outward from $0.56 R_S$ at a radial distance of $1 R_S$ to a FWHM of $1.7 R_S$ at $4 R_S$ [Shemansky *et al.*, 2009]. As a result, the largest emission intensities are observed below the ring plane rather than in the equatorial plane as shown in Figure 1.4 [Shemansky *et al.*, 2009; Melin *et al.*, 2009].

1.1.3 Titan

Titan has a dense atmosphere (surface pressure ~ 1 atm.) that is over 95% N_2 with CH_4 and H_2 being the second and third most abundant constituents [See Strobel *et al.*, 2009 for a summary of the composition of Titan's atmosphere]. The escape of neutral particles from Titan's atmosphere makes it a potential source of H_2 , CH_4 , N, and N_2 . Several processes may be responsible for the escape of these neutrals and these escape processes are still not fully understood [See Johnson *et al.*, 2009 for details]. To escape from the atmosphere, a neutral particle must have an outward radial velocity greater than the escape velocity and have a low probability of colliding with other particles. Therefore, atmospheric escape typically occurs in a region of the upper atmosphere called the exosphere or corona where the mean free path is greater than the atmospheric scale height. The lower boundary of the exosphere is called the exobase.

Neutrals in Titan's upper atmosphere can be heated by absorbing solar UV and EUV photons (i.e. photochemical induced escape) or by the impact of plasma on Titan's upper atmosphere (i.e. plasma induced escape or sputtering), leading to the production of hot

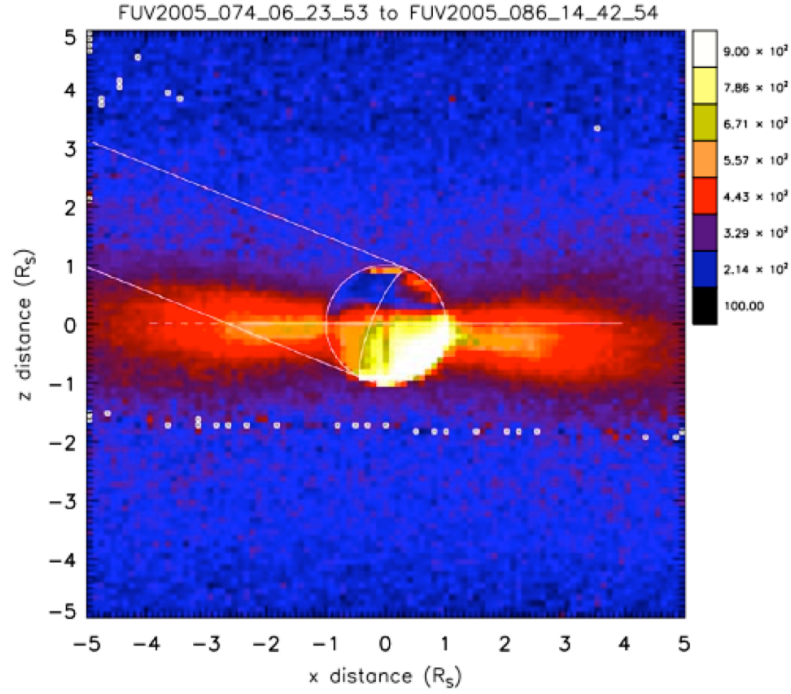


Figure 1.4: Lyman alpha emissions detected by Cassini UVIS prior to SOI [Melin *et al.*, 2009]. The sun is to the right. The strongest atomic H emissions are observed on the sunlit side of Saturn's atmosphere beneath the equatorial plane suggesting that a hydrogen plume from Saturn's upper atmosphere emits the majority of the neutral H.

neutrals and atmospheric escape [Johnson 1990; Johnson *et al.*, 2008a, 2009]. Because Titan can be in a variety of plasma environments depending on where it is in its orbit and solar wind conditions (plasma sheet, lobes, magnetosheath) [Rymer *et al.*, 2009a], the escape rate due to atmospheric sputtering will vary greatly [Johnson *et al.*, 2009; Cui *et al.*, 2011; Westlake *et al.*, 2011].

The estimates of the H_2 escape rates have been relatively consistent. Prior to Cassini, the H_2 escape rate was estimated to be $\sim 1-3 \times 10^{28} H_2/s$ [Lebonnois *et al.*, 2003]. Cui *et al.* [2008] analyzed Cassini INMS data from several Titan fly-bys and calculated a similar escape rate of $\sim 10^{28} H_2/s$. Neutral H_2 can also be produced by the dissociation of water emitted by Enceladus, but this source rate is only $\sim 3 \times 10^{26} H_2/s$ [Tseng *et al.*, 2011a].

Thus, Titan appears to be the dominant source of H₂ outside of ~6 R_S, while the Enceladus H₂ source plays a more significant role inside of 6 R_S [Tseng *et al.*, 2011a].

While the estimated H₂ escape rates appear to be consistent, there are large variations in the estimates of the heavy neutral escape rates. Using INMS observations from three Titan fly-bys, *De La Haye et al.* [2007a] fit the energy distribution of N₂ and CH₄ and estimated an escape rate of 1.6×10^{26} N/s and 5.9×10^{25} CH₄/s. *Shematovich et al.* [2003] modeled the heating rates due to sputtering and solar photons and calculated an escape rate ($\sim 3.6 \times 10^{25}$ N/s) much less than that predicted by *De La Haye et al.* [2007a].

Similarly, *De La Haye et al.* [2007b] estimated the photochemical induced escape rates and concluded that the heating was not sufficient to result in the escape rate estimated by *De La Haye et al.* [2007a].

Slow hydrodynamic escape has been proposed to explain the heating of the neutral particles in Titan's upper atmosphere [Strobel, 2008, 2009]. Unlike photochemical escape, hydrodynamic escape occurs when the atmosphere is heated well below the exobase by solar UV photons. The heating is transported upward via thermal conduction resulting in an outward expansion of the atmosphere and a large escape rate. The hydrodynamic escape rate of N₂ is negligible, but the hydrodynamic escape of H₂ and CH₄ is estimated to be 9.2×10^{27} H₂/s and 1.7×10^{27} CH₄, respectively [Strobel, 2008, 2009]. While the H₂ escape rate is consistent with *Cui et al.* [2008], the CH₄ escape rate is much larger than the estimates by *De La Haye et al.* [2007a]. Monte Carlo models suggest that thermal conduction above the exobase is not able to heat neutrals as much as

predicted by *Strobel's* [2008, 2009] model and that *Strobel's* [2008, 2009] hydrodynamic escape rates likely overestimate the escape of neutral particles from Titan's atmosphere [Tucker and Johnson, 2009; Johnson 2010; Schaufelberger et al., 2012].

1.1.4 Sputtering of Icy Moons

The sputtering of Saturn's icy moons (e.g. Enceladus, Tethys, Dione, Rhea, etc.) by magnetospheric plasma is another potential source of H₂O. Sputtering occurs when energetic ions collide with the surfaces of Saturn's icy moons and eject neutral particles into the surrounding space [Johnson 1990; Johnson et al., 2008b]. Prior to the Cassini mission, sputtering was thought to be a significant source of H₂O, but the discovery of the Enceladus plumes revealed that it was a relatively weak source. The estimated source strength of sputtering ($\sim 1\text{--}8 \times 10^{25}$ H₂O/s) is two to three orders of magnitude less than the Enceladus plume source strength [Burger et al., 2007; Johnson et al., 2008b].

1.1.5 Saturn's Rings

Saturn's main rings extend from 1.23–2.27 R_S and consist mostly of water ice [Cuzzi et al., 2009]. H₂O can be emitted from the rings via sputtering, photolysis, and collisions with meteoroids [Cuzzi et al., 2009; Mauk et al., 2009], but the H₂O quickly re-condenses over the main rings making the rings a weak H₂O source in Saturn's magnetosphere [Johnson et al., 2006]. Both O₂ and H₂ are produced via photodecomposition of ice and do not re-condense as quickly as H₂O, making the rings a source of H₂ and O₂ [Johnson et al., 2006a; Tseng et al., 2010, 2011a]. Tseng et al. [2011a] estimate the ring H₂ source strength to be $\sim 2.0 \times 10^{26}$ H₂/s, which is much less than the estimated Titan source strength

of 10^{28} H₂/s calculated by *Cui et al.* [2008]. The H₂ ring source is only significant in Saturn's inner magnetosphere, while the Titan H₂ source dominates outside of $\sim 6 R_S$ [*Tseng et al.*, 2011a].

The ring O₂ source strength depends on the incident angle between the solar UV photons and the rings. The O₂ source is estimated to be $\sim 1 \times 10^{26}$ O₂/s during Saturn Orbit Insertion (SOI) when the incident angle was 24° , and drops an order of magnitude to $\sim 1 \times 10^{25}$ O₂/s during equinox [*Tseng et al.*, 2010]. Even near the solstice, the ring source is relatively weak compared to the Enceladus water source. The O₂ production rate may be enhanced due to the ring absorption of plasma and also of neutrals from the Enceladus plumes [*Tseng et al.*, 2011b]. Further modeling is needed to obtain a better estimate of this effect.

We have discussed the major neutral sources in Saturn's magnetosphere. We will now describe the resulting neutral cloud and provide recent estimates of the neutral particle density for the atomic H, water group neutrals, and H₂. These three species become the most abundant suprathermal ion species. Understanding how these particles are spread from their sources is important to the production of suprathermal particles since the primary acceleration processes occur or are initiated in the middle and outer magnetosphere.

1.2 Distribution of Neutral Particles

The neutral particles from the Enceladus plumes are spread throughout Saturn's magnetosphere by charge exchange collisions, dissociation, and neutral-neutral collisions

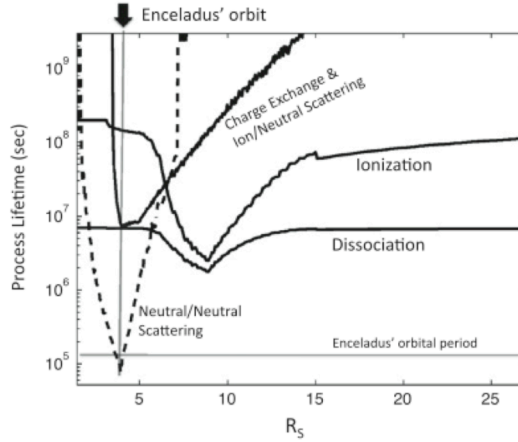


Figure 1.5: Lifetimes of water group neutrals (O, OH, H₂O) due to various processes [Cassidy and Johnson 2010]. All three ion species have approximately the same ionization lifetimes. The dissociation lifetime is approximately the same for OH and H₂O and does not apply to O. Cassidy and Johnson [2010] only included the most common reactions (H₂O → H + OH and OH → O + H) in their dissociation lifetime calculations.

[Johnson *et al.*, 2006b; Melin *et al.*, 2009;

Farmer 2009; Smith *et al.*, 2010; Cassidy

and Johnson 2010]. The estimated

lifetimes due to these collisions are shown

in Figure 1.5. Remote observations by

Cassini UVIS and HST revealed that

Saturn's magnetosphere contains extensive

O and OH clouds with the atomic O cloud

being about twice as broad as the OH

cloud [Shemansky *et al.*, 1993; Melin *et*

al., 2009]. Smith *et al.* [2010] concluded

that photo-dissociation of H₂O and OH is largely responsible for spreading the OH and O throughout the magnetosphere. However, outside of ~8 R_s the O cloud predicted by Smith *et al.* [2010] is not in agreement with the UVIS observations. Assuming the UVIS results are correct, the discrepancy may be the result of neglecting the effect of neutral-neutral collisions in the model, which is another effective mechanism for spreading neutral particles [Farmer 2009].

Cassidy and Johnson [2010] include the effects of neutral-neutral collisions in their model, and although their estimates of the O density are in better agreement with the observations of Melin *et al.* [2009], there is still a factor of two discrepancy between their model and the UVIS results outside of 10 R_s. The O, OH, and H₂O densities predicted by the Cassidy and Johnson [2010] model are shown in Figure 1.6. Including the collisions

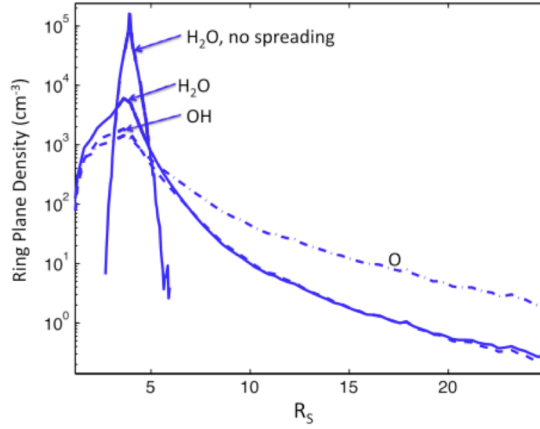


Figure 1.6: Equatorial water group density of O, OH, and H₂O from *Cassidy and Johnson* [2010] model. The H₂O, no spreading line does not include the effect of neutral-neutral collisions and results in a very narrow H₂O torus. Including the collisions between neutral particles results in a much broader H₂O distribution.

between neutrals significantly increases the H₂O density in Saturn's middle and outer magnetosphere. Models that ignore neutral-neutral collisions [*Johnson et al.*, 2006b; *Smith et al.*, 2010] predict a narrow H₂O torus centered on Enceladus with a negligible H₂O density outside of 6 R_S, while including the neutral-neutral collisions results in an H₂O cloud with approximately the same density as OH

outside of 7 R_S [*Cassidy and Johnson* 2010].

The atomic hydrogen cloud consists of a ballistic component confined to Saturn's inner magnetosphere ($< 5 R_S$) and an orbiting component that extends to $> 45 R_S$ in the equatorial plane [*Shemansky et al.*, 2009; *Melin et al.*, 2009]. To escape Saturn's atmosphere, atomic H requires a launching energy of 5.5 eV at the equator and 7.2 eV at the poles [*Shemansky et al.*, 2009]. Hydrogen atoms launched at energies less than the escape energy make up the ballistic component that has a short average lifetime of ~ 5 hours due to re-absorption by Saturn's atmosphere [*Shemansky et al.*, 2009]. The ballistic component comprises about 25% of the hydrogen within 5 R_S [*Shemansky et al.*, 2009]. The hydrogen cloud shows significant local time asymmetries. The brightest H emissions are observed on the dusk side [*Shemansky and Hall* 1992] and the H cloud on the dayside tends to be more compact [*Melin et al.*, 2009]. The H density at the orbit of Enceladus is

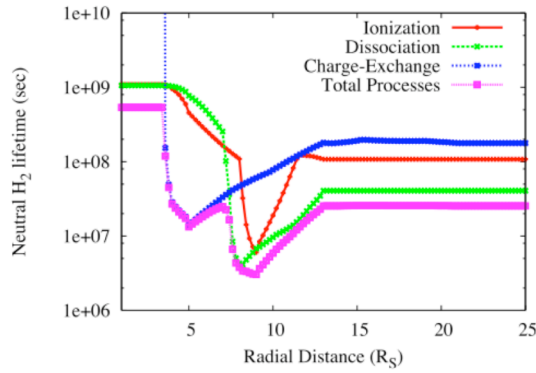


Figure 1.7: H_2 lifetimes versus radial distance [Tseng *et al.*, 2011a]. Blue is the charge exchange lifetime, red is the ionization lifetime, and green is the dissociation lifetime. Magenta is for all three processes combined.

estimated to range from 450 cm^{-3} to 1600 cm^{-3} depending on the local time

[Shemansky *et al.*, 2009].

Since H_2 has multiple sources (Titan, dissociation of H_2O from Enceladus, Rhea, and Saturn's rings), its distribution is more complicated. The H_2 lifetimes due

to ionization, dissociation, and charge exchange are shown in Figure 1.7 [Tseng *et al.*, 2011a]. The distribution of H_2 from all four sources was modeled by Tseng *et al.* [2011a] and is shown in Figure 1.8. The H_2 from the Titan source clearly dominates outside of $6 R_S$, while the Enceladus and ring source produce a dense H_2 cloud over the main rings [Tseng *et al.*, 2011a]. The Rhea source is much weaker than the other three sources and appears to play a minor role [Tseng *et al.*, 2011a].

1.3 Plasma Sources

Ionization of these neutral particles from local sources produces most of the plasma in Saturn's magnetosphere, so ion composition information can provide insight into the strength of the neutral sources. However, differences among the dissociation and ionization rates, and possibly acceleration times, prevent a one to one correspondence between the ion densities and relative neutral source strengths. Other plasma sources include the solar wind and Saturn's ionosphere, but these sources are less important.

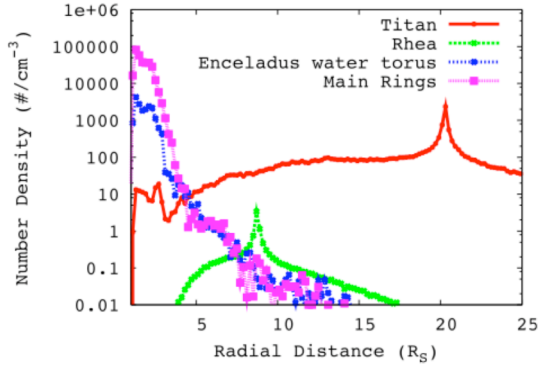


Figure 1.8: H_2 equatorial density versus radial distance from the four major H_2 sources [Tseng et al., 2011a]. Red is the H_2 cloud produced by Titan, magenta is the H_2 cloud produced by the rings, blue is the H_2 cloud produced by Enceladus, and green is the H_2 cloud produced by Rhea.

1.3.1 Ionization of Neutrals

Neutral particles can be ionized by electron impact, photo-ionization, and charge exchange. The ionization lifetimes for the water group neutrals [Cassidy and Johnson 2010] and H_2 [Tseng et al., 2011a] are shown in Figures 1.5 and 1.7, respectively. The electrons in Saturn's magnetosphere consist of a cold

component and a hot component [Sittler et al., 1983; Rymer et al., 2007, 2008; Schippers et al., 2008]. The temperature of both components were observed to peak near $\sim 9 R_S$ [Schippers et al., 2008] resulting in the low ionization lifetimes in this region. The photoionization lifetimes are much longer at $9 R_S$ and are estimated to be $\sim 2 \times 10^8$ s for the neutral water group [Cassidy and Johnson 2010] and $\sim 1.1 \times 10^9$ s for H_2 [Tseng et al., 2011a]. Photoionization only appears to play a significant role inside of $5 R_S$ and outside of ~ 13 - $15 R_S$.

The charge exchange lifetimes minimize near $\sim 4 R_S$ at the center of the Enceladus torus. Although charge exchange collisions do not change the total ion density, they can cause variations in the ion composition. The majority of the H_3O^+ in Saturn's magnetosphere is likely produced in the Enceladus torus by charge exchange reactions between H_2O and the ions O^+ , OH^+ , and H_2O^+ [Cravens et al., 2009; Fleshman et al., 2010a].

The pick-up ion source rate is determined by dividing the neutral density of a particular species by its ionization lifetime. Because neutrals have a much lower velocity than the plasma, an ion produced via ionization of Saturn's neutral cloud initially has a much lower energy than the thermal plasma, let alone the suprathermal ions detected by CHEMS. The newly created ion will be accelerated by the corotation electric field and will be given energy by drifting eastward at the corotation velocity as well as gyrating about the magnetic field lines at the corotation speed [Hill et al., 1983; Mauk et al., 2009]. The corotation energy E_{corot} is given by

$$E_{\text{corot}} = \frac{1}{2} m V_{\text{corot}}^2 \quad (1.1)$$

where m is the mass of the ion and V_{corot} is the local corotation speed. The amount of energy gained by the newly created ion is twice the local corotation energy and depends on the radial distance at which the ionization occurs. The local corotation speed is estimated to range from 50% to 70% of the full corotation speed [Thomsen et al., 2010]. At 60% of full corotation, V_{corot} is 30 km/s at 5 R_S and 119 km/s at 20 R_S . At these local corotation velocities, the total energy (i.e. corotation plus cyclotron energy) of newly created H^+ would be increased to 9.4 eV at 5 R_S and 150 eV at 20 R_S , while the total energy of newly created O^+ ions would be increased to 150 eV at 5 R_S and 2.4 keV at 20 R_S .

The pick-up ion source rate of O^+ , OH^+ , and H_2O^+ from the *Smith et al.* [2010] model is shown in Figure 1.9. The small H_2O^+ production rate outside of $\sim 6 R_S$ is due to the very small H_2O densities in this region predicted by the *Smith et al.* [2010] model and not a

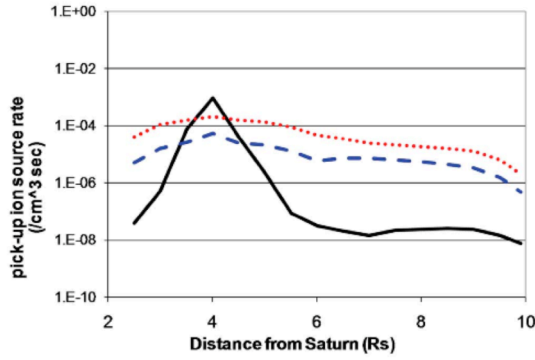


Figure 1.9: Pick up ion source rate of O^+ , OH^+ , and H_2O^+ assuming an Enceladus source strength $\sim 6 \times 10^{27}$ H_2O/s [Smith et al., 2010]. The black line is H_2O^+ , the blue dashed line is OH^+ , and the red line is O^+ .

peak near $\sim 9 R_S$, the pick-up ion source rates do not decrease as quickly away from the Enceladus torus as do the neutral densities.

The H_2^+ source rates from the Tseng et al. [2011a] study are shown in Figure 1.10. With the exception of the peaks near Titan's orbit, $\sim 9 R_S$, and over the main rings, the H_2^+ source rate is $\sim 10^{-6}$ $H_2/cm^3/s$, which is less than the pick-up source rate of the water group ions. The peak near Titan's orbit reflects that Titan is a significant source of H_2 . The peak near Rhea, however, is due to the peak in electron impact ionization near $\sim 9 R_S$ and does not indicate that Rhea is a significant source of H_2 . The photoionization of the dense neutral cloud over the main rings produces the large H_2^+ source rate in Saturn's inner magnetosphere.

1.3.2 Solar Wind

Some solar wind plasma can enter the magnetosphere via magnetic reconnection at the magnetopause. Studies involving reconnection at Saturn's magnetopause is relatively

difference in ionization rates. If the H_2O is spread to the outer magnetosphere like Cassidy and Johnson [2010] predict, then the H_2O^+ pick up ion source rate would increase considerably in the outer magnetosphere. Because the electron impact ionization rates are predicted to increase outward away from $4 R_S$ and

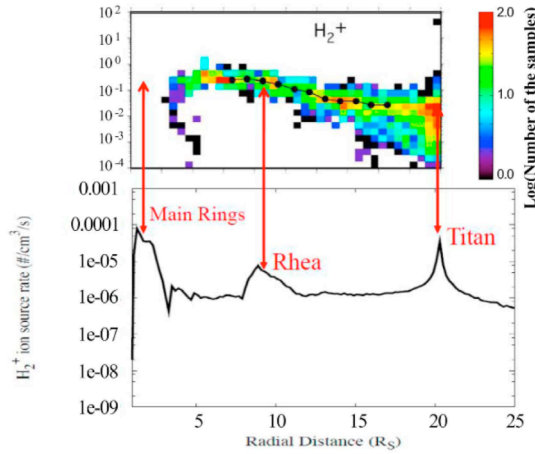


Figure 1.10: The bottom plot shows H_2^+ production rates at the equator as predicted by the *Tseng et al.* [2011a] model. The top plot is the thermal H_2^+ number density vs. L from *Thomsen et al.* [2010].

estimated source strength of $\sim 4 \times 10^{26} \text{ H}^+/\text{s}$ [Hamilton et al., 1983]. However, the $\text{H}^+/\text{He}^{++}$ ratio is observed to be much larger in Saturn's magnetosphere than in the solar wind [McDonald et al., 1980; Hamilton et al., 1983]. These observations suggest that the majority of H^+ is produced from local sources and that the solar wind provides only $\sim 10\%$ of the H^+ .

1.3.3 Ionosphere

At high latitudes along open field lines, a supersonic flow called polar wind escapes from Saturn's ionosphere to Saturn's magnetosphere. Since Saturn's ionosphere is dominated by H^+ and H_3^+ , the polar wind is a source for these two species. Applying a polar wind outflow model, *Glocer et al.* [2007] estimated the source strength to be 2.1×10^{26} - 7.5×10^{27} ions/s with comparable amounts of H^+ and H_3^+ . However, CHEMS has observed a much lower abundance of H_3^+ relative to H^+ ($\text{H}_3^+/\text{H}^+ \sim 0.1\%$) [Mauk et al., 2009] indicating that

limited, but there is some evidence that it occurs [McAndrews et al., 2008]. Because Saturn's magnetosphere does not contain an internal source of helium, He^{++} and He^+ are tracers for the solar wind source and interplanetary pick-up ions of interstellar origin that are carried by the solar wind, respectively. The solar wind

is also a potential source of H^+ with an

the polar wind plasma source is probably much less than that predicted by *Glocer et al.* [2007].

Both the ionosphere and solar wind are much weaker plasma sources than the ionization of neutral particles in Saturn's magnetosphere. The thermal ions dominate the plasma density and have velocities approximately equal to the local corotation speed. To reach the suprathermal (3-220 keV/e) energies detected by CHEMS, the thermal ions must be accelerated. We will now discuss the processes largely responsible for accelerating thermal ions to surpathermal energies.

1.4 Ion Transport and Acceleration

As in Jupiter's magnetosphere, the combination of a strong internal plasma source and a fast rotation rate makes Saturn's magnetosphere centrifugally unstable [*Mauk et al.*, 2009]. The centrifugal instability causes injection events where hot, tenuous plasma from the outer magnetosphere moves inward and replaces outward moving, dense thermal plasma inside of $\sim 10-11 R_S$ [*Hill et al.*, 2005; *Burch et al.*, 2005; *Mauk et al.*, 2005]. The hot inward flows occupy only about 5-10% of the longitudinal space indicating that the outward flows of the thermal plasma are much broader [*Chen and Hill*, 2008, 2010]. The outward radial velocity is much less than the local corotation velocity, so the thermal plasma velocity is largely in the azimuthal direction, particularly inside of $20 R_S$ [*Chen and Hill* 2010; *Wilson et al.*, 2008; *Thomsen et al.*, 2010].

Injection events are grouped into two categories: low energy and high energy [Mitchell *et al.*, 2009a]. Low energy events accelerate ions to tens of keV and largely originate in the middle magnetosphere ($\sim 9-11 R_S$) [Burch *et al.*, 2005; Hill *et al.*, 2005; Rymer *et al.*, 2009b]. The low energy events occur at all local times, but show a preference of occurring at the local times between three and nine (LT=12 is midnight) [Chen and Hill, 2008]. High energy events accelerate ions to hundreds of keV and originate near midnight at larger radial distances in the magnetotail [Mauk *et al.*, 2005; Paranicas *et al.*, 2007; Mitchell *et al.*, 2009b]. These high energy events appear to be triggered by reconnection in the magnetotail and the creation of plasmoids [Mitchell *et al.*, 2009b].

Ions are also energized by inward radial diffusion into regions of stronger magnetic field [Van Allen 1980; Armstrong *et al.*, 1983; Kollmann *et al.*, 2011]. Acceleration by inward radial diffusion occurs when plasma from the outer magnetosphere is transported inward while conserving its first and second adiabatic invariant:

$$\mu = \frac{p_{\perp}^2}{2mB} \quad (1.2)$$

$$J = \int_{M1}^{M2} p_{\parallel} ds \quad (1.3)$$

[Mauk *et al.*, 2009]. The first adiabatic invariant μ is the magnetic moment and depends on the momentum perpendicular to the magnetic field p_{\perp} , the particle mass m , and the magnetic field strength B . The second invariant J is the longitudinal invariant and is determined by integrating the momentum parallel to the magnetic field p_{\parallel} along the magnetic field line between the mirror points $M1$ and $M2$. Because the magnetic field strength increases inward and the distance between the mirror points decreases inward,

plasma will gain energy when it is adiabatically transported from the outer to the inner magnetosphere.

1.5 Ion Composition

Prior to Cassini, plasma composition measurements were largely limited to the Voyager fly-bys. Observations of the thermal ions by the Voyager Plasma Science Experiment (PLS) revealed Saturn's plasma to consist of a proton component and a heavy ion component [Lazarus and McNutt 1983; Richardson 1998]. Voyager could not conclusively determine the composition of the heavy ions, but fits to the data gave an estimate of ~ 16 amu for the heavy ion component [Lazarus and McNutt 1983; Richardson 1998]. This estimate suggested the heavy ion component consisted largely of O^+ , but the possibility that it contained significant amounts of N^+ [Eviatar et al., 1983] as well as OH^+ and H_2O^+ [Richardson 1998] could not be ruled out.

Observations of the high energy (> 0.5 MeV) ions by the Voyager Low Energy Charged Particle (LECP) revealed that the energetic ion composition was dominated by H^+ with H_2^+ being the second most abundant species [Hamilton et al., 1983]. Since the composition of the He, C, and O ions were similar to that of the solar wind, Hamilton et al. [1983] concluded that the solar wind was the most likely source for plasma at these high energies. At lower energies, however, the sources of the heavy ions are local.

Cassini has provided the first mass resolved measurements of Saturn's ion composition at low energies and greatly improved our understanding of the plasma environment. Cassini

observations of both the thermal (< 30 keV) [Young *et al.*, 2005; Thomsen *et al.*, 2010] and the suprathermal (> 3 keV) [Krimigis *et al.*, 2005; DiFabio *et al.*, 2011] ions revealed that Saturn's ion composition is dominated by H^+ and W^+ with H_2^+ being the third most abundant ion species. In the equatorial plane, W^+ dominates the thermal ion density in Saturn's inner magnetosphere, but the W^+ and H^+ density becomes comparable outside of $\sim 13 R_S$ [Thomsen *et al.*, 2010]. The H_2^+/H^+ ratio peaks near the orbit of Titan suggesting that Titan is a strong source of H_2 [Thomsen *et al.*, 2010].

Cassini observations revealed that N^+ is a relatively minor ion species at both thermal [Young *et al.*, 2005; Smith *et al.*, 2005, 2007] and suprathermal [Krimigis *et al.*, 2005] energies. For radial distances between ~ 4 to $13 R_S$, the thermal N^+/W^+ ratio is typically ~ 0.10 , but can be as high as 0.15 - 0.40 inside the Enceladus torus [Smith *et al.*, 2007]. At suprathermal energies, however, the N^+/O^+ ratio was observed to be less than 0.05 during SOI [Krimigis *et al.*, 2005]. The reason for this discrepancy is not clear, but these low N^+/W^+ ratios suggest that the Titan nitrogen source is weaker than previously expected and that Enceladus can in fact be the strongest source of nitrogen in Saturn's inner magnetosphere as well as the overwhelming source of water group ions [Smith *et al.*, 2005; 2007].

In this thesis, the CHEMS data are analyzed to study the suprathermal ion composition in Saturn's magnetosphere. In chapters 3 and 4, we determine the partial number densities and fractional abundances of six ion species (H^+ , H_2^+ , W^+ , He^{++} , He^+ , and O^{++}) to study how these quantities vary with energy and L . In chapter 5 we separate W^+ into its four

main components (O^+ , OH^+ , H_2O^+ , H_3O^+) to study the composition of the water group ions. In chapter 6 we examine the C^+ and N^+ abundances and compare them to that of W^+ . The analysis in chapters 5 and 6 can only be done for a relatively narrow energy range, so we only consider the composition in the main ring current region (dipole $L=7-16$) and the L variations in these two chapters. In chapter 7, we study the long-term time variations of the 27-220 keV/e partial number densities and fractional abundances of the six species studied in chapters 3 and 4.

The estimates of the neutral source strength contain a great deal of uncertainty. The ion composition measurements presented in this paper provide constraints on the neutral source strengths. We compare our fractional abundances and abundance ratios to the current estimates of the source strengths. Determining the W^+ composition provides insight into the composition and distribution of the neutral cloud produced by the Enceladus plumes. We estimate the collision lifetimes of each suprathermal ion species and compare them to the L variations of the fractional abundances in Saturn's inner magnetosphere. Studying the temporal variations will provide insight into whether or not the neutral source strengths varied with time during the six year period between the end of 2004 to the end of 2010.

Chapter 2

CHEMS Instrument Description and Data Analysis Methods

In this chapter we describe the CHEMS instrument and how to calculate the differential intensities and partial number densities for several ion species: H^+ , H_2^+ , He^{++} , He^+ , O^{++} , C^+ , N^+ , and W^+ (O^+ , OH^+ , H_2O^+ , H_3O^+). The data presented in this thesis are from several equatorial orbits from the end of 2004 to the end of 2010. We will discuss the criteria used to select these orbits and show their trajectories at the end of this chapter. See *Krimigis et al.* [2004] for a more detailed description of the CHEMS instrument. A more detailed discussion about how to calculate the differential intensities can be found in the MIMI user guide [*Vandegriff et al.*, 2012]. Here, we only briefly summarize how we perform this calculation.

2.1 Instrument Description

A diagram showing the principle of operation of CHEMS is shown in Figure 2.1.

CHEMS uses energy per charge (E/Q) selection followed by time-of-flight (TOF) versus energy measurements to identify positive ions with $E/Q=3-220$ keV/e. CHEMS has an overall field of view of $159^\circ \times 4^\circ$ with the large angle divided into three independent sections called telescopes. With the measurement of E/Q , TOF, and kinetic energy with a solid-state detector (SSD) located at the end of the TOF path, the mass, energy and charge state can be determined. The SSD has an electronic threshold of 26 keV. When nuclear defect is included, energy measurements can only be made for protons above 27

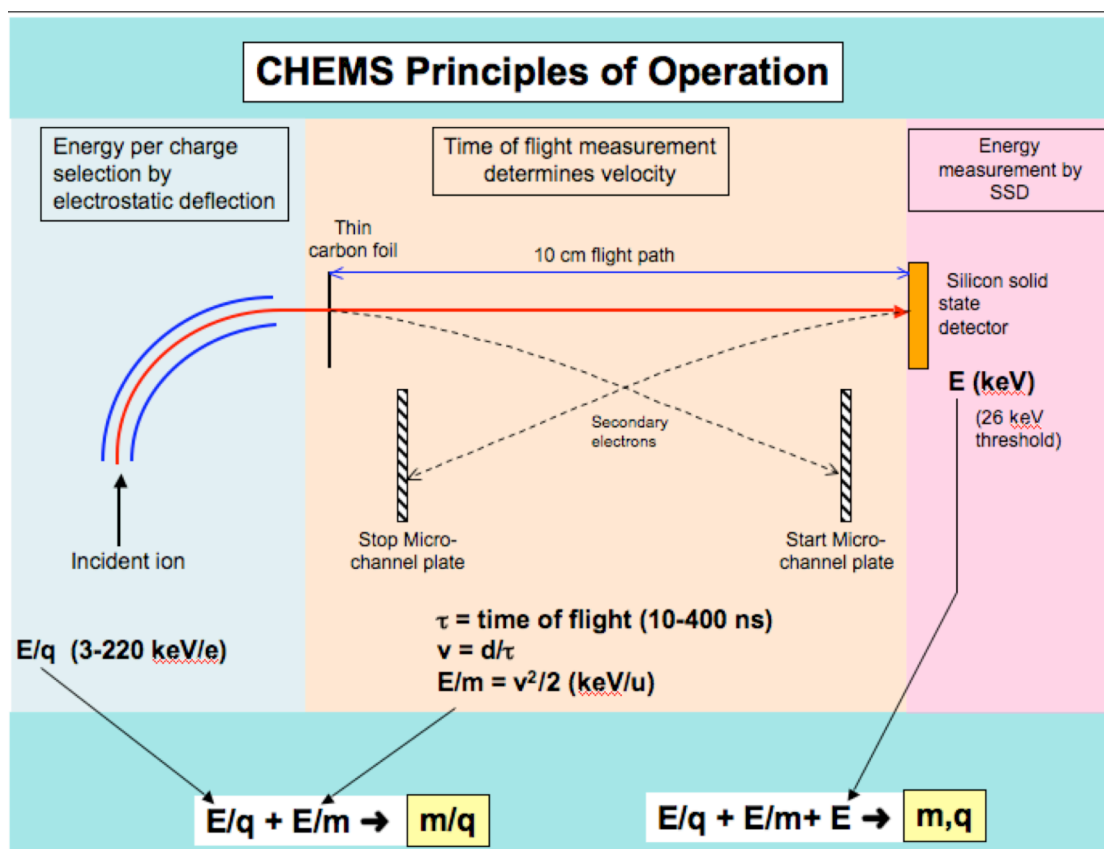


Figure 2.1: Principles of operation of CHEMS

keV and oxygen above 47 keV. Below that energy, only the E/Q and mass per charge (M/Q) of an ion are determined.

First, the incoming ions encounter an electrostatic deflection analyzer system. The system consists of two concentric spherical plates with a positive voltage applied to the outer plate and a negative voltage applied to the inner plate. The voltage is supplied by the deflection plate power supply (DPPS), which supplies 32 output voltages. Incoming ions with only a particular energy per charge (with a 3% pass band) are able to pass through the electrostatic analyzer. The E/Q values are logarithmically spaced and shown in Table 2.1.

Table 2.1: The E/Q (keV/e) and deflection voltage for all 32 DPPS steps of the CHEMS instrument [Krimigis *et al.*, 2004].

TABLE VIII
CHEMS deflection system.

Step no.	Energy per charge (keV/e)	Measured deflection voltage (kV)
0	2.81	0.235
1	3.29	0.275
2	3.78	0.316
3	4.40	0.368
4	5.05	0.422
5	5.86	0.490
6	6.75	0.564
7	7.81	0.653
8	8.92	0.745
9	10.3	0.861
10	11.8	0.984
11	13.6	1.141
12	15.7	1.309
13	18.1	1.509
14	20.8	1.734
15	23.9	1.996
16	27.4	2.290
17	31.5	2.635
18	36.2	3.027
19	41.6	3.48
20	47.8	3.99
21	54.9	4.59
22	63.2	5.28
23	72.6	6.07
24	83.4	6.97
25	95.9	8.01
26	110.1	9.20
27	126.6	10.58
28	145.3	12.14
29	166.9	13.95
30	191.6	16.01
31	220.2	18.40

After passing through the electrostatic analyzer, the ion penetrates a thin carbon foil causing the emission of secondary electrons. The emitted electrons are deflected by electric fields to the start MCP generating the start signal for the TOF system. The ion then strikes one of the SSDs producing secondary electrons that are guided to the stop MCP providing the stop signal. For cases when the ion is able to overcome the 26 keV threshold of the SSD, the kinetic energy of the ion is measured.

Particles that do not have enough energy to trigger the SSD are called double coincident. In that case we only have a

measurement of the energy per charge (E/Q) and TOF τ , so we cannot determine the mass. We can, however, determine the mass per charge M/Q. Using the formula for kinetic energy, the E/Q of the ion can be calculated: $E/Q = (1/2)(M/Q)v^2$, where v is the velocity. We can determine the velocity using our TOF measurement: $v = d/\tau$. Here, d is flight path in the TOF section (10.0 cm) of the instrument. Solving for M/Q, we have

$$\frac{M}{Q} = 2 \left(\frac{\tau}{d} \right)^2 \left(\frac{E}{Q} \right) \quad (2.1)$$

In the above equation, E'/Q is slightly less than the E/Q measured by the electrostatic analyzer because of the small energy loss in the thin ($2.5 \mu\text{g}/\text{cm}^2$) carbon foil.

Particles that do trigger the SSD are called triple coincident. In addition to the E/Q and TOF measurements, we also have an energy measurement from the SSD. We can use this measured energy E_{meas} to determine the mass, charge, and initial energy of the incoming ion. To calculate the mass M and charge Q , we use:

$$M = 2 \left(\frac{\tau}{d} \right)^2 \left(\frac{E_{meas}}{\alpha} \right) \quad (2.2)$$

$$Q = \frac{\left(\frac{E_{meas}}{\alpha} \right)}{\left(\frac{E'}{Q} \right)} \quad (2.3)$$

In the above equation, α gives the ratio of the energy measured in the SSD to the energy incident at the detector. Because of nuclear defect, α is always less than one. Nuclear defect is caused by the collisions between the incoming ions and Si nuclei of the SSD (that do not create electron hole pairs) and becomes more significant for particles at lower energies and higher atomic masses. For example, protons trigger the SSD at a 50% rate at an incident energy of ~ 30 keV, while oxygen ions do so at ~ 55 keV.

2.2 CHEMS Data Types

CHEMS creates three types of counting rate data as well as pulse height analysis (PHA) data for each detected ion [Krimigis et al., 2004]. One type of counting rate data is the engineering rates. These rates are associated with the individual detectors or detector coincidence. They include the counting rates of the start and stop MCPs, the SSDs,

Table 2.2: Data included in each PHA event
[Krimigis *et al.*, 2004].

Quantity	Number of bits
SSD energy channel number	10
TOF channel number	10
SSD ID	2
Start MCP ID	2
Range ID	3
DPPS step number	5

double coincident counting rate (DCR), and triple coincident counting rate (TCR). The engineering rates are used to determine the health of the instrument, the number of expected accidental coincidences, and normalizing fluxes in high rate periods.

The information of a PHA event along with the number of bits is shown in Table 2.2. The SSD ID and Start MCP ID specify which SSD and start MCP were triggered (i.e. which telescope). Because the SSD is not always triggered, we use the Start MCP ID to separate events by telescope. The range ID is determined by the calculations of the mass and M/Q. The Data Processing Unit (DPU) assigns two integers, NM and NQ, which are logarithmically related to the mass and M/Q, respectively. The mass and M/Q bounds on each range ID are shown in Table 2.3.

There are two other types of counting rate data. One basic rate is associated with each range ID. The DPU also defines species rate, which are essentially smaller regions of the mass versus M/Q space. The boxes for the species rates are shown in Table 2.4. A mass vs. M/Q plot showing the bounds of each range ID and each species rate box is shown in Figure 2.2. To determine the counting rate for each DPPS step, we add the total number of events that occur within each box or range ID for each step and then divide that total by the accumulation time for each corresponding step. Counts divided by accumulation

Table 2.3: Range data and Basic rates [Krimigis et al., 2004]

Range	Coincidence required	NM	NQ	Mass range	M/Q range
0	Double	0-0	1-22	0-0	0.7-1.60
1	Double	0-0	23-73	0-0	1.60-10.9
2	Double	0-0	74-126	0-0	10.9-80.0
3	Triple	1-62	1-22	0.5-95.0	0.7-1.6
4	Triple	1-32	23-73	0.5-7.5	1.60-10.9
5	Triple	1-62	74-126	0.5-95.0	10.9-80.0
6	Triple	33-62	23-73	7.5-95.0	1.60-10.9

Table 2.4: Species Rates boxes [Krimigis et al., 2004]

Species	Coincidence requirement	NM	NQ	Mass range	M/Q range
He ⁺	Double	0-0	44-52	0-0	3.53-4.95
He ⁺	Triple	14-32	44-52	1.50-7.50	3.53-4.95
He ²⁺	Double	0-0	22-33	0-0	1.60-4.42
He ²⁺	Triple	14-32	22-33	1.50-7.50	1.60-2.42
N ⁺ ,O ⁺	Double	0-0	77-91	0-0	12.2-21.4
N ⁺ ,O ⁺	Triple	28-51	77-91	4.91-37.4	12.2-21.4
N ²⁺ ,O ²⁺	Double	0-0	62-70	0-0	6.94-9.74
N ²⁺ ,O ²⁺	Triple	33-51	62-70	7.50-37.4	6.94-9.74
CNO > 4 ⁺	Triple	36-45	23-45	9.67-22.5	1.60-3.80

time gives us the counting rates. For a more detailed description of calculating the counting rates, see the MIMI user guide [Vandegriff et al., 2012].

2.3 Differential Intensity from PHA Events

In this paper we use the PHA data rather than the species rates boxes to calculate the differential intensity. To perform this calculation, both the PHA data and basic rates data is needed. Using the PHA data rather than the rates boxes has several advantages. We only have rates boxes for H⁺, He⁺⁺, He⁺, O⁺, O⁺⁺, and CNO > 4⁺. Using the PHA data we can get flux calculations for additional ion species (H₂⁺, C⁺, N⁺, etc.). Another advantage is that we can separate the flux calculations by telescope. The He⁺ and He⁺⁺ data cannot

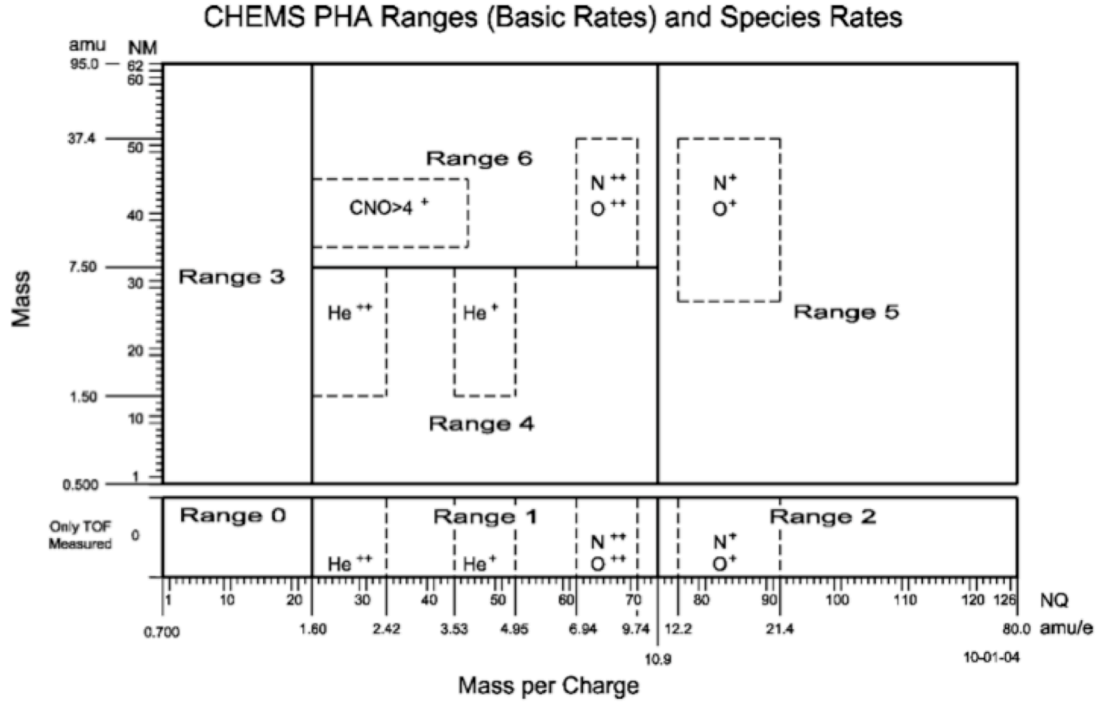


Figure 2.2: A mass (amu) versus M/Q (amu/e) plot showing the box limits of each range ID and species rate box [Krimigis *et al.*, 2004].

be separated by telescope using the rates boxes, but we can separate them by telescope using PHA data. A third advantage is that it is easy to adjust the box limits of the PHA data. Therefore, we can avoid background issues more easily using the PHA boxes rather than the rates boxes.

To determine the PHA counts for each ion species, we define boxes using the SSD energy channel $\text{Essd}(\text{ch})$ and time-of-flight channel $\text{TOF}(\text{ch})$ for each ion species. We do not convert $\text{Essd}(\text{ch})$ and $\text{TOF}(\text{ch})$ to Mass (amu) and M/Q (amu/e), because using the raw channel values makes it easier to avoid background issues. After determining the boxes, we use the calibration data and in flight PHA data to determine the detection efficiencies. Once we have these quantities, we can calculate the differential intensity.

We separate species counts into two categories: double counts and triple counts. There are three criteria used for determining the species counts. The double counts of a species are all PHA events that occur in a specified doubles range ID (range ID=0,1, or 2), within the specified TOF(ch) range, and Essd(ch)=0. The triple counts of an ion species are all PHA events that occur in a specified triples range ID (range ID=3,4,5, or 6), within a specified TOF(ch) range, and within a specified Essd(ch) range. In most cases, each ion species is confined to one doubles range ID and one triples range ID. O^{++} is the only species that has counts two triples range IDs (range ID 4 and 6).

We calculate the differential intensity in two ways. One involves using the combined number of doubles plus triples and the other involves using triples only. The differential intensity is calculated for each telescope separately and then combined to determine the flux for all telescopes combined. Since each telescope has the same geometric factor, we can calculate the differential intensity of all telescopes combined by adding the differential intensities from all three telescopes and then dividing by three. To calculate the doubles plus triples differential intensity $J_{D\&T}$ for each species we need the double counts in the species box $D_{box,cts}$, the PHA counts in the doubles range ID $D_{range,cts}$, the doubles basic rate D_{BR} , the TOF efficiency $Eff_{D\&T}$, the counts in the triples box $T_{box,cts}$, the PHA counts in the triples range ID $T_{range,cts}$, and the triples basic rate T_{BR} . Using this data, we can calculate the flux for doubles and triples combined:

$$J_{D\&T} = \frac{1}{G * \Delta E * Eff_{D\&T}} \left(\frac{D_{box,cts} D_{BR}}{D_{range,cts}} + \frac{T_{box,cts} T_{BR}}{T_{range,cts}} \right) \quad (2.4)$$

In the above equation, G is the geometric factor and equals $0.007 \text{ cm}^2 \text{ sr}$ for each telescope. The quantity ΔE is the passband of the energy per charge and is 3% of the E/Q.

To calculate the differential intensity for the triples only, we need $T_{\text{box},\text{cts}}$, $T_{\text{range},\text{cts}}$, T_{BR} , and efficiency for triples only Eff_T . We calculate the triples only differential intensity using the following equation:

$$J_{\text{Trip}} = \frac{T_{\text{box},\text{cts}} T_{\text{BR}}}{G * \Delta E * \text{Eff}_T * T_{\text{range},\text{cts}}} \quad (2.5)$$

Because triple coincident events have less background, we prefer to use the triples only differential intensity whenever possible. However, at low E/Q the SSD trigger efficiency drops and the number of triples counts become very small (or zero) resulting in large uncertainties. To determine the differential intensity uncertainty, we divide the differential intensity by the square root of the species counts.

2.3.1 O^{++} Differential Intensity

Because the O^{++} triples box contains counts from range IDs 4 and 6, we use a slightly different formula for this species. We determine the box counts in range ID 4 $T_{\text{box},r4}$ and range ID 6 $T_{\text{box},r6}$ to calculate the O^{++} differential intensity:

$$\begin{aligned} \text{O}^{++} J_{D\&T} &= \frac{1}{G * \Delta E * \text{Eff}_{D\&T}} \left(\frac{D_{\text{box},\text{cts}} D_{\text{BR}}}{D_{\text{range},\text{cts}}} + \frac{T_{\text{box},r4} T_{\text{BR}4}}{T_{\text{range}4,\text{cts}}} + \frac{T_{\text{box},r6} T_{\text{BR}6}}{T_{\text{range}6,\text{cts}}} \right) \\ \text{O}^{++} J_{\text{Trip}} &= \frac{1}{G * \Delta E * \text{Eff}_T} \left(\frac{T_{\text{box},r4} T_{\text{BR}4}}{T_{\text{range}4,\text{cts}}} + \frac{T_{\text{box},r6} T_{\text{BR}6}}{T_{\text{range}6,\text{cts}}} \right) \end{aligned} \quad (2.6)$$

In the above formula $T_{\text{BR}4}$ and $T_{\text{BR}6}$ are the basic rates for ranges 4 and 6, respectively, while the quantities $T_{\text{range}4,\text{cts}}$ and $T_{\text{range}6,\text{cts}}$ are the PHA range ID counts for ranges 4 and 6, respectively. In the next two sections, we will show how we define the species boxes for each ion and discuss how we determined the TOF efficiencies. After obtaining these

values, we can use the above equations to calculate the differential intensities for the ion species examined in this paper.

2.3.2 PHA Species Boxes

We use time periods from the Cassini earth fly-by, interplanetary space, and Saturn's magnetosphere to define the boxes for 8 different ion species: H^+ , He^{++} , H_2^+ , He^+ , O^{++} , C^+ , N^+ , and W^+ (O^+ , OH^+ , H_2O^+ , H_3O^+). The magnetospheric period consists of a non-contiguous sum of equatorial ring current passes (dipole $L=7-16$, Latitude= -10° to 10°) from 2004-2010. We will discuss how we selected these magnetospheric periods later in this chapter. The interplanetary period consists of a non-contiguous sum of active interplanetary periods from 2001 to Cassini Saturn Orbit Insertion (SOI). The Cassini earth fly-by occurred on day 230 in 1999. Different locations were chosen because Earth's magnetosphere, interplanetary space, and Saturn's magnetosphere have different ion composition. We use the magnetospheric period to identify the H^+ , H_2^+ , O^{++} , C^+ , and W^+ boxes. Because the helium ions are more abundant in interplanetary space, we use the interplanetary period to identify the boxes for He^+ and He^{++} . A combination of the earth fly-by and magnetospheric periods was used to identify the N^+ box.

To determine the doubles counts, we create TOF(ch) histograms for each period. If there are significant counts of an ion species, a peak will form in the TOF(ch) histogram. To determine which species each peak corresponds to, we convert the TOF(ch) at the center of each distribution to the M/Q. For example, a peak centered on the TOF channel corresponding to $M/Q=1$ is H^+ , and the peak centered on the TOF channel corresponding

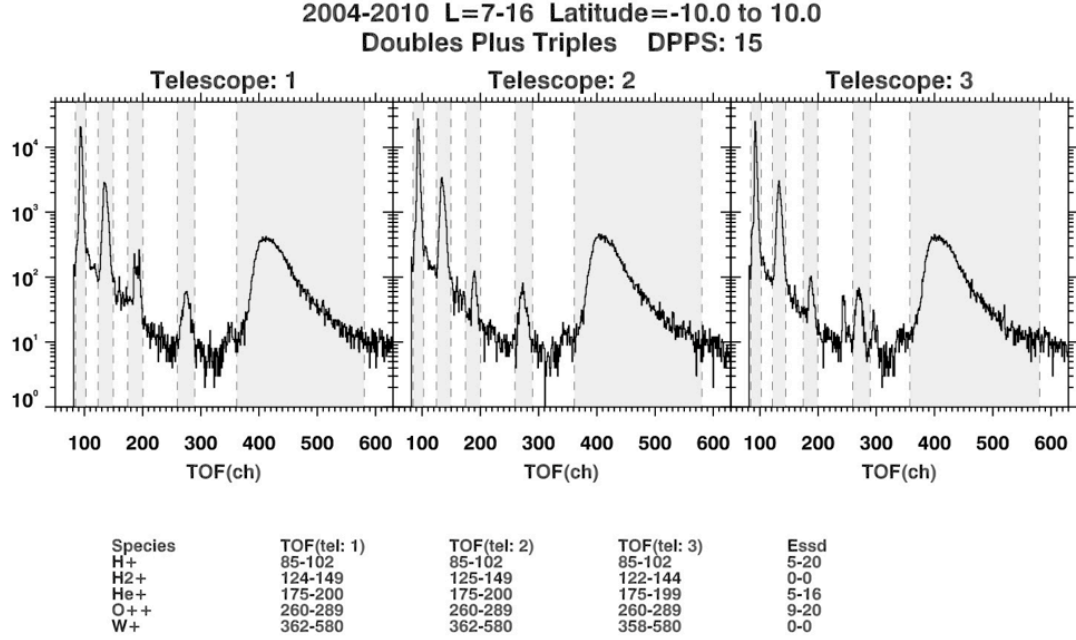


Figure 2.3: A TOF(ch) histogram of the doubles plus triples data from a combination of equatorial ring current passes. The gray areas highlight the species peaks. The TOF bounds used are shown beneath the plot. The E/Q step shown is 23.9 keV/e [Vandegriff et al., 2012].

to $M/Q=4$ is He^+ . With the exception of the $M/Q = 2$ peak, we can use the M/Q value to identify the ion species to which each peak corresponds. The $M/Q = 2$ distribution contains both He^{++} and H_2^+ , so we need an Essd(ch) measurement to separate these species. The TOF distributions on telescope 3 tend to be slightly shifted to lower TOF channels compared to the other telescopes, so the TOF bounds vary by telescope. Since TOF(ch) for each ion species shift to lower TOF(ch) as the E/Q increases, we must create these histograms for each E/Q step. Figure 2.3 shows a TOF histogram for E/Q=23.9 keV/e (DPPS step 15).

As the SSD becomes more efficient in measuring the kinetic energy, we are able to identify species peaks in the triples only data. We use Essd(ch) versus TOF(ch) plots to determine the box limits for the triples species. Because the triples data contain lower background, the species peaks are easily distinguished in the Essd(ch) versus TOF(ch)

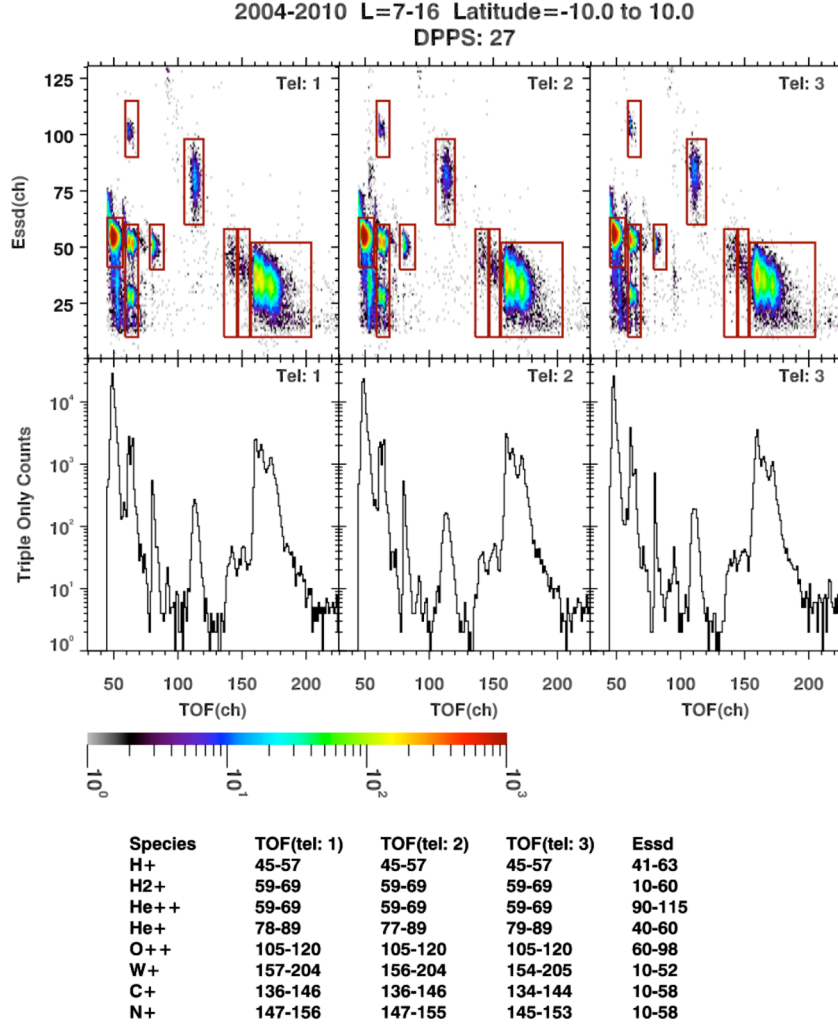


Figure 2.4: An Essd(ch) versus TOF(ch) plot from a combination of equatorial ring current passes from 2004 to 2010. The color indicates the number of counts in each bin. Beneath the Essd(ch) versus TOF(ch) plots is a TOF(ch) histogram containing only the triples data. The dark red boxes show the box limits for each ion species used in this study and the box limits are shown beneath the plots. The E/Q step shown is 127 keV/e [Vandegriff *et al.*, 2012].

plots and are easy to identify. An example of an Essd(ch) versus TOF(ch) plot along with the box limits is shown in Figure 2.4. Beneath the plot is a TOF(ch) histogram containing triples only data. The Essd(ch) and TOF(ch) bounds for each species at all the E/Q steps can be found in Vandegriff *et al.* [2012].

As shown in Figure 2.4, the H_2^+ ion produces two peaks in the $\text{Essd}(\text{ch})$ versus $\text{TOF}(\text{ch})$ plot. The double peak is due to the break-up of H_2^+ when it passes through the carbon foil. An H_2^+ peak will occur near the mass equals one channels when only one component triggers the SSD. When both components trigger the SSD, a peak will occur near the mass equals two channels.

2.3.3 Efficiencies

We use the pre-launch calibration data to determine the TOF efficiencies as a function of E/Q . Calibration data were obtained from two different models: the flight unit (FU) and the engineering model (EM). The flight unit is the instrument that is on Cassini. Most of the calibration data taken with the flight unit are from telescope 2. The engineering model functions the same way as the flight unit, with slight differences in energy steps and efficiency. Because the flight unit is the instrument on Cassini, we will weight the flight unit points more heavily when trying to determine efficiencies, but data for some species at the highest portion of the CHEMS energy range are only available for the EM unit.

Calibration was performed at the NASA Goddard Space Flight Center. For the flight unit, ion beams of varying energy were focused on the aperture of CHEMS. A small electrostatic accelerator was used with a maximum energy of approximately 100 keV. The EM calibration data was done with a Van de Graff accelerator with energies up to 220 keV (the max of CHEMS).

To calculate the TOF efficiencies, we determine the start and stop efficiencies as a function of energy per charge. We calculate the start and stop efficiencies using the engineering rates:

$$start_eff = \frac{DCR}{STOP} \quad (2.7)$$

$$stop_eff = \frac{DCR}{START} \quad (2.8)$$

As discussed earlier, DCR refers to the doubles counting rate, while TCR refers to the triples counting rates. DCR counts contain all the TCR counts, so the DCR is actually doubles plus triples. STOP and START refers to the stop singles rates and start singles rates, respectively. The TOF efficiency for doubles plus triples combined ($Eff_{D\&T}$) is determined by multiplying the start and stop efficiency.

The H^+ TOF efficiency is 3.25×10^{-3} at the lowest E/Q step ($E/Q = 3$ keV/e) and reaches its peak value of 4.62×10^{-1} at $E/Q = 83.4$ keV/e. Above 83.4 keV/e, the H^+ TOF efficiency decreases with energy and is 3.17×10^{-1} at the highest E/Q step ($E/Q = 220$ keV/e). We are unable to calculate the abundances of O^+ at $E/Q < 9$ keV/e, because the detection efficiencies are too low. Most of the O^+ ions at those energies don't penetrate the carbon foil. The O^+ TOF efficiency increases from 3.08×10^{-3} at $E/Q = 9$ keV/e to 6.26×10^{-1} at $E/Q = 220$ keV/e. The low efficiencies at low energies are a combined result of small energy loss in the carbon foil, resulting in very few secondary electrons, and increased scattering in the carbon foil, resulting in a small fraction of the particles hitting the SSD and producing STOP counts. The TOF efficiencies for all the species included in this thesis can be found in *Vandegriff et al.* [2012].

Because we only use the triple counts at higher energies, the triples only efficiencies must also be determined. To calculate the triples only efficiency (Eff_T), we determine TCR/DCR as a function of E/Q and multiply this ratio by $\text{Eff}_{D\&T}$. TCR/DCR calibration data approaches one at high E/Q as the SSD efficiency approaches one and scattering in the foil becomes small. However, the TCR/DCR ratio of the in-flight data approaches ~ 0.85 - 0.90 at high E/Q . This difference results from the fact that narrow ion beams during calibration are aimed at the center of the telescope, so that scattering does not cause as many ions to miss the SSD and fail to produce stop counts. We will use in flight PHA data to determine TCR/DCR as a function of E/Q .

Since the SSD on telescope 3 has a lower threshold, the triples only efficiency on telescope 3 is higher than telescopes 1 and 2. The difference in triples only efficiency among the three telescopes is largest at energies where we first began to detect triples PHA events efficiently (TCR/DCR ~ 0.1). As E/Q increases, the triples efficiencies for the telescopes converge and approach the same value. The TCR/DCR for light ions (e.g. H^+ and H_2^+) typically approach 0.90 at high energies, while the TCR/DCR for heavier ions (e.g. W^+) typically approach 0.85.

To get the TCR/DCR ratio, we use the PHA box counts to determine the double and triple counts for each ion species. We combine time periods over several years of the Cassini mission to get good counting statistics. For O^{++} and He^+ , we use the $\text{Essd}(\text{ch})$ vs. $\text{TOF}(\text{ch})$ boxes discussed in the previous section. We determined the TCR/DCR for H^+ ,

W^+ , and H_2^+ before we switched to using Essd(ch) vs. TOF(ch) boxes, so our current TCR/DCR values for these three species are based on Mass versus M/Q boxes. Because the TCR/DCR ratio of H^+ , W^+ , and H_2^+ based on the Mass versus M/Q boxes do not differ significantly from the values based on the Essd(ch) versus TOF(ch) boxes, we do not need to update these values using the new boxes. The TCR/DCR is calculated by dividing the triple box counts by the total box counts (triple plus double counts).

Using the in flight data to get the TCR/DCR creates a few problems. Doubles background counts can make it difficult to get an accurate measurement at certain DPPS steps.

Interpolation is used to estimate the TCR/DCR at DPPS steps where doubles background is a problem. Another problem occurs when we need to use active periods to get the TCR/DCR. Because of limitations in telemetry, the DPU does not send down all PHA events. The DPU selects a random number of events and gives equal weighting to each range ID. Therefore, if the period is active, the ratio of the triple counts to total counts of the PHA data may not represent the actual TCR/DCR value.

Initially, we used the equatorial ring current data ($L=7-16$, $|Z| < 1.0 R_s$) from 2004-2009 to get the TCR/DCR for H^+ , W^+ , and H_2^+ . L is dipole L shell and Z is the distance above the equatorial plane. However, this period was too active and resulted in us overestimating the TCR/DCR at certain E/Q steps. Therefore, we switched to quieter time periods in the outer ring current ($L=16-21$) where the limited telemetry was not a problem. We still use the $L=7-16$ periods for O^{++} and O_2^+ , because we do not get sufficient counting statistics in the $L=16-21$ time periods.

We cannot use magnetospheric time periods to get the TCR/DCR for the helium data.

The He^+ doubles data contains a large amount of background in Saturn's magnetosphere and the H_2^+ data dominate the $M/Q = 2$ box. Thus, we use interplanetary data to get the TCR/DCR for the helium data. Since most of the interplanetary periods are quiet, our statistics are not so good as that from the magnetosphere. This creates a problem for telescope 1, since this telescope is rarely facing in the direction of the solar wind.

Because of the lack of statistics for telescope 1 in interplanetary space, we assume that the TCR/DCR for He^+ and He^{++} for telescope 1 is the same as telescope 2. The SSD thresholds for telescopes 1 and 2 are the same, so this is a reasonable approximation. See *Vandegriff et al.* [2012] for the triples only efficiencies for each ion species included in this thesis.

2.3.4 Transitioning to Triples Only Data

We have two equations that calculate the differential intensity. To review, the two equations used to calculate the differential intensity are

$$J_{D\&T} = \frac{1}{G * \Delta E * \text{Eff}_{D\&T}} \left(\frac{D_{box,cts} D_{BR}}{D_{range,cts}} + \frac{T_{box,cts} T_{BR}}{T_{range,cts}} \right) \quad (2.9)$$

$$J_{Trip} = \frac{T_{box,cts} T_{BR}}{G * \Delta E * \text{Eff}_T * T_{range,cts}} \quad (2.10)$$

At low energies, where there are not a sufficient number of triple counts and the triples only efficiency is very small, we use the formula for doubles and triples. At high E/Q steps where the triples are detected more efficiently, we are able to use the triples only calculation. The triples only differential intensity will have lower background and is more

reliable, so we use triples only data whenever possible. As stated previously, G is the geometric factor for each telescope and is equal to $0.007 \text{ cm}^2\text{-sr}$. ΔE is the 3% E/Q (keV/e) passband.

With the information obtained in the previous sections, we can calculate the differential intensity for a given time period. First, the basic rates for the time period are calculated as a function of E/Q for all three telescopes. Using the PHA data and the species boxes, the total number of double counts and triple counts are determined for each ion species as well as the total number of PHA counts in each range ID. We then have the box counts, basic rates, PHA range ID counts, and efficiencies all as a function of E/Q . We can use equations 2.9 and 2.10 to calculate the differential intensity for the specified time period. We perform the calculation for each telescope. We then add the differential intensities from all three telescopes and divide by three to calculate the differential intensity for all telescopes combined.

We now have two differential intensity calculations for each ion species. We combine the two calculations by determining which E/Q step to transition from doubles plus triples to triples only. We pick an E/Q step where there are a sufficient number of triples counts to perform a triples only differential intensity calculation. Typically, we transition to triples only when the TCR/DCR ratio becomes greater than 0.10. The E/Q transition steps are shown in Table 2.5.

Table 2.5: DPPS step and E/Q (keV/e) where we transition to using triples only data when calculating the differential intensity [Vandegriff *et al.* 2012].

Species	Transition Step	E/Q (keV/e)
H ⁺	16	27.4
H ₂ ⁺	16	27.4
He ⁺	16	27.4
He ⁺⁺	12	15.7
O ⁺⁺	16	27.4
C ⁺	20	47.8
N ⁺	20	47.8
W ⁺	20	47.8

To check that our triples only and doubles plus triples calculations are in agreement, we plot the differential intensities for each species versus E/Q (i.e. the spectra). We don't want to see a large jump in the differential intensity at the transition step. We use a magnetospheric period and two interplanetary periods to check the

calculations. Our magnetospheric period consists of a non-contiguous sum of equatorial ring current passes (L=7-16, Latitude = -10° to 10°) from 2004-2010. We use two periods for our interplanetary data. One period consists of non-contiguous time periods taken from 2004 001-179, while the other is 2003 314 0000- 2004 319 0000. We use the 2004 time periods to check the results from telescope 2, while the 2003 time period is used to check the results from telescope 3.

When plotting the spectra, we found that our differential intensity spectra changed smoothly from doubles plus triples to triples only and that the results from equations 2.9 and 2.10 were in agreement. Figure 2.5 shows an example of the H⁺ spectra from an interplanetary period and the W⁺ spectra from the magnetospheric period. The MIMI user guide [Vandegriff *et al.*, 2012] contains the spectra for the other species used in this study. The H⁺ spectra illustrate the importance of using triples only at high energies. The doubles data contains a significant amount of background at E/Q > 63 keV/e, and using the triples only data greatly reduces this background problem.

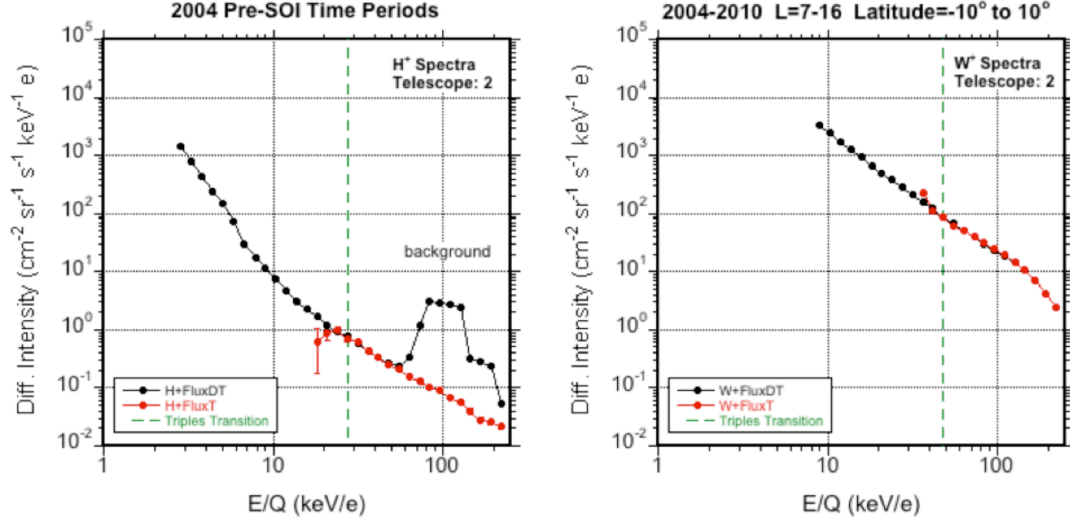


Figure 2.5: An H^+ flux spectra for an interplanetary period and a W^+ flux spectra for a combination of magnetospheric periods. The black points use double plus triples counts, while the red points use triples only counts. The vertical green dashed line shows the E/Q step where we transition to triples only data. In both cases, the transition from doubles plus triples to triples only is smooth. The background peak labeled in the doubles plus triples H^+ data illustrates why it is usually best to use the triples only data whenever possible [Vandegriff *et al.*, 2012].

2.3.5 Calculating Partial Number Density

After calculating the differential intensity J , we then convert J for each of the E/Q steps into partial number density per step Δn :

$$\Delta n(\text{cm}^{-3}) = \frac{4\pi * J(\text{cm}^{-2}\text{sr}^{-1}\text{sec}^{-1}\text{keV}^{-1}\text{e}) * \Delta\left(\frac{E}{Q}(\text{keV/e})\right)}{v(\text{cm/s})} \quad (2.11)$$

$$v(\text{cm/sec}) = (4.377 \times 10^7 \text{ cm/sec}) * \sqrt{(\text{amu/kev})} * \sqrt{\left(\frac{Q}{M}(\text{e/amu})\right)\left(\frac{E}{Q}(\text{keV/e})\right)} \quad (2.12)$$

In the above equation v is velocity. When calculating the number density, we do not use the passband for $\Delta(E/Q)$. Instead we use the geometric mean between the individual steps. For example, the minimum E/Q for step 1 is the geometric mean of the E/Q between steps 0 and 1. Similarly, the maximum E/Q for step 1 is the geometric mean of the E/Q between steps 1 and 2. The $\Delta(E/Q)$ values used are given in Table 2.6. We add

Table 2.6: The minimum and maximum E/Q used when calculating partial number density [Vandegriff *et al.*, 2012]. The delta E/Q column contains the number used to calculate the partial number density for each E/Q step (see equation 2.12).

DPPS step	Midpoint E/Q	Passband	Lower E/Q	Upper E/Q	Delta E/Q
0	2.81	0.0843	2.61	3.04	0.427
1	3.29	0.0987	3.04	3.53	0.486
2	3.78	0.1134	3.53	4.08	0.552
3	4.4	0.132	4.08	4.71	0.636
4	5.05	0.1515	4.71	5.44	0.726
5	5.86	0.1758	5.44	6.29	0.849
6	6.75	0.2025	6.29	7.26	0.971
7	7.81	0.2343	7.26	8.35	1.086
8	8.92	0.2676	8.35	9.59	1.239
9	10.3	0.309	9.59	11.02	1.439
10	11.8	0.354	11.02	12.67	1.644
11	13.6	0.408	12.67	14.61	1.944
12	15.7	0.471	14.61	16.86	2.245
13	18.1	0.543	16.86	19.4	2.546
14	20.8	0.624	19.4	22.3	2.893
15	23.9	0.717	22.3	25.59	3.294
16	27.4	0.822	25.59	29.38	3.788
17	31.5	0.945	29.38	33.77	4.39
18	36.2	1.086	33.77	38.81	5.038
19	41.6	1.248	38.81	44.59	5.786
20	47.8	1.434	44.59	51.23	6.635
21	54.9	1.647	51.23	58.9	7.677
22	63.2	1.896	58.9	67.74	8.833
23	72.6	2.178	67.74	77.81	10.076
24	83.4	2.502	77.81	89.43	11.619
25	95.9	2.877	89.43	102.75	13.323
26	110.1	3.303	102.75	118.06	15.307
27	126.6	3.798	118.06	135.63	17.566
28	145.3	4.359	135.63	155.73	20.098
29	166.9	5.007	155.73	178.82	23.098
30	191.6	5.748	178.82	205.4	26.579
31	220.2	6.606	205.4	236.05	30.652

the partial number densities from consecutive steps to combine the results from several E/Q steps.

2.4 Data Set

The data presented in this thesis are from the same set of Cassini equatorial passes. We selected inbound and outbound passes that were within 10° of the equatorial plane in the dipole L=6-21 region. We required Cassini to be in the magnetosphere for the entire L=6-21 range, and we removed passes that contain data gaps greater than $\Delta L=1$. H.J.

McAndrews, S.J. Kanani, A. Masters, and J.C. Cutler created a list of Cassini bow shock and magnetopause crossings that can be found on the University of Michigan MAPS website (<http://mapsview.engin.umich.edu/BSMP/index.php>). This list was used to determine whether Cassini was inside or outside the magnetosphere.

We identified 78 passes in the years 2004-2010 that satisfy these three criteria and their trajectories are shown in Figure 2.6. The blue lines in Figure 2.6 highlight the main ring current region ($L=7-16$) where the largest suprathermal ion intensities are observed. The tables in Appendix A contain the time ranges for each pass through the ring current and the $L=6-21$ region. The time ranges for each L range ($L=6-7$, $L=7-8$, etc.) are also listed in Appendix A.

We do not include data inside of $L=6$, because the suprathermal ion abundances decrease significantly inside this L shell and we have poor counting statistics. During typical solar wind conditions, Cassini would be outside the magnetosphere beyond $L=21$ on the dayside [Kanani et al., 2010], so we do not include any data beyond this L shell. At $L=21$, 10° latitude is $3.7 R_S$ from the equatorial plane. The thickness of the energetic particles in the plasma sheet on the night side is $\pm 5 R_S$, while the latitudinal extent is even larger on the dayside ($\pm 50^\circ$) [Krimigis et al., 2007; Sergis et al., 2009]. Therefore, we expect that all of our passes are within the plasma sheet and that latitudinal variations from pass to pass should be modest.

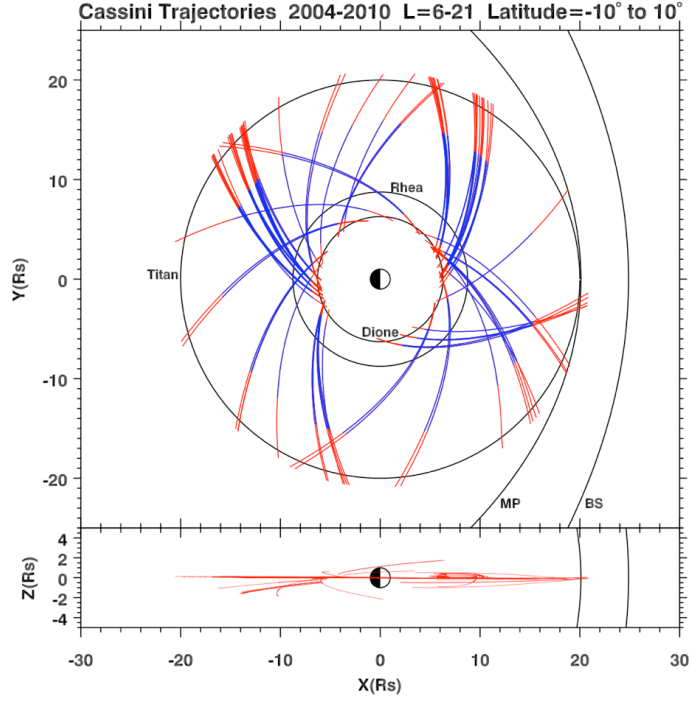


Figure 2.6: Cassini passes used in this study in the SZS Saturn equatorial coordinate system. Each pass is within 10 degrees of the equatorial plane. The blue lines highlight the main ring current region ($L=7-16$). The red portions extend the passes from $L=6-21$. Typical locations of the magnetopause and bow shock were taken from *Arridge et al. [2006]* and *Masters et al. [2008]*, respectively.

The partial number densities of each ion species vary significantly from pass to pass depending on the local time of the pass, injection events, solar wind conditions, etc. To average out these short-term variations and focus on long-term averages, we combine the data from several passes. Combining several passes is necessary to determine the abundances of the rare ion species (e.g. He^{++} , He^+ , O^{++} , C^+ , N^+ etc.) where the counting statistics from a single pass are sometimes too low to obtain an accurate estimate of the partial number densities. Using the procedure discussed in this chapter, we can examine the energy, L , and long-term time variations of the suprathermal ion partial number density and fractional abundance.

Chapter 3

Energy and L Variations of the Suprathermal Ions: Implications for the Neutral and Plasma Source Strengths

Saturn's magnetosphere contains multiple sources of neutral particles. The Enceladus plumes are the dominant source of H₂O as well as O and OH via water dissociation [Smith *et al.*, 2010; Cassidy and Johnson 2010]. Typical estimates of the Enceladus source strength range from $\sim 1\text{--}4 \times 10^{28}$ H₂O/s [Burger *et al.*, 2007; Jia *et al.*, 2010; Dong *et al.*, 2011], but some studies suggest that the source strength varies significantly with time and can be as low as $\sim 0.6\text{--}0.7 \times 10^{28}$ H₂O/s [Saur *et al.*, 2008; Smith *et al.*, 2010].

The dissociation of water can also produce H and H₂, but this process does not appear to be the strongest source of these two neutral species. Cassini UVIS observations prior to SOI suggest that the strongest atomic H source is Saturn's atmosphere where H is emitted at a rate of $\sim 3 \times 10^{30}$ H/s [Shemansky *et al.*, 2009]. Cui *et al.* [2008] modeled the escape of H₂ from Titan and estimated a source strength of $\sim 10^{28}$ H₂/s. The predicted strengths of the other H₂ sources are much lower ($\sim 3 \times 10^{26}$ H₂/s for Enceladus, $\sim 2.0 \times 10^{26}$ H₂/s for Saturn's rings, and $\sim 1.8 \times 10^{24}$ H₂/s for Rhea) [Tseng *et al.*, 2011a].

Ionization of these neutral particles produces a significant amount of plasma in Saturn's magnetosphere, and therefore, ion composition information can provide insight into the strength of the neutral sources. However, differences among the dissociation and ionization rates, and possibly acceleration times, prevent a one to one correspondence

between the ion densities and neutral source strengths. Cassini observations revealed that the ion composition in Saturn's magnetosphere is dominated by H^+ and W^+ with H_2^+ being the third most abundant species [Young *et al.*, 2005; Krimigis *et al.*, 2005; Thomsen *et al.*, 2010]. The ratio of H^+/He^{++} is much larger in Saturn's magnetosphere than in the solar wind indicating that the solar wind is a weak source compared to the local sources [McDonald *et al.*, 1980; Hamilton *et al.*, 1983]. Observations of energetic protons by MIMI LEMMS revealed that outside $L=12$ the radial variations of the protons can be explained by radial diffusion [Kollmann *et al.*, 2011]. In Saturn's inner magnetosphere, however, diffusion is no longer the dominant process, and the protons with energy ranging from ~ 10 to several hundred keV are depleted due to collisions with Saturn's neutral cloud [Paranicas *et al.*, 2008; Kollmann *et al.*, 2011].

In this chapter and the next we study the energy and L variations of six suprathermal ion species: H^+ , H_2^+ , W^+ , He^+ , He^{++} , and O^{++} . This chapter focuses on the suprathermal ion composition in the outer magnetosphere where radial diffusion dominates over the losses. We compare our results to estimates of the plasma and neutral source strengths. In the next chapter, we present our observations and analysis of the suprathermal ion composition in the inner magnetosphere.

3.1 Data Analysis Methods

We separate each pass shown in Figure 2.6 by L using a bin size of $\Delta L=1$ and combine the CHEMS data in each L shell from all 78 passes. We determine the differential intensity for each L shell in the $L=6-21$ region and average the data from all three

CHEMS telescopes. We convert the differential intensity for each of the 32 E/Q steps into partial number density per E/Q step.

Only the H^+ and H_2^+ abundances can be accurately measured at $E/Q < 9$ keV/e, because the detection efficiencies for the heavy ions (O^{++} and W^+) are too low. Therefore, the partial number densities of W^+ and O^{++} can only be calculated for $E/Q > 9$ keV/e. Since we require an energy measurement from the SSD to separate He^{++} from H_2^+ , we are only able to distinguish these two species above $E/Q \geq 27$ keV/e where the SSD begins to efficiently measure the kinetic energy of the H_2^+ and He^{++} ions. Observations above this energy revealed that H_2^+ dominates the He^{++} in Saturn's magnetosphere [Krimigis *et al.*, 2005], so we assume that all the double coincidence counts in the $M/Q = 2$ amu/e distribution are H_2^+ . Background problems in the He^+ doubles data require us to only use the triple coincidence data for He^+ . This requirement limits our He^+ energy range to $E/Q \geq 27$ keV/e. With these energy limitations, CHEMS can easily distinguish all six species.

Using the partial number density (PND) calculations, we create E/Q (keV/e) versus L spectrograms with full 32 pixel E/Q resolution. We then combine the data into five E/Q intervals by adding the single step partial number densities for E/Q steps in the 3-8 keV/e, 9-14 keV/e, 36-55 keV/e, 73-110 keV/e, and 145-220 keV/e ranges. We plot these combined partial number densities and fractional abundances versus L to determine the way the ion composition changes with energy and L.

3.2 Results

The E/Q (keV/e) versus L PND spectrograms for the three major species (H^+ , W^+ , H_2^+) and three minor species (He^{++} , He^+ , O^{++}) are shown in Figures 3.1 and 3.2, respectively. The partial number density values for each bin can be found in the Tables in Appendix B. White bins indicate either the PND of the bin was less than the lowest color bar level or the PND of the bin could not be calculated due to low detection efficiencies or background issues. Since the PND's of He^+ , He^{++} , and O^{++} are much less than those of H^+ , W^+ , and H_2^+ , we use lower values on the color bar in Figure 3.2.

All six of the suprathermal ion species show similar overall L variations. The PND of each ion species increases inward from L=21, typically peaks between L=8 and L=11, and then decreases inward. The L shell at which the PND peaks and the rate at which it decreases in Saturn's inner magnetosphere depends on the ion species and energy.

Figure 3.3 shows the low energy (3-8 keV/e) (a) H^+ and H_2^+ PND's and (b) their ratio. At these energies we cannot calculate the PND's for any other species. The H^+ PND increases by a factor of 5 from $3.9 \times 10^{-3} \text{ cm}^{-3}$ at L=20-21 to a maximum of $2.0 \times 10^{-2} \text{ cm}^{-3}$ at L=8-9, while the H_2^+ PND increases by a factor of 3.9 from $1.6 \times 10^{-3} \text{ cm}^{-3}$ at L=20-21 to $6.2 \times 10^{-3} \text{ cm}^{-3}$ at L=9-10. The thermal H^+ and H_2^+ number densities at L=8.5 is 1.1 cm^{-3} and 0.17 cm^{-3} , respectively [Thomsen *et al.*, 2010], so the 3-8 keV/e H^+ makes up only 1.8% of the total H^+ density, while 3-8 keV/e H_2^+ make up about 3.6% of the total H_2^+ density. From L=15-21, the H_2^+/H^+ ratios is relatively constant and averages 0.39 with a standard deviation of 0.01.

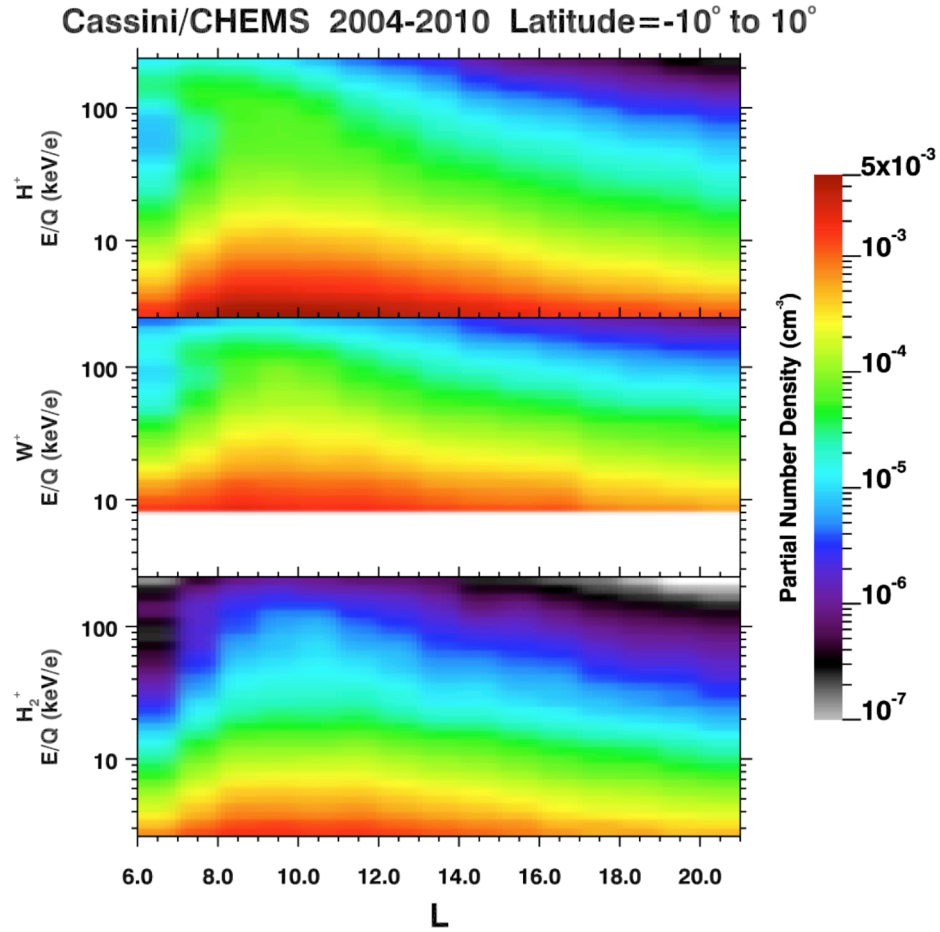


Figure 3.1: The E/Q versus L partial number density spectrograms for the three major ion species: H^+ , W^+ , and H_2^+ . The partial number density of each bin is indicated by the color bar on the right. The white region in the middle panel indicates no measurement of W^+ below ~ 9 keV.

Above 9 keV, we can also measure the W^+ and determine the PND of all species combined. We cannot determine the abundances of the helium ions at our second lowest energy range (9-14 keV/e), but these species are relatively rare and don't contribute appreciably to the combined PND. In Figure 3.4 we show (a) the PND's and (b) the fractional abundances (FA) of each species in the 9-14 keV/e range. The PND's and FA's at the other three energy ranges (36-55 keV/e, 73-110 keV/e, 145-220 keV/e) are shown in Figure 3.5.

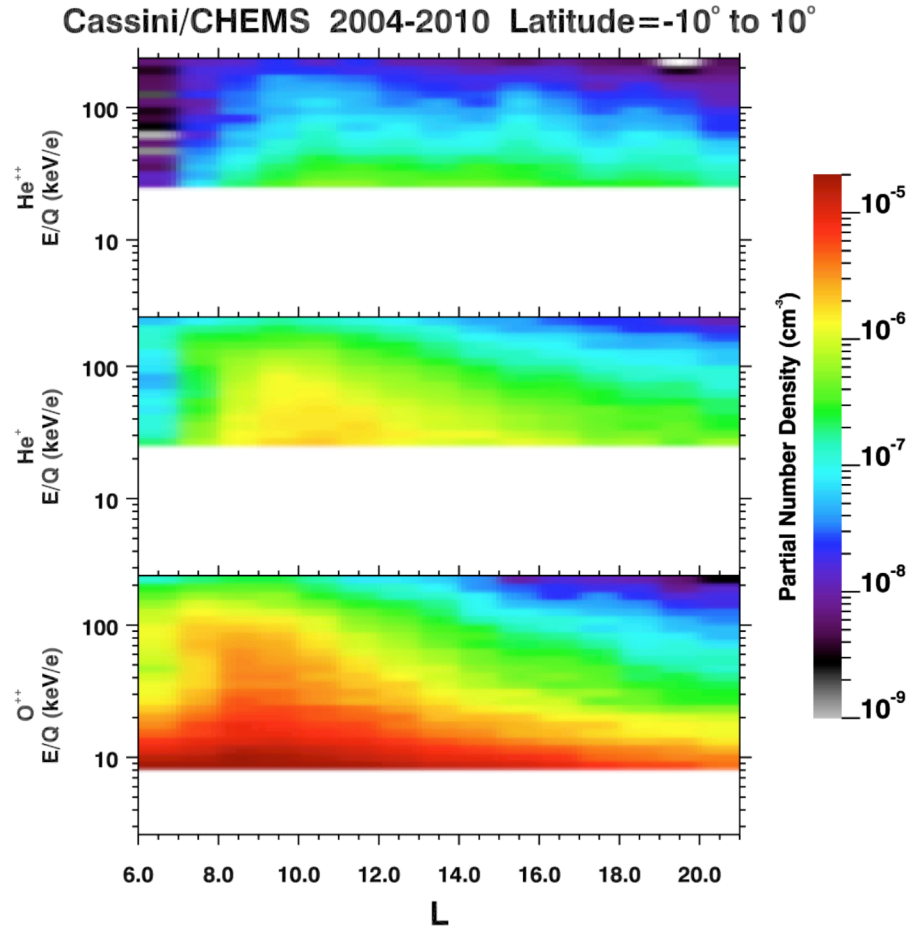


Figure 3.2: The E/Q versus L partial number density spectrogram for He^{++} , He^+ , and O^{++} . Because these species are much less abundant than H^+ and W^+ , the color bar levels used in this spectrogram is less than the color bar levels used in Figure 3.1. White bins in the third panel indicate no measurement of O^{++} below ~ 9 keV. No measurement of He^{++} or He^+ at $E/Q < 27$ keV/e is included in this study.

The 9-14 keV/e PND's are about an order of magnitude less than those at 3-8 keV/e. The combined 9-14 keV/e PND peaks at $8.7 \times 10^{-3} \text{ cm}^{-3}$, which is 0.1% of the total ion number density [Thomsen *et al.*, 2010]. At higher energies, the PND continues decline and show the same trend with L. At the highest energy range (145-220 keV/e), the PND's tend to maximize a lower L shells and do not decrease as quickly inward as at lower energies. This trend is strongest for H^+ and O^{++} for which the PND's peak at $L=7-8$ and only begin to decline inside of $L=7$.

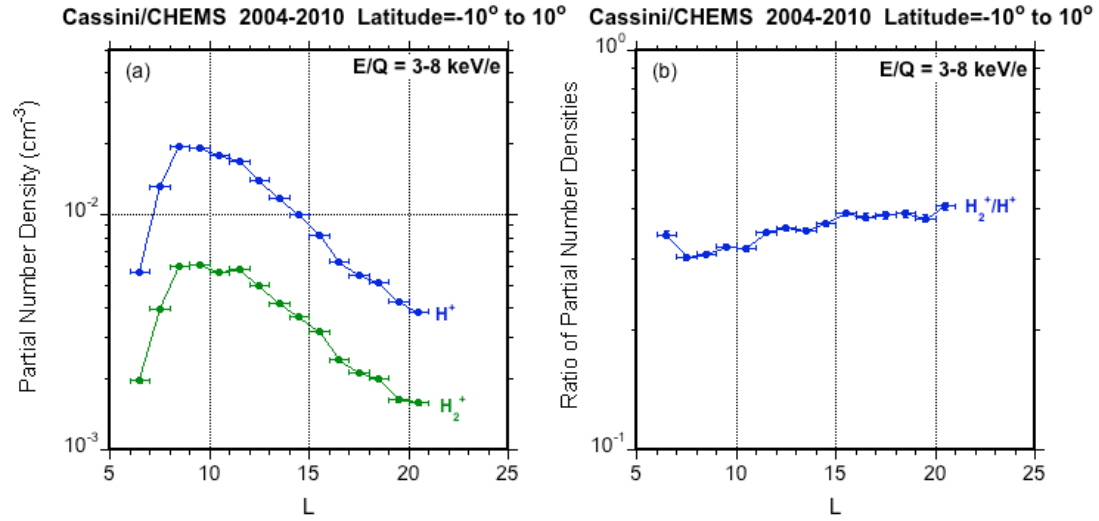


Figure 3.3: (a) The 3-8 keV/e H⁺ and H₂⁺ partial number densities versus L. (b) The 3-8 keV/e H₂⁺/H⁺ partial number density ratio versus L.

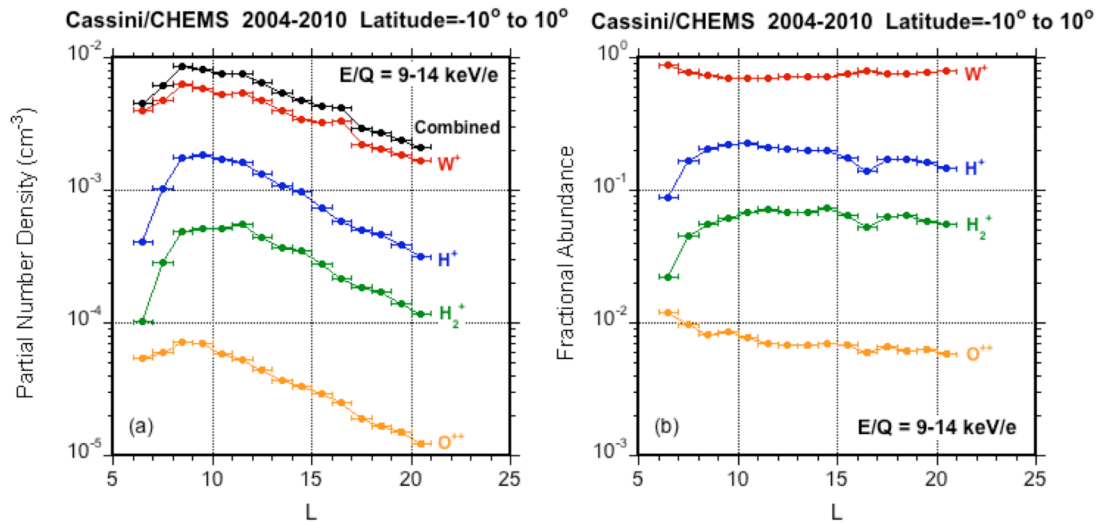


Figure 3.4: (a) The partial number densities of 9-14 keV/e ions versus L. (b) The fractional abundance of 9-14 keV/e ion species versus L.

In the outer magnetosphere (L=15-21), the fractional abundances of all six species show little variation with L. To determine the typical FA's in the outer magnetosphere, we average the FA's in the six L shells from L=15-21. These average values and their standard deviations are shown in Table 3.1 for all six species and at all four energy ranges.

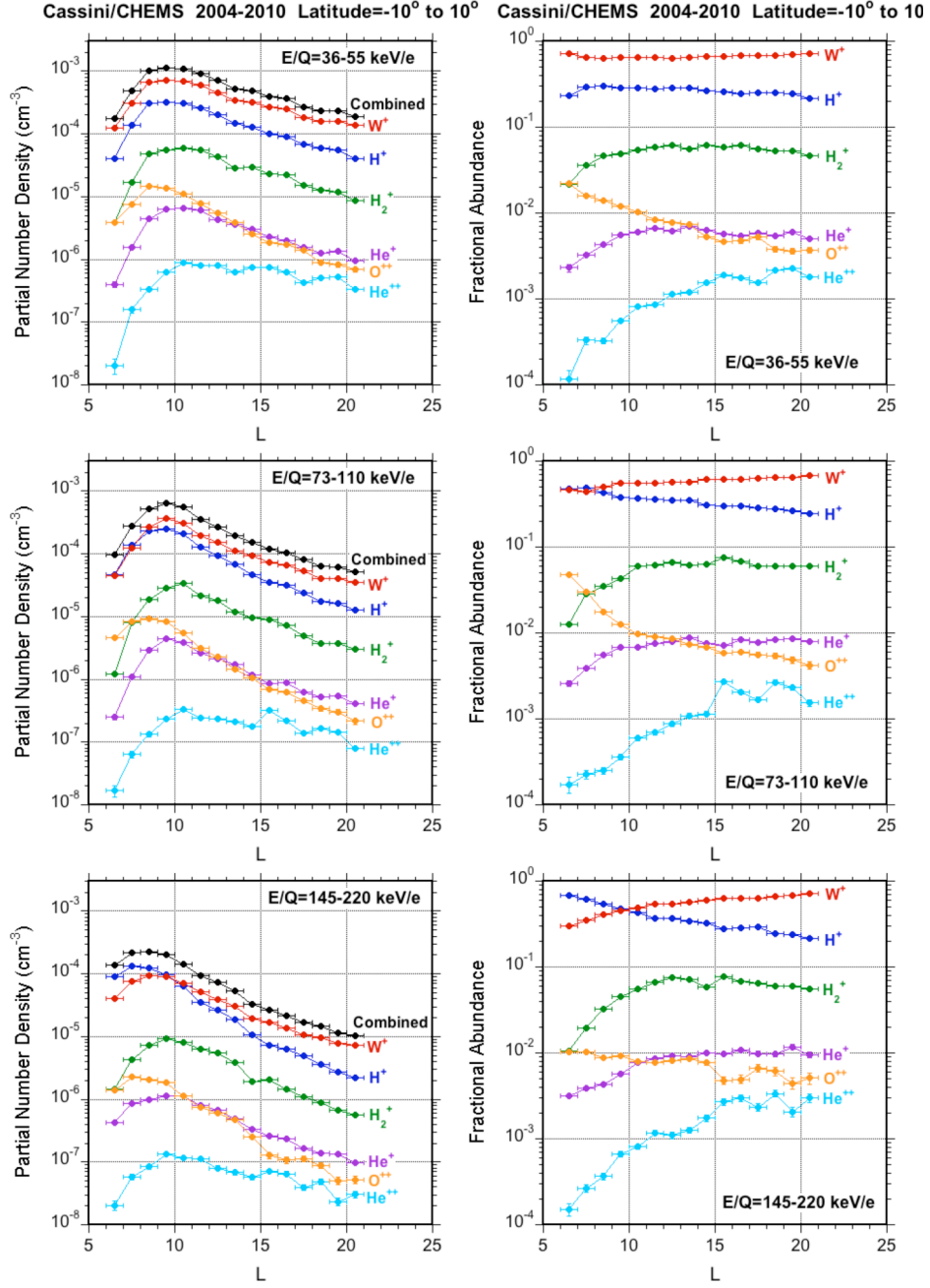


Figure 3.5: The partial number densities (left) and fractional abundances (right) at three E/Q ranges: 36-55 keV/e, 73-110 keV/e, 145-220 keV/e.

The average 9-14 keV/e W^+ and H^+ FA's in the outer magnetosphere are 0.77 and 0.16, respectively. At higher energies ($E/Q > 36$ keV/e) the average W^+ fractional abundance decreases and ranges from 0.64-0.69, while the average H^+ fractional abundance

Table 3.1: The average of the fractional abundances (FA) from the six L shells between L=15 and L=21. The uncertainties are the standard deviation of the six FA values.

Species	FA L=15-21 9-14 keV/e	FA L=15-21 36-55 keV/e	FA L=15-21 73-110 keV/e	FA L=15-21 145-220 keV/e
H ⁺	(1.6±0.1)x10 ⁻¹	(2.4±0.1)x10 ⁻¹	(2.8±0.2)x10 ⁻¹	(2.6±0.3)x10 ⁻¹
W ⁺	(7.7±0.2)x10 ⁻¹	(6.9±0.2)x10 ⁻¹	(6.4±0.3)x10 ⁻¹	(6.6±0.4)x10 ⁻¹
H ₂ ⁺	(6.0±0.5)x10 ⁻²	(5.4±0.5)x10 ⁻²	(6.4±0.6)x10 ⁻²	(6.4±0.8)x10 ⁻²
O ⁺⁺	(6.3±0.4)x10 ⁻³	(4.3±0.7)x10 ⁻³	(5.3±0.7)x10 ⁻³	(5.3±0.8)x10 ⁻³
He ⁺	-	(5.6±0.4)x10 ⁻³	(8.0±0.5)x10 ⁻³	(1.03±0.09)x10 ⁻²
He ⁺⁺	-	(1.9±0.3)x10 ⁻³	(2.2±0.5)x10 ⁻³	(2.7±0.4)x10 ⁻³

increases and ranges from 0.24-0.28. H₂⁺ is the third most abundant ion species and its average FA in the outer magnetosphere ranges from 0.054 to 0.064 depending on the energy range.

The other three ion species have much smaller fractional abundances. The average O⁺⁺ FA in the outer magnetosphere ranges from 0.0043 to 0.0063 depending on the energy. The average He⁺ and He⁺⁺ FA's in the outer magnetosphere increase with energy. The He⁺ FA averages 0.0056 at E/Q=36-55 keV/e, while the He⁺⁺ FA averages 0.0019. At the highest energy range examined (145-220), the average He⁺ and He⁺⁺ FA increases to 0.0103 and 0.0027, respectively.

Since this chapter only focuses on the suprathermal ion composition in the outer magnetosphere, we will not discuss our observations in the inner magnetosphere here. Our results in the inner magnetosphere are addressed in the next chapter.

3.3 Discussion

3.3.1 L Variations of the Partial Number Density

The spatial variations of the suprathermal ions differ from the spatial variations of the thermal ions. To reach suprathermal energies, the thermal ions must be accelerated. The most likely acceleration processes are injections [*Mauk et al.*, 2005; *Burch et al.*, 2005; *Paranicas et al.*, 2007; *Rymer et al.*, 2009] and inward radial diffusion [*Van Allen et al.*, 1980; *Armstrong et al.*, 1983] conserving the first and second adiabatic invariant. Since the acceleration sites typically differ from the source location, the acceleration processes mix the ions from different sources. As a result, suprathermal partial number densities for the different ion species examined have similar L variations that probably don't reflect any source locations. Unlike the thermal ions whose spatial variations do reflect source locations, it is almost impossible to determine the source locations using the spatial variations of the suprathermal ions.

As discussed in the introduction, an ion that moves from the outer to inner magnetosphere while conserving its first and second adiabatic invariants will gain energy. We can estimate the amount of energy gained by an ion transported from the outer magnetosphere ($L=20$) to $L=7-8$ where the 145-220 keV/e H^+ PND peaks. If we assume that the pitch angle is 90° , then all the energy is in motion perpendicular to the magnetic field, and the energy increases linearly with magnetic field strength (see equation 1.2). According to the magnetic field model by *Achilleos et al.* [2010], the magnetic field strength is 4.4×10^{-5} G at $L=20$ and 4.4×10^{-4} G at $L=7$. Therefore, the energy of an ion

adiabatically transported from $L=20$ to $L=7$ will increase by a factor of 10. A similar increase in energy will occur assuming other pitch angles.

As discussed in the introduction, pick-up acceleration processes will increase the energy of newly created H^+ and O^+ to ~ 150 eV and 2.4 keV at $L=20$, respectively. If these thermal ions were adiabatically transported inward to $L=7$, H^+ would have an energy of 1.5 keV, and O^+ would have an energy of 24 keV. These energies are much less than our highest energy range (145-220 keV/e), so simple adiabatic transport of thermal ions cannot be the only acceleration mechanism in Saturn's magnetosphere. Quasi-adiabatic and non-adiabatic processes have been proposed for Jupiter's magnetosphere [Hill *et al.*, 1983] and are also thought to occur in Saturn's magnetosphere. Quasi-adiabatic processes occur when ions are adiabatically accelerated by inward radial diffusion and then non-adiabatically transported outward. The non-adiabatic outward transport does not cool the plasma, so the accelerated plasma can repeat the process of adiabatic acceleration followed by non-adiabatic outward transport and continue to gain energy.

Rymer *et al.* [2008] proposed such a circulation model to explain their observations of hot electrons at Saturn. During injection events, narrow "fingers" of hot plasma are transported inward and replace broad, outward flowing cooler plasma. The hot, inward moving electrons conserve their adiabatic invariants [Rymer *et al.*, 2007, 2008] and experience gradient and curvature drifts [Mauk *et al.*, 2005; Hill *et al.*, 2005]. The larger drift speeds of the hot electrons cause them to move out of the flux tubes containing the inward flows and into the region containing the cooler, outward flows [Rymer *et al.*,

2008]. As a result, the hot electrons will move outward with the cold plasma. Whether this circulation process also occurs for ions has not been determined.

Non-adiabatic acceleration processes, such as magnetic reconnection, may also be responsible for the energization of plasma. *Mitchell et al.* [2009b] observed the recurrent energization of ions between 15 R_S and 20 R_S on Saturn's nightside and concluded that these events were likely triggered by reconnection in the magnetotail and the creation of plasmoids. In situ magnetic field observations by the Cassini Magnetometer have detected plasmoids [*Jackman et al.*, 2011], but the processes that create them are not fully understood. Based on these observations, non-adiabatic heating of plasma on the nightside in Saturn's outer magnetosphere appears to be a significant acceleration mechanism. Further work is needed to better understand the processes that accelerate thermal ions to energies of 200 keV and higher.

The L variations of the suprathermal ions are qualitatively consistent with inward radial diffusion followed by significant loss processes inside of L=11. These losses are mostly caused by collisions with Saturn's dense neutral cloud in Saturn's inner magnetosphere [*Paranicas et al.*, 2008; *Kollmann et al.*, 2011]. In the outer magnetosphere, where the neutral densities are lower, diffusion appears to be the dominant processes. This is reflected in the lack of L variation in the fractional abundances outside L=15. When comparing source strengths to the suprathermal ion composition, the observations in the outer magnetosphere should be used. The L variations in the suprathermal ion composition in the inner magnetosphere are mostly due to differences in collision

lifetimes among the ion species and are not reflective of the source strength (See chapter 4). We compare our fractional abundances shown in Table 3.1 to current estimates of the source strength.

3.3.2 Implications for H^+ and W^+ Sources

In the outer magnetosphere, W^+ and H^+ dominate the suprathermal ion partial number density with a combined fractional abundance ranging from 0.92-0.93 depending on the energy range. The dominant water group source is Enceladus with a source strength of $\sim 1-4 \times 10^{28}$ H_2O/s [Burger *et al.*, 2007; Jia *et al.*, 2010; Dong *et al.*, 2011]. Most of the atomic H is predicted to originate from Saturn's atmosphere at a rate of $\sim 3 \times 10^{30}$ H/s [Shemansky *et al.*, 2009]. These source strength estimates appear to conflict with our observation that W^+ is more abundant than H^+ in the outer magnetosphere. Our results could indicate that either the atomic H source strength is overestimated or the water group source is underestimated, but the neutral ionization lifetimes must be considered along with other neutral loss processes.

The photoionization lifetimes of H and O is estimated to be $\sim 1.1 \times 10^9$ s and $\sim 2-4 \times 10^8$ s, respectively [Melin *et al.*, 2009; Cassidy and Johnson 2010]. We can calculate the electron impact ionization lifetimes of H and O using the cross sections from Mattioli *et al.* [2007] and the electron observations from Schippers *et al.* [2008]. The ionization lifetimes for the other water group neutrals (OH and H_2O) are estimated to be about the same as O [Cassidy and Johnson 2010]. Figure 3.6 shows our estimates of the H and O electron impact ionization lifetimes as a function of L. Appendix C contains a more

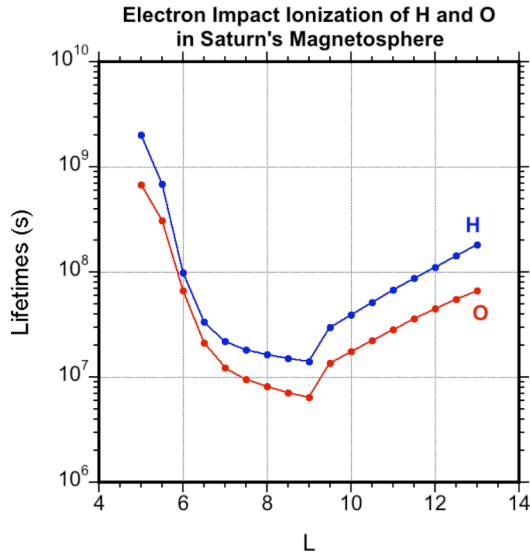


Figure 3.6: Electron impact ionization lifetimes of H and O in Saturn's magnetosphere.

detailed discussion of how we calculate these ionization lifetimes. Depending on the L shell, the H electron impact ionization lifetime is about a factor of 1.5-3.0 longer than that of atomic O. The shorter ionization lifetimes of W^+ will enhance the W^+/H^+ ratio over the ratio of their neutral densities.

Because the estimated source strengths vary by about two orders of magnitude, a factor of 1.5-3.0 difference in the ionization lifetimes cannot entirely explain the discrepancy between our observations and the neutral source strengths. We also must consider the differences in the total number of neutral particles for each species. *Shemansky et al.* [2009] estimates that the total number of H atoms in Saturn's magnetosphere is $\sim 2 \times 10^{35}$, while the total number of O and OH particles is 3×10^{34} and 4×10^{34} , respectively. Even though the difference in neutral source strengths is about 2 orders of magnitude, the total number of H atoms only outnumbers the combined O and OH particles by a factor of 3. Including the total magnetospheric population of H_2O , which has not yet been estimated, will reduce the ratio of total H atoms to total neutral water group particles even further. These estimates indicate the H^+/W^+ ratio will be significantly reduced relative to the ratios of their neutral source strengths. To make a more quantitative comparison between our results and the neutral source strengths, the H^+ source rates must be modeled and include neutral loss processes

such as absorption by Saturn's atmosphere, absorption by the rings, and escape from Saturn's magnetosphere. These loss processes and source rates have been estimated for the water group [*Jurac and Richardson 2007; Smith et al., 2010; Cassidy and Johnson 2010*], but not for H^+ .

The suprathermal ion composition can also be affected by differences in acceleration rates. Cassini Ion and Neutral Camera (INCA) observations of energetic neutral atoms (ENA) in Saturn's magnetotail during a substorm revealed that oxygen was accelerated earlier and more steeply than hydrogen [*Mitchell et al., 2005*]. If W^+ is preferentially accelerated over H^+ , then the suprathermal W^+ PND will be enhanced relative to the suprathermal H^+ PND.

3.3.3 Implications for H_2^+ Source

The majority of H_2 is predicted to originate from Titan with an estimated source strength of $\sim 10^{28}$ H_2/s [*Cui et al., 2008*]. Although the neutral source strengths of H_2 and the neutral water group are predicted to be approximately the same, the H_2^+/W^+ ratio in the outer magnetosphere is much less than 1 and averages 0.0078-0.10 depending on the energy. This relatively low H_2^+/W^+ ratio can be largely explained by differences in ion source rates rather than differences in neutral source strengths. *Smith et al.* [2010] modeled the densities and lifetimes of the neutral water group species and concluded that the W^+ source rate (see Figure 1.9) is above $\sim 10^{-5}$ $W^+/cm^3/s$ at $L < 9$ and peaks at $\sim 10^{-3}$ $W^+/cm^3/s$ near Enceladus' orbit. *Tseng et al.* [2011a] predicts that the H_2^+ source rate has peaks near Titan ($\sim 2 \times 10^{-5}$ $H_2^+/cm^3/s$), at ~ 9 R_S ($\sim 7 \times 10^{-6}$ $H_2^+/cm^3/s$), and over the main

rings ($\sim 6 \times 10^{-5} \text{ H}_2^+/\text{cm}^3/\text{s}$), but has a much lower source rate ($\sim 10^{-6} \text{ H}_2^+/\text{cm}^3/\text{s}$) elsewhere (see Figure 1.10). Therefore, even assuming similar neutral H_2 and H_2O source strengths, the H_2^+ source rate is significantly less than the W^+ source strength.

The loss of H_2^+ prior to acceleration will also reduce the suprathermal H_2^+/W^+ ratio.

Hamilton et al. [1983] estimated the H_2^+ photodissociation lifetimes for all the vibrational states v and concluded that H_2^+ ions with $v \geq 4$ have very short lifetimes of about 1800 seconds or less. As a result of these short lifetimes, a large fraction of the H_2^+ with $v \geq 4$ will be lost prior to acceleration reducing the suprathermal H_2^+/W^+ ratio relative to the ratio of their neutral source strengths. Therefore, the relatively low H_2^+/W^+ ratio observed here does not appear to be due to a significantly weaker H_2 source, but due to smaller H_2^+ source rates and the loss of H_2^+ via photodissociation.

3.3.4 Implication for O^{++} Source

The majority of O^{++} is produced by the single ionization of O^+ and the double ionization of neutral O, so O^{++} is a tracer for the Enceladus source. The fact that the O^{++} PND is more than two orders of magnitude less than that of the W^+ suggests that the O^{++} source rate is significantly smaller than the W^+ source rate. To calculate the thermal O^{++} source rate, we must calculate the collision lifetimes for electron impact ionization of O^+ , photoionization of O^+ , and double electron impact ionization of O.

To calculate the electron impact lifetimes, we use the electron observations by *Schippers et al.* [2008] and perform the calculation for the hot and cold electron components

separately. We use the O^+ single electron impact ionization cross sections from *Mattioli et al.* [2007] and the atomic O double electron impact ionization cross sections from *Talukder et al.* [2009] and *Thompson et al.* [1995]. To evaluate the photoionization lifetimes, we use cross sections from *Verner et al.* [1996] and the results of *Huebner et al.* [1992] who list the solar fluxes at 1 astronomical unit (AU) over several wavelength bins. We multiply these fluxes by $1/r^2$ where r is the average distance of Saturn from the Sun in AU ($r=9.6$ AU). Appendix C contains a more detailed discussion about how we calculate these lifetimes.

To calculate the source rate S of an ion produced by the ionization of a particle A (A can be a neutral or ion), we divide the number density of particle A n_A by the collision lifetime τ :

$$S = \frac{n_A}{\tau} \quad (3.1)$$

To calculate the thermal O^{++} source rate due to single ionization of O^+ , we set n_A equal to the thermal W^+ densities observed by *Thomsen et al.* [2010]. Because W^+ does not consist entirely of O^+ , we are probably overestimating the thermal O^{++} source. We use the neutral O densities predicted by the *Cassidy and Johnson* [2010] model to determine the O^{++} source rate due to the double ionization of O. Figure 3.7 shows the O^{++} source rate due to each process as well as the total O^{++} source rate from all processes combined.

The production rate of O^{++} peaks at $\sim 4\text{-}5 \times 10^{-7} O^{++}/\text{cm}^3/\text{s}$ at $L=7\text{-}9$. In this region, the cold electrons are mostly responsible for the production of O^{++} . Inside of $L=7$, the temperature of cold electrons decreases and no longer produce O^{++} so efficiently. Therefore, the

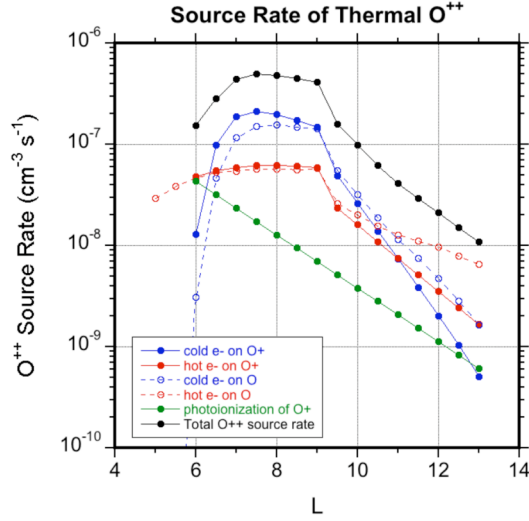


Figure 3.7: Source rate of thermal O^{++} as a function of L .

production of O^{++} due to the hot electrons and photoionization becomes more important in Saturn's inner magnetosphere. The O^{++} source rates estimated here are much lower than the W^+ source rates estimated by *Smith et al.* [2010]. As discussed earlier, *Smith et al.* [2010] calculated a W^+ source rate that is greater than $10^{-5} W^+/cm^3/s$ inside of $L=9$ and peaks at $\sim 10^{-3} W^+/cm^3/s$ near

Enceladus' orbit. Our low O^{++} fractional abundances are qualitatively consistent with these results.

3.3.5 Implication for He^{++} and He^+ Source

Since Saturn's magnetosphere does not contain any local sources of helium, He^+ and He^{++} are tracers for interplanetary pick-up ions of interstellar origin and solar wind ions, respectively [Hamilton et al., 1983; Möbius et al., 1985]. Like the O^{++} , the helium ions have very low fractional abundances and are relatively minor ions. Since the abundance ratios in the solar wind are typically reported at equal energy per nucleon (E/nuc) rather than E/Q , it is more useful to compare the He^{++}/H^+ and He^+/H^+ ratios at the same E/nuc . At equal E/nuc , He^{++} ions have twice the E/Q as H^+ ions, while He^+ ions have four times the E/Q as H^+ ions.

Using the data presented here, we can calculate the abundance ratios $\text{He}^{++}/\text{H}^+$ and He^+/H^+ at 36-55 keV/nuc. From L=15-21 the 36-55 keV/nuc $\text{He}^{++}/\text{H}^+$ ratio averages 0.0025 with a standard deviation of 0.0005, while the 36-55 keV/nuc He^+/H^+ ratio averages 0.0025 with a standard deviation of 0.0001. During typical solar wind conditions, $\text{He}^{++}/\text{H}^+$ is ~ 0.048 [Bame *et al.*, 1977]. The much smaller $\text{He}^{++}/\text{H}^+$ ratio observed in Saturn's magnetosphere indicates that the solar wind is a relatively weak source and that most of the H^+ is produced by local sources. This conclusion is consistent with prior studies [McDonald *et al.*, 1980; Hamilton *et al.*, 1983].

At 36-55 keV/nuc, the He^+ and He^{++} abundances are approximately the same. This is somewhat surprising since the 41.7 keV/nuc $\text{He}^+/\text{He}^{++}$ ratio in interplanetary space near Saturn is about 10 [Hill *et al.*, 2009]. Therefore, the $\text{He}^+/\text{He}^{++}$ ratio must change substantially when these ions enter the magnetosphere. Understanding the processes that lead to this change in helium charge states is outside the scope of this thesis.

Chapter 4

Energy and L Variations of the Suprathermal Ions: Loss Processes in Saturn's Inner Magnetosphere

As shown in the previous chapter, the suprathermal ion partial number density (PND) decreases in Saturn's inner magnetosphere. The depletion of the suprathermal ions has been observed in prior studies and is largely due to collisions with Saturn's extensive neutral cloud [*Paranicas et al.*, 2008; *Kollmann et al.*, 2011]. Unlike the outer magnetosphere, the suprathermal fractional abundances (FA) in the inner magnetosphere show significant variations with energy and L. These variations are mostly due to differences in collision lifetimes. Here we summarize our results from the inner magnetosphere and compare them to the estimated lifetimes in the inner magnetosphere.

4.1 Results

Inside of L=7-8, ions with energies ranging from 100-200 keV appear to persist longer than those at lower energies (See spectrograms shown in Figures 3.1 and 3.2). This trend is strongest in the H^+ data, but also occurs in the W^+ , He^+ , and O^{++} data. However, for the O^{++} it occurs at roughly half the E/Q indicating a dependence on energy rather than E/Q. The He^{++} drops substantially inside of L=8 and does not appear to persist at any energy. The O^{++} and W^+ at the E/Q=9 keV/e and E/Q=10 keV/e steps also show a longer persistence compared to the ions at energies between 10-100 keV/e, but no other species shows this trend at these energies.

We presented the FA's of six ion species versus L as well as the 3-8 keV/e H_2^+/H^+ ratio versus L in the previous chapter. When trying to understand the loss processes in the inner magnetosphere, it is more useful to focus on the change in FA from the outer to inner magnetosphere rather than the FA values of each species in the inner magnetosphere. We take the ratio of the FA at the innermost point (L=6-7) to the average FA in the outer magnetosphere (L=15-21). We plot this ratio for all six species versus E/Q in Figure 4.1. A ratio of greater than one indicates that the FA increased inward, while a ratio of less than one indicates the FA decreased inward.

The H^+ and W^+ FA's show significant variations with energy and L in Saturn's inner magnetosphere. The 9-14 keV/e H^+ FA decreases by a factor of 1.8 from the outer magnetosphere to L=6-7, while the 9-14 keV/e W^+ FA increases by a factor of 1.1. At E/Q=36-55 keV/e, the H^+ and W^+ FA's in the inner magnetosphere do not significantly deviate from their average values in the outer magnetosphere. At the two highest energy ranges, the H^+ FA increases inward, while the W^+ FA decreases inward. This trend is strongest at E/Q=145-220 keV/e where the W^+ FA decreases by a factor of 2.2 from the outer magnetosphere to L=6-7, while the H^+ FA increases by a factor of 2.6.

As shown in Figure 4.1, the H_2^+ FA decreases inward for all energy ranges with the most substantial decrease occurring at the two highest energy ranges. Although the decline in the H_2^+ FA is not so large at 9-14 keV/e and 36-55 keV/e, it's still larger than that of H^+ and W^+ . The 3-8 keV/e H_2^+/H^+ ratio decreases inward from its average value of 0.39 in the outer magnetosphere to its lowest value of 0.30 at L=7-8. Therefore, throughout the

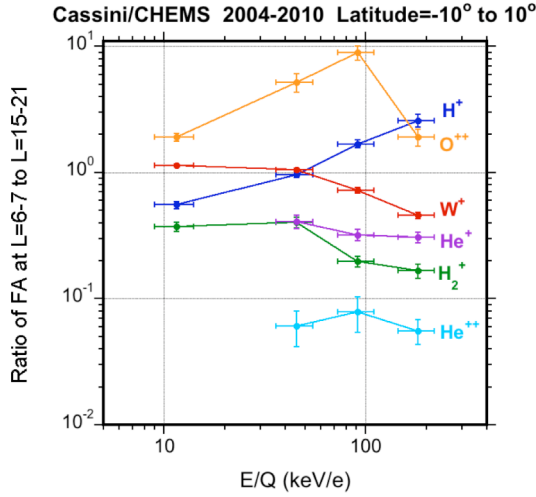


Figure 4.1: The ratio of the FA at L=6-7 to the FA at L=15-21 versus E/Q.

entire CHEMS energy range, the inward decrease of the H_2^+ FA is greater than both the H^+ and W^+ FA. While H_2^+ is the third most abundant suprathermal ion species in the outer magnetosphere, its FA in the inner magnetosphere ($L < 7-8$) drops below that of O^{++} at some energy ranges.

The O^{++} FA increases inward at all energy ranges, but the size of this increase varies significantly with energy. The 9-14 keV/e and 145-220 keV/e O^{++} fractional abundance increases by a factor of 1.9 from the outer magnetosphere to L=6-7. At the other two energy ranges, this increase is much larger particularly at 73-110 keV/e, where the O^{++} FA increases by a factor of 8.9.

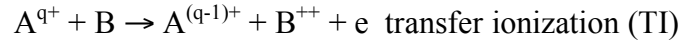
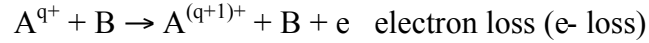
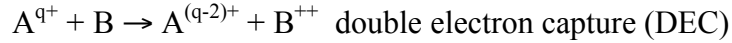
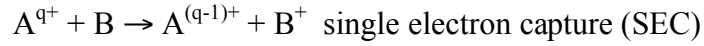
The FA of both helium charge states decrease inward. Compared to the other species included in this study, He^{++} FA shows the largest inward decrease dropping more than an order of magnitude from the outer magnetosphere to L=6-7. The He^+ FA also shows a large decline compared to that of H^+ and W^+ , but it is not so large as the decrease observed in the He^{++} FA. Like the H_2^+ , the He^+ FA abundance shows its largest inward decline at the highest energy range where it decreases by a factor of 3.3 from the outer magnetosphere to L=6-7.

4.2 Discussion

The inward decline of the suprathermal ion partial number densities is due to loss processes in Saturn's inner magnetosphere. Recent studies suggest ion-neutral collisions are the dominant loss process [*Paranicas et al.*, 2008; *Kollmann et al.*, 2011], but electron impact, photoionization, and photodissociation are other potential loss processes. We estimate the lifetimes for all six species due to these collisions and compare them to the L variations of the fractional abundances in Saturn's inner magnetosphere.

4.2.1 Lifetimes of Suprathermal Ions

When an ion A^{q+} with charge q collides with a neutral B , a few possible reactions can occur:



The electron capture reaction is also called charge exchange or charge transfer. Each of these processes will result in the loss of the suprathermal ion A^{q+} . Some reactions (e.g. single electron capture when $q=1$) produce an energetic neutral that escapes Saturn's magnetosphere and a cold ion that is not detected by CHEMS. These reactions result in a decrease in the combined partial number density of the suprathermal ions. Single electron capture of ions with $q > 1$ or electron loss collisions only change the charge states of the ions and do not reduce the combined suprathermal ion partial number density. Some of these processes also lead to the production of A^{q+} . As we will discuss later in this section,

the electron loss collision of O^+ on O results in the production of suprathermal O^{++} in the inner magnetosphere.

To calculate the lifetime of a suprathermal ion, we need estimates of the collision cross section σ , the neutral density n_n , and the ion velocity v_i :

$$\tau = \frac{1}{n_n v_i \sigma} \quad (4.1)$$

The neutral particle velocities are negligible, because they are much less than those of the suprathermal ions. We use the results from the *Cassidy and Johnson* [2010] model to obtain the neutral densities of O, OH, and H₂O. Because the suprathermal ion partial number densities typically peak between L=9-10, we calculate the lifetimes at L=9.5 where the O, OH, and H₂O densities are estimated to be 54 cm⁻³, 14 cm⁻³, and 13 cm⁻³, respectively [*Cassidy and Johnson* 2010].

We obtained collision cross sections for the reactions shown in Table 4.1. The cross sections for every relevant ion-neutral collision in Saturn's magnetosphere were not available, so we had to make some assumptions when calculating the lifetimes. Collisions between suprathermal ions and OH were not available, so we assumed these collisions have the same cross sections as ions colliding with either O or H₂O. Collisions involving suprathermal OH⁺, H₂O⁺, and H₃O⁺ colliding with neutrals could not be found, so we assumed that W⁺ consists entirely of O⁺ when calculating the lifetimes. Appendix C contains a more detailed discussion about these assumptions and the studies used to estimate the lifetimes. The suprathermal ion lifetimes at L=9.5 as a function of E/Q are shown in Figure 4.2. We also average the lifetimes of the four E/Q steps within each of

Table 4.1: Each reaction considered when calculating the suprathermal ion lifetimes along with their references. The assumptions we made when calculated are also shown. See text and Appendix C for details.

Reaction	References	Assumptions
$H^+ + O$ (SEC)	• <i>Lindsay and Stebbings</i> [2005]	Transfer ionization is negligible
$H^+ + H_2O$ (SEC)	• <i>Dagnac et al.</i> [1970] • <i>Rudd et al.</i> [1985a] • <i>Lindsay et al.</i> [1997] • <i>Greenwood et al.</i> [2000] • <i>Gobet et al.</i> [2004] • <i>Luna et al.</i> [2007]	Same as H^+ on OH
$O^+ + O$ (SEC)	• <i>Lindsay and Stebbings</i> [2005]	Same as OH^+ , H_2O^+ , and H_3O^+ on O. Same as O^+ on OH and H_2O
$O^+ + O$ (e- loss)	• <i>Lo et al.</i> [1971]	
$H_2^+ + H_2O$ (SEC)	• <i>Dagnac et al.</i> [1970]	Dissociation is negligible from 1-60 keV
$H_2^+ + H$ (all loss processes)	• <i>McGrath et al.</i> [2001] • <i>Hennecart and Pascale</i> [2005]	Same as H_2^+ on O, OH, and H_2O at $E > 60$ keV
$O^{++} + H$ (SEC)	• <i>Phaneuf et al.</i> [1987]	Same as O^{++} on O, OH, and H_2O
$He^+ + H_2O$ (SEC)	• <i>Rudd et al.</i> [1985b]	Same as He^+ on O and OH
$He^+ + H_2O$ (e- loss)	• <i>Rudd et al.</i> [1985b]	
$He^{++} + H_2O$ (SEC)	• <i>Rudd et al.</i> [1985c] • <i>Greenwood</i> [2004]	Same as He^{++} on OH
$He^{++} + H_2O$ (DEC)	• <i>Rudd et al.</i> [1985c] • <i>Greenwood</i> [2004]	
$He^{++} + O$ (SEC)	• <i>Thompson et al.</i> [1997]	
$He^{++} + O$ (TI)	• <i>Thompson et al.</i> [1997]	
$He^{++} + O$ (DEC)	• <i>Thompson et al.</i> [1997]	

the following energy ranges: 9-14 keV/e, 36-55 keV/e, 73-110 keV/e, and 145-220 keV/e (See Table 4.2).

If the diffusion time scales are much shorter than the collision lifetimes, then suprathermal ions will diffuse quickly through the region and the loss processes due to collisions will be negligible. Thus, it is necessary to compare the collision lifetimes to the diffusion time scales at $L=9.5$. Based on analysis of the phase space density observations

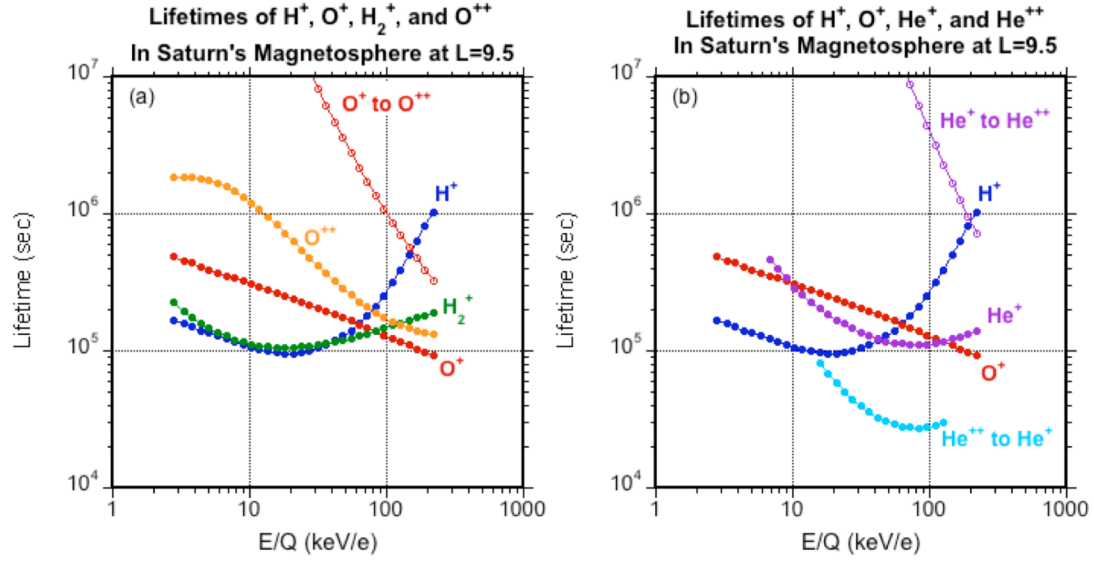


Figure 4.2: (a) H^+ , H_2^+ , O^+ , and O^{++} lifetimes due to ion-neutral collisions at L=9.5. The O^+ to O^{++} indicates the lifetimes due to the electron loss collision of O^+ on O. (b) H^+ , O^+ , He^+ , and He^{++} lifetimes due to ion-neutral collisions at L=9.5. The He^+ to He^{++} indicates the lifetimes due to the He^+ on H_2O electron loss collision

by Voyager and Pioneer, the diffusion timescales at L=9.5 have been estimated to be $\sim 4.2 \times 10^5$ s for 20 keV protons [Hood 1985] and $\sim 4.2 \times 10^6$ s for 150 keV protons [Hood 1989]. Unfortunately, these estimates contain a great deal of uncertainty and the upper and lower limits of the diffusion coefficients differ by about two orders of magnitude [Paonessa and Cheng 1986]. However, the estimates by Hood [1985, 1989] suggest that the diffusion timescales are comparable to or larger than the electron capture lifetimes at L=9.5.

Electron impact and photoionization are also potential loss processes for the suprathermal ions. As discussed in chapter 3, we use the electron impact ionization cross sections from Mattioli *et al.* [2007] and the electron observations by Schippers *et al.* [2008] to calculate the electron impact ionization lifetimes (See Appendix C for details). We also obtained cross sections for the electron impact dissociation of H_2^+ from a number of studies [Dunn

Table 4.2: Average lifetimes (in seconds) of each suprathermal ion species due to ion-neutral collisions.

Species	9-14 keV/e	36-55 keV/e	73-110 keV/e	145-220 keV/e
H ⁺	1.0x10 ⁵	1.2x10 ⁵	2.4x10 ⁵	7.4x10 ⁵
W ⁺	3.0x10 ⁵	1.8x10 ⁵	1.3x10 ⁵	1.0x10 ⁵
H ₂ ⁺	1.1x10 ⁵	1.2x10 ⁵	1.4x10 ⁵	1.8x10 ⁵
O ⁺⁺	1.1x10 ⁶	3.1x10 ⁵	1.8x10 ⁵	1.4x10 ⁵
O ⁺ to O ⁺⁺	-	4.2x10 ⁶	1.3x10 ⁶	4.4x10 ⁵
He ⁺	-	1.2x10 ⁵	1.1x10 ⁵	1.3x10 ⁵
He ⁺⁺	-	2.9x10 ⁴	2.7x10 ⁴	-

Table 4.3: Suprathermal ion lifetimes (in seconds) due to electron impact and photoionization.

Species	Electron impact (cold e-) ^a	Electron impact (hot e-)	Photoionization
He ⁺	7.3-9.7x10 ⁸	1.6x10 ⁹	7x10 ⁸
O ⁺	6-7x10 ⁷	1.6x10 ⁸	7.9x10 ⁹
H ₂ ⁺	1.5-1.6x10 ⁶	8.5-8.6x10 ⁷	-

^a Because the suprathermal ion velocity is comparable to the velocity of the cold e, the electron impact lifetime depends on the ion energy. The longer lifetimes are the lifetimes of 2.8 keV ions, while the shorter lifetimes are the lifetimes of 220 keV ions.

and Van Zyl 1967; Peart and Dolder 1972; Yousif and Mitchell 1995]. Photoionization lifetimes are calculated using the cross sections from *Verner et al.* [1996] and the solar fluxes reported in *Huebner et al.* [1992]. The photoionization and electron impact lifetimes of H₂⁺, He⁺ and O⁺ are shown in Table 4.3. Compared to ion-neutral collision, the electron impact and photoionization lifetimes are much longer and are negligible loss processes.

4.2.2 Persistence of ~100-200 keV Ions

Inside of L=7-8, ions with energies ranging from 100-200 keV appear to persist longer than those at lower energies. This result is surprising because although the H⁺ lifetime

increases rapidly above 100 keV, the W^+ lifetime decreases with increasing energy over the entire CHEMS energy range. Therefore, our lifetime calculations cannot explain this trend. Estimates of the diffusion timescales are also inconsistent with the longer persistence of 100-200 keV ions. If the 100-200 keV ions had a shorter diffusion timescale compared to ~10-100 keV ions, then they would diffuse inward more quickly and experience fewer losses due to ion-neutral collisions. However, as discussed above, the diffusion timescales at $L=9.5$ for 150 keV protons are about an order of magnitude longer than that of 20 keV protons [Hood 1985, 1989].

Analysis of the energetic (30-1000 keV) protons detected by Cassini LEMMS revealed a similar inconsistency between the predicted lifetimes due to ion-neutral collisions and the proton observations in Saturn's inner magnetosphere [Kollmann *et al.*, 2011]. Kollmann *et al.* [2011] estimated the energetic proton collision lifetimes at $L=7$ and concluded that it increases with energy. However, their energetic proton observations suggest that the energetic protons have a lifetime longer than predicted and that their lifetime peaks near 200 keV. Kollmann *et al.* [2011] suggested that injection events are an additional source of energetic protons in the inner magnetosphere and could lead to the discrepancy between observations and lifetime calculations. Injection rates vary from pass to pass and are at least partly controlled by solar wind condition [Mitchell *et al.*, 2005; Bunce *et al.*, 2005; Kellett *et al.*, 2011]. Therefore, we cannot examine their effect using our long sum of data and would have to consider short-term time variations in the suprathermal ion partial number density to better understand their effect. Studying the variations from pass to pass is outside the scope of this thesis.

4.2.3 Energy and L Variations of H^+ and W^+ FA

The L variations of the H^+ FA and W^+ FA can be largely explained by differences in their electron capture lifetimes. At 9-14 keV/e W^+ has a lifetime that is three times longer than that of H^+ , so the inward increase of the W^+ FA and decrease of the H^+ FA at these energies is consistent with our lifetime calculations. At $E/Q=36-55$ keV/e, where neither the H^+ nor W^+ FA varies significantly with L, the H^+ and W^+ lifetimes are comparable at 1.2×10^5 s and 1.8×10^5 s, respectively. The H^+ lifetime at 145-220 keV/e is longer than the W^+ lifetime by a factor of 7.4 resulting in the substantial inward increase of the H^+ FA and the decline of the W^+ FA.

4.2.4 Energy and L Variations of H_2^+ FA

Based on our lifetime calculations shown in Figure 4.2, the inward decline of the H_2^+ FA is larger than expected. At 3-8 keV/e, the H_2^+ lifetime is slightly longer than that of H^+ , so we would expect the H_2^+/H^+ ratio at this energy to show a small increase inward rather than decrease. As shown in Table 4.2, the H_2^+ lifetime is approximately the same as the H^+ lifetime at 36-55 keV/e, while the H_2^+ lifetime at $E/Q > 73$ keV/e is slightly longer than the W^+ lifetime. However, at all energies included in this study, the H_2^+ FA decreases more than that of H^+ and W^+ . There are obvious uncertainties in our calculation such as assuming that the H_2^+ on H collision cross section is the same as H_2^+ on O or H_2O . Also, our collision cross sections at $E/Q < 60$ keV/e ignores the dissociation of H_2^+ .

As H_2^+ diffuses inward, it can also be lost via photodissociation. Because the photodissociation lifetime varies significantly with vibrational state v [Hamilton *et al.*, 1983], we must know the vibrational states of the suprathermal H_2^+ ions to predict their overall photodissociation lifetime. Determining the distribution of vibrational states in Saturn's magnetosphere is almost impossible. As discussed in the previous chapter, H_2^+ ions with $v \geq 4$ have lifetimes of about 1800 seconds or less and are likely lost before they are accelerated. The H_2^+ vibrational states of $v=2$ and $v=3$ also have relatively short lifetimes of 8.2×10^4 s and 1.0×10^4 s, respectively [Hamilton *et al.*, 1983]. If the suprathermal H_2^+ population consists of a significant fraction of these two vibrational states, then photodissociation would be the dominant loss process. At the two lowest vibrational states where the photodissociation lifetime is 1.8×10^7 s for $v=0$ and 1.3×10^6 s for $v=1$ [Hamilton *et al.*, 1983], ion-neutral collisions will be the dominant loss process. Based on our observations, it appears unlikely that photodissociation of suprathermal H_2^+ is a significant loss process. If it were an important process, then H_2^+ would be lost at all radial distances, and we would expect the H_2^+ FA to decline throughout the magnetosphere rather than just in the inner magnetosphere.

4.2.5 Energy and L Variations of O^{++} FA

Variations of the suprathermal O^{++} FA in the inner magnetosphere are due mostly to the loss of O^{++} via single electron capture and the production of suprathermal O^{++} via the electron loss collision of O^+ . At 9-14 keV/e the electron loss collision of O^+ on O is negligible, so the inward increase of the O^{++} FA at this energy is largely due O^{++} having a longer lifetime at this energy than any other species included in this study.

At higher energies the O^{++} lifetime decreases, but the production of O^{++} by the electron loss collision of O^+ on O becomes significant. While the single electron capture of O^{++} reduces the O^{++} abundance, the electron loss collision of O^+ on O increases the O^{++} abundance. To determine the more significant reaction, we must compare the O^{++} source and loss rate due to these reactions. The O^{++} loss rate is determined by dividing the O^{++} PND by the O^{++} electron capture lifetimes shown in Table 4.2.

The electron loss collision of O^+ on O at a specific E/Q will produce an O^{++} ion at half the E/Q. Using our PND observations of 73-110 keV/e W^+ and 145-220 keV/e W^+ , we can estimate the source rate of 36-55 keV/e O^{++} and 73-110 keV/e O^{++} , respectively. The suprathermal W^+ consists of about 53% O^+ (See chapter 5), so we multiply our W^+ PND by this percentage to obtain the O^+ PND. To estimate the source rate, we divide the O^+ PND by the O^+ electron loss collision lifetime shown in Table 4.2. As shown in Table 4.3, the ionization of O^+ by electron impact and photoionization is negligible compared to the electron loss collision, so unlike the production of thermal O^{++} , the production of suprathermal O^{++} is dominated by ion-neutral collisions.

At L=9.5, the suprathermal O^{++} source rate is $1.1 \times 10^{-10} O^{++}/cm^3/s$ and $1.5 \times 10^{-10} O^{++}/cm^3/s$ at 73-110 keV/e and 36-55 keV/e, respectively. The O^{++} loss rate is $4.6 \times 10^{-11} O^{++}/cm^3/s$ and $4.4 \times 10^{-11} O^{++}/cm^3/s$ at 73-110 keV/e and 36-55 keV/e, respectively. Since the source rate is greater than the loss rate, we would expect the O^{++} PND to continue to increase inward at L=9-10. While this calculation is consistent with our observations at

L=9-10, the O^{++} source rate remains higher than the O^{++} loss rate inside of L=7. This is inconsistent with our observation that the O^{++} PND decreases inward inside of L=7. The reason for this discrepancy is most likely due to our loss rate calculation where we assume that O^{++} on H has the same cross sections as O^{++} on O. However, these calculations show that the production of O^{++} via the O^+ on O electron loss collision plays a significant role in the inward increase of the O^{++} FA at $E/Q > 36$ keV/e.

The factor of 8.9 increase of the 73-110 keV/e O^{++} FA from the outer magnetosphere to L=6-7 is not entirely due to ion-neutral collisions. As discussed earlier, ~100-200 keV ions tend to persist longer than ions at lower energies inside of L=7-8. This longer persistence is not consistent with lifetime calculations and has been attributed to injection events [Kollmann *et al.*, 2011]. Because this trend depends on energy rather than E/Q, the 73-110 keV/e O^{++} will appear to persist longer than singly ionized particles at the same E/Q. When we plot the O^{++}/W^+ at equal energies (not shown here), the O^{++}/W^+ ratio still increases inward, but the increase not as substantial.

4.2.6 Energy and L Variations of He^{++} FA

As shown in Table 4.2, the lifetime of He^{++} is more than a factor of three lower than the lifetimes of the other ion species. We were unable to obtain He^{++} lifetimes at the highest energy range, but based on the plot shown in Figure 4.2b, the He^{++} lifetime at 145-220 keV/e likely remains significantly less than the other ion species. Like the O^{++} , suprathermal He^{++} can be produced by the electron loss collision of He^+ , but this reaction has a very long lifetime and does contribute significantly to the He^{++} abundances. Given

these lifetime estimates, it is not surprising that the He^{++} FA drops more than an order of magnitude from the outer magnetosphere to $L=6-7$.

4.2.7 Energy and L Variations of He^+ FA

Like the H_2^+ , our observation that the He^+ FA shows a larger inward decrease than that of H^+ and W^+ is inconsistent with our lifetime calculations. The He^+ lifetime at 36-55 keV/e is the same as the H^+ lifetime, while the He^+ lifetime at 73-110 keV/e and 145-220 keV/e is very close to the W^+ lifetime. As previously discussed, there are obvious uncertainties in our lifetime calculations. At the energies considered here, the He^{++} on O cross sections are larger than the He^{++} on H_2O . If this trend is the same for He^+ , then we are overestimating the He^+ lifetime by assuming the He^+ on H_2O has the same cross section as He^+ on O.

We also consider the production of suprathermal He^+ via the single electron capture and transfer ionization collisions of He^{++} . A He^{++} ion that experiences either of these collisions will produce a He^+ ion at twice the E/Q. We can use our observed He^{++} PND's at 36-55 keV/e and 73-110 keV/e to calculate the He^+ source rate at 73-110 keV/e and 145-220 keV/e, respectively. At $L=9.5$, the 73-110 keV/e He^+ source and loss rate is $1.9 \times 10^{-11} \text{ He}^+/\text{cm}^3/\text{s}$ and $4.1 \times 10^{-11} \text{ He}^+/\text{cm}^3/\text{s}$, respectively. At the same L shell, the 145-220 keV/e He^+ source and loss rate is 8.4×10^{-12} to 8.7×10^{-12} , respectively. Although the source and loss rates are comparable in the middle magnetosphere, the source rate becomes negligible in the inner magnetosphere where the He^{++} PND drops substantially.

Therefore, we would expect the He^+ PND to decrease in the inner magnetosphere, but our observed decrease is larger than expected based on our lifetime calculations.

Chapter 5

Composition of 96 keV W^+

In the previous chapters, we did not attempt to separate the W^+ ions into its four main components: O^+ , OH^+ , H_2O^+ , and H_3O^+ . Determining the composition of the water group ions provides insight into the composition of Saturn's extensive neutral cloud. Remote observations by the Hubble Space Telescope and Cassini UVIS revealed that Saturn's magnetosphere contains a broad OH cloud and O cloud [Shemansky *et al.*, 1993; Melin *et al.*, 2009]. Based on these observations, the O cloud is estimated to be twice as broad as the OH cloud [Melin *et al.*, 2009]. A variety of processes can spread the neutral particles emitted by Enceladus throughout Saturn's magnetosphere and produce the extensive O and OH clouds. These processes include charge exchange, photodissociation, and neutral-neutral collisions [Johnson *et al.*, 2006; Smith *et al.*, 2010; Farmer *et al.*, 2009; Cassidy and Johnson 2010].

Smith *et al.* [2010] modeled the lifetimes of the neutral water group (O, OH, and H_2O) due to charge exchange, electron impact, photoionization, and photodissociation and concluded that photodissociation of H_2O and OH is the mechanism largely responsible for spreading neutral O and OH throughout the magnetosphere. However, neutral-neutral collisions have also been shown to be an effective spreading mechanism and including these collisions produces a broader neutral cloud, particularly for H_2O [Farmer 2009; Cassidy and Johnson 2010]. Models that ignore neutral-neutral collisions [Johnson *et al.*, 2006; Smith *et al.*, 2010] predict a narrow H_2O torus centered on Enceladus with

negligible H₂O density outside of 6 R_S, while including the neutral-neutral collisions results an H₂O cloud with approximately the same density as OH outside of 7 R_S [Cassidy and Johnson 2010].

The ionization of the water group neutrals by electron impact, solar photons, and charge exchange produce O⁺, OH⁺, and H₂O⁺ [Smith *et al.*, 2010; Cassidy and Johnson 2010], while H₃O⁺ is largely produced by charge exchange reactions in the Enceladus torus [Cravens *et al.*, 2009; Fleshman *et al.*, 2010a]. The combination of these four ion species makes up the water group ions W⁺. CAPS observations from SOI indicate that inside of 10 R_S the thermal W⁺ consists mostly of molecular ions with an average mass of 18 amu [Sittler *et al.*, 2008]. In this chapter, we determine the composition of 96 keV W⁺ and compare our results to the neutral cloud models and the CAPS observations.

5.1 Data Analysis Methods

We combine the CHEMS data from the 78 equatorial ring current passes (L=7-16; Latitude = -10° to 10°) shown in Figure 2.6 to determine the composition of W⁺. We focus on the 96 keV/e E/Q channel and telescope 1 data where it is easiest to resolve all four W⁺ components. Anisotropies of the suprathermal ions at the energies considered here are very modest in the equatorial ring current, so only using telescope 1 does not affect our results significantly. We only use the CHEMS data that include an energy measurement from the SSD because of the lower background in the triples data.

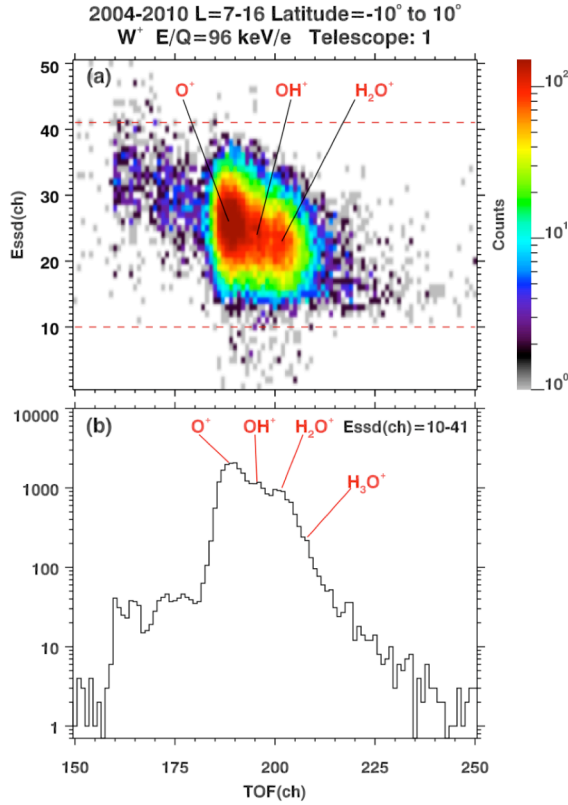


Figure 5.1: (a) Solid State Detector (SSD) energy channel $\text{Essd}(\text{ch})$ versus time-of-flight channel $\text{TOF}(\text{ch})$ of the 96 keV W^+ . (b) 96 keV W^+ time-of-flight histogram for the data between the energy channels indicated by the horizontal red dashed lines. We combine the data from 78 equatorial ring current passes. These data are from CHEMS telescope 1 which has the best heavy ion resolution.

A plot of the SSD energy channel $\text{Essd}(\text{ch})$ versus the time-of-flight channel $\text{TOF}(\text{ch})$ for all 78 ring current passes combined is shown in Figure 5.1a. Separating the W^+ components is easier using the raw channel values, so we do not convert $\text{Essd}(\text{ch})$ and $\text{TOF}(\text{ch})$ to Mass (amu) and mass per charge M/Q (amu/e). We make an $\text{Essd}(\text{ch})$ cut selecting the data between the horizontal red dashed lines shown in Figure 5.1a and create a $\text{TOF}(\text{ch})$ histogram of the data (See Figure 5.1b). All four major components of the W^+ group can be identified, although the H_3O^+ appears as a

shoulder. We fit these peaks to estimate the abundances of these four species.

We have used the 96 keV O^{++} ($E/Q=48$ keV/e) TOF distribution as a guide to choosing appropriate fitting parameters for the W^+ species, which overlap. We do not use the pre-launch calibration data for 96 keV O^+ and H_2O^+ , because the distributions in the calibration data were narrower than those in the in flight data due to the monoenergetic and unidirectional nature of the calibration beam. Since the O^{++} ions at $E/Q=48$ keV/e

have the same energy as 96 keV O^+ , the 48 keV/e O^{++} TOF distribution is nearly identical to that of 96 keV O^+ . We can easily fit the 96 keV O^{++} (i.e. 48 keV/e O^{++}) since there is no overlap from other ion species and use the result in fitting the 96 keV O^+ .

A TOF histogram of the 96 keV O^{++} distribution for all 78 equatorial ring current passes is shown in Figure 5.2. An asymmetric Gaussian fits the center of the distribution. At higher TOF(ch) away from the center the counts decline more slowly than Gaussian, so we must add a small additional term to the Gaussian on the right side of the peak. We refer to this section as the “tail”. The function we use to fit the counts at each TOF channel τ is

$$f(\tau) = A \left[e^{-\frac{(\tau-\tau_c)^2}{2\sigma_1^2}} P(-\tau + \tau_c) + \left(e^{-\frac{(\tau-\tau_c)^2}{2\sigma_2^2}} + \frac{(\tau - \tau_c)^2}{100 + [(\tau - \tau_c)^2]^\alpha} \right) P(\tau - \tau_c) \right] \quad (5.1)$$

This function peaks at $\tau = \tau_c$ with an amplitude A. The sigmoid function $P(x)=1/(1+e^{-x})$ is an approximation to the Heavyside function which is ~ 0 for $x < 0$ and ~ 1 for $x > 0$. The parameters σ_1 and σ_2 are the Gaussian sigma (i.e. width) for the left side and right side of the distribution, respectively.

Gaussian fits performed by *von Steiger et al.* [2000] on ion species distributions from the Ulysses Solar Wind Composition Spectrometer revealed that the Gaussian sigma to center ratios of the TOF distributions is relatively constant. Therefore, we use the σ_1/τ_c and σ_2/τ_c ratios as fitting parameters rather than σ_1 and σ_2 . For $\tau \gg \tau_c$, the function declines as $\sim [(\tau-\tau_c)^2]^{(1-\alpha)}$, so the parameter α controls the rate of decline in the tail. The

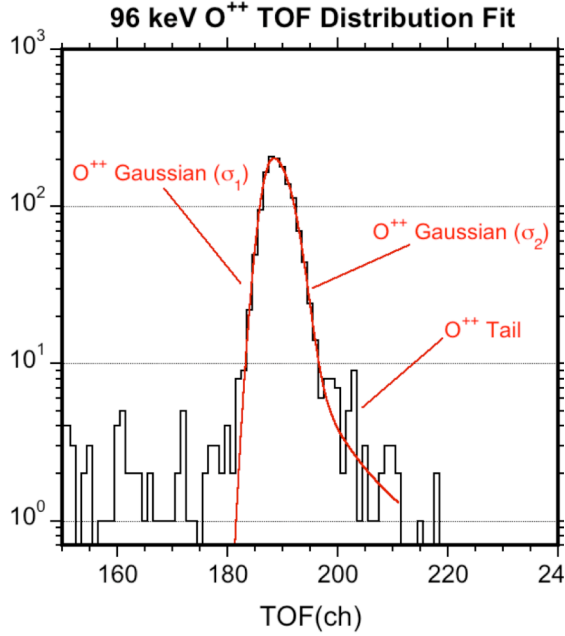


Figure 5.2: 96 keV O^{++} ($E/Q=48$ keV/e) distribution for all 78 equatorial ring current passes ($L=7-16$, Latitude = -10° to 10°) combined. The solid red line represents the best fit to the distribution using equation 1 (See text). We use an asymmetric Gaussian to fit the counts near the center of the distribution, but must add a small additional term to the Gaussian on the right side to fit the counts in the “tail.”

form of our fitting function is similar to the kappa distribution used by *Allegini et al.* [2006] to fit the energy distribution of 1-50 keV ions traveling through thin, carbon foils.

Using the Levenberg-Marquardt fitting procedure [*Press et al.*, 1989], we fit the 96 keV O^{++} distribution using the function given in equation 1. The best fit (reduced $\chi^2=0.73$) is obtained with $\alpha=1.81$ and is shown in Figure 5.2.

When fitting the O^+ distribution, we require that the σ_1/τ_c and σ_2/τ_c ratios of

96 keV O^+ are the same as 96 keV O^{++} . The widths of the molecular ion distributions tend to differ from those of atomic ions, so the σ_1/τ_c and σ_2/τ_c ratios of OH^+ , H_2O^+ , and H_3O^+ are not the same as O^+ . However, we force these ratios to be the same for all three molecular species. The α parameter is assumed to be the same for all four species.

In order to determine the sensitivity of our results to the form of the fitting function, we have performed three different fits on the W^+ distribution: (1) asymmetric Gaussian ($\alpha=\infty$), (2) requiring α to equal the value from the O^{++} fit ($\alpha=1.81$), and (3) allowing α to vary. For the first two fits, we require the σ_1/τ_c and σ_2/τ_c values for O^+ to equal the results

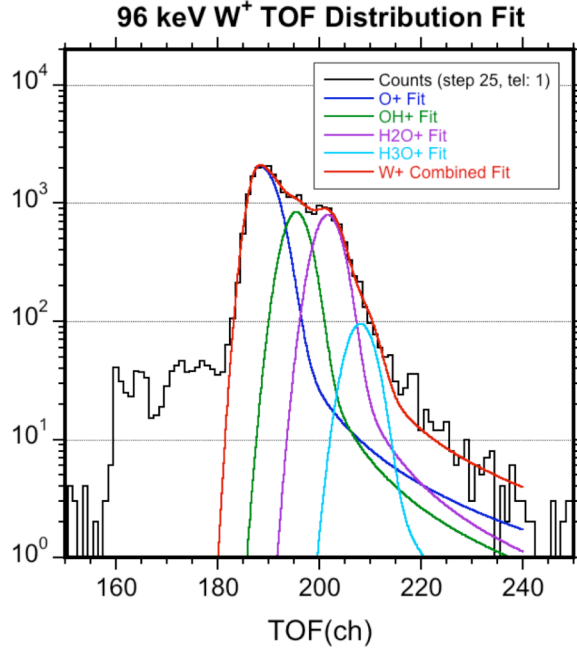


Figure 5.3: Best fit of the 96 keV W^+ distribution. The fits to each individual species are shown along with the sum of the four fits in red. The data are from CHEMS telescope 1.

from the O^{++} fits. Since the value of α affects the value of σ_2 , we let both σ_2 and α vary for the third fit. Our best fit (reduced $\chi^2 = 4.0$) of the entire W^+ distribution is found using the type 3 fit and with $\alpha=1.90$. These results are shown in Figure 5.3. We numerically integrate the fits from each peak to determine the counts for each species. We then convert the counts into partial number density (PND) and calculate the fractional abundance relative to W^+ .

After obtaining the fits in the main ring current ($L=7-16$; Latitude = -10° to 10°), we divide our passes by L shell and look for variations with L in the $L=7-21$ range. We cannot perform a fit at $L=6-7$, because of poor counting statistics. When fitting the data by L shell, the statistics are worse, and we only let the amplitudes of the peaks vary. We force the center τ_c , σ_1 , σ_2 , and α of each species peak to be the same as the results from the $L=7-16$ fit. We can use a $\Delta L=1$ between $L=7$ and $L=11$ where there are sufficient counts, but we must combine L shells beyond this distance where the counting statistics decline. We include a more detailed discussion about fitting the W^+ distribution along with the fitting parameters from each fit in Appendix D.

Table 5.1: Partial number density (PND) and relative abundance of four major 89-103 keV W^+ components in the equatorial ring current region^a.

Species	Counts	Partial Number Density ($\times 10^{-6} \text{ cm}^{-3}$)	Fraction of W^+
O^+	14400	23.4 ± 0.7	0.53 ± 0.02
OH^+	5743	9.6 ± 0.4	0.22 ± 0.01
H_2O^+	5607	9.7 ± 0.4	0.22 ± 0.01
H_3O^+	690	1.2^b	0.028^b

^a The abundances are determined using the results from our best fit ($\alpha=1.90$). The uncertainties of O^+ , OH^+ , and H_2O^+ reflect the statistical uncertainties from our fits.

^b The uncertainty of the H_3O^+ partial number density and fractional abundance reflects the range of values from our three fits. The H_3O^+ has a lower limit of $7.2 \times 10^{-7} \text{ cm}^{-3}$ and an upper limit of $1.6 \times 10^{-6} \text{ cm}^{-3}$, while the H_3O^+ fractional abundance has a lower limit of 0.016 and an upper limit of 0.036.

5.2 Results and Discussion

Table 5.1 lists the counts from the best fit ($\alpha=1.90$) along with the partial number densities and the relative abundances of the 89-103 keV water group ions. The W^+ group consists of $\sim 53\%$ O^+ , $\sim 22\%$ OH^+ , $\sim 22\%$ H_2O^+ , and $\sim 3\%$ H_3O^+ . Since the counts in the distribution tails contain only a small percentage of the total counts, our estimates of the O^+ , OH^+ , and H_2O^+ abundances do not vary significantly among the three types of fits. The quoted uncertainties for these three species reflect the statistical uncertainties from our fits. Because H_3O^+ is much less abundant and the tails from the other three species make up a significant fraction of the counts at the location of the H_3O^+ peak, our estimate of the H_3O^+ counts strongly depends on the α parameter. This introduces a larger systematic error and the quoted H_3O^+ uncertainties reflect the range of values from our three different fits. The asymmetric Gaussian fit with no tail provides an upper limit on the H_3O^+ abundance, while forcing $\alpha=1.81$, which overestimates the tail counts, provides a lower limit on the H_3O^+ abundance.

The majority of the water group ions are produced by the dissociation and ionization of the neutral H_2O emitted from the Enceladus plumes. Since the ions observed here are much more energetic than the thermal ions, we must consider the acceleration and transport processes when comparing our results to the thermal ion observations and neutral cloud models. The region where an injection event originates depends on whether it is a low energy or high energy event [Mitchell *et al.*, 2009a]. Low energy events largely originate at $L=9-11$ [Rymer *et al.*, 2009b], while high energy events originate at larger radial distances in the magnetotail [Mitchell *et al.*, 2009b]. Acceleration by inward radial diffusion [Van Allen 1980; Armstrong *et al.*, 1983; Kollmann *et al.*, 2011] requires the thermal ions to start in the outer magnetosphere, so the accelerated ions studied here likely reflect the plasma ion composition in the outer magnetosphere.

The composition of the thermal ions in the outer magnetosphere depends on a number of factors. One is the ionization rate of the neutral particles in the outer magnetosphere. Although possible differences among the neutral species' ionization and dissociation rates prevent us from directly comparing the ion composition to the neutral densities, our results do provide constraints. If a large fraction of the thermal ions in the outer magnetosphere is produced by the ionization of neutrals in this region, then the suprathermal ion composition will closely reflect the neutral particles that were initially ionized in the outer magnetosphere.

Because the ionization rates are much higher in the inner magnetosphere, we must consider the possibility that thermal ions are produced in the inner magnetosphere and

then transported to the outer magnetosphere where they are accelerated. As discussed in the introduction, broad outward flows of thermal plasma are consistent with the properties of the centrifugal interchange instability [Hill *et al.*, 2005; Rymer *et al.*, 2008]. Electron and ion observations suggest that this outward transport process is not adiabatic and does not cool the plasma [Rymer *et al.*, 2007, 2008; Wilson *et al.*, 2008]. Therefore, the outward transport of thermal ions followed by acceleration in the outer magnetosphere can produce ions at suprathermal energies.

Observations by Cassini UVIS [Melin *et al.*, 2009] and recent models of the neutral cloud [Smith *et al.*, 2010; Cassidy and Johnson 2010] indicate that the neutral O cloud is much broader than OH and H₂O. Outside of 6 R_S, the neutral O density is larger than OH and H₂O, and in the outer magnetosphere (~20 R_S) the O density is about an order of magnitude greater than that of the other water group neutrals [Cassidy and Johnson 2010]. Since the ionization rates of the neutral particles in the outer magnetosphere are estimated to be approximately the same [Cassidy and Johnson 2010], we would have expected the suprathermal O⁺/OH⁺ and O⁺/H₂O⁺ ratios to be larger than our observed value of ~2.4.

It is possible that a large fraction of the ions in the outer magnetosphere is produced inside of 10 R_S, where the difference between neutral O densities and the densities of the molecular neutrals is not as large, and is then transported to the outer magnetosphere. Sittler *et al.* [2008] reported that the thermal W⁺ consists mostly of molecular ions inside of Rhea's orbit (8.75 R_S). The thermal O⁺ fractional abundance relative to W⁺ appears to

increase outside of Rhea's orbit to values as high as 0.60-0.65, but there is a quite a bit of scatter in the data and whether this trend will continue outside of 10 R_S has not been determined [Sittler *et al.*, 2008]. Because of the larger fractional abundance of molecular ions inside of 10 R_S , the outward transport of these ions would result in a lower O^+/W^+ ratio relative to the neutral oxygen to neutral water group ratio. To perform a more quantitative analysis, better constraints on the ion transport rates, production rates, and loss rates are needed. However, our observation that W^+ consists mostly of O^+ is qualitatively consistent with the broad atomic O cloud observed by Cassini UVIS [Melin *et al.*, 2009] and predicted by recent models [Smith *et al.*, 2010; Cassidy and Johnson 2010].

The observation of nearly equal amounts of suprathermal OH^+ and H_2O^+ suggest that neutral H_2O is spread to Saturn's middle or outer magnetosphere rather than confined to a narrow torus centered on Enceladus' orbit. This result supports the conclusions of the Cassidy and Johnson [2010] model, that predicts the neutral OH and H_2O densities are approximately equal outside of 7 R_S . If neutral H_2O were confined to a narrow torus near 4 R_S as suggested by other models [e.g. Johnson *et al.*, 2006; Smith *et al.*, 2010], we would expect very low abundances of suprathermal H_2O^+ compared to O^+ and OH^+ .

Our results do not rule out the possibility that most of the H_2O^+ is produced near Enceladus' orbit and then transported to the outer magnetosphere where it is then accelerated. However, this scenario seems unlikely, because we would expect the suprathermal H_2O^+ fractional abundance to be similar to that of the suprathermal H_3O^+ .

Thermal H_3O^+ is the most abundant ion species in the Enceladus torus where the majority of it is produced via charge exchange reactions [Sittler *et al.*, 2008; Cravens *et al.*, 2009; Fleshman *et al.*, 2010a]. As the H_3O^+ is transported outward, its fractional abundance drops significantly due to its short recombination lifetime in the Enceladus torus [Ip 2000; Sittler *et al.*, 2008]. Because the recombination lifetime of H_2O^+ is even shorter than the H_3O^+ lifetime in the Enceladus torus [Fleshman *et al.*, 2010b], we would expect a similar decrease in the thermal H_2O^+ fractional abundance. Therefore, the production of H_2O^+ in the inner magnetosphere followed by outward transport and acceleration in the outer magnetosphere would probably not result in our observed suprathermal $\text{H}_2\text{O}^+/\text{H}_3\text{O}^+$ ratio of ~ 7.8 . A more detailed model is necessary before this possibility can be conclusively ruled out.

The partial number densities (PND) and relative abundances of the four 89-103 keV W^+ components are plotted versus L in Figure 5.4a and 5.4b, respectively. As discussed in chapters 3 and 4, the L variations of the suprathermal ion partial number densities are qualitatively consistent with inward radial diffusion followed by significant loss processes in Saturn's inner magnetosphere. The PND's of all four 89-103 keV water group ion species peak at L=9-10.

The O^+ , OH^+ , and H_2O^+ fractional abundances show no significant variations with L and do not deviate from their average values in the main ring current. From L=13-21 the H_3O^+ fractional abundance shows no dependence on L and averages 0.017. Inside of L=13, however, the fractional abundance H_3O^+ increases substantially to 0.048 at L=7-8.

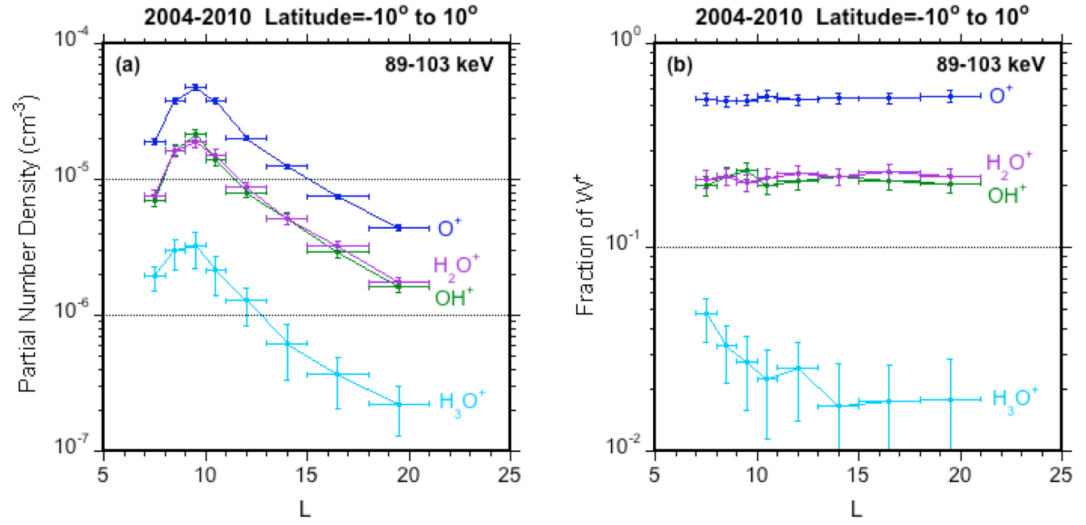


Figure 5.4: (a) The partial number density of 89-103 keV water group components versus L. (b) The fractional abundance of 89-103 keV water group components versus L. The error bars of O⁺, OH⁺, and H₂O⁺ represent the statistical uncertainties from the best fit. The error bars of H₃O⁺ represent the spread of the values from the three different fits.

The fractional abundance of the suprathermal ions with longer charge exchange lifetimes would be expected to increase inward after losses become important. Unfortunately, most of the cross sections involving 96 keV water group ion species colliding with Saturn's neutral cloud are not available. Thus, we can only make qualitative statements about the charge exchange lifetimes.

Consider the charge exchange reaction involving an ion A⁺ colliding with the neutral B ($A^+ + B \rightarrow A + B^+ + \Delta E$), where ΔE is the difference between the ionization energies of A and B. For resonant processes (i.e. $\Delta E=0$), the charge exchange cross section decreases with energy and behaves like $\sigma = [C-D*\ln(v)]^2$, where C and D are constants and v is the relative velocity [Dalgarno 1958]. For non-resonant collisions at low velocities, the cross sections are smaller than resonant cross sections and increase with increasing velocity

[*Rapp and Francis* 1962]. The non-resonant cross section maximizes at a velocity that can be approximated by the Massey adiabatic hypothesis [*Massey* 1949]:

$$v_{\max} = \frac{a|\Delta E|}{h} \quad (5.2)$$

where $a = 7 \times 10^{-8}$ cm and h is Planck's constant. Above this maximum velocity, the non-resonant cross section converges with the cross section of the resonant collision. The collision cross section maximizes at higher velocities as the difference in ionization energies increase.

We can apply equation 5.2 to collisions of the water group ions with atomic O, which is the densest heavy neutral outside of 7 R_s . The ionization energies of O, OH, and H₂O are 13.6 eV, 13.0 eV, and 12.6 eV [*CRC Handbook of Chemistry and Physics 49th Edition*, page E-71; *Wiedmann et al.*, 1992], respectively, while the ionization energy of H₃O is much less at 5.5 eV [*Melin et al.*, 2005]. Using these ionization energies, the collision cross sections of OH⁺ on O and H₂O⁺ on O are estimated to peak near $\sim 1\text{--}2 \times 10^7$ cm/s, while the H₃O⁺ on O cross section is estimated to peak near $\sim 1.4 \times 10^8$ cm/s. Because of velocity of 96 keV OH⁺ and H₂O⁺ is much greater than the velocity at which the cross section maximizes, we would expect the charge exchange cross sections of these species to be approximately the same.

The cross section of 96 keV H₃O⁺, however, will not have reached its maximum value and will be less than the cross sections of the other three ion species. Therefore 96 keV H₃O⁺ will have a longer lifetime than the other water group ion species. As a result, the fractional abundance of H₃O⁺ would be expected to increase inward, while the relative

abundance of O^+ , OH^+ , and H_2O^+ would not show significant variations. This result is qualitatively consistent with our observations. To perform a more detailed analysis, the charge exchange cross sections of these ions must be obtained and other reactions (e.g. dissociation) must also be included.

Chapter 6

C⁺ and N⁺ in Saturn's Magnetosphere

The Enceladus plumes and atmospheric escape from Titan are both potential sources for carbon and nitrogen. Carbon containing molecules were reported to be the second most abundant neutral in the plumes with CO₂ making up ~5.3% and CO making up less than 3% of the plume composition [Waite *et al.*, 2009; Hansen *et al.*, 2008]. Nitrogen appears to be a relatively minor neutral in the plumes with both NH₃ and N₂ making up less than 1% of the plume composition [Waite *et al.*, 2009; Hansen *et al.*, 2011]. The escape of neutrals from Titan is still not fully understood and estimates of the escape rate vary significantly [See Johnson *et al.*, 2009 for a summary]. Models of the Titan escape rate range from $\sim 3.6 \times 10^{25}$ N/s to $\sim 1.6 \times 10^{26}$ N/s [Shematovich *et al.*, 2003; De La Haye *et al.*, 2007a] for nitrogen and $\sim 5.9 \times 10^{25}$ CH₄/s to $\sim 1.7 \times 10^{27}$ CH₄/s for methane [De La Haye *et al.*, 2007a; Strobel 2008, 2009; Yelle *et al.*, 2008].

Cassini observations during SOI revealed that the heavy ions were dominated by W⁺ with N⁺ being a relatively minor ion species [Young *et al.*, 2005; Krimigis *et al.*, 2005]. A preliminary analysis of CHEMS data from several years of Cassini orbits at Saturn was reported in the *Saturn After Cassini-Huygens* book, and the N⁺/W⁺ ratio and C⁺/W⁺ ratio were estimated to be ~0.0095 and 0.006, respectively [Mauk *et al.*, 2009, Table 11.3]. These ratios suggest that the neutral sources of carbon and nitrogen are much weaker than the water group. In this chapter, we use CHEMS data to extend and refine the analysis reported in Mauk *et al.* [2009] and examine the radial variations for the first time. We

discuss the implications for the neutral carbon and nitrogen source strengths in Saturn's magnetosphere.

6.1 Data Analysis Methods

We combine the data from all 78 equatorial ring current passes shown in Figure 2.6 and create a TOF histogram for each E/Q step. We find that CHEMS can easily distinguish C^+ and N^+ only for energies > 96 keV and > 127 keV, respectively. In this study we only use the CHEMS data that includes an energy measurement from the solid-state detector (SSD) because of its lower background. Since the N^+ is not resolved at some energy steps in telescopes 1 and 2, here we only use the data from telescope 3. Anisotropies of the suprathermal ions at the energies considered here are very modest in the equatorial ring current, so only using telescope 3 does not affect our results significantly.

Although the C^+ , N^+ , and W^+ TOF peaks distinguish themselves, their distributions overlap. For instrumental reasons, the distributions cannot be fit by Gaussian, kappa, or other standard shapes, so we instead determine lower and upper limits by making reasonable assumptions concerning the content of TOF channels where the species overlap. A TOF histogram for the 127 keV energy step is shown in Figure 6.1. The C^+ , N^+ , and W^+ peaks can be distinguished and are labeled in the figure. The vertical dashed lines show the TOF bounds used to determine the counts for each ion species. The W^+ TOF bounds are the red dashed lines. We can determine the W^+ counts by simply adding all the counts between the red dashed lines.

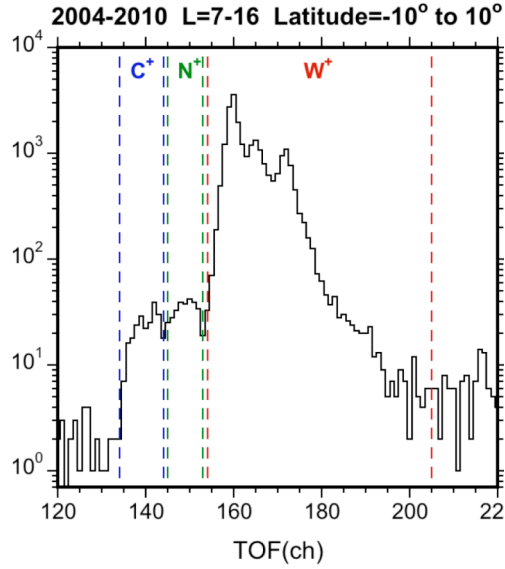


Figure 6.1: Time-of-Flight (TOF) histogram of 127 keV events from 78 equatorial ring current passes (L=7-16). Only triple coincidence events (TOF plus SSD energy) from CHEMS telescope 3 are included. The dashed lines indicate the TOF bounds used for C^+ , N^+ , and W^+ .

The right side of the C^+ distribution overlaps the left side of the N^+ distribution, and the right side of the N^+ distribution overlaps the left side of the W^+ . To identify the left edge of the N^+ distribution, we have used the CHEMS data from Cassini's earth fly-by, which contains a significant amount of N^+ and very low abundances of C^+ . The C^+

bounds are the blue dashed lines, and all the counts between these lines are C^+ . The N^+ bounds are the green dashed lines. The

lowest N^+ TOF bin contains a combination of

C^+ and N^+ , but the rest of the TOF channels between these bounds are essentially all N^+ .

The lowest TOF bin in the W^+ contains a combination of W^+ and N^+ . We cannot separate the species counts where the distributions overlap.

To determine the lower limit of C^+ , we only use the counts between the C^+ TOF bounds and ignore the counts where C^+ and N^+ overlap. The upper limit of C^+ is determined by adding to that number all the counts in the lowest N^+ TOF channel. To determine the lower limit of N^+ we add all the counts between the N^+ bounds and subtract half the counts from the lowest N^+ TOF channel to compensate for the C^+ counts in this channel.

Adding all the counts between the N^+ TOF bounds to all the counts in the lowest W^+ TOF channel, which contains some N^+ , gives us the upper N^+ limit.

Averaging the lower and upper limits of C^+ and N^+ provides our best estimate of the C^+ and N^+ counts. When determining the uncertainty of the C^+ and N^+ counts, we use the uncertainty from estimating the upper and lower limits as well as the statistical uncertainty. The statistical uncertainty of the species counts is determined by taking the square root of the counts. To calculate the total uncertainty for C^+ and N^+ , we combine in quadrature their statistical uncertainties with half the difference between their upper and lower limits.

We perform this analysis for each E/Q step between 96 keV/e and 220 keV/e to create the C^+ , N^+ , and W^+ spectra. We examine the L variations of C^+ and N^+ by dividing each pass into the following L ranges: L=6-7, L=7-8, 8-9, 9-10, 10-11, 11-13, 13-15, 15-18, 18-21. We only consider the L variations of ~ 127 keV C^+ , N^+ , and W^+ . Since the C^+ and N^+ peaks are distinct in all three telescopes at ~ 127 keV, we are able to combine the data from all three telescopes to improve our counting statistics. We use a bin size of $\Delta L=1$ in Saturn's inner magnetosphere where there are sufficient counts in the C^+ and N^+ distributions. At larger distances the counts decrease, so we combine the data over $\Delta L=2$ or 3 outside of $L=11$.

6.2 Results and Discussion

The partial number densities (PND) of C^+ , N^+ , and W^+ versus energy are shown in Figure 6.2. Table E.1 in Appendix E contains the PND values for each E/Q step in the main ring current. From 127-220 keV in Saturn's main ring current region ($L=7-16$), the C^+/W^+ and

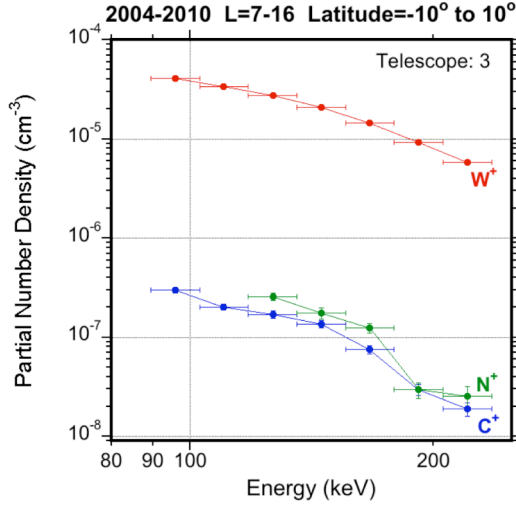


Figure 6.2: Partial number densities of C^+ , N^+ , and W^+ in the equatorial ring current ($L=7-16$). N^+ is not well resolved from W^+ below 110 keV and is not shown below this energy. Error bars represent statistical uncertainties for W^+ and are often smaller than the data points. For C^+ and N^+ , the error bars combine the statistical uncertainties with the range of estimates of C^+ and N^+ counts using different assumptions. See text for details.

N^+/W^+ PND ratios are 5.5×10^{-3} and 7.8×10^{-3} , respectively. At the two highest E/Q steps, 192 keV/e and 220 keV/e, both C^+ and N^+ show a significant drop in partial number density compared to W^+ . This large decrease in C^+ and N^+ at 192-220 keV is difficult to explain. If the drop in the C^+ and N^+ were due to common acceleration processes, we would expect the W^+ partial number density to show a similar decrease at that energy.

The PND's of 118-136 keV C^+ , N^+ , and W^+

versus L are shown in Figure 6.3a. Table E.2 in Appendix E contains the 118-136 keV PND values for each L range used. The 118-136 keV C^+ and N^+ PND increases inward, peaks at $L=9-10$, and then decrease inside of $L=9$. Like the ion species examined in chapters 3 and 4, these L variations of the 118-136 keV C^+ and N^+ PND's are qualitatively consistent with inward radial diffusion followed by loss processes inside of $L=9$. The 118-136 keV ion PND makes up a very small percentage of the total ion density. For example, the peak PND of 118-136 keV W^+ is $5.23 \times 10^{-5} \text{ cm}^{-3}$ at $L=9-10$, while the total number density of W^+ at $L=9-10$ in the equatorial plane is $\sim 1-2 \text{ cm}^{-3}$ [Thomsen *et al.*, 2010].

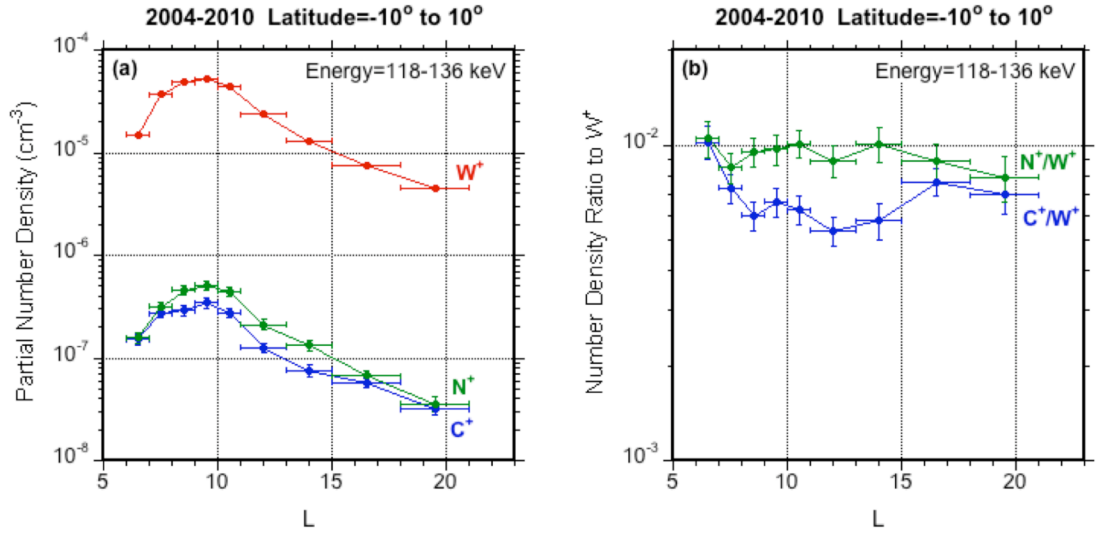


Figure 6.3: (a) 118-136 keV C^+ , N^+ , and W^+ partial number densities versus L . (b) 118-136 keV C^+/W^+ and N^+/W^+ ratios versus L . Error bars in both plots represent the combined statistical uncertainties and range of estimates for C^+ and N^+ abundances based on the TOF distributions.

The PND ratios C^+/W^+ and N^+/W^+ versus L are shown in Figure 6.3b. The N^+/W^+ ratio averages about 9.3×10^{-3} with a standard deviation of 8.5×10^{-4} and shows no significant variation with L . The C^+/W^+ ratio has an average value of 6.9×10^{-3} and shows larger variations with a standard deviation of 1.4×10^{-3} . Inside of $L=9$ C^+/W^+ tends to increase inward. This increase is not currently understood. A previous preliminary analysis of a smaller set of CHEMS data gave average values of 0.0095 and 0.006 for the N^+/W^+ and C^+/W^+ ratios, respectively [Mauk *et al.*, 2009 Table 11.3] in the ring current region. Our results are consistent with these estimates.

The water group originates largely from Enceladus, while carbon and nitrogen have two potential sources: Enceladus and Titan. Carbon can be produced by the dissociation of carbon containing molecules (e.g. CO_2 , CO , HCN , CH_4) from the Enceladus plumes and the dissociation of CH_4 from Titan. Nitrogen can be produced by dissociation of nitrogen

containing molecules (e.g. NH_3 , N_2 , HCN) from the Enceladus plumes and the escape of nitrogen from Titan's atmosphere. The dissociation of these molecules followed by ionization processes results in the production of C^+ and N^+ . Thus, in addition to differences in neutral source strengths, variations in dissociation and ionization rates can affect the ion abundance ratios. The escape of ions produced near Titan's orbit down the magnetotail [Smith *et al.*, 2007] is another factor that affects ion abundance ratios within the magnetosphere. The C^+/W^+ and N^+/W^+ abundance ratios provide constraints on the estimates of the relative source strengths within the uncertainties in the dissociation, ionization and escape rates.

The C^+/W^+ ratio is somewhat lower than expected. Current estimates of the Enceladus plume composition suggest that carbon-containing molecules are the second most abundant neutral in the plumes ($\sim 5.3\%$ CO_2 , $\sim 0.9\%$ CH_4 , $< 3\%$ CO) [Hansen *et al.*, 2008; Waite *et al.*, 2009]. If the large CH_4 Titan escape rates ($> 10^{27}$ CH_4/s) estimated by Strobel [2008, 2009] and Yelle *et al.* [2008] are confirmed, Titan would also be expected to provide a significant source of carbon to Saturn's magnetosphere, but these CH_4 escape rates are much larger than those deduced in the De La Haye *et al.* [2007a] study (5.9×10^{25} CH_4/s). Our results imply that the neutral sources of carbon containing molecules are less than currently estimated by Strobel [2008, 2009], Yelle *et al.* [2008], and Waite *et al.* [2009].

Estimates of the nitrogen source strengths appear to be much less than the water source strengths. Each type of nitrogen containing molecule emitted by the plumes is estimated

to make up less than 1% of the plume composition [Waite *et al.*, 2009; Hansen *et al.*, 2011] and estimates of the Titan nitrogen source strength ($\sim 1.6 \times 10^{26}$ N/s) [De La Haye *et al.*, 2007] are about two orders of magnitude less than the water group source strength ($\sim 1\text{--}4 \times 10^{28}$ H₂O/s) [Burger *et al.*, 2007; Jia *et al.*, 2010; Dong *et al.*, 2011]. These weak nitrogen source strengths compared to the water source strength are qualitatively consistent with our low 127-220 keV N⁺/W⁺ ratio of 7.8×10^{-3} .

There is a rather large discrepancy between the suprathermal N⁺/W⁺ ratio of 7.8×10^{-3} and the observed thermal N⁺/W⁺ ratio of ~ 0.1 between 4-13 R_S [Smith *et al.*, 2007]. There are a number of possible causes for this discrepancy. One involves the uncertainty of the detection efficiencies of the CAPS instrument. According to Smith *et al.* [2007], the estimates of the N⁺/W⁺ ratios may change as knowledge of the species-dependent detection efficiencies of the CAPS instrument is improved. As of this writing, no new study involving CAPS N⁺ data with updated detection efficiencies has been published. Since CAPS detects the thermal ions and CHEMS detects the more energetic suprathermal ions, differences in acceleration rates of N⁺ and W⁺ would also cause the suprathermal N⁺/W⁺ ratio to differ from the thermal N⁺/W⁺ ratio. However, there is currently no known acceleration mechanism that would preferentially accelerate W⁺ over N⁺.

The decrease in PND in Saturn's inner magnetosphere is due to electron capture and electron loss collisions with Saturn's neutral cloud. We use equation 4.1 to calculate the ~ 127 keV C⁺, N⁺, and W⁺ collision lifetimes and compare them to the L variations of the

abundance ratios C^+/W^+ and N^+/W^+ in Saturn's inner magnetosphere. We calculate the lifetimes at $L=9.5$ where the O, OH, and H_2O densities are estimated to be 54 cm^{-3} , 14 cm^{-3} , and 13 cm^{-3} , respectively [Cassidy and Johnson 2010]. Unfortunately, we were only able to obtain the cross sections for O^+ and N^+ colliding with atomic oxygen [Lo et al., 1971] and C^+ colliding with H_2O [Montenegro et al., 2007]. The Montenegro et al. [2007] study only went up to 100 keV, so we had to extrapolate slightly to estimate the cross section of 127 keV C^+ on H_2O . The electron loss collision of C^+ on H_2O was not found, but we can estimate the cross section using the N^+ on O data. At $\sim 127 \text{ keV}$, the ratio of the electron loss cross section to the electron capture cross section of N^+ on O is $\sim 25\%$. Therefore, we multiply the electron capture cross section of C^+ on H_2O by this percentage to estimate the C^+ electron loss cross section.

Because of the missing cross section information, we were forced to make several assumptions when calculating the lifetimes. We assume that the cross-section for N^+ on O is the same as N^+ on OH and H_2O . Similarly, we assume that the cross-section for C^+ on H_2O is the same as C^+ on O and OH. When calculating the lifetime for W^+ , we assume that W^+ is entirely O^+ and that the collision cross section of O^+ on O is the same as O^+ on OH and H_2O . Our lifetime calculations are shown in Table 6.1.

The estimated lifetimes of C^+ , N^+ , and W^+ are $1.1 \times 10^5 \text{ s}$, $1.3 \times 10^5 \text{ s}$, and $1.1 \times 10^5 \text{ s}$, respectively. The relatively small differences between the lifetimes of N^+ and W^+ are consistent with the small variations of the N^+/W^+ ratio with L . The similar lifetime does not explain the increase in the C^+/W^+ ratio inside of $L=9$. There are obvious uncertainties

Table 6.1: Lifetimes of ~127 keV C^+ , N^+ , and W^+ colliding with Saturn's neutral cloud at L=9.5 in the equatorial plane^a

Species	Velocity (cm/s)	e- cap σ (cm ²)	e- loss σ (cm ²)	Lifetime (s)
C^+	1.42×10^8	6.2×10^{-16}	1.5×10^{-16} ^b	1.1×10^5
N^+	1.32×10^8	5.7×10^{-16}	1.4×10^{-16}	1.3×10^5
W^+	1.23×10^8	7.3×10^{-16}	1.6×10^{-16}	1.1×10^5

^a The neutral densities are taken from the model by *Cassidy and Johnson [2010]*. The neutral densities at L=9.5 are estimated to be 54 cm⁻³ for O, 14 cm⁻³ for OH, and 13 cm⁻³ for H₂O. The cross sections involving N^+ and W^+ are from *Lo et al. [1971]*, while the cross section for C^+ is from *Montenegro et al. [2007]*.

^b The e- loss cross section for C^+ could not be found, so we estimated this value using the N^+ on O data. The e- loss cross section for N^+ on O is about 25% of the electron capture cross section. We multiply the e- capture cross section of C^+ by this percentage to estimate the C^+ electron capture cross section.

in our lifetime calculations such as our assumption the C^+ on H₂O collision has the same cross section as C^+ on O. Additional cross section measurements are needed to more accurately predict the different lifetimes.

Chapter 7

Long-term Time Variations of the Suprathermal Ions

Models based on Cassini observations from Enceladus fly-bys have provided conflicting evidence about whether the plume source strength varies with time. The model by *Saur et al.* [2008] concludes that the source strength decreased from 5.4×10^{28} H₂O/s to 0.67×10^{28} H₂O/s in 20 day period from the E0 to the E1 fly-bys, while the *Smith et al.* [2010] model concludes that the source strength increased from 0.63×10^{28} H₂O/s to 2.5×10^{28} H₂O/s in the seven month period from the E3 to the E5 fly-bys (See Table 1.3). The models by *Dong et al.* [2011] and *Jia et al.* [2010], however, suggest that the plume source strength only ranges from ~ 1.5 - 3.5×10^{28} H₂O/s and does not change significantly with time. Analysis of Cassini UVIS observations prior to SOI indicated that the total number of oxygen atoms only varied from ~ 3.0 - 3.5×10^{34} , suggesting a nearly constant source of atomic oxygen [*Melin et al.*, 2009]. In this chapter, we examine the long-term time variations of the suprathermal ion partial number density. These observations will provide insight into whether the neutral source strengths changed over the period during 2004-2010 or remained relatively constant.

7.1 Data Analysis Methods

We calculate the partial number density (PND) of 27-220 keV/e ions for each inbound and outbound ring current (L=7-16; Latitude= -10° to 10°) pass shown in Figure 2.6. The species examined are H⁺, H₂⁺, He⁺⁺, He⁺, O⁺⁺, and W⁺. As discussed in chapter 3, all six species easily distinguish themselves above 27 keV/e and calculating the PND is

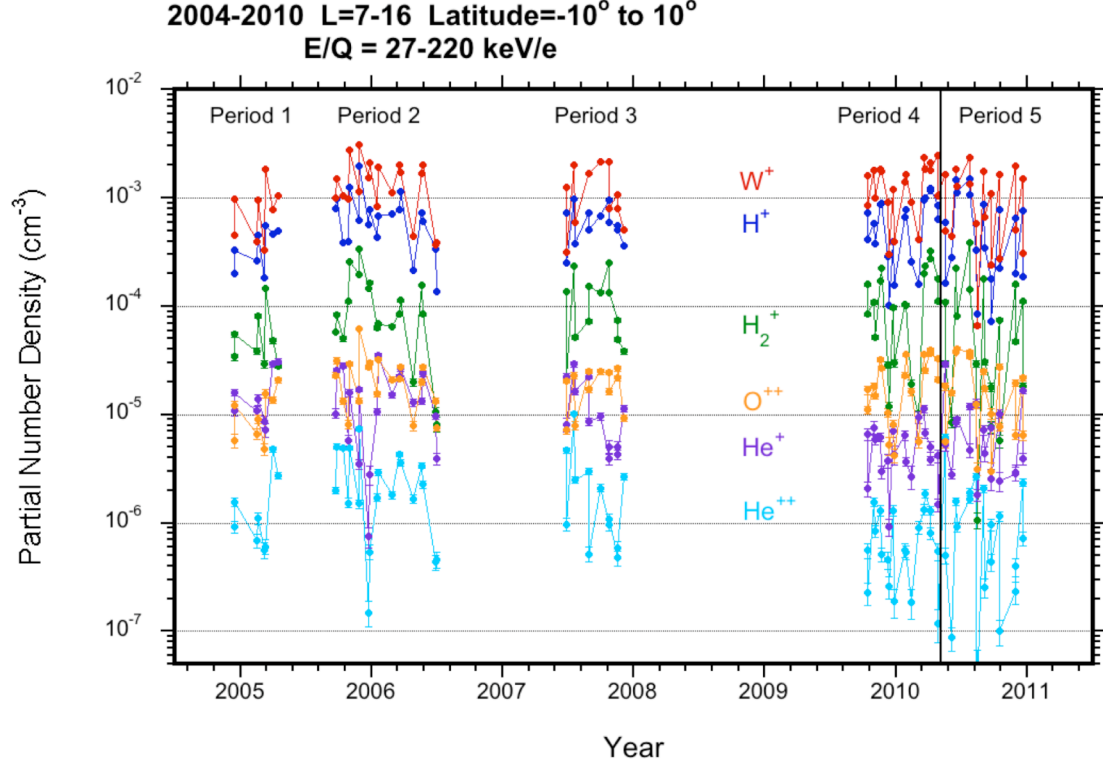


Figure 7.1: The partial number density for each inbound or outbound pass through the equatorial ring current (L=7-16, Latitude=-10° to 10°). The solid vertical black line separates period 4 from period 5. The error bars represent the absolute statistical uncertainty of each data point. In some cases the error bars are smaller than the data points.

straightforward. A plot of the PND's from each ring current pass versus time is shown in Figure 7.1. Each data point represents either an inbound or outbound pass through the ring current.

The PND's show significant short-term variations from pass to pass, which reflect day-night and other local time variations as well as temporal variations. To focus on the long-term temporal variations, we define five long averaging periods as shown in Figure 7.1. The trajectories for each ring current pass are shown in Figure 7.2, with passes belonging to each long averaging period coded by color. We then calculate the PND's for each of the five long averaging periods as well as for all 78 passes combined. When combining

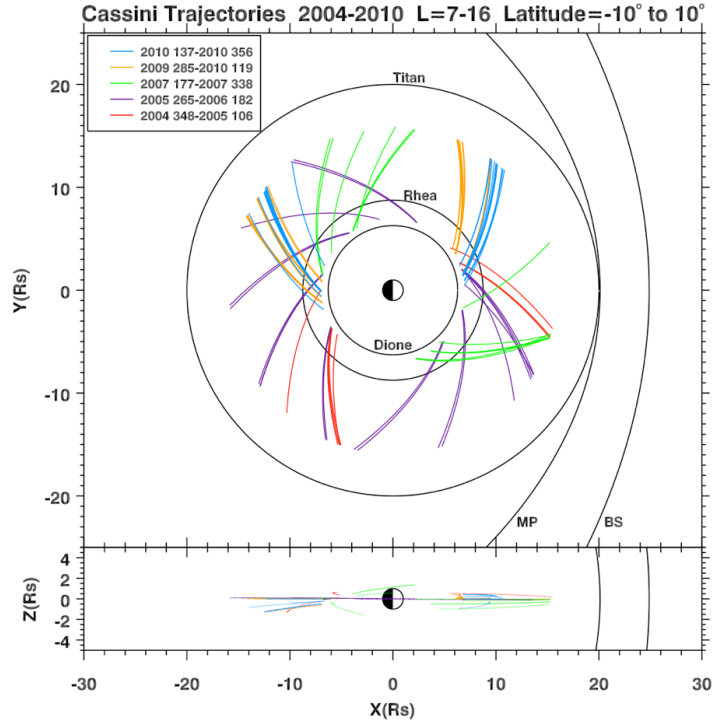


Figure 7.2: Cassini passes used in this study in the SZS Saturn equatorial coordinate system. Each pass is within 10 degrees of the equatorial plane and in the ring current region. Typical locations of the magnetopause and bow shock were taken from *Arridge et al. (2006)* and *Masters et al. (2008)*, respectively.

the passes, we do not average the individual PND's from each individual pass. Instead, we combine the raw CHEMS data from each ring current pass and then calculate the PND and fractional abundance (FA). We use these results to look for changes in the ion composition and in the overall PND.

7.2 Results and Discussion

The partial number densities and fractional abundances for each long-term time period are plotted in Figure 7.3. Table 7.1 lists the combined PND as well as that for each ion species, while Table 7.2 lists the H^+/W^+ and H_2^+/W^+ ratios. Using the PND's and abundance ratios from the long averaging periods, we calculate the standard deviation of those five numbers as well as the maximum to minimum ratio. The FA's are given in

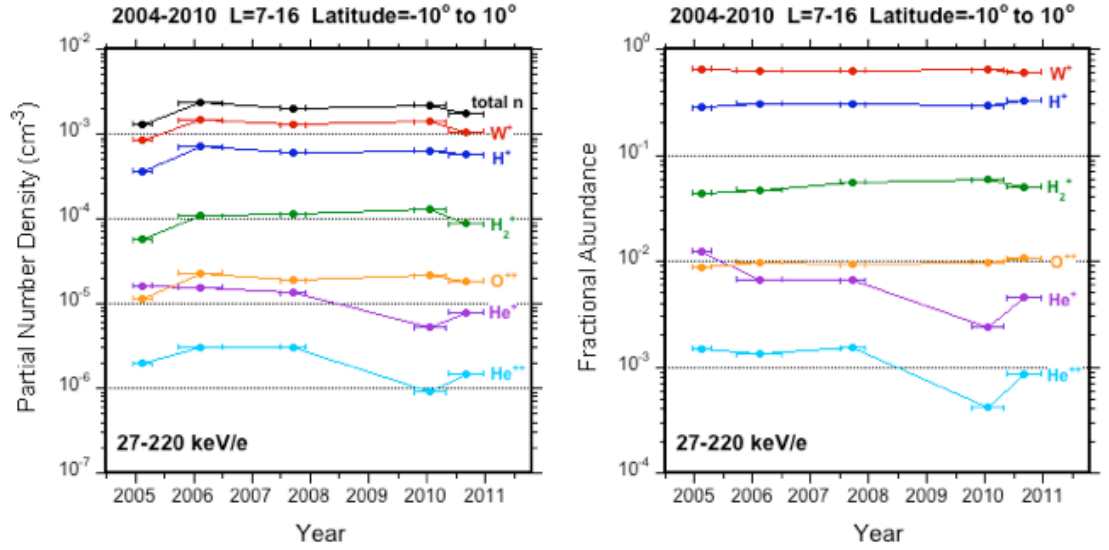


Figure 7.3: Partial number density and fractional abundance from our five long averaging periods. The horizontal error bars represent the length of each long averaging period. Vertical error bars represent the absolute statistical uncertainty of each data point. In all cases, the vertical error bars are smaller than the data point and are invisible.

Table 7.3. The standard deviation of the PND for all species combined is 21% with a max to min ratio of 1.78. W^+ and H^+ dominate, with a FA ranging from 0.60-0.66 and 0.28-0.33, respectively. H_2^+ is the third most abundant species and has a FA ranging from 0.04-0.06. Each of the minor species (O^{++} , He^+ , He^{++}) have a FA of ~ 0.01 or less.

The W^+ PND, assumed to be largely from Enceladus, shows no long-term trends and only modest variations from period to period (std. dev. = 21%, max/min=1.71). Even if we interpret all the observed variations as resulting from changes in neutral source strength, their modest amplitude apparently rules out large changes in average plume strength over this period. The models of *Saur et al.* [2008] and *Smith et al.* [2010] showed much larger plume strength variations on much shorter time scales. Our long averaging periods would smooth out the more rapid variations.

Table 7.1: Partial number densities (PND) in 10^6 cm^{-3} for 27-220 keV/e ions in each time period^a

Time period	Combined species	H ⁺	W ⁺	H ₂ ⁺	O ⁺⁺	He ⁺	He ⁺⁺
All Passes	1990±10	606±1	1250±10	103±1	19.6±0.1	11.0±0.1	2.05±0.02
2004 348-2005 106 (8 passes)	1300±10	366±1	846±5	57±1	11.4±0.4	16.2±0.5	1.95±0.07
2005 265-2006 182 (19 passes)	2310±10	708±1	1450±10	108±1	22.7±0.3	15.6±0.2	3.07±0.05
2007 177-2007 338 (12 passes)	2020±10	605±1	1270±10	113±1	18.8±0.3	13.3±0.3	3.09±0.07
2009 285-2010 119 (20 passes)	2170±10	630±1	1390±10	127±1	21.2±0.3	5.2±0.2	0.90±0.03
2010 137-2010 356 (19 passes)	1740±10	573±1	1050±10	87.4±0.6	18.5±0.2	7.9±0.2	1.50±0.04
% Standard Dev.	21%	22%	21%	27%	23%	42%	46%
Max/Min	1.78	1.93	1.71	2.2	1.99	3.1	3.4
Correlation with W ⁺ Coefficient R	0.99	0.94	≡1.00	0.92	0.94	-0.24	0.23
Probability P _c	0.00056	0.019	-	0.025	0.017	0.70	0.70

^a The uncertainties of the partial number densities are absolute statistical uncertainties, which depend on the number of species counts. To obtain the partial number densities in the “All Passes” row, we combine the raw CHEMS data from all 78 passes shown in Figure 7.2 and calculate the partial number densities. Using the partial number densities from the long averaging periods, we calculate the percent standard deviation of those five numbers and the ratio of the maximum to minimum. The correlation coefficient R with W⁺ and the probability P_c that a random sample of five data points would result in a correlation coefficient greater than or equal to |R| is also shown.

H⁺, H₂⁺, and O⁺⁺ also show no long-term trends and are correlated with W⁺. The correlation coefficient of H⁺ and O⁺⁺ with W⁺ is 0.94, while the correlation coefficient for H₂⁺ with W⁺ is 0.92. Because of this correlation, the variations in the PND ratios H⁺/W⁺ and H₂⁺/W⁺ are only half as large as the variations in the individual PND's. The standard deviation of H⁺ is 22%, while the standard deviation of H⁺/W⁺ is only 9.0%. H₂⁺ shows somewhat larger variations with a standard deviation of 27%, while the standard deviation of H₂⁺/W⁺ is only 13%. The relatively small variations in these ratios could be understood if Enceladus were the largest source of all three species, directly or via dissociation. If true this would conflict with current estimates of the Saturn source of H

Table 7.2: The same as Table 7.1, but with the 27-220 keV/e H^+/W^+ and H_2^+/W^+ ratios for for each time period^a

Time period	H^+/W^+	H_2^+/W^+
All Passes	0.485±0.001	0.0824±0.0003
2004 348-2005 106 (10 passes)	0.433±0.003	0.067±0.001
2005 265-2006 182 (21 passes)	0.488±0.002	0.0745±0.0006
2007 177-2007 338 (12 passes)	0.476±0.002	0.0890±0.0009
2009 285-2010 119 (20 passes)	0.453±0.001	0.0914±0.0006
2010 137-2010 356 (19 passes)	0.546±0.002	0.0832±0.0006
% Standard Dev.	9.0%	13%
Max/Min	1.26	1.36

[*Shemansky et al.*, 2009] and the Titan source of H_2 [*Cui et al.*, 2008; *Tseng et al.*, 2011a] compared with the Enceladus source for these species.

But our results could also accommodate differing neutral sources for the three species if the suprathermal ion density variations

are largely caused by changes in the overall acceleration rate of the thermal plasma rather than by changes in the neutral source strengths. Then the suprathermal species would tend to increase and decrease together. At Saturn frequent particle injections [*Mauk et al.*, 2005; *Burch et al.*, 2005; *Paranicas et al.*, 2007; *Rymer et al.*, 2009] play an important role in ion energization along with inward radial diffusion [*Van Allen et al.*, 1980; *Armstrong et al.*, 1983] conserving first and second adiabatic invariants. The injections are at least partly controlled by the solar wind [*Mitchell et al.*, 2005; *Bunce et al.*, 2005] and their frequency could be expected to vary leading to density variations in the suprathermal particles. Currently, no long-term studies of injection rate variations have been published.

Another possibility exists to explain the correlation of the H^+ and W^+ densities. Inside of $L=6$, charge exchange of W^+ with neutral H is the largest source of H^+ [*Richardson et al.*,

Table 7.3: Fractional Abundances (FA) for 27-220 keV/e ions in each time period^b

Time Period	H ⁺ (x10 ⁻³)	W ⁺ (x10 ⁻³)	H ₂ ⁺ (x10 ⁻³)	O ⁺⁺ (x10 ⁻³)	He ⁺ (x10 ⁻³)	He ⁺⁺ (x10 ⁻³)
All Passes	304±1	627±1	51.8±0.2	9.83±0.07	5.51±0.05	1.03±0.01
2004 348-2005 106	282±1	651±4	44.2±0.7	8.8±0.3	12.5±0.4	1.50±0.05
2005 265-2006 182	307±1	629±2	46.7±0.3	9.8±0.1	6.8±0.1	1.33±0.02
2007 177-2007 338	299±1	627±3	56.0±0.5	9.3±0.2	6.6±0.1	1.53±0.03
2009 285-2010 119	290±1	639±2	58.5±0.4	9.8±0.1	2.42±0.07	0.42±0.01
2010 137-2010 356	329±1	605±2	50.2±0.4	10.6±0.1	4.5±0.1	0.86±0.02
% Standard Dev.	6.0%	2.7%	12%	6.9%	57%	43%
Max/Min	1.17	1.08	1.32	1.2	5.2	3.6

^b The uncertainties of the fractional abundances are the absolute statistical uncertainties. The fractional abundances in the “All Passes” row are obtained by combining the raw CHEMS from all 78 passes shown in Figure 1 and then calculating the fractional abundance for each ion species. Using the fractional abundances from the long averaging periods, we calculate the percent standard deviation of those five numbers and the ratio of maximum to minimum.

1998]. Therefore, changes in the Enceladus plume strength resulting in W⁺ density changes would be accompanied by similar changes in H⁺. The correlation of H₂⁺ with W⁺ would not be expected to be as strong, since electron impact ionization is the largest source of H₂⁺ [Tseng *et al.*, 2011a]. More detailed analysis is required to understand the relatively small variations in H⁺/W⁺ and H₂⁺/W⁺ ratios.

He⁺⁺ and He⁺ are tracers for the solar wind and interplanetary pick-up ions [Hamilton *et al.*, 1983; Möbius *et al.*, 1985]. The PND's of He⁺⁺ and He⁺ are relatively uncorrelated with those of the major species and show larger variations with time. The standard deviations of He⁺⁺ and He⁺ PND's are 46% and 42%, respectively. From the third time period to the fourth, the PND's for He⁺ and He⁺⁺ dropped by factors of 2.6 and 3.4, respectively. We expect long-term variations of the helium species to be due to the solar

cycle. During solar maximum conditions, the $\text{He}^{++}/\text{H}^+$ ratio in the solar wind tends to increase [Aellig *et al.*, 2001; Ogilvie *et al.*, 1989]. The production of pick-up He^+ ions also depends on the solar cycle [Rucinski *et al.*, 2003]. Close to the sun ($r < 3$ AU in the helium focusing cone; $r < 1$ elsewhere), the production of He^+ is expected to decrease at solar maximum. At larger distances from the sun ($r \sim 10$ AU), however, the He^+ flux is expected to increase during solar maximum and decrease near solar minimum. Therefore, at Saturn's orbit, we expect the abundance of both He^{++} and He^+ to decrease during solar minimum.

Although the lowest helium time period (period 4) occurs near solar minimum, the large drop in the helium densities cannot be entirely explained by solar cycle changes. The sunspot number in the fourth time period is low, but it is not significantly different from that of the third period. Studying the helium variations over the next few years when the sunspot number is expected to increase will provide more insight into the solar cycle control of the helium partial number densities.

Chapter 8

Conclusions and Future Work

The Cassini CHEMS observations greatly improved our understanding of the suprathermal ion composition in Saturn's magnetosphere and have provided a great deal of insight into the strength of the neutral and plasma sources. Here we summarize our results and discuss topics for future research.

8.1 L Variations

To reach suprathermal energies, the thermal ions must be accelerated. The most likely acceleration processes are inward radial diffusion [*Van Allen* 1980; *Armstrong et al.*, 1983; *Kollmann et al.*, 2011] and injection events [*Hill et al.*, 2005; *Burch et al.*, 2005; *Mauk et al.*, 2005]. Because the acceleration site typically differs from the source location, the acceleration processes mix the ions from different sources. As a result, the partial number densities (PND) of all the suprathermal ion species examined have similar L variations that probably do not reflect the source locations. As the suprathermal ions diffuse inward, they gain energy and their PND increases. The PND of all species combined typically peaks between L=8-10 and then decreases inward due largely to collisions with Saturn's neutral cloud.

The fractional abundances (FA) of the ion species show little variation with L in the outer magnetosphere (L=15-21), suggesting that diffusion is likely the dominant process in this region. In the inner magnetosphere, however, the suprathermal ion FA's show large

variations with L . These variations can be mostly explained by differences in the ion-neutral collision lifetimes of the different ion species. The suprathermal ion composition in the inner magnetosphere does not reflect the neutral source strengths, but the collision lifetimes of each species. Therefore, when comparing our observations to the source strengths, we use the suprathermal ion composition in the outer magnetosphere ($L=15-21$) before the loss processes become significant.

8.2 Implications for the Source Strengths

W^+ and H^+ dominate the suprathermal PND with H_2^+ being the third most abundant ion species. In the outer magnetosphere ($L=15-21$), W^+ has a FA ranging from 0.64-0.77 depending on the energy. In the same region, the H^+ FA ranges from 0.16-0.28 depending on the energy, while the H_2^+ FA ranges from 0.054-0.064. The majority of these three ion species are produced by the ionization of neutral particles within Saturn's magnetosphere, but their dominant neutral sources are predicted to be different. The neutral water group originates largely from Enceladus at a rate of $\sim 1-4 \times 10^{28}$ H_2O/s [Burger *et al.*, 2007; Jia *et al.*, 2010; Dong *et al.*, 2011]. The strongest H_2 source is predicted to be atmospheric escape from Titan where H_2 escapes at a rate of $\sim 10^{28}$ H_2/s [Cui *et al.*, 2008]. Saturn's atmosphere is predicted to be the dominant H source with a strength of $\sim 3 \times 10^{30}$ H/s [Shemansky *et al.*, 2009]. The fact that W^+ is significantly more abundant than the other two ion species could indicate that the H and H_2 neutral source strengths are currently overestimated, but the ion source rates and acceleration process must be considered.

Even though the estimated atomic H source strength is two orders of magnitude greater than that of the water group source strength, the total number of H atoms in the magnetosphere only outnumbers the total number of O and OH particles by a factor of 3 [Shemansky *et al.*, 2009]. These estimates indicate that the H^+/W^+ ratio will be much less than the ratio of their estimated neutral source strengths. The shorter electron impact and photoionization [Melin *et al.*, 2009; Cassidy and Johnson 2010] lifetime of atomic oxygen compared to atomic hydrogen will reduce the H^+/W^+ ratio relative to the ratio of the neutral densities. INCA observations of energetic neutral atoms during a substorm revealed that oxygen was accelerated earlier and more steeply than hydrogen [Mitchell *et al.*, 2005]. If W^+ is preferentially accelerated over H^+ , then the suprathermal W^+ PND will be enhanced relative to the H^+ PND. Therefore, a number of factors can affect the suprathermal PND. A detailed model of the H^+ source rates is required to make a more quantitative comparison between our ion composition observations and the neutral source strengths of H and the water group.

Our observation that the H_2^+ PND is about an order of magnitude less than that of W^+ is likely due to difference in ion source rates rather than neutral source strengths. Tseng *et al.* [2011a] modeled the H_2 lifetimes and concluded that the H_2^+ production rate (See Figure 1.10) is much less than the W^+ production rate (See Figure 1.9) estimated by Smith *et al.* [2010]. Therefore, even though the neutral source strengths are approximately the same, the H_2^+/W^+ ratio would be expected to be much less than 1. This is qualitatively consistent with our results.

O^{++} is a relatively rare ion species with its FA ranging from 0.0043-0.0063 in the outer magnetosphere ($L=15-21$). O^{++} is produced by the further ionization of O^+ and the double ionization of neutral O. The source rate of thermal O^{++} is estimated to peak between $L=7-9$ due largely to the single electron impact ionization of O^+ and double electron impact ionization of O by the cold electrons. Compared to the W^+ production rates calculated by Smith et al. [2010], the O^{++} production rates are much smaller, so our low O^{++} fractional FA are qualitatively consistent with these calculations.

We studied the long-term temporal variations of the 27-220 keV/e ions and found that the 27-220 W^+ PND's varied by a factor of 1.71 from 2004 to 2010. Our observations imply that variations in the Enceladus source strength were modest during this period. Our observations do not rule out the possibility that source strength variations happen on a shorter timescale, because our long-averaging periods smooth out the more rapid variations. H^+ , H_2^+ , and O^{++} show a strong correlation with W^+ . This correlation is expected for O^{++} since it has the same source as W^+ , but H and H_2 are believed to have different sources. The strong correlation could indicate that the dominant source of H and H_2 is Enceladus. However, our results can accommodate different neutral sources if the PND variations are due to changes in the overall acceleration rates rather than changes in the neutral source strengths.

Both helium charge states are much less abundant than W^+ and their FA's appear to increase with energy. From $L=15-21$ the average He^+ FA increases from 0.0056 at $E/Q=36-55$ keV/e to 0.0103 at $E/Q=145-220$ keV/e, while the He^{++} FA increases from

0.0019 at $E/Q=36-55$ keV/e to 0.0027 at $E/Q=145-220$ keV/e. Because Saturn's magnetosphere does not contain local sources of helium, He^{++} is a tracer for the solar wind, and He^+ is a tracer for interplanetary pick-up ions of interstellar origin. The 36-55 keV/nuc $\text{He}^{++}/\text{H}^+$ ratio in the magnetosphere is 0.0025, which is more than an order of magnitude less than the $\text{He}^{++}/\text{H}^+$ ratio during typical solar wind conditions [Bame *et al.*, 1977]. The low helium abundances indicate that the solar wind is a weak source and that the majority of the H^+ is from local sources. The He^+ and He^{++} PND's showed much larger temporal variations than those of the locally produced ions and showed a substantial decrease between 2009-2010 near solar minimum.

The 127-220 keV C^+/W^+ and N^+/W^+ ratios in the main ring current region are 5.5×10^{-3} and 7.8×10^{-3} , respectively. The potential sources for carbon and nitrogen are escape from Titan's atmosphere and the Enceladus plumes. Our low abundance ratios indicate that the sources of neutral carbon and nitrogen are much weaker than that of the water group source. These results are qualitatively consistent with current estimates of the nitrogen source strengths [De La Haye *et al.*, 2007a; Hansen *et al.*, 2011]. However, our results imply that the neutral source strengths of carbon containing molecules are less than currently estimated by Strobel [2008,2009], Yelle *et al.* [2008], and Waite *et al.* [2009].

8.3 Loss Processes in Saturn's Inner Magnetosphere

The PND's of all the ion species examined in this study decrease in Saturn's inner magnetosphere. The loss of suprathermal ions in Saturn's inner magnetosphere is largely due to electron capture collisions with Saturn's neutral cloud, but electron loss and

transfer ionization also play a small role. Electron impact and photoionization are negligible loss processes compared to the ion-neutral collisions.

The L variations of the H^+ and W^+ FA's in Saturn's magnetosphere depend strongly on energy. At $E/Q=9-14$ keV/e, the W^+ FA increases in Saturn's inner magnetosphere and the H^+ FA decreases inward. The FA's of 36-55 keV/e W^+ and H^+ do not change significantly with L in Saturn's inner magnetosphere. At higher energies ($E/Q > 73$ keV/e), the W^+ FA decreases inward, while the H^+ FA increases inward. These L variations are qualitatively consistent with their single electron capture lifetimes.

The fractional abundances of H_2^+ , He^+ , and He^{++} decrease inward for all energies examined. While this decrease is expected based on our collision lifetime calculations, the magnitudes of this inward decrease of the H_2^+ and He^+ are larger than expected. This discrepancy is likely due to one of the several assumptions made when calculating the lifetimes. These assumptions include ignoring H_2^+ dissociation collisions between 3-60 keV, assuming H_2^+ on H has the same cross section as H_2^+ on O, assuming He^+ on H_2O has the same cross section as He^+ on O, etc. The He^{++} lifetimes are much shorter than all the other ion species, so its substantial inward decrease at all energies is expected.

The O^{++} FA increases inward for all energies examined. At $E/Q=9-14$ keV/e, this increase is due to its much longer lifetime compared to the other ion species. At $E/Q > 36$ keV/e, the production of O^{++} via the electron loss collision of O^+ on O is the most likely cause of the inward increase in the O^{++} FA. To make a more quantitative comparison between the

loss rate of suprathermal O^{++} via electron capture and the source rate of O^{++} via electron loss of O^+ , the cross sections for O^{++} on either O or H_2O must be obtained.

The lifetimes of 127 keV of C^+ , N^+ , and W^+ are approximately the same. This is consistent with the small L variations of the N^+/W^+ ratio, but is not consistent with the inward increase of C^+/W^+ . Like our other lifetime calculations, there are obvious uncertainties in our lifetime calculations such as our assumption the C^+ on H_2O collision has the same cross section as C^+ on O. Additional cross section measurements are needed to more accurately predict the different lifetimes.

8.4 Implications for Saturn's Neutral Cloud

We separated the 96 keV W^+ into its four major components: O^+ , OH^+ , H_2O^+ , and H_3O^+ . O^+ makes up 53% of the W^+ , while OH^+ and H_2O^+ each make up 22% of the W^+ . H_3O^+ is relatively rare and only makes up $\sim 3\%$ of the W^+ . The large O^+ abundance is qualitatively consistent with Cassini UVIS observations [*Melin et al.*, 2009] and recent models [*Cassidy and Johnson* 2010; *Smith et al.*, 2010] that predict an extensive O cloud much broader than either the OH or H_2O cloud. Our observation of $H_2O^+/W^+ > \sim 20\%$ throughout the magnetosphere suggests that neutral H_2O particles may be spread throughout Saturn's middle to outer magnetosphere rather than confined to a narrow H_2O torus centered on Enceladus. This is consistent with the *Cassidy and Johnson* [2010] model that predicts the OH and H_2O density is approximately equal outside of 7 R_S .

8.5 Future Work

There are numerous topics for future work involving the CHEMS data. Additional ion species can be detected by CHEMS (e.g. H_3^+ , O^{+++} , etc) and their abundances have yet to be examined in detail. This study focused on temporal, energy, and L variations from equatorial passes. Variations with latitude and local time have not been examined in detail and are another possible topic for future research.

Another topic for future work is adding the equatorial orbits from 2011 and the beginning of 2012 to our data set. This would be most useful when studying the long-term time variations of the suprathermal ions. We could add an additional three long-averaging periods to our study of the temporal variations using the passes from 2011 and 2012. It will be interesting to see if the correlation among the three major species (H^+ , W^+ , H_2^+) persists and how He^+ and He^{++} PND's vary during periods of increasing solar activity.

8.6 Concluding Remarks

Prior to the Cassini mission, plasma composition measurements were largely limited to the Voyager fly-bys. The CHEMS instrument was designed to provide the first mass resolved measurements of the suprathermal (3-220 keV/e) ion composition in Saturn's magnetosphere. The species resolution of the CHEMS instrument is much better than that of the Voyager spacecraft allowing us to determine the abundances of several different ion species for the first time. We were able to combine the data from a large number of passes to study the energy, L, and temporal variations of the suprathermal ion composition. These observations have greatly improved our understanding of the neutral

and plasma source strengths as well as the transport and loss processes of the suprathermal ions in Saturn's magnetosphere.

Appendix A

List of Time Ranges

Here we list all the time ranges used in this study. We include the time ranges from L=6-21, the main ring current (L=7-16), and the individual L shells. As a reminder, here are the criteria for our passes:

1. Cassini must be within 10° of the equatorial plane for the entire L=6-21 region.
2. Cassini must be in the magnetosphere out to L=21
3. Each pass cannot contain a data gap greater than $\Delta L=1$.

In each table we include the Rev. number and whether the pass was inbound or outbound.

The trajectories of each space can be viewed on the following website:

space.umd.edu/Projects/Cassini/trajectories/Trajectories.html.

Here are some of the passes that were not included along with the reason for removing them from the list:

1. Rev. 5 inbound: data gaps
2. Rev. 6 inbound: Cassini crossed magnetopause inside of L=21
3. Rev 16 inbound: Cassini crossed magnetopause inside of L=21
4. Rev 21 inbound: Cassini crossed magnetopause inside of L=21
5. Rev 23 outbound: data gaps
6. Rev 50 outbound: Cassini crossed magnetopause inside of L=21
7. Rev 53 inbound: Cassini moved outside equatorial region
8. Rev 124 inbound: Cassini moved outside equatorial region

9. Rev 126 outbound: data gaps
10. Rev 127 inbound: data gaps
11. Rev 132 inbound: Cassini moved outside equatorial plane
12. Rev 134 in and outbound: Cassini moved outside equatorial plane
13. Rev 140 in and outbound: data gaps

The passes from the end of 2007 through most of 2009 contain high latitude passes, so we do not include any ring current passes from 2007 day 340 to 2009 day 284. There is a blank row between each of our long-averaging periods. All the times have the format yyyy ddd hhmm.

Rev	L=6-21	L=7-16	L=6-7
B inbound	2004 348 0850-2004 350 0010	2004 348 2320-2004 349 2130	2004 349 2140-2004 350 0010
B outbound	2004 350 1140-2004 352 0230	2004 350 1420-2004 351 1200	2004 350 1140-2004 350 1410
3 inbound	2005 046 0400-2005 047 1750	2005 046 1900-2005 047 1550	2005 047 1600-2005 047 1750
3 outbound	2005 048 0800-2005 049 2210	2005 048 1000-2005 049 0650	2005 048 0800-2005 048 0950
4 inbound	2005 066 1430-2005 068 0440	2005 067 0550-2005 068 0240	2005 068 0250-2005 068 0440
4 outbound	2005 068 1840-2005 070 0850	2005 068 2040-2005 069 1730	2005 068 1840-2005 068 2030
5 outbound	2005 089 0640-2005 090 2050	2005 089 0840-2005 090 0530	2005 089 0640-2005 089 0830
6 outbound	2005 105 0620-2005 106 2000	2005 105 0800-2005 106 0420	2005 105 0620-2005 105 0750
15 inbound	2005 265 0050-2005 266 1430	2005 265 1610-2005 266 1240	2005 266 1250-2005 266 1430
15 outbound	2005 267 0440-2005 268 1830	2005 267 0640-2005 268 0300	2005 267 0440-2005 267 0630
16 outbound	2005 285 0840-2005 286 2230	2005 285 1030-2005 286 0700	2005 285 0840-2005 285 1020
17 inbound	2005 301 0120-2005 302 1650	2005 301 1620-2005 302 1420	2005 302 1430-2005 302 1650
17 outbound	2005 303 0500-2005 304 2020	2005 303 0730-2005 304 0530	2005 303 0500-2005 303 0720
18 inbound	2005 329 1350-2005 331 0510	2005 330 0440-2005 331 0240	2005 331 0250-2005 331 0510
18 outbound	2005 331 1730-2005 333 0900	2005 331 2000-2005 332 1800	2005 331 1730-2005 331 1950
19 inbound	2005 356 2340-2005 358 1510	2005 357 1440-2005 358 1240	2005 358 1250-2005 358 1510
19 outbound	2005 359 0330-2005 360 1900	2005 359 0600-2005 360 0400	2005 359 0330-2005 359 0550
20 inbound	2006 015 0910-2006 017 0320	2006 016 0000-2006 016 2340	2006 016 2350-2006 017 0320
20 outbound	2006 017 1030-2006 019 0440	2006 017 1420-2006 018 1350	2006 017 1030-2006 017 1410
21 outbound	2006 056 1430-2006 058 0830	2006 056 1820-2006 057 1750	2006 056 1430-2006 056 1810
22 inbound	2006 077 2240-2006 079 1600	2006 078 1320-2006 079 1230	2006 079 1240-2006 079 1600
22 outbound	2006 080 0010-2006 081 1730	2006 080 0340-2006 081 0250	2006 080 0010-2006 080 0330
23 inbound	2006 117 0230-2006 118 2000	2006 117 1710-2006 118 1630	2006 118 1640-2006 118 2000
24 inbound	2006 140 1140-2006 142 0450	2006 141 0210-2006 142 0130	2006 142 0140-2006 142 0450
24 outbound	2006 142 1310-2006 144 0630	2006 142 1630-2006 143 1550	2006 142 1310-2006 142 1620
25 inbound	2006 179 1540-2006 181 0900	2006 180 0620-2006 181 0530	2006 181 0540-2006 181 0900
25 outbound	2006 181 1720-2006 183 1030	2006 181 2040-2006 182 1950	2006 181 1720-2006 181 2030
47 inbound	2007 177 0430-2007 178 1750	2007 177 2010-2007 178 1610	2007 178 1620-2007 178 1750
47 outbound	2007 179 0800-2007 180 2100	2007 179 0940-2007 180 0540	2007 179 0800-2007 179 0930
48 inbound	2007 199 2320-2007 201 1600	2007 200 1350-2007 201 1250	2007 201 1300-2007 201 1600
48 outbound	2007 202 0100-2007 203 1740	2007 202 0410-2007 203 0310	2007 202 0100-2007 202 0400
49 inbound	2007 239 1550-2007 241 0840	2007 240 0630-2007 241 0520	2007 241 0530-2007 241 0840
49 outbound	2007 241 1730-2007 243 1020	2007 241 2050-2007 242 1940	2007 241 1730-2007 241 2040
50 inbound	2007 271 1510-2007 273 0530	2007 272 0530-2007 273 0300	2007 273 0310-2007 273 0530
51 inbound	2007 295 1140-2007 297 0100	2007 296 0220-2007 296 2300	2007 296 2310-2007 297 0100
51 outbound	2007 297 1440-2007 299 0440	2007 297 1650-2007 298 1350	2007 297 1440-2007 297 1640
52 inbound	2007 319 1130-2007 321 0100	2007 320 0220-2007 320 2300	2007 320 2310-2007 321 0100
52 outbound	2007 321 1440-2007 323 0450	2007 321 1650-2007 322 1340	2007 321 1440-2007 321 1640
53 outbound	2007 337 1430-2007 339 0420	2007 337 1610-2007 338 1230	2007 337 1430-2007 337 1600
119 inbound	2009 285 0810-2009 286 2200	2009 285 2330-2009 286 2010	2009 286 2020-2009 286 2200
119 outbound	2009 287 1220-2009 289 0210	2009 287 1410-2009 288 1050	2009 287 1220-2009 287 1400
120 inbound	2009 304 0740-2009 305 2130	2009 304 2300-2009 305 1940	2009 305 1950-2009 305 2130
120 outbound	2009 306 1150-2009 308 0140	2009 306 1340-2009 307 1010	2009 306 1150-2009 306 1330
121 inbound	2009 323 0810-2009 324 2210	2009 323 2340-2009 324 2010	2009 324 2020-2009 324 2210
121 outbound	2009 325 1220-2009 327 0220	2009 325 1420-2009 326 1050	2009 325 1220-2009 325 1410
122 inbound	2009 342 0910-2009 343 2300	2009 343 0030-2009 343 2100	2009 343 2110-2009 343 2300
122 outbound	2009 344 1310-2009 346 0300	2009 344 1510-2009 345 1140	2009 344 1310-2009 344 1500
123 inbound	2009 358 0910-2009 359 2240	2009 359 0050-2009 359 2100	2009 359 2110-2009 359 2240
123 outbound	2009 360 1240-2009 362 0230	2009 360 1430-2009 361 1040	2009 360 1240-2009 360 1420
125 inbound	2010 025 0740-2010 026 2110	2010 025 2320-2010 026 1920	2010 026 1930-2010 026 2110
125 outbound	2010 027 1110-2010 029 0050	2010 027 1300-2010 028 0910	2010 027 1110-2010 027 1250
126 inbound	2010 042 2000-2010 044 0950	2010 043 1140-2010 044 0800	2010 044 0810-2010 044 0950
127 outbound	2010 062 1310-2010 064 0250	2010 062 1500-2010 063 1120	2010 062 1310-2010 062 1450
128 inbound	2010 078 0020-2010 079 1410	2010 078 1600-2010 079 1220	2010 079 1230-2010 079 1410
128 outbound	2010 080 0430-2010 081 1810	2010 080 0620-2010 081 0240	2010 080 0430-2010 080 0610
129 inbound	2010 095 1540-2010 097 0550	2010 096 0700-2010 097 0350	2010 097 0400-2010 097 0550
129 outbound	2010 097 2000-2010 099 1010	2010 097 2200-2010 098 1850	2010 097 2000-2010 097 2150
130 inbound	2010 116 0020-2010 117 1440	2010 116 1540-2010 117 1240	2010 117 1250-2010 117 1440
130 outbound	2010 118 0440-2010 119 1900	2010 118 0650-2010 119 0340	2010 118 0440-2010 118 0640
131 inbound	2010 136 1120-2010 138 0130	2010 137 0240-2010 137 2330	2010 137 2340-2010 138 0130
131 outbound	2010 138 1540-2010 140 0550	2010 138 1740-2010 139 1430	2010 138 1540-2010 138 1730
132 outbound	2010 154 1440-2010 156 0500	2010 154 1630-2010 155 1310	2010 154 1440-2010 154 1620
133 inbound	2010 168 1010-2010 170 0000	2010 169 0200-2010 169 2210	2010 169 2220-2010 170 0000
133 outbound	2010 170 1410-2010 172 0400	2010 170 1600-2010 171 1210	2010 170 1410-2010 170 1550
135 inbound	2010 204 0620-2010 205 2010	2010 204 2140-2010 205 1810	2010 205 1820-2010 205 2010
135 outbound	2010 206 1020-2010 208 0030	2010 206 1210-2010 207 0910	2010 206 1020-2010 206 1200
136 inbound	2010 224 0410-2010 225 1800	2010 224 1930-2010 225 1600	2010 225 1610-2010 225 1800
136 outbound	2010 226 0810-2010 227 2220	2010 226 1000-2010 227 0700	2010 226 0810-2010 226 0950
137 inbound	2010 244 0450-2010 245 1840	2010 244 2000-2010 245 1640	2010 245 1650-2010 245 1840
137 outbound	2010 246 0840-2010 247 2300	2010 246 1040-2010 247 0730	2010 246 0840-2010 246 1030
138 inbound	2010 264 0300-2010 265 1700	2010 264 1820-2010 265 1500	2010 265 1510-2010 265 1700
138 outbound	2010 266 0700-2010 267 2110	2010 266 0900-2010 267 0550	2010 266 0700-2010 266 0850
139 inbound	2010 287 2040-2010 289 1110	2010 288 1140-2010 289 0900	2010 289 0910-2010 289 1110
139 outbound	2010 290 0040-2010 291 1530	2010 290 0250-2010 291 0020	2010 290 0040-2010 290 0240
141 inbound	2010 332 1210-2010 334 0230	2010 333 0330-2010 334 0030	2010 334 0040-2010 334 0230
141 outbound	2010 334 1640-2010 336 0650	2010 334 1840-2010 335 1530	2010 334 1640-2010 334 1830
142 inbound	2010 353 0130-2010 354 1550	2010 353 1650-2010 354 1340	2010 354 1350-2010 354 1550
142 outbound	2010 355 0550-2010 356 2010	2010 355 0750-2010 356 0450	2010 355 0550-2010 355 0740

Rev	L=7-8	L=8-9	L=9-10
B inbound	2004 349 1920-2004 349 2130	2004 349 1650-2004 349 1910	2004 349 1430-2004 349 1640
B outbound	2004 350 1420-2004 350 1630	2004 350 1640-2004 350 1850	2004 350 1900-2004 350 2110
3 inbound	2005 047 1400-2005 047 1550	2005 047 1200-2005 047 1350	2005 047 0950-2005 047 1150
3 outbound	2005 048 1000-2005 048 1150	2005 048 1200-2005 048 1400	2005 048 1410-2005 048 1600
4 inbound	2005 068 0040-2005 068 0240	2005 067 2240-2005 068 0030	2005 067 2030-2005 067 2230
4 outbound	2005 068 2040-2005 068 2230	2005 068 2240-2005 069 0040	2005 069 0050-2005 069 0250
5 outbound	2005 089 0840-2005 089 1030	2005 089 1040-2005 089 1240	2005 089 1250-2005 089 1450
6 outbound	2005 105 0800-2005 105 0940	2005 105 0950-2005 105 1140	2005 105 1150-2005 105 1340
15 inbound	2005 266 1050-2005 266 1240	2005 266 0850-2005 266 1040	2005 266 0650-2005 266 0840
15 outbound	2005 267 0640-2005 267 0820	2005 267 0830-2005 267 1020	2005 267 1030-2005 267 1220
16 outbound	2005 285 1030-2005 285 1220	2005 285 1230-2005 285 1410	2005 285 1420-2005 285 1620
17 inbound	2005 302 1210-2005 302 1420	2005 302 0950-2005 302 1200	2005 302 0730-2005 302 0940
17 outbound	2005 303 0730-2005 303 0940	2005 303 0950-2005 303 1200	2005 303 1210-2005 303 1420
18 inbound	2005 331 0030-2005 331 0240	2005 330 2210-2005 331 0020	2005 330 1950-2005 330 2200
18 outbound	2005 331 2000-2005 331 2210	2005 331 2220-2005 332 0030	2005 332 0040-2005 332 0250
19 inbound	2005 358 1030-2005 358 1240	2005 358 0820-2005 358 1020	2005 358 0600-2005 358 0810
19 outbound	2005 359 0600-2005 359 0810	2005 359 0820-2005 359 1030	2005 359 1040-2005 359 1250
20 inbound	2006 016 2100-2006 016 2340	2006 016 1820-2006 016 2050	2006 016 1550-2006 016 1810
20 outbound	2006 017 1420-2006 017 1700	2006 017 1710-2006 017 1940	2006 017 1950-2006 017 2210
21 inbound	2006 056 1820-2006 056 2100	2006 056 2110-2006 056 2340	2006 056 2350-2006 057 0210
22 inbound	2006 079 1000-2006 079 1230	2006 079 0720-2006 079 0950	2006 079 0450-2006 079 0710
22 outbound	2006 080 0340-2006 080 0610	2006 080 0620-2006 080 0850	2006 080 0900-2006 080 1120
23 inbound	2006 118 1350-2006 118 1630	2006 118 1120-2006 118 1340	2006 118 0850-2006 118 1110
24 inbound	2006 141 2250-2006 142 0130	2006 141 2020-2006 141 2240	2006 141 1750-2006 141 2010
24 outbound	2006 142 1630-2006 142 1910	2006 142 1920-2006 142 2140	2006 142 2150-2006 143 0010
25 inbound	2006 181 0300-2006 181 0530	2006 181 0020-2006 181 0250	2006 180 2150-2006 181 0010
25 outbound	2006 181 2040-2006 181 2320	2006 181 2330-2006 182 0150	2006 182 0200-2006 182 0420
47 inbound	2007 178 1430-2007 178 1610	2007 178 1240-2007 178 1420	2007 178 1040-2007 178 1230
47 outbound	2007 179 0940-2007 179 1120	2007 179 1130-2007 179 1310	2007 179 1320-2007 179 1510
48 inbound	2007 201 1020-2007 201 1250	2007 201 0750-2007 201 1010	2007 201 0520-2007 201 0740
48 outbound	2007 202 0410-2007 202 0640	2007 202 0650-2007 202 0910	2007 202 0920-2007 202 1140
49 inbound	2007 241 0250-2007 241 0520	2007 241 0020-2007 241 0240	2007 240 2150-2007 241 0010
49 outbound	2007 241 2050-2007 241 2320	2007 241 2330-2007 242 0150	2007 242 0200-2007 242 0420
50 inbound	2007 273 0050-2007 273 0300	2007 272 2230-2007 273 0040	2007 272 2020-2007 272 2220
51 inbound	2007 296 2110-2007 296 2300	2007 296 1900-2007 296 2100	2007 296 1650-2007 296 1850
51 outbound	2007 297 1650-2007 297 1850	2007 297 1900-2007 297 2050	2007 297 2100-2007 297 2300
52 inbound	2007 320 2100-2007 320 2300	2007 320 1900-2007 320 2050	2007 320 1650-2007 320 1850
52 outbound	2007 321 1650-2007 321 1840	2007 321 1850-2007 321 2050	2007 321 2100-2007 321 2300
53 outbound	2007 337 1610-2007 337 1800	2007 337 1810-2007 337 1950	2007 337 2000-2007 337 2150
119 inbound	2009 286 1820-2009 286 2010	2009 286 1620-2009 286 1810	2009 286 1410-2009 286 1610
119 outbound	2009 287 1410-2009 287 1600	2009 287 1610-2009 287 1800	2009 287 1810-2009 287 2010
120 inbound	2009 305 1750-2009 305 1940	2009 305 1550-2009 305 1740	2009 305 1340-2009 305 1540
120 outbound	2009 306 1340-2009 306 1530	2009 306 1540-2009 306 1730	2009 306 1740-2009 306 1930
121 inbound	2009 324 1830-2009 324 2010	2009 324 1620-2009 324 1820	2009 324 1420-2009 324 1610
121 outbound	2009 325 1420-2009 325 1600	2009 325 1610-2009 325 1810	2009 325 1820-2009 325 2010
122 inbound	2009 343 1920-2009 343 2100	2009 343 1710-2009 343 1910	2009 343 1510-2009 343 1700
122 outbound	2009 344 1510-2009 344 1650	2009 344 1700-2009 344 1850	2009 344 1900-2009 344 2100
123 inbound	2009 359 1920-2009 359 2100	2009 359 1720-2009 359 1910	2009 359 1520-2009 359 1710
123 outbound	2009 360 1430-2009 360 1610	2009 360 1620-2009 360 1810	2009 360 1820-2009 360 2010
125 inbound	2010 026 1740-2010 026 1920	2010 026 1550-2010 026 1730	2010 026 1350-2010 026 1540
125 outbound	2010 027 1300-2010 027 1440	2010 027 1450-2010 027 1630	2010 027 1640-2010 027 1830
126 inbound	2010 044 0610-2010 044 0800	2010 044 0410-2010 044 0600	2010 044 0210-2010 044 0400
127 outbound	2010 062 1500-2010 062 1640	2010 062 1650-2010 062 1840	2010 062 1850-2010 062 2050
128 inbound	2010 079 1030-2010 079 1220	2010 079 0840-2010 079 1020	2010 079 0630-2010 079 0830
128 outbound	2010 080 0620-2010 080 0800	2010 080 0810-2010 080 1000	2010 080 1010-2010 080 1200
129 inbound	2010 097 0200-2010 097 0350	2010 096 2350-2010 097 0150	2010 096 2140-2010 096 2340
129 outbound	2010 097 2200-2010 097 2350	2010 098 0000-2010 098 0150	2010 098 0200-2010 098 0400
130 inbound	2010 117 1050-2010 117 1240	2010 117 0840-2010 117 1040	2010 117 0630-2010 117 0830
130 outbound	2010 118 0650-2010 118 0840	2010 118 0850-2010 118 1040	2010 118 1050-2010 118 1250
131 inbound	2010 137 2140-2010 137 2330	2010 137 1930-2010 137 2130	2010 137 1720-2010 137 1920
131 outbound	2010 138 1740-2010 138 1930	2010 138 1940-2010 138 2130	2010 138 2140-2010 138 2340
132 outbound	2010 154 1630-2010 154 1810	2010 154 1820-2010 154 2010	2010 154 2020-2010 154 2220
133 inbound	2010 169 2030-2010 169 2210	2010 169 1830-2010 169 2020	2010 169 1630-2010 169 1820
133 outbound	2010 170 1600-2010 170 1740	2010 170 1750-2010 170 1930	2010 170 1940-2010 170 2140
135 inbound	2010 205 1620-2010 205 1810	2010 205 1420-2010 205 1610	2010 205 1220-2010 205 1410
135 outbound	2010 206 1210-2010 206 1410	2010 206 1420-2010 206 1610	2010 206 1620-2010 206 1820
136 inbound	2010 225 1410-2010 225 1600	2010 225 1210-2010 225 1400	2010 225 1000-2010 225 1200
136 outbound	2010 226 1000-2010 226 1200	2010 226 1210-2010 226 1400	2010 226 1410-2010 226 1610
137 inbound	2010 245 1450-2010 245 1640	2010 245 1250-2010 245 1440	2010 245 1040-2010 245 1240
137 outbound	2010 246 1040-2010 246 1230	2010 246 1240-2010 246 1440	2010 246 1450-2010 246 1650
138 inbound	2010 265 1310-2010 265 1500	2010 265 1110-2010 265 1300	2010 265 0900-2010 265 1100
138 outbound	2010 266 0900-2010 266 1050	2010 266 1100-2010 266 1300	2010 266 1310-2010 266 1500
139 inbound	2010 289 0700-2010 289 0900	2010 289 0450-2010 289 0650	2010 289 0240-2010 289 0440
139 outbound	2010 290 0250-2010 290 0450	2010 290 0500-2010 290 0700	2010 290 0710-2010 290 0920
141 inbound	2010 333 2240-2010 334 0030	2010 333 2030-2010 333 2230	2010 333 1820-2010 333 2020
141 outbound	2010 334 1840-2010 334 2030	2010 334 2040-2010 334 2230	2010 334 2240-2010 335 0040
142 inbound	2010 354 1150-2010 354 1340	2010 354 0950-2010 354 1140	2010 354 0740-2010 354 0940
142 outbound	2010 355 0750-2010 355 0940	2010 355 0950-2010 355 1150	2010 355 1200-2010 355 1400

Rev	L=10-11	L=11-12	L=12-13
B inbound	2004 349 1210-2004 349 1420	2004 349 0940-2004 349 1200	2004 349 0720-2004 349 0930
B outbound	2004 350 2120-2004 350 2330	2004 350 2340-2004 351 0150	2004 351 0200-2004 351 0410
3 inbound	2005 047 0740-2005 047 0940	2005 047 0520-2005 047 0730	2005 047 0250-2005 047 0510
3 outbound	2005 048 1610-2005 048 1820	2005 048 1830-2005 048 2040	2005 048 2050-2005 048 2300
4 inbound	2005 067 1820-2005 067 2020	2005 067 1600-2005 067 1810	2005 067 1340-2005 067 1550
4 outbound	2005 069 0300-2005 069 0500	2005 069 0510-2005 069 0720	2005 069 0730-2005 069 0940
5 outbound	2005 089 1500-2005 089 1700	2005 089 1710-2005 089 1920	2005 089 1930-2005 089 2140
6 outbound	2005 105 1350-2005 105 1550	2005 105 1600-2005 105 1810	2005 105 1820-2005 105 2030
15 inbound	2005 266 0440-2005 266 0640	2005 266 0220-2005 266 0430	2005 266 0000-2005 266 0210
15 outbound	2005 267 1230-2005 267 1430	2005 267 1440-2005 267 1650	2005 267 1700-2005 267 1910
16 outbound	2005 285 1630-2005 285 1830	2005 285 1840-2005 285 2050	2005 285 2100-2005 285 2310
17 inbound	2005 302 0510-2005 302 0720	2005 302 0250-2005 302 0500	2005 302 0020-2005 302 0240
17 outbound	2005 303 1430-2005 303 1640	2005 303 1650-2005 303 1910	2005 303 1920-2005 303 2130
18 inbound	2005 330 1730-2005 330 1940	2005 330 1510-2005 330 1720	2005 330 1240-2005 330 1500
18 outbound	2005 332 0300-2005 332 0510	2005 332 0520-2005 332 0740	2005 332 0750-2005 332 1010
19 inbound	2005 358 0330-2005 358 0550	2005 358 0110-2005 358 0320	2005 357 2240-2005 358 0100
19 outbound	2005 359 1300-2005 359 1510	2005 359 1520-2005 359 1740	2005 359 1750-2005 359 2010
20 inbound	2006 016 1310-2006 016 1540	2006 016 1040-2006 016 1300	2006 016 0810-2006 016 1030
20 outbound	2006 017 2220-2006 018 0040	2006 018 0050-2006 018 0310	2006 018 0320-2006 018 0550
21 outbound	2006 057 0220-2006 057 0440	2006 057 0450-2006 057 0710	2006 057 0720-2006 057 0950
22 inbound	2006 079 0220-2006 079 0440	2006 078 2350-2006 079 0210	2006 078 2120-2006 078 2340
22 outbound	2006 080 1130-2006 080 1350	2006 080 1400-2006 080 1620	2006 080 1630-2006 080 1850
23 inbound	2006 118 0620-2006 118 0840	2006 118 0350-2006 118 0610	2006 118 0110-2006 118 0340
24 inbound	2006 141 1520-2006 141 1740	2006 141 1250-2006 141 1510	2006 141 1010-2006 141 1240
24 outbound	2006 143 0020-2006 143 0240	2006 143 0250-2006 143 0510	2006 143 0520-2006 143 0750
25 inbound	2006 180 1920-2006 180 2140	2006 180 1650-2006 180 1910	2006 180 1420-2006 180 1640
25 outbound	2006 182 0430-2006 182 0650	2006 182 0700-2006 182 0920	2006 182 0930-2006 182 1150
47 inbound	2007 178 0830-2007 178 1030	2007 178 0620-2007 178 0820	2007 178 0400-2007 178 0610
47 outbound	2007 179 1520-2007 179 1720	2007 179 1730-2007 179 1930	2007 179 1940-2007 179 2150
48 inbound	2007 201 0250-2007 201 0510	2007 201 0020-2007 201 0240	2007 200 2150-2007 201 0010
48 outbound	2007 202 1150-2007 202 1410	2007 202 1420-2007 202 1640	2007 202 1650-2007 202 1910
49 inbound	2007 240 1920-2007 240 2140	2007 240 1650-2007 240 1910	2007 240 1420-2007 240 1640
49 outbound	2007 242 0430-2007 242 0640	2007 242 0650-2007 242 0910	2007 242 0920-2007 242 1140
50 inbound	2007 272 1800-2007 272 2010	2007 272 1540-2007 272 1750	2007 272 1310-2007 272 1530
51 inbound	2007 296 1440-2007 296 1640	2007 296 1220-2007 296 1430	2007 296 1000-2007 296 1210
51 outbound	2007 297 2310-2007 298 0120	2007 298 0130-2007 298 0340	2007 298 0350-2007 298 0600
52 inbound	2007 320 1440-2007 320 1640	2007 320 1220-2007 320 1430	2007 320 1000-2007 320 1210
52 outbound	2007 321 2310-2007 322 0110	2007 322 0120-2007 322 0330	2007 322 0340-2007 322 0600
53 outbound	2007 337 2200-2007 338 0000	2007 338 0010-2007 338 0220	2007 338 0230-2007 338 0440
119 inbound	2009 286 1200-2009 286 1400	2009 286 0940-2009 286 1150	2009 286 0720-2009 286 0930
119 outbound	2009 287 2020-2009 287 2220	2009 287 2230-2009 288 0030	2009 288 0040-2009 288 0300
120 inbound	2009 305 1130-2009 305 1330	2009 305 0910-2009 305 1120	2009 305 0650-2009 305 0900
120 outbound	2009 306 1940-2009 306 2150	2009 306 2200-2009 307 0000	2009 307 0010-2009 307 0230
121 inbound	2009 324 1210-2009 324 1410	2009 324 0950-2009 324 1200	2009 324 0730-2009 324 0940
121 outbound	2009 325 2020-2009 325 2220	2009 325 2230-2009 326 0040	2009 326 0050-2009 326 0300
122 inbound	2009 343 1300-2009 343 1500	2009 343 1040-2009 343 1250	2009 343 0820-2009 343 1030
122 outbound	2009 344 2110-2009 344 2310	2009 344 2320-2009 345 0130	2009 345 0140-2009 345 0350
123 inbound	2009 359 1310-2009 359 1510	2009 359 1100-2009 359 1300	2009 359 0840-2009 359 1050
123 outbound	2009 360 2020-2009 360 2220	2009 360 2230-2009 361 0030	2009 361 0040-2009 361 0250
125 inbound	2010 026 1140-2010 026 1340	2010 026 0930-2010 026 1130	2010 026 0710-2010 026 0920
125 outbound	2010 027 1840-2010 027 2040	2010 027 2050-2010 027 2300	2010 027 2310-2010 028 0120
126 inbound	2010 044 0000-2010 044 0200	2010 043 2140-2010 043 2350	2010 043 1920-2010 043 2130
127 outbound	2010 062 2100-2010 062 2300	2010 062 2310-2010 063 0110	2010 063 0120-2010 063 0330
128 inbound	2010 079 0420-2010 079 0620	2010 079 0210-2010 079 0410	2010 078 2340-2010 079 0200
128 outbound	2010 080 1210-2010 080 1410	2010 080 1420-2010 080 1630	2010 080 1640-2010 080 1850
129 inbound	2010 096 1930-2010 096 2130	2010 096 1710-2010 096 1920	2010 096 1450-2010 096 1700
129 outbound	2010 098 0410-2010 098 0620	2010 098 0630-2010 098 0830	2010 098 0840-2010 098 1100
130 inbound	2010 117 0420-2010 117 0620	2010 117 0200-2010 117 0410	2010 116 2330-2010 117 0150
130 outbound	2010 118 1300-2010 118 1500	2010 118 1510-2010 118 1720	2010 118 1730-2010 118 1950
131 inbound	2010 137 1510-2010 137 1710	2010 137 1250-2010 137 1500	2010 137 1030-2010 137 1240
131 outbound	2010 138 2350-2010 139 0150	2010 139 0200-2010 139 0410	2010 139 0420-2010 139 0640
132 outbound	2010 154 2230-2010 155 0030	2010 155 0040-2010 155 0250	2010 155 0300-2010 155 0510
133 inbound	2010 169 1420-2010 169 1620	2010 169 1210-2010 169 1410	2010 169 0950-2010 169 1200
133 outbound	2010 170 2150-2010 170 2340	2010 170 2350-2010 171 0200	2010 171 0210-2010 171 0420
135 inbound	2010 205 1000-2010 205 1210	2010 205 0750-2010 205 0950	2010 205 0520-2010 205 0740
135 outbound	2010 206 1830-2010 206 2030	2010 206 2040-2010 206 2250	2010 206 2300-2010 207 0110
136 inbound	2010 225 0750-2010 225 0950	2010 225 0540-2010 225 0740	2010 225 0310-2010 225 0530
136 outbound	2010 226 1620-2010 226 1820	2010 226 1830-2010 226 2040	2010 226 2050-2010 226 2310
137 inbound	2010 245 0830-2010 245 1030	2010 245 0610-2010 245 0820	2010 245 0350-2010 245 0600
137 outbound	2010 246 1700-2010 246 1900	2010 246 1910-2010 246 2120	2010 246 2130-2010 246 2340
138 inbound	2010 265 0650-2010 265 0850	2010 265 0430-2010 265 0640	2010 265 0210-2010 265 0420
138 outbound	2010 266 1510-2010 266 1720	2010 266 1730-2010 266 1940	2010 266 1950-2010 266 2200
139 inbound	2010 289 0020-2010 289 0230	2010 288 2200-2010 289 0010	2010 288 1930-2010 288 2150
139 outbound	2010 290 0930-2010 290 1140	2010 290 1150-2010 290 1400	2010 290 1410-2010 290 1620
141 inbound	2010 333 1610-2010 333 1810	2010 333 1350-2010 333 1600	2010 333 1120-2010 333 1340
141 outbound	2010 335 0050-2010 335 0300	2010 335 0310-2010 335 0520	2010 335 0530-2010 335 0740
142 inbound	2010 354 0520-2010 354 0730	2010 354 0300-2010 354 0510	2010 354 0040-2010 354 0250
142 outbound	2010 355 1410-2010 355 1610	2010 355 1620-2010 355 1830	2010 355 1840-2010 355 2100

Rev	L=13-14	L=14-15	L=15-16
B inbound	2004 349 0440-2004 349 0710	2004 349 0210-2004 349 0430	2004 348 2320-2004 349 0200
B outbound	2004 351 0420-2004 351 0650	2004 351 0700-2004 351 0920	2004 351 0930-2004 351 1200
3 inbound	2005 047 0020-2005 047 0240	2005 046 2150-2005 047 0010	2005 046 1900-2005 046 2140
3 outbound	2005 048 2310-2005 049 0130	2005 049 0140-2005 049 0410	2005 049 0420-2005 049 0650
4 inbound	2005 067 1110-2005 067 1330	2005 067 0830-2005 067 1100	2005 067 0550-2005 067 0820
4 outbound	2005 069 0950-2005 069 1210	2005 069 1220-2005 069 1450	2005 069 1500-2005 069 1730
5 inbound	2005 089 2150-2005 090 0010	2005 090 0020-2005 090 0250	2005 090 0300-2005 090 0530
6 inbound	2005 105 2040-2005 105 2300	2005 105 2310-2005 106 0130	2005 106 0140-2005 106 0420
15 inbound	2005 265 2130-2005 265 2350	2005 265 1900-2005 265 2120	2005 265 1610-2005 265 1850
15 outbound	2005 267 1920-2005 267 2140	2005 267 2150-2005 268 0020	2005 268 0030-2005 268 0300
16 inbound	2005 285 2320-2005 286 0140	2005 286 0150-2005 286 0410	2005 286 0420-2005 286 0700
17 inbound	2005 301 2140-2005 302 0010	2005 301 1910-2005 301 2130	2005 301 1620-2005 301 1900
17 outbound	2005 303 2140-2005 304 0010	2005 304 0020-2005 304 0240	2005 304 0250-2005 304 0530
18 inbound	2005 330 1010-2005 330 1230	2005 330 0730-2005 330 1000	2005 330 0440-2005 330 0720
18 outbound	2005 332 1020-2005 332 1240	2005 332 1250-2005 332 1520	2005 332 1530-2005 332 1800
19 inbound	2005 357 2010-2005 357 2230	2005 357 1730-2005 357 2000	2005 357 1440-2005 357 1720
19 outbound	2005 359 2020-2005 359 2240	2005 359 2250-2005 360 0120	2005 360 0130-2005 360 0400
20 inbound	2006 016 0530-2006 016 0800	2006 016 0250-2006 016 0520	2006 016 0000-2006 016 0240
20 outbound	2006 018 0600-2006 018 0830	2006 018 0840-2006 018 1110	2006 018 1120-2006 018 1350
21 inbound	2006 057 1000-2006 057 1230	2006 057 1240-2006 057 1510	2006 057 1520-2006 057 1750
22 inbound	2006 078 1840-2006 078 2110	2006 078 1600-2006 078 1830	2006 078 1320-2006 078 1550
22 outbound	2006 080 1900-2006 080 2130	2006 080 2140-2006 081 0010	2006 081 0020-2006 081 0250
23 inbound	2006 117 2240-2006 118 0100	2006 117 2000-2006 117 2230	2006 117 1710-2006 117 1950
24 inbound	2006 141 0740-2006 141 1000	2006 141 0500-2006 141 0730	2006 141 0210-2006 141 0450
24 outbound	2006 143 0800-2006 143 1020	2006 143 1030-2006 143 1300	2006 143 1310-2006 143 1550
25 inbound	2006 180 1140-2006 180 1410	2006 180 0900-2006 180 1130	2006 180 0620-2006 180 0850
25 outbound	2006 182 1200-2006 182 1430	2006 182 1440-2006 182 1710	2006 182 1720-2006 182 1950
47 inbound	2007 178 0130-2007 178 0350	2007 177 2250-2007 178 0120	2007 177 2010-2007 177 2240
47 outbound	2007 179 2200-2007 180 0020	2007 180 0030-2007 180 0300	2007 180 0310-2007 180 0540
48 inbound	2007 200 1910-2007 200 2140	2007 200 1640-2007 200 1900	2007 200 1350-2007 200 1630
48 outbound	2007 202 1920-2007 202 2150	2007 202 2200-2007 203 0020	2007 203 0030-2007 203 0310
49 inbound	2007 240 1150-2007 240 1410	2007 240 0910-2007 240 1140	2007 240 0630-2007 240 0900
49 outbound	2007 242 1150-2007 242 1420	2007 242 1430-2007 242 1700	2007 242 1710-2007 242 1940
50 inbound	2007 272 1040-2007 272 1300	2007 272 0810-2007 272 1030	2007 272 0530-2007 272 0800
51 inbound	2007 296 0730-2007 296 0950	2007 296 0500-2007 296 0720	2007 296 0220-2007 296 0450
51 outbound	2007 298 0610-2007 298 0830	2007 298 0840-2007 298 1110	2007 298 1120-2007 298 1350
52 inbound	2007 320 0730-2007 320 0950	2007 320 0500-2007 320 0720	2007 320 0220-2007 320 0450
52 outbound	2007 322 0610-2007 322 0830	2007 322 0840-2007 322 1100	2007 322 1110-2007 322 1340
53 inbound	2007 338 0450-2007 338 0710	2007 338 0720-2007 338 0950	2007 338 1000-2007 338 1230
119 inbound	2009 286 0450-2009 286 0710	2009 286 0220-2009 286 0440	2009 285 2330-2009 286 0210
119 outbound	2009 288 0310-2009 288 0530	2009 288 0540-2009 288 0800	2009 288 0810-2009 288 1050
120 inbound	2009 305 0420-2009 305 0640	2009 305 0150-2009 305 0410	2009 304 2300-2009 305 0140
120 outbound	2009 307 0240-2009 307 0500	2009 307 0510-2009 307 0730	2009 307 0740-2009 307 1010
121 inbound	2009 324 0500-2009 324 0720	2009 324 0220-2009 324 0450	2009 323 2340-2009 324 0210
121 outbound	2009 326 0310-2009 326 0530	2009 326 0540-2009 326 0810	2009 326 0820-2009 326 1050
122 inbound	2009 343 0550-2009 343 0810	2009 343 0310-2009 343 0540	2009 343 0030-2009 343 0300
122 outbound	2009 345 0400-2009 345 0620	2009 345 0630-2009 345 0900	2009 345 0910-2009 345 1140
123 inbound	2009 359 0610-2009 359 0830	2009 359 0340-2009 359 0600	2009 359 0050-2009 359 0330
123 outbound	2009 361 0300-2009 361 0520	2009 361 0530-2009 361 0800	2009 361 0810-2009 361 1040
125 inbound	2010 026 0440-2010 026 0700	2010 026 0210-2010 026 0430	2010 025 2320-2010 026 0200
125 outbound	2010 028 0130-2010 028 0350	2010 028 0400-2010 028 0620	2010 028 0630-2010 028 0910
126 inbound	2010 043 1650-2010 043 1910	2010 043 1420-2010 043 1640	2010 043 1140-2010 043 1410
127 outbound	2010 063 0340-2010 063 0600	2010 063 0610-2010 063 0840	2010 063 0850-2010 063 1120
128 inbound	2010 078 2120-2010 078 2330	2010 078 1840-2010 078 2110	2010 078 1600-2010 078 1830
128 outbound	2010 080 1900-2010 080 2120	2010 080 2130-2010 080 2350	2010 081 0000-2010 081 0240
129 inbound	2010 096 1220-2010 096 1440	2010 096 0940-2010 096 1210	2010 096 0700-2010 096 0930
129 outbound	2010 098 1110-2010 098 1330	2010 098 1340-2010 098 1610	2010 098 1620-2010 098 1850
130 inbound	2010 116 2100-2010 116 2320	2010 116 1830-2010 116 2050	2010 116 1540-2010 116 1820
130 outbound	2010 118 2000-2010 118 2220	2010 118 2230-2010 119 0100	2010 119 0110-2010 119 0340
131 inbound	2010 137 0800-2010 137 1020	2010 137 0520-2010 137 0750	2010 137 0240-2010 137 0510
131 outbound	2010 139 0650-2010 139 0910	2010 139 0920-2010 139 1140	2010 139 1150-2010 139 1430
132 inbound	2010 155 0520-2010 155 0740	2010 155 0750-2010 155 1020	2010 155 1030-2010 155 1310
133 inbound	2010 169 0720-2010 169 0940	2010 169 0440-2010 169 0710	2010 169 0200-2010 169 0430
133 outbound	2010 171 0430-2010 171 0650	2010 171 0700-2010 171 0930	2010 171 0940-2010 171 1210
135 inbound	2010 205 0250-2010 205 0510	2010 205 0020-2010 205 0240	2010 204 2140-2010 205 0010
135 outbound	2010 207 0120-2010 207 0350	2010 207 0400-2010 207 0620	2010 207 0630-2010 207 0910
136 inbound	2010 225 0040-2010 225 0300	2010 224 2210-2010 225 0030	2010 224 1930-2010 224 2200
136 outbound	2010 226 2320-2010 227 0140	2010 227 0150-2010 227 0410	2010 227 0420-2010 227 0700
137 inbound	2010 245 0120-2010 245 0340	2010 244 2240-2010 245 0110	2010 244 2000-2010 244 2230
137 outbound	2010 246 2350-2010 247 0210	2010 247 0220-2010 247 0450	2010 247 0500-2010 247 0730
138 inbound	2010 264 2340-2010 265 0200	2010 264 2100-2010 264 2330	2010 264 1820-2010 264 2050
138 outbound	2010 266 2210-2010 267 0030	2010 267 0040-2010 267 0310	2010 267 0320-2010 267 0550
139 inbound	2010 288 1700-2010 288 1920	2010 288 1420-2010 288 1650	2010 288 1140-2010 288 1410
139 outbound	2010 290 1630-2010 290 1900	2010 290 1910-2010 290 2130	2010 290 2140-2010 291 0020
141 inbound	2010 333 0850-2010 333 1110	2010 333 0620-2010 333 0840	2010 333 0330-2010 333 0610
141 outbound	2010 335 0750-2010 335 1010	2010 335 1020-2010 335 1250	2010 335 1300-2010 335 1530
142 inbound	2010 353 2210-2010 354 0030	2010 353 1930-2010 353 2200	2010 353 1650-2010 353 1920
142 outbound	2010 355 2110-2010 355 2330	2010 355 2340-2010 356 0200	2010 356 0210-2010 356 0450

Rev	L=16-17	L=17-18	L=18-19
B inbound	2004 348 2040-2004 348 2310	2004 348 1750-2004 348 2030	2004 348 1450-2004 348 1740
B outbound	2004 351 1210-2004 351 1440	2004 351 1450-2004 351 1730	2004 351 1740-2004 351 2030
3 inbound	2005 046 1610-2005 046 1850	2005 046 1320-2005 046 1600	2005 046 1010-2005 046 1310
3 outbound	2005 049 0700-2005 049 0940	2005 049 0950-2005 049 1240	2005 049 1250-2005 049 1540
4 inbound	2005 067 0300-2005 067 0540	2005 067 0000-2005 067 0250	2005 066 2100-2005 066 2350
4 outbound	2005 069 1740-2005 069 2020	2005 069 2030-2005 069 2320	2005 069 2330-2005 070 0220
5 outbound	2005 090 0540-2005 090 0820	2005 090 0830-2005 090 1120	2005 090 1130-2005 090 1420
6 outbound	2005 106 0430-2005 106 0710	2005 106 0720-2005 106 1010	2005 106 1020-2005 106 1320
15 inbound	2005 265 1330-2005 265 1600	2005 265 1030-2005 265 1320	2005 265 0720-2005 265 1020
15 outbound	2005 268 0310-2005 268 0550	2005 268 0600-2005 268 0850	2005 268 0900-2005 268 1150
16 outbound	2005 286 0710-2005 286 0950	2005 286 1000-2005 286 1250	2005 286 1300-2005 286 1550
17 inbound	2005 301 1340-2005 301 1610	2005 301 1040-2005 301 1330	2005 301 0740-2005 301 1030
17 outbound	2005 304 0540-2005 304 0820	2005 304 0830-2005 304 1110	2005 304 1120-2005 304 1410
18 inbound	2005 330 0200-2005 330 0430	2005 329 2300-2005 330 0150	2005 329 2000-2005 329 2250
18 outbound	2005 332 1810-2005 332 2050	2005 332 2100-2005 332 2350	2005 333 0000-2005 333 0250
19 inbound	2005 357 1150-2005 357 1430	2005 357 0900-2005 357 1140	2005 357 0600-2005 357 0850
19 outbound	2005 360 0410-2005 360 0650	2005 360 0700-2005 360 0950	2005 360 1000-2005 360 1250
20 inbound	2006 015 2110-2006 015 2350	2006 015 1820-2006 015 2100	2006 015 1520-2006 015 1810
20 outbound	2006 018 1400-2006 018 1640	2006 018 1650-2006 018 1930	2006 018 1940-2006 018 2230
21 outbound	2006 057 1800-2006 057 2040	2006 057 2050-2006 057 2330	2006 057 2340-2006 058 0230
22 inbound	2006 078 1030-2006 078 1310	2006 078 0740-2006 078 1020	2006 078 0440-2006 078 0730
22 outbound	2006 081 0300-2006 081 0540	2006 081 0550-2006 081 0830	2006 081 0840-2006 081 1130
23 inbound	2006 117 1430-2006 117 1700	2006 117 1130-2006 117 1420	2006 117 0840-2006 117 1120
24 inbound	2006 140 2330-2006 141 0200	2006 140 2040-2006 140 2320	2006 140 1740-2006 140 2030
24 outbound	2006 143 1600-2006 143 1830	2006 143 1840-2006 143 2120	2006 143 2130-2006 144 0020
25 inbound	2006 180 0330-2006 180 0610	2006 180 0040-2006 180 0320	2006 179 2150-2006 180 0030
25 outbound	2006 182 2000-2006 182 2240	2006 182 2250-2006 183 0130	2006 183 0140-2006 183 0430
47 inbound	2007 177 1720-2007 177 2000	2007 177 1420-2007 177 1710	2007 177 1120-2007 177 1410
47 outbound	2007 180 0550-2007 180 0830	2007 180 0840-2007 180 1130	2007 180 1140-2007 180 1440
48 inbound	2007 200 1110-2007 200 1340	2007 200 0820-2007 200 1100	2007 200 0520-2007 200 0810
48 outbound	2007 203 0320-2007 203 0550	2007 203 0600-2007 203 0840	2007 203 0850-2007 203 1140
49 inbound	2007 240 0340-2007 240 0620	2007 240 0050-2007 240 0330	2007 239 2200-2007 240 0040
49 outbound	2007 242 1950-2007 242 2230	2007 242 2240-2007 243 0120	2007 243 0130-2007 243 0410
50 inbound	2007 272 0250-2007 272 0520	2007 272 0000-2007 272 0240	2007 271 2110-2007 271 2350
51 inbound	2007 295 2340-2007 296 0210	2007 295 2050-2007 295 2330	2007 295 1750-2007 295 2040
51 outbound	2007 298 1400-2007 298 1630	2007 298 1640-2007 298 1930	2007 298 1940-2007 298 2220
52 inbound	2007 319 2340-2007 320 0210	2007 319 2050-2007 319 2330	2007 319 1750-2007 319 2040
52 outbound	2007 322 1350-2007 322 1630	2007 322 1640-2007 322 1920	2007 322 1930-2007 322 2220
53 outbound	2007 338 1240-2007 338 1520	2007 338 1530-2007 338 1830	2007 338 1840-2007 338 2130
119 inbound	2009 285 2040-2009 285 2320	2009 285 1750-2009 285 2030	2009 285 1440-2009 285 1740
119 outbound	2009 288 1100-2009 288 1330	2009 288 1340-2009 288 1630	2009 288 1640-2009 288 1940
120 inbound	2009 304 2010-2009 304 2250	2009 304 1720-2009 304 2000	2009 304 1410-2009 304 1710
120 outbound	2009 307 1020-2009 307 1300	2009 307 1310-2009 307 1600	2009 307 1610-2009 307 1910
121 inbound	2009 323 2050-2009 323 2330	2009 323 1750-2009 323 2040	2009 323 1450-2009 323 1740
121 outbound	2009 326 1100-2009 326 1340	2009 326 1350-2009 326 1640	2009 326 1650-2009 326 1940
122 inbound	2009 342 2140-2009 343 0020	2009 342 1840-2009 342 2130	2009 342 1540-2009 342 1830
122 outbound	2009 345 1150-2009 345 1430	2009 345 1440-2009 345 1730	2009 345 1740-2009 345 2030
123 inbound	2009 358 2200-2009 359 0040	2009 358 1900-2009 358 2150	2009 358 1600-2009 358 1850
123 outbound	2009 361 1050-2009 361 1330	2009 361 1340-2009 361 1640	2009 361 1650-2009 361 1940
125 inbound	2010 025 2030-2010 025 2310	2010 025 1740-2010 025 2020	2010 025 1430-2010 025 1730
125 outbound	2010 028 0920-2010 028 1200	2010 028 1210-2010 028 1500	2010 028 1510-2010 028 1810
126 inbound	2010 043 0840-2010 043 1130	2010 043 0550-2010 043 0830	2010 043 0240-2010 043 0540
127 outbound	2010 063 1130-2010 063 1410	2010 063 1420-2010 063 1710	2010 063 1720-2010 063 2020
128 inbound	2010 078 1310-2010 078 1550	2010 078 1010-2010 078 1300	2010 078 0700-2010 078 1000
128 outbound	2010 081 0250-2010 081 0530	2010 081 0540-2010 081 0820	2010 081 0830-2010 081 1130
129 inbound	2010 096 0410-2010 096 0650	2010 096 0110-2010 096 0400	2010 095 2210-2010 096 0100
129 outbound	2010 098 1900-2010 098 2140	2010 098 2150-2010 099 0040	2010 099 0050-2010 099 0340
130 inbound	2010 116 1250-2010 116 1530	2010 116 1000-2010 116 1240	2010 116 0650-2010 116 0950
130 outbound	2010 119 0350-2010 119 0630	2010 119 0640-2010 119 0930	2010 119 0940-2010 119 1230
131 inbound	2010 136 2350-2010 137 0230	2010 136 2050-2010 136 2340	2010 136 1750-2010 136 2040
131 outbound	2010 139 1440-2010 139 1720	2010 139 1730-2010 139 2010	2010 139 2020-2010 139 2320
132 outbound	2010 155 1320-2010 155 1600	2010 155 1610-2010 155 1900	2010 155 1910-2010 155 2210
133 inbound	2010 168 2310-2010 169 0150	2010 168 2010-2010 168 2300	2010 168 1700-2010 168 2000
133 outbound	2010 171 1220-2010 171 1500	2010 171 1510-2010 171 1800	2010 171 1810-2010 171 2110
135 inbound	2010 204 1850-2010 204 2130	2010 204 1550-2010 204 1840	2010 204 1250-2010 204 1540
135 outbound	2010 207 0920-2010 207 1200	2010 207 1210-2010 207 1450	2010 207 1500-2010 207 1800
136 inbound	2010 224 1640-2010 224 1920	2010 224 1340-2010 224 1630	2010 224 1040-2010 224 1330
136 outbound	2010 227 0710-2010 227 0950	2010 227 1000-2010 227 1240	2010 227 1250-2010 227 1550
137 inbound	2010 244 1710-2010 244 1950	2010 244 1420-2010 244 1700	2010 244 1120-2010 244 1410
137 outbound	2010 247 0740-2010 247 1020	2010 247 1030-2010 247 1320	2010 247 1330-2010 247 1630
138 inbound	2010 264 1530-2010 264 1810	2010 264 1240-2010 264 1520	2010 264 0930-2010 264 1230
138 outbound	2010 267 0600-2010 267 0840	2010 267 0850-2010 267 1140	2010 267 1150-2010 267 1450
139 inbound	2010 288 0850-2010 288 1130	2010 288 0600-2010 288 0840	2010 288 0300-2010 288 0550
139 outbound	2010 291 0030-2010 291 0310	2010 291 0320-2010 291 0600	2010 291 0610-2010 291 0900
141 inbound	2010 333 0040-2010 333 0320	2010 332 2150-2010 333 0030	2010 332 1840-2010 332 2140
141 outbound	2010 335 1540-2010 335 1820	2010 335 1830-2010 335 2120	2010 335 2130-2010 336 0020
142 inbound	2010 353 1400-2010 353 1640	2010 353 1100-2010 353 1350	2010 353 0800-2010 353 1050
142 outbound	2010 356 0500-2010 356 0740	2010 356 0750-2010 356 1030	2010 356 1040-2010 356 1340

Rev	L=19-20	L=20-21
B inbound	2004 348 1150-2004 348 1440	2004 348 0850-2004 348 1140
B outbound	2004 351 2040-2004 351 2330	2004 351 2340-2004 352 0230
3 inbound	2005 046 0710-2005 046 1000	2005 046 0400-2005 046 0700
3 outbound	2005 049 1550-2005 049 1850	2005 049 1900-2005 049 2210
4 inbound	2005 066 1750-2005 066 2050	2005 066 1430-2005 066 1740
4 outbound	2005 070 0230-2005 070 0530	2005 070 0540-2005 070 0850
5 outbound	2005 090 1430-2005 090 1730	2005 090 1740-2005 090 2050
6 outbound	2005 106 1330-2005 106 1640	2005 106 1650-2005 106 2000
15 inbound	2005 265 0410-2005 265 0710	2005 265 0050-2005 265 0400
15 outbound	2005 268 1200-2005 268 1500	2005 268 1510-2005 268 1830
16 outbound	2005 286 1600-2005 286 1910	2005 286 1920-2005 286 2230
17 inbound	2005 301 0440-2005 301 0730	2005 301 0120-2005 301 0430
17 outbound	2005 304 1420-2005 304 1710	2005 304 1720-2005 304 2020
18 inbound	2005 329 1700-2005 329 1950	2005 329 1350-2005 329 1650
18 outbound	2005 333 0300-2005 333 0550	2005 333 0600-2005 333 0900
19 inbound	2005 357 0250-2005 357 0550	2005 356 2340-2005 357 0240
19 outbound	2005 360 1300-2005 360 1550	2005 360 1600-2005 360 1900
20 inbound	2006 015 1220-2006 015 1510	2006 015 0910-2006 015 1210
20 outbound	2006 018 2240-2006 019 0130	2006 019 0140-2006 019 0440
21 inbound	2006 058 0240-2006 058 0530	2006 058 0540-2006 058 0830
22 inbound	2006 078 0140-2006 078 0430	2006 077 2240-2006 078 0130
22 outbound	2006 081 1140-2006 081 1430	2006 081 1440-2006 081 1730
23 inbound	2006 117 0540-2006 117 0830	2006 117 0230-2006 117 0530
24 inbound	2006 140 1440-2006 140 1730	2006 140 1140-2006 140 1430
24 outbound	2006 144 0030-2006 144 0320	2006 144 0330-2006 144 0630
25 inbound	2006 179 1850-2006 179 2140	2006 179 1540-2006 179 1840
25 outbound	2006 183 0440-2006 183 0730	2006 183 0740-2006 183 1030
47 inbound	2007 177 0800-2007 177 1110	2007 177 0430-2007 177 0750
47 outbound	2007 180 1450-2007 180 1750	2007 180 1800-2007 180 2100
48 inbound	2007 200 0220-2007 200 0510	2007 199 2320-2007 200 0210
48 outbound	2007 203 1150-2007 203 1440	2007 203 1450-2007 203 1740
49 inbound	2007 239 1900-2007 239 2150	2007 239 1550-2007 239 1850
49 outbound	2007 243 0420-2007 243 0710	2007 243 0720-2007 243 1020
50 inbound	2007 271 1810-2007 271 2100	2007 271 1510-2007 271 1800
51 inbound	2007 295 1450-2007 295 1740	2007 295 1140-2007 295 1440
51 outbound	2007 298 2230-2007 299 0130	2007 299 0140-2007 299 0440
52 inbound	2007 319 1440-2007 319 1740	2007 319 1130-2007 319 1430
52 outbound	2007 322 2230-2007 323 0130	2007 323 0140-2007 323 0450
53 outbound	2007 338 2140-2007 339 0050	2007 339 0100-2007 339 0420
119 inbound	2009 285 1130-2009 285 1430	2009 285 0810-2009 285 1120
119 outbound	2009 288 1950-2009 288 2250	2009 288 2300-2009 289 0210
120 inbound	2009 304 1100-2009 304 1400	2009 304 0740-2009 304 1050
120 outbound	2009 307 1920-2009 307 2220	2009 307 2230-2009 308 0140
121 inbound	2009 323 1140-2009 323 1440	2009 323 0810-2009 323 1130
121 outbound	2009 326 1950-2009 326 2300	2009 326 2310-2009 327 0220
122 inbound	2009 342 1230-2009 342 1530	2009 342 0910-2009 342 1220
122 outbound	2009 345 2040-2009 345 2340	2009 345 2350-2009 346 0300
123 inbound	2009 358 1240-2009 358 1550	2009 358 0910-2009 358 1230
123 outbound	2009 361 1950-2009 361 2300	2009 361 2310-2009 362 0230
125 inbound	2010 025 1110-2010 025 1420	2010 025 0740-2010 025 1100
125 outbound	2010 028 1820-2010 028 2120	2010 028 2130-2010 029 0050
126 inbound	2010 042 2330-2010 043 0230	2010 042 2000-2010 042 2320
127 outbound	2010 063 2030-2010 063 2330	2010 063 2340-2010 064 0250
128 inbound	2010 078 0350-2010 078 0650	2010 078 0020-2010 078 0340
128 outbound	2010 081 1140-2010 081 1440	2010 081 1450-2010 081 1810
129 inbound	2010 095 1900-2010 095 2200	2010 095 1540-2010 095 1850
129 outbound	2010 099 0350-2010 099 0650	2010 099 0700-2010 099 1010
130 inbound	2010 116 0340-2010 116 0640	2010 116 0020-2010 116 0330
130 outbound	2010 119 1240-2010 119 1540	2010 119 1550-2010 119 1900
131 inbound	2010 136 1430-2010 136 1740	2010 136 1120-2010 136 1420
131 outbound	2010 139 2330-2010 140 0230	2010 140 0240-2010 140 0550
132 outbound	2010 155 2220-2010 156 0130	2010 156 0140-2010 156 0500
133 inbound	2010 168 1340-2010 168 1650	2010 168 1010-2010 168 1330
133 outbound	2010 171 2120-2010 172 0030	2010 172 0040-2010 172 0400
135 inbound	2010 204 0940-2010 204 1240	2010 204 0620-2010 204 0930
135 outbound	2010 207 1810-2010 207 2110	2010 207 2120-2010 208 0030
136 inbound	2010 224 0730-2010 224 1030	2010 224 0410-2010 224 0720
136 outbound	2010 227 1600-2010 227 1900	2010 227 1910-2010 227 2220
137 inbound	2010 244 0810-2010 244 1110	2010 244 0450-2010 244 0800
137 outbound	2010 247 1640-2010 247 1940	2010 247 1950-2010 247 2300
138 inbound	2010 264 0620-2010 264 0920	2010 264 0300-2010 264 0610
138 outbound	2010 267 1500-2010 267 1800	2010 267 1810-2010 267 2110
139 inbound	2010 287 2350-2010 288 0250	2010 287 2040-2010 287 2340
139 outbound	2010 291 0910-2010 291 1210	2010 291 1220-2010 291 1530
141 inbound	2010 332 1530-2010 332 1830	2010 332 1210-2010 332 1520
141 outbound	2010 336 0030-2010 336 0340	2010 336 0350-2010 336 0650
142 inbound	2010 353 0450-2010 353 0750	2010 353 0130-2010 353 0440
142 outbound	2010 356 1350-2010 356 1650	2010 356 1700-2010 356 2010

Appendix B

Tables of Partial Number Densities

The tables in this appendix contain the partial number densities of H^+ , H_2^+ , He^{++} , He^+ , O^{++} , and W^+ for each of the CHEMS energy per charge (E/Q) steps. The partial number density values are in units of cm^{-3} and the E/Q values are in units of keV/e. The uncertainties are the statistical uncertainties equal to the partial number density divided by the square root of the species counts. Each table represents the data from a different L range. We include a table for the main ring current (L=7-16) and each individual L shell used in this study. To combine the partial number densities over several E/Q steps, we simply add the partial number density in each step. A partial number density of zero means that the partial number density for the species at that E/Q step could not be calculated because of background issues or low detection efficiencies.

2004-2010 L=7-16 Latitude=-10° to 10°

DPPS	E/Q(keV/e)	H ⁺ n	sigma	He ⁺⁺ n	sigma	H ₂ ⁺ n	sigma	He ⁺ n	sigma	O ⁺⁺ n	sigma	W ⁺ n	sigma
0	2.81	3.90E-03	1.68E-05	0.00E+00	0.00E+00	1.34E-03	1.53E-05	0.00E+00	0.00E+00	0.00E+00	0.00E+00	0.00E+00	0.00E+00
1	3.29	3.20E-03	1.17E-05	0.00E+00	0.00E+00	1.03E-03	1.02E-05	0.00E+00	0.00E+00	0.00E+00	0.00E+00	0.00E+00	0.00E+00
2	3.78	2.16E-03	7.07E-06	0.00E+00	0.00E+00	6.88E-04	6.07E-06	0.00E+00	0.00E+00	0.00E+00	0.00E+00	0.00E+00	0.00E+00
3	4.4	1.54E-03	4.55E-06	0.00E+00	0.00E+00	5.36E-04	4.03E-06	0.00E+00	0.00E+00	0.00E+00	0.00E+00	0.00E+00	0.00E+00
4	5.05	1.20E-03	3.23E-06	0.00E+00	0.00E+00	4.26E-04	2.86E-06	0.00E+00	0.00E+00	0.00E+00	0.00E+00	0.00E+00	0.00E+00
5	5.86	9.33E-04	2.34E-06	0.00E+00	0.00E+00	3.33E-04	2.01E-06	0.00E+00	0.00E+00	0.00E+00	0.00E+00	0.00E+00	0.00E+00
6	6.75	7.35E-04	1.72E-06	0.00E+00	0.00E+00	2.55E-04	1.40E-06	0.00E+00	0.00E+00	0.00E+00	0.00E+00	0.00E+00	0.00E+00
7	7.81	5.66E-04	1.26E-06	0.00E+00	0.00E+00	1.88E-04	9.45E-07	0.00E+00	0.00E+00	0.00E+00	0.00E+00	0.00E+00	0.00E+00
8	8.92	4.50E-04	9.78E-07	0.00E+00	0.00E+00	1.46E-04	6.81E-07	0.00E+00	0.00E+00	0.00E+00	0.00E+00	0.00E+00	0.00E+00
9	10.3	3.68E-04	7.71E-07	0.00E+00	0.00E+00	1.15E-04	4.92E-07	0.00E+00	0.00E+00	0.00E+00	0.00E+00	0.00E+00	0.00E+00
10	11.8	2.82E-04	5.74E-07	0.00E+00	0.00E+00	8.83E-05	3.37E-07	0.00E+00	0.00E+00	0.00E+00	0.00E+00	0.00E+00	0.00E+00
11	13.6	2.22E-04	4.46E-07	0.00E+00	0.00E+00	6.79E-05	2.64E-07	0.00E+00	0.00E+00	0.00E+00	0.00E+00	0.00E+00	0.00E+00
12	15.7	1.81E-04	3.54E-07	0.00E+00	0.00E+00	5.07E-05	1.91E-07	0.00E+00	0.00E+00	0.00E+00	0.00E+00	0.00E+00	0.00E+00
13	18.1	1.44E-04	2.80E-07	0.00E+00	0.00E+00	3.73E-05	1.39E-07	0.00E+00	0.00E+00	0.00E+00	0.00E+00	0.00E+00	0.00E+00
14	20.8	1.18E-04	2.27E-07	0.00E+00	0.00E+00	2.76E-05	1.04E-07	0.00E+00	0.00E+00	0.00E+00	0.00E+00	0.00E+00	0.00E+00
15	23.9	9.67E-05	1.84E-07	0.00E+00	0.00E+00	2.18E-05	8.22E-08	0.00E+00	0.00E+00	0.00E+00	0.00E+00	0.00E+00	0.00E+00
16	27.4	8.15E-05	2.79E-07	0.00E+00	0.00E+00	1.75E-05	3.09E-07	0.00E+00	0.00E+00	0.00E+00	0.00E+00	0.00E+00	0.00E+00
17	31.5	7.09E-05	1.79E-07	0.00E+00	0.00E+00	1.49E-05	1.50E-07	0.00E+00	0.00E+00	0.00E+00	0.00E+00	0.00E+00	0.00E+00
18	36.2	6.14E-05	1.34E-07	0.00E+00	0.00E+00	1.25E-05	8.71E-08	0.00E+00	0.00E+00	0.00E+00	0.00E+00	0.00E+00	0.00E+00
19	41.6	5.41E-05	1.13E-07	0.00E+00	0.00E+00	1.05E-05	6.25E-08	0.00E+00	0.00E+00	0.00E+00	0.00E+00	0.00E+00	0.00E+00
20	47.8	4.84E-05	9.96E-08	0.00E+00	0.00E+00	8.69E-06	4.83E-08	0.00E+00	0.00E+00	0.00E+00	0.00E+00	0.00E+00	0.00E+00
21	54.9	4.41E-05	9.02E-08	0.00E+00	0.00E+00	7.50E-06	3.99E-08	0.00E+00	0.00E+00	0.00E+00	0.00E+00	0.00E+00	0.00E+00
22	63.2	3.89E-05	7.97E-08	0.00E+00	0.00E+00	6.41E-06	3.26E-08	0.00E+00	0.00E+00	0.00E+00	0.00E+00	0.00E+00	0.00E+00
23	72.6	3.56E-05	7.26E-08	0.00E+00	0.00E+00	5.42E-06	2.71E-08	0.00E+00	0.00E+00	0.00E+00	0.00E+00	0.00E+00	0.00E+00
24	83.4	3.30E-05	6.68E-08	0.00E+00	0.00E+00	4.68E-06	2.37E-08	0.00E+00	0.00E+00	0.00E+00	0.00E+00	0.00E+00	0.00E+00
25	95.9	3.07E-05	6.24E-08	0.00E+00	0.00E+00	3.93E-06	2.06E-08	0.00E+00	0.00E+00	0.00E+00	0.00E+00	0.00E+00	0.00E+00
26	110.1	2.83E-05	5.78E-08	0.00E+00	0.00E+00	3.28E-06	1.79E-08	0.00E+00	0.00E+00	0.00E+00	0.00E+00	0.00E+00	0.00E+00
27	126.6	2.50E-05	5.33E-08	0.00E+00	0.00E+00	2.67E-06	1.54E-08	0.00E+00	0.00E+00	0.00E+00	0.00E+00	0.00E+00	0.00E+00
28	145.3	2.00E-05	4.66E-08	0.00E+00	0.00E+00	2.05E-06	1.46E-08	0.00E+00	0.00E+00	0.00E+00	0.00E+00	0.00E+00	0.00E+00
29	166.9	1.54E-05	4.09E-08	0.00E+00	0.00E+00	1.51E-06	1.18E-08	0.00E+00	0.00E+00	0.00E+00	0.00E+00	0.00E+00	0.00E+00
30	191.6	1.09E-05	3.38E-08	0.00E+00	0.00E+00	1.01E-06	9.21E-09	0.00E+00	0.00E+00	0.00E+00	0.00E+00	0.00E+00	0.00E+00
31	220.2	7.41E-06	2.76E-08	0.00E+00	0.00E+00	6.50E-07	7.08E-09	0.00E+00	0.00E+00	0.00E+00	0.00E+00	0.00E+00	0.00E+00

2004-2010 L=6-7 Latitude=-10° to 10°

DPPS	E/Q(keV/e)	H ⁺ n	sigma	He ⁺⁺ n	sigma	H ₂ ⁺ n	sigma	He ⁺ n	sigma	O ⁺⁺ n	sigma	W ⁺ n	sigma
0	2.81	1.70E-03	3.51E-05	0.00E+00	0.00E+00	6.64E-04	3.42E-05	0.00E+00	0.00E+00	0.00E+00	0.00E+00	0.00E+00	0.00E+00
1	3.29	1.38E-03	2.40E-05	0.00E+00	0.00E+00	4.31E-04	2.10E-05	0.00E+00	0.00E+00	0.00E+00	0.00E+00	0.00E+00	0.00E+00
2	3.78	8.40E-04	1.37E-05	0.00E+00	0.00E+00	2.90E-04	1.26E-05	0.00E+00	0.00E+00	0.00E+00	0.00E+00	0.00E+00	0.00E+00
3	4.4	6.03E-04	8.79E-06	0.00E+00	0.00E+00	1.93E-04	7.67E-06	0.00E+00	0.00E+00	0.00E+00	0.00E+00	0.00E+00	0.00E+00
4	5.05	4.24E-04	5.89E-06	0.00E+00	0.00E+00	1.49E-04	5.40E-06	0.00E+00	0.00E+00	0.00E+00	0.00E+00	0.00E+00	0.00E+00
5	5.86	3.32E-04	4.25E-06	0.00E+00	0.00E+00	1.10E-04	3.63E-06	0.00E+00	0.00E+00	0.00E+00	0.00E+00	0.00E+00	0.00E+00
6	6.75	2.42E-04	2.98E-06	0.00E+00	0.00E+00	7.66E-05	2.41E-06	0.00E+00	0.00E+00	0.00E+00	0.00E+00	0.00E+00	0.00E+00
7	7.81	1.81E-04	2.14E-06	0.00E+00	0.00E+00	5.13E-05	1.54E-06	0.00E+00	0.00E+00	0.00E+00	0.00E+00	0.00E+00	0.00E+00
8	8.92	1.44E-04	1.65E-06	0.00E+00	0.00E+00	3.79E-05	1.08E-06	0.00E+00	0.00E+00	0.00E+00	0.00E+00	1.53E-03	3.55E-05
9	10.3	1.13E-04	1.28E-06	0.00E+00	0.00E+00	2.80E-05	7.50E-07	0.00E+00	0.00E+00	1.54E-05	9.02E-07	1.10E-03	2.21E-05
10	11.8	8.40E-05	9.31E-07	0.00E+00	0.00E+00	2.12E-05	5.38E-07	0.00E+00	0.00E+00	9.71E-06	6.14E-07	7.75E-04	1.44E-05
11	13.6	6.42E-05	7.10E-07	0.00E+00	0.00E+00	1.48E-05	3.75E-07	0.00E+00	0.00E+00	7.32E-06	4.62E-07	5.86E-04	1.01E-05
12	15.7	5.17E-05	5.66E-07	1.00E-07	5.07E-08	1.03E-05	2.61E-07	0.00E+00	0.00E+00	4.83E-06	3.25E-07	3.66E-04	6.50E-06
13	18.1	3.87E-05	4.39E-07	2.91E-08	2.34E-08	7.00E-06	1.82E-07	0.00E+00	0.00E+00	3.50E-06	2.44E-07	2.42E-04	4.33E-06
14	20.8	3.04E-05	3.45E-07	4.31E-08	1.68E-08	4.64E-06	1.28E-07	0.00E+00	0.00E+00	2.99E-06	1.94E-07	1.70E-04	3.05E-06
15	23.9	2.40E-05	2.77E-07	1.05E-08	1.05E-08	3.51E-06	9.76E-08	0.00E+00	0.00E+00	2.03E-06	1.48E-07	1.26E-04	2.23E-06
16	27.4	1.92E-05	4.14E-07	1.13E-08	5.64E-09	2.52E-06	3.94E-07	2.00E-07	1.15E-07	1.50E-06	1.95E-07	8.99E-05	1.62E-06
17	31.5	1.63E-05	2.62E-07	1.27E-08	5.20E-09	1.84E-06	1.68E-07	1.31E-07	4.66E-08	1.24E-06	1.40E-07	6.90E-05	1.23E-06
18	36.2	1.35E-05	1.87E-07	5.38E-09	3.10E-09	1.46E-06	9.43E-08	1.13E-07	2.75E-08	1.24E-06	1.07E-07	4.85E-05	9.09E-07
19	41.6	1.03E-05	1.43E-07	7.53E-09	3.37E-09	1.05E-06	6.07E-08	1.13E-07	2.07E-08	9.91E-07	7.80E-08	3.57E-05	6.86E-07
20	47.8	8.50E-06	1.19E-07	1.34E-09	1.34E-09	7.56E-07	4.36E-08	7.68E-08	1.51E-08	7.46E-07	5.67E-08	2.37E-05	1.42E-06
21	54.9	7.65E-06	1.06E-07	6.02E-09	2.70E-09	5.27E-07	3.15E-08	9.83E-08	1.56E-08	9.23E-07	6.02E-08	1.79E-05	7.07E-07
22	63.2	7.72E-06	9.95E-08	1.07E-09	1.07E-09	4.60E-07	2.58E-08	7.66E-08	1.26E-08	1.03E-06	5.64E-08	1.46E-05	4.30E-07
23	72.6	8.18E-06	9.78E-08	2.78E-09	1.61E-09	3.45E-07	1.99E-08	5.04E-08	9.34E-09	1.16E-06	5.55E-08	1.25E-05	3.06E-07
24	83.4	8.51E-06	9.67E-08	4.24E-09	1.89E-09	2.46E-07	1.57E-08	4.67E-08	8.40E-09	1.24E-06	5.38E-08	1.07E-05	2.44E-07
25	95.9	1.12E-05	1.05E-07	3.30E-09	1.65E-09	2.56E-07	1.37E-08	7.46E-08	1.02E-08	1.22E-06	5.17E-08	9.69E-06	2.12E-07
26	110.1	1.81E-05	1.30E-07	6.45E-09	2.15E-09	3.69E-07	1.79E-08	7.74E-08	9.70E-09	9.51E-07	4.14E-08	1.19E-05	2.17E-07
27	126.6	2.69E-05	1.60E-07	1.94E-09	1.12E-09	6.27E-07	2.23E-08	8.73E-08	9.69E-09	8.75E-07	4.06E-08	1.50E-05	2.26E-07
28	145.3	3.03E-05	1.65E-07	5.37E-09	1.91E-09	6.34E-07	2.63E-08	1.33E-07	1.21E-08	5.73E-07	2.96E-08	1.53E-05	2.09E-07
29	166.9	2.80E-05	1.56E-07	4.95E-09	1.65E-09	3.96E-07	1.86E-08	1.21E-07	1.03E-08	3.98E-07	2.41E-08	1.23E-05	1.75E-07
30	191.6	2.05E-05	1.33E-07	3.50E-09	1.33E-09	2.70E-07	1.47E-08	1.19E-07	9.60E-09	2.89E-07	2.08E-08	9.04E-06	1.39E-07
31	220.2	1.29E-05	1.06E-07	6.56E-09	1.75E-09	1.41E-07	1.04E-08	5.52E-08	6.31E-09	1.30E-07	1.34E-08	4.36E-06	9.07E-08

2004-2010 L=7-8 Latitude=-10° to 10°

DPPS	E/Q(keV/e)	H ⁺ n	sigma	He ⁺⁺ n	sigma	H ₂ ⁺ n	sigma	He ⁺ n	sigma	O ⁺⁺ n	sigma	W ⁺ n	sigma
0	2.81	3.79E-03	5.41E-05	0.00E+00	0.00E+00	1.22E-03	4.77E-05	0.00E+00	0.00E+00	0.00E+00	0.00E+00	0.00E+00	0.00E+00
1	3.29	3.05E-03	3.72E-05	0.00E+00	0.00E+00	8.55E-04	3.04E-05	0.00E+00	0.00E+00	0.00E+00	0.00E+00	0.00E+00	0.00E+00
2	3.78	1.97E-03	2.19E-05	0.00E+00	0.00E+00	5.62E-04	1.80E-05	0.00E+00	0.00E+00	0.00E+00	0.00E+00	0.00E+00	0.00E+00
3	4.4	1.37E-03	1.38E-05	0.00E+00	0.00E+00	4.41E-04	1.19E-05	0.00E+00	0.00E+00	0.00E+00	0.00E+00	0.00E+00	0.00E+00
4	5.05	1.03E-03	9.55E-06	0.00E+00	0.00E+00	3.33E-04	8.28E-06	0.00E+00	0.00E+00	0.00E+00	0.00E+00	0.00E+00	0.00E+00
5	5.86	7.87E-04	6.85E-06	0.00E+00	0.00E+00	2.51E-04	5.68E-06	0.00E+00	0.00E+00	0.00E+00	0.00E+00	0.00E+00	0.00E+00
6	6.75	6.03E-04	4.96E-06	0.00E+00	0.00E+00	1.85E-04	3.90E-06	0.00E+00	0.00E+00	0.00E+00	0.00E+00	0.00E+00	0.00E+00
7	7.81	4.66E-04	3.65E-06	0.00E+00	0.00E+00	1.32E-04	2.59E-06	0.00E+00	0.00E+00	0.00E+00	0.00E+00	0.00E+00	0.00E+00
8	8.92	3.58E-04	2.73E-06	0.00E+00	0.00E+00	1.03E-04	1.87E-06	0.00E+00	0.00E+00	0.00E+00	1.36E-06	1.74E-03	3.89E-05
9	10.3	2.83E-04	2.12E-06	0.00E+00	0.00E+00	7.89E-05	1.32E-06	0.00E+00	0.00E+00	1.64E-05	9.82E-07	1.29E-03	2.47E-05
10	11.8	2.16E-04	1.57E-06	0.00E+00	0.00E+00	5.77E-05	9.28E-07	0.00E+00	0.00E+00	1.18E-05	7.07E-07	1.01E-03	1.72E-05
11	13.6	1.68E-04	1.22E-06	0.00E+00	0.00E+00	4.37E-05	6.79E-07	0.00E+00	0.00E+00	9.24E-06	5.48E-07	7.79E-04	1.22E-05
12	15.7	1.35E-04	9.64E-07	2.96E-07	1.00E-07	3.12E-05	4.84E-07	0.00E+00	0.00E+00	6.26E-06	3.93E-07	5.54E-04	8.38E-06
13	18.1	1.06E-04	7.60E-07	2.18E-07	4.46E-08	2.29E-05	3.47E-07	0.00E+00	0.00E+00	6.22E-06	3.38E-07	3.97E-04	5.83E-06
14	20.8	8.49E-05	6.05E-07	2.28E-07	4.20E-08	1.62E-05	2.56E-07	0.00E+00	0.00E+00	4.50E-06	2.54E-07	3.11E-04	4.31E-06
15	23.9	6.94E-05	4.87E-07	1.39E-07	2.62E-08	1.25E-05	1.97E-07	0.00E+00	0.00E+00	3.56E-06	2.01E-07	2.42E-04	3.21E-06
16	27.4	5.65E-05	7.32E-07	7.61E-08	1.49E-08	1.03E-05	8.08E-07	6.83E-07	0.00E+00	2.66E-06	2.67E-07	1.85E-04	2.43E-06
17	31.5	4.75E-05	4.42E-07	4.79E-08	1.05E-08	7.04E-06	3.42E-07	5.43E-07	9.87E-08	2.45E-06	1.85E-07	1.41E-04	1.82E-06
18	36.2	4.09E-05	3.27E-07	5.62E-08	1.04E-08	5.75E-06	1.93E-07	5.28E-07	6.09E-08	1.93E-06	1.23E-07	1.11E-04	1.42E-06
19	41.6	3.53E-05	2.78E-07	4.18E-08	8.40E-09	4.58E-06	1.32E-07	4.11E-07	4.09E-08	1.92E-06	1.09E-07	8.70E-05	1.09E-06
20	47.8	3.27E-05	2.45E-07	3.28E-08	7.01E-09	3.71E-06	1.01E-07	3.11E-07	3.18E-08	1.79E-06	9.27E-08	6.57E-05	2.48E-06
21	54.9	2.97E-05	2.18E-07	2.64E-08	5.90E-09	3.00E-06	7.84E-08	3.17E-07	2.90E-08	1.91E-06	8.47E-08	4.93E-05	1.20E-06
22	63.2	2.65E-05	1.93E-07	1.61E-08	4.29E-09	2.61E-06	6.32E-08	2.16E-07	2.18E-08	2.11E-06	8.47E-08	4.10E-05	7.54E-07
23	72.6	2.56E-05	1.83E-07	2.34E-08	4.89E-09	2.12E-06	5.08E-08	2.32E-07	2.09E-08	2.43E-06	8.51E-08	3.19E-05	5.13E-07
24	83.4	2.94E-05	1.91E-07	1.84E-08	4.11E-09	2.05E-06	4.74E-08	2.37E-07	1.97E-08	2.13E-06	7.24E-08	2.84E-05	4.14E-07
25	95.9	3.67E-05	2.06E-07	1.18E-08	3.16E-09	2.02E-06	4.54E-08	2.58E-07	1.96E-08	2.05E-06	6.67E-08	2.98E-05	3.85E-07
26	110.1	4.65E-05	2.26E-07	9.82E-09	2.73E-09	1.76E-06	4.03E-08	3.55E-07	2.12E-08	1.77E-06	6.17E-08	3.40E-05	3.80E-07
27	126.6	5.28E-05	2.37E-07	2.16E-08	3.82E-09	1.81E-06	3.87E-08	3.85E-07	2.07E-08	1.36E-06	4.87E-08	3.71E-05	3.71E-07
28	145.3	4.75E-05	2.21E-07	1.39E-08	2.97E-09	1.67E-06	4.11E-08	3.31E-07	1.83E-08	1.08E-06	4.59E-08	3.30E-05	3.28E-07
29	166.9	3.86E-05	2.04E-07	1.49E-08	2.92E-09	1.33E-06	3.48E-08	2.48E-07	1.50E-08	6.17E-07	3.02E-08	2.31E-05	2.56E-07
30	191.6	2.84E-05	1.73E-07	1.69E-08	2.98E-09	8.12E-07	2.61E-08	1.81E-07	1.21E-08	3.56E-07	2.15E-08	1.31E-05	1.75E-07
31	220.2	2.02E-05	1.43E-07	1.21E-08	2.41E-09	4.46E-07	1.86E-08	8.33E-08	7.80E-09	1.99E-07	1.55E-08	6.46E-06	1.13E-07

2004-2010 L=8-9 Latitude=-10° to 10°

DPPS	E/Q(keV/e)	H ⁺ n	sigma	He ⁺⁺ n	sigma	H ₂ ⁺ n	sigma	He ⁺ n	sigma	O ⁺⁺ n	sigma	W ⁺ n	sigma
0	2.81	5.48E-03	6.54E-05	0.00E+00	0.00E+00	1.76E-03	5.74E-05	0.00E+00	0.00E+00	0.00E+00	0.00E+00	0.00E+00	0.00E+00
1	3.29	4.31E-03	4.47E-05	0.00E+00	0.00E+00	1.27E-03	3.73E-05	0.00E+00	0.00E+00	0.00E+00	0.00E+00	0.00E+00	0.00E+00
2	3.78	2.98E-03	2.73E-05	0.00E+00	0.00E+00	8.49E-04	2.20E-05	0.00E+00	0.00E+00	0.00E+00	0.00E+00	0.00E+00	0.00E+00
3	4.4	2.12E-03	1.78E-05	0.00E+00	0.00E+00	6.86E-04	1.49E-05	0.00E+00	0.00E+00	0.00E+00	0.00E+00	0.00E+00	0.00E+00
4	5.05	1.61E-03	1.24E-05	0.00E+00	0.00E+00	5.06E-04	1.02E-05	0.00E+00	0.00E+00	0.00E+00	0.00E+00	0.00E+00	0.00E+00
5	5.86	1.27E-03	9.19E-06	0.00E+00	0.00E+00	4.10E-04	7.29E-06	0.00E+00	0.00E+00	0.00E+00	0.00E+00	0.00E+00	0.00E+00
6	6.75	9.96E-04	6.82E-06	0.00E+00	0.00E+00	3.10E-04	5.04E-06	0.00E+00	0.00E+00	0.00E+00	0.00E+00	0.00E+00	0.00E+00
7	7.81	7.65E-04	5.04E-06	0.00E+00	0.00E+00	2.24E-04	3.39E-06	0.00E+00	0.00E+00	0.00E+00	0.00E+00	0.00E+00	0.00E+00
8	8.92	6.10E-04	3.92E-06	0.00E+00	0.00E+00	1.72E-04	2.43E-06	0.00E+00	0.00E+00	2.50E-05	1.45E-06	2.19E-03	4.36E-05
9	10.3	4.96E-04	3.10E-06	0.00E+00	0.00E+00	1.35E-04	1.76E-06	0.00E+00	0.00E+00	2.02E-05	1.11E-06	1.71E-03	2.84E-05
10	11.8	3.79E-04	2.31E-06	0.00E+00	0.00E+00	1.02E-04	1.28E-06	0.00E+00	0.00E+00	1.60E-05	8.50E-07	1.35E-03	1.97E-05
11	13.6	2.96E-04	1.82E-06	0.00E+00	0.00E+00	7.91E-05	9.49E-07	0.00E+00	0.00E+00	1.04E-05	6.03E-07	1.10E-03	1.45E-05
12	15.7	2.43E-04	1.47E-06	8.99E-07	1.79E-07	5.78E-05	6.83E-07	0.00E+00	0.00E+00	8.88E-06	4.88E-07	8.11E-04	1.02E-05
13	18.1	1.93E-04	1.17E-06	5.65E-07	7.44E-08	4.24E-05	5.02E-07	0.00E+00	0.00E+00	8.75E-06	4.28E-07	6.26E-04	7.43E-06
14	20.8	1.62E-04	9.71E-07	3.92E-07	4.67E-08	3.15E-05	3.79E-07	0.00E+00	0.00E+00	6.75E-06	3.30E-07	5.04E-04	5.66E-06
15	23.9	1.34E-04	7.91E-07	5.73E-07	6.66E-08	2.49E-05	3.04E-07	0.00E+00	0.00E+00	5.74E-06	2.89E-07	4.06E-04	4.35E-06
16	27.4	1.13E-04	1.17E-06	1.95E-07	2.31E-08	2.17E-05	1.15E-06	1.32E-06	2.91E-07	5.49E-06	4.15E-07	3.35E-04	3.51E-06
17	31.5	9.91E-05	7.85E-07	1.63E-07	1.92E-08	1.74E-05	5.36E-07	1.36E-06	1.57E-07	4.60E-06	2.70E-07	2.69E-04	2.73E-06
18	36.2	8.81E-05	6.02E-07	1.20E-07	1.56E-08	1.51E-05	3.20E-07	1.20E-06	9.40E-08	3.55E-06	1.64E-07	2.20E-04	2.17E-06
19	41.6	7.97E-05	5.08E-07	9.23E-08	1.35E-08	1.29E-05	2.39E-07	1.22E-06	7.58E-08	3.68E-06	1.51E-07	1.82E-04	1.74E-06
20	47.8	7.18E-05	4.38E-07	7.09E-08	1.09E-08	1.06E-05	1.81E-07	1.06E-06	6.24E-08	3.64E-06	1.34E-07	1.40E-04	3.54E-06
21	54.9	6.73E-05	3.96E-07	4.97E-08	8.76E-09	8.93E-06	1.47E-07	9.41E-07	5.40E-08	3.54E-06	1.19E-07	1.14E-04	1.88E-06
22	63.2	6.09E-05	3.48E-07	5.73E-08	8.93E-09	7.54E-06	1.18E-07	9.82E-07	5.12E-08	3.29E-06	1.08E-07	9.73E-05	1.23E-06
23	72.6	5.80E-05	3.18E-07	4.12E-08	7.05E-09	6.04E-06	9.40E-08	8.67E-07	4.39E-08	2.93E-06	9.07E-08	8.03E-05	8.79E-07
24	83.4	5.69E-05	2.97E-07	2.16E-08	4.72E-08	4.95E-06	7.79E-08	7.52E-07	3.72E-08	2.69E-06	8.43E-08	6.88E-05	7.00E-07
25	95.9	5.78E-05	2.93E-07	3.74E-08	5.75E-09	4.08E-06	6.63E-08	6.78E-07	3.24E-08	2.16E-06	6.90E-08	6.21E-05	6.00E-07
26	110.1	5.70E-05	2.85E-07	3.26E-08	5.08E-09	3.68E-06	5.98E-08	6.26E-07	2.90E-08	1.59E-06	5.75E-08	5.65E-05	5.30E-07
27	126.6	5.19E-05	2.69E-07	3.16E-08	4.88E-09	3.37E-06	5.58E-08	4.94E-07	2.48E-08	1.16E-06	4.80E-08	4.84E-05	4.66E-07
28	145.3	4.45E-05	2.43E-07	2.69E-08	4.25E-09	2.78E-06	5.48E-08	3.67E-07	1.99E-08	8.51E-07	3.93E-08	3.93E-05	3.87E-07
29	166.9	3.65E-05	2.22E-07	2.42E-08	3.97E-09	2.24E-06	4.82E-08	2.82E-07	1.70E-08	5.50E-07	2.79E-08	2.82E-05	3.07E-07
30	191.6	2.60E-05	1.81E-07	1.92E-08	3.34E-09	1.47E-06	3.70E-08	1.96E-07	1.32E-08	3.86E-07	2.31E-08	1.67E-05	2.15E-07
31	220.2	1.71E-05	1.44E-07	1.41E-08	2.77E-09	8.81E-07	2.78E-08	1.29E-07	1.03E-08	2.41E-07	1.76E-08	9.65E-06	1.54E-07

2004-2010 L=9-10 Latitude=-10° to 10°

DPPS	E/Q(keV/e)	H ⁺ n	sigma	He ⁺⁺ n	sigma	H ₂ ⁺ n	sigma	He ⁺ n	sigma	O ⁺⁺ n	sigma	W ⁺ n	sigma
0	2.81	5.29E-03	6.46E-05	0.00E+00	0.00E+00	1.71E-03	5.59E-05	0.00E+00	0.00E+00	0.00E+00	0.00E+00	0.00E+00	0.00E+00
1	3.29	4.25E-03	4.47E-05	0.00E+00	0.00E+00	1.38E-03	3.83E-05	0.00E+00	0.00E+00	0.00E+00	0.00E+00	0.00E+00	0.00E+00
2	3.78	2.90E-03	2.75E-05	0.00E+00	0.00E+00	8.61E-04	2.21E-05	0.00E+00	0.00E+00	0.00E+00	0.00E+00	0.00E+00	0.00E+00
3	4.4	2.10E-03	1.80E-05	0.00E+00	0.00E+00	6.65E-04	1.45E-05	0.00E+00	0.00E+00	0.00E+00	0.00E+00	0.00E+00	0.00E+00
4	5.05	1.59E-03	1.28E-05	0.00E+00	0.00E+00	5.49E-04	1.06E-05	0.00E+00	0.00E+00	0.00E+00	0.00E+00	0.00E+00	0.00E+00
5	5.86	1.26E-03	9.43E-06	0.00E+00	0.00E+00	4.34E-04	7.52E-06	0.00E+00	0.00E+00	0.00E+00	0.00E+00	0.00E+00	0.00E+00
6	6.75	9.87E-04	7.03E-06	0.00E+00	0.00E+00	3.22E-04	5.14E-06	0.00E+00	0.00E+00	0.00E+00	0.00E+00	0.00E+00	0.00E+00
7	7.81	7.68E-04	5.24E-06	0.00E+00	0.00E+00	2.35E-04	3.49E-06	0.00E+00	0.00E+00	0.00E+00	0.00E+00	0.00E+00	0.00E+00
8	8.92	6.13E-04	4.09E-06	0.00E+00	0.00E+00	1.77E-04	2.46E-06	0.00E+00	0.00E+00	2.50E-05	1.44E-06	1.99E-03	4.12E-05
9	10.3	5.05E-04	3.30E-06	0.00E+00	0.00E+00	1.42E-04	1.82E-06	0.00E+00	0.00E+00	1.91E-05	1.08E-06	1.55E-03	2.69E-05
10	11.8	3.93E-04	2.48E-06	0.00E+00	0.00E+00	1.09E-04	1.32E-06	0.00E+00	0.00E+00	1.55E-05	8.35E-07	1.26E-03	1.90E-05
11	13.6	3.14E-04	1.96E-06	0.00E+00	0.00E+00	8.40E-05	9.84E-07	0.00E+00	0.00E+00	1.11E-05	6.25E-07	1.04E-03	1.41E-05
12	15.7	2.61E-04	1.58E-06	1.17E-06	1.65E-07	6.45E-05	7.34E-07	0.00E+00	0.00E+00	8.79E-06	4.92E-07	8.11E-04	1.01E-05
13	18.1	2.10E-04	1.28E-06	8.97E-07	8.80E-08	4.87E-05	5.48E-07	0.00E+00	0.00E+00	7.73E-06	4.07E-07	6.37E-04	7.50E-05
14	20.8	1.75E-04	1.04E-06	7.37E-07	6.27E-08	3.64E-05	4.15E-07	0.00E+00	0.00E+00	6.69E-06	3.36E-07	5.16E-04	5.83E-06
15	23.9	1.43E-04	8.28E-07	1.20E-06	1.01E-07	2.91E-05	3.32E-07	0.00E+00	0.00E+00	6.01E-06	3.14E-07	4.30E-04	4.59E-06
16	27.4	1.21E-04	1.20E-06	3.38E-07	2.89E-08	2.28E-05	1.10E-06	1.86E-06	3.13E-07	4.46E-06	3.42E-07	3.44E-04	3.58E-06
17	31.5	1.05E-04	8.05E-07	2.43E-07	2.31E-08	1.97E-05	5.61E-07	1.48E-06	1.63E-07	4.45E-06	2.49E-07	2.90E-04	2.92E-06
18	36.2	9.15E-05	6.16E-07	2.17E-07	2.08E-08	1.70E-05	3.36E-07	1.64E-06	1.08E-07	3.44E-06	1.62E-07	2.34E-04	2.32E-06
19	41.6	8.17E-05	5.34E-07	1.65E-07	1.80E-08	1.52E-05	2.59E-07	1.62E-06	8.82E-08	3.68E-06	1.50E-07	1.95E-04	1.90E-06
20	47.8	7.46E-05	4.79E-07	1.24E-07	1.47E-08	1.21E-05	1.97E-07	1.50E-06	7.56E-08	3.36E-06	1.26E-07	1.60E-04	3.76E-06
21	54.9	7.15E-05	4.50E-07	1.12E-07	1.37E-08	1.05E-05	1.66E-07	1.45E-06	7.03E-08	3.09E-06	1.11E-07	1.34E-04	2.11E-06
22	63.2	6.76E-05	4.05E-07	6.86E-08	1.05E-08	9.20E-06	1.40E-07	1.35E-06	6.38E-08	2.77E-06	9.57E-08	1.21E-04	1.46E-06
23	72.6	6.76E-05	3.80E-07	7.29E-08	1.03E-08	8.25E-06	1.20E-07	1.31E-06	5.90E-08	2.68E-06	9.00E-08	1.08E-04	1.14E-06
24	83.4	6.57E-05	3.56E-07	6.35E-08	9.18E-08	7.74E-06	1.11E-07	1.32E-06	5.60E-08	2.27E-06	7.60E-08	1.00E-04	9.69E-07
25	95.9	6.13E-05	3.29E-07	4.57E-08	7.29E-09	6.52E-06	9.61E-08	1.05E-06	4.62E-08	1.86E-06	6.53E-08	8.58E-05	8.07E-07
26	110.1	5.49E-05	2.98E-07	5.44E-08	7.52E-09	5.77E-06	8.58E-08	7.94E-07	3.74E-08	1.51E-06	5.88E-08	7.02E-05	6.72E-07
27	126.6	4.70E-05	2.70E-07	5.16E-08	6.91E-09	4.80E-06	7.36E-08	6.23E-07	3.09E-08	1.03E-06	4.40E-08	5.23E-05	5.29E-07
28	145.3	3.65E-05	2.29E-07	4.41E-08	5.90E-09	3.58E-06	6.72E-08	4.04E-07	2.27E-08	6.35E-07	3.19E-08	3.81E-05	4.01E-07
29	166.9	2.73E-05	1.90E-07	4.19E-08	5.28E-09	2.58E-06	5.21E-08	3.22E-07	1.84E-08	5.85E-07	3.11E-08	2.61E-05	2.94E-07
30	191.6	1.95E-05	1.55E-07	2.47E-08	3.76E-09	1.86E-06	4.12E-08	2.37E-07	1.46E-08	3.73E-07	2.39E-08	1.74E-05	2.16E-07
31	220.2	1.27E-05	1.23E-07	2.32E-08	3.42E-09	1.13E-06	3.03E-08	1.69E-07	1.14E-08	2.43E-07	1.76E-08	1.01E-05	1.51E-07

2004-2010 L=10-11 Latitude=-10° to 10°

DPPS	E/Q(keV/e)	H ⁺ n	sigma	He ⁺⁺ n	sigma	H ₂ ⁺ n	sigma	He ⁺ n	sigma	O ⁺⁺ n	sigma	W ⁺ n	sigma
0	2.81	4.83E-03	6.01E-05	0.00E+00	0.00E+00	1.54E-03	5.24E-05	0.00E+00	0.00E+00	0.00E+00	0.00E+00	0.00E+00	0.00E+00
1	3.29	3.99E-03	4.22E-05	0.00E+00	0.00E+00	1.23E-03	3.55E-05	0.00E+00	0.00E+00	0.00E+00	0.00E+00	0.00E+00	0.00E+00
2	3.78	2.68E-03	2.55E-05	0.00E+00	0.00E+00	7.96E-04	2.09E-05	0.00E+00	0.00E+00	0.00E+00	0.00E+00	0.00E+00	0.00E+00
3	4.4	1.93E-03	1.67E-05	0.00E+00	0.00E+00	6.49E-04	1.42E-05	0.00E+00	0.00E+00	0.00E+00	0.00E+00	0.00E+00	0.00E+00
4	5.05	1.51E-03	1.20E-05	0.00E+00	0.00E+00	5.14E-04	1.01E-05	0.00E+00	0.00E+00	0.00E+00	0.00E+00	0.00E+00	0.00E+00
5	5.86	1.20E-03	8.89E-06	0.00E+00	0.00E+00	4.02E-04	7.05E-06	0.00E+00	0.00E+00	0.00E+00	0.00E+00	0.00E+00	0.00E+00
6	6.75	9.40E-04	6.61E-06	0.00E+00	0.00E+00	3.08E-04	4.92E-06	0.00E+00	0.00E+00	0.00E+00	0.00E+00	0.00E+00	0.00E+00
7	7.81	7.28E-04	4.93E-06	0.00E+00	0.00E+00	2.32E-04	3.39E-06	0.00E+00	0.00E+00	0.00E+00	0.00E+00	0.00E+00	0.00E+00
8	8.92	5.87E-04	3.86E-06	0.00E+00	0.00E+00	1.80E-04	2.43E-06	0.00E+00	0.00E+00	1.97E-05	1.25E-06	1.75E-03	3.79E-05
9	10.3	4.75E-04	3.05E-06	0.00E+00	0.00E+00	1.44E-04	1.78E-06	0.00E+00	0.00E+00	1.63E-05	9.75E-07	1.44E-03	2.55E-05
10	11.8	3.66E-04	2.29E-06	0.00E+00	0.00E+00	1.10E-04	1.29E-06	0.00E+00	0.00E+00	1.35E-05	7.61E-07	1.10E-03	1.73E-05
11	13.6	2.87E-04	1.81E-06	0.00E+00	0.00E+00	8.40E-05	9.60E-07	0.00E+00	0.00E+00	9.37E-06	5.60E-07	9.47E-04	1.31E-05
12	15.7	2.32E-04	1.42E-06	1.44E-06	2.00E-07	6.28E-05	6.97E-07	0.00E+00	0.00E+00	7.87E-06	4.48E-07	7.51E-04	9.58E-06
13	18.1	1.84E-04	1.12E-06	1.06E-06	8.70E-08	4.56E-05	5.09E-07	0.00E+00	0.00E+00	6.56E-06	3.60E-07	5.63E-04	6.92E-06
14	20.8	1.53E-04	9.05E-07	8.12E-07	6.37E-08	3.53E-05	3.92E-07	0.00E+00	0.00E+00	5.41E-06	2.89E-07	4.58E-04	5.28E-06
15	23.9	1.25E-04	7.23E-07	1.17E-06	9.59E-08	2.82E-05	3.13E-07	0.00E+00	0.00E+00	5.28E-06	2.85E-07	3.69E-04	4.08E-06
16	27.4	1.06E-04	1.06E-06	5.32E-07	3.70E-08	2.44E-05	1.17E-06	2.16E-06	3.40E-07	3.29E-06	3.07E-07	3.04E-04	3.19E-06
17	31.5	9.35E-05	7.06E-07	3.74E-07	2.82E-08	2.01E-05	5.55E-07	1.88E-06	1.76E-07	3.33E-06	2.22E-07	2.54E-04	2.58E-06
18	36.2	8.38E-05	5.44E-07	3.06E-07	2.41E-08	1.70E-05	3.28E-07	1.64E-06	1.06E-07	3.12E-06	1.58E-07	2.17E-04	2.11E-06
19	41.6	7.81E-05	4.82E-07	2.53E-07	2.11E-08	1.55E-05	2.48E-07	1.64E-06	8.35E-08	2.54E-06	1.19E-07	1.85E-04	1.73E-06
20	47.8	7.37E-05	4.32E-07	1.76E-07	1.66E-08	1.34E-05	1.96E-07	1.70E-06	7.62E-08	2.90E-06	1.27E-07	1.64E-04	3.82E-06
21	54.9	7.15E-05	4.02E-07	1.52E-07	1.50E-08	1.26E-05	1.71E-07	1.48E-06	6.67E-08	2.48E-06	1.02E-07	1.30E-04	2.00E-06
22	63.2	6.47E-05	3.60E-07	1.36E-07	1.36E-08	1.11E-05	1.41E-07	1.46E-06	6.16E-08	2.00E-06	8.07E-08	1.16E-04	1.34E-06
23	72.6	6.04E-05	3.32E-07	1.14E-07	1.19E-08	9.98E-06	1.22E-07	1.29E-06	5.44E-08	1.68E-06	6.79E-08	9.79E-05	9.95E-07
24	83.4	5.55E-05	3.01E-07	8.15E-08	9.54E-09	9.13E-06	1.10E-07	1.04E-06	4.58E-08	1.47E-06	6.17E-08	8.50E-05	8.05E-07
25	95.9	4.96E-05	2.72E-07	6.35E-08	8.01E-09	7.90E-06	9.78E-08	8.45E-07	3.85E-08	1.20E-06	5.25E-08	7.13E-05	6.73E-07
26	110.1	4.19E-05	2.38E-07	7.52E-08	6.17E-09	6.45E-06	8.35E-08	7.01E-07	3.24E-08	1.15E-06	5.62E-08	5.77E-05	5.51E-07
27	126.6	3.38E-05	2.12E-07	5.30E-08	6.47E-09	4.85E-06	6.85E-08	5.98E-07	2.79E-08	7.16E-07	3.62E-08	4.40E-05	4.43E-07
28	145.3	2.54E-05	1.79E-07	4.56E-08	5.65E-09	3.50E-06	6.28E-08	4.61E-07	2.28E-08	4.74E-07	2.86E-08	3.18E-05	3.45E-07
29	166.9	1.78E-05	1.49E-07	3.45E-08	4.58E-09	2.17E-06	4.56E-08	3.25E-07	1.76E-08	3.00E-07	2.05E-08	1.95E-05	2.48E-07
30	191.6	1.20E-05	1.20E-07	2.40E-08	3.62E-09	1.36E-06	3.44E-08	1.98E-07	1.29E-08	2.11E-07	1.69E-08	1.21E-05	1.77E-07
31	220.2	7.94E-06	9.78E-08	1.31E-08	2.57E-09	9.57E-07	2.79E-08	1.47E-07	1.06E-08	1.65E-07	1.44E-08	8.14E-06	1.36E-07

2004-2010 L=11-12 Latitude=-10° to 10°

DPPS	E/Q(keV/e)	H ⁺ n	sigma	He ⁺⁺ n	sigma	H ₂ ⁺ n	sigma	He ⁺ n	sigma	O ⁺⁺ n	sigma	W ⁺ n	sigma
0	2.81	4.51E-03	5.64E-05	0.00E+00	0.00E+00	1.59E-03	5.20E-05	0.00E+00	0.00E+00	0.00E+00	0.00E+00	0.00E+00	0.00E+00
1	3.29	3.78E-03	3.96E-05	0.00E+00	0.00E+00	1.26E-03	3.55E-05	0.00E+00	0.00E+00	0.00E+00	0.00E+00	0.00E+00	0.00E+00
2	3.78	2.58E-03	2.40E-05	0.00E+00	0.00E+00	8.60E-04	2.12E-05	0.00E+00	0.00E+00	0.00E+00	0.00E+00	0.00E+00	0.00E+00
3	4.4	1.84E-03	1.55E-05	0.00E+00	0.00E+00	6.63E-04	1.39E-05	0.00E+00	0.00E+00	0.00E+00	0.00E+00	0.00E+00	0.00E+00
4	5.05	1.43E-03	1.10E-05	0.00E+00	0.00E+00	5.35E-04	1.00E-05	0.00E+00	0.00E+00	0.00E+00	0.00E+00	0.00E+00	0.00E+00
5	5.86	1.12E-03	8.08E-06	0.00E+00	0.00E+00	4.10E-04	6.92E-06	0.00E+00	0.00E+00	0.00E+00	0.00E+00	0.00E+00	0.00E+00
6	6.75	8.96E-04	6.07E-06	0.00E+00	0.00E+00	3.20E-04	4.89E-06	0.00E+00	0.00E+00	0.00E+00	0.00E+00	0.00E+00	0.00E+00
7	7.81	6.82E-04	4.44E-06	0.00E+00	0.00E+00	2.40E-04	3.33E-06	0.00E+00	0.00E+00	0.00E+00	0.00E+00	0.00E+00	0.00E+00
8	8.92	5.48E-04	3.47E-06	0.00E+00	0.00E+00	1.89E-04	2.41E-06	0.00E+00	0.00E+00	1.87E-05	1.19E-06	1.81E-03	3.75E-05
9	10.3	4.49E-04	2.74E-06	0.00E+00	0.00E+00	1.52E-04	1.77E-06	0.00E+00	0.00E+00	1.43E-05	8.84E-07	1.43E-03	2.48E-05
10	11.8	3.43E-04	2.07E-06	0.00E+00	0.00E+00	1.18E-04	1.30E-06	0.00E+00	0.00E+00	1.11E-05	6.72E-07	1.19E-03	1.76E-05
11	13.6	2.72E-04	1.61E-06	0.00E+00	0.00E+00	9.11E-05	9.62E-07	0.00E+00	0.00E+00	8.77E-06	5.22E-07	9.66E-04	1.28E-05
12	15.7	2.23E-04	1.28E-06	1.50E-06	1.67E-07	6.86E-05	7.04E-07	0.00E+00	0.00E+00	6.67E-06	3.99E-07	7.44E-04	9.18E-06
13	18.1	1.77E-04	1.01E-06	1.22E-06	9.14E-08	5.09E-05	5.21E-07	0.00E+00	0.00E+00	6.18E-06	3.39E-07	5.71E-04	6.63E-06
14	20.8	1.47E-04	8.23E-07	1.00E-06	7.01E-08	3.82E-05	3.92E-07	0.00E+00	0.00E+00	4.82E-06	2.62E-07	4.63E-04	5.05E-06
15	23.9	1.23E-04	6.67E-07	1.54E-06	1.01E-07	3.07E-05	3.13E-07	0.00E+00	0.00E+00	4.39E-06	2.55E-07	3.76E-04	3.87E-06
16	27.4	1.03E-04	9.65E-07	5.29E-07	3.56E-08	2.48E-05	1.14E-06	1.65E-06	2.87E-07	2.48E-06	2.49E-07	3.03E-04	3.00E-06
17	31.5	9.01E-05	6.37E-07	3.90E-07	2.82E-08	2.21E-05	5.71E-07	1.73E-06	1.68E-07	2.88E-06	2.06E-07	2.50E-04	2.39E-06
18	36.2	7.87E-05	4.79E-07	3.35E-07	2.43E-08	1.80E-05	3.27E-07	1.81E-06	1.08E-07	2.25E-06	1.30E-07	2.05E-04	1.90E-06
19	41.6	6.99E-05	4.07E-07	2.04E-07	1.80E-08	1.45E-05	2.29E-07	1.61E-06	7.89E-08	2.13E-06	1.13E-07	1.65E-04	1.50E-06
20	47.8	5.97E-05	3.49E-07	1.43E-07	1.45E-08	1.20E-05	1.80E-07	1.52E-06	6.96E-08	1.78E-06	9.43E-08	1.29E-04	3.25E-06
21	54.9	5.18E-05	3.01E-07	1.07E-07	1.21E-08	1.00E-05	1.45E-07	1.20E-06	5.72E-08	1.61E-06	8.22E-08	9.87E-05	1.65E-06
22	63.2	4.40E-05	2.59E-07	8.75E-08	1.05E-08	8.30E-06	1.18E-07	1.06E-06	5.02E-08	1.18E-06	6.07E-08	7.89E-05	1.02E-06
23	72.6	3.87E-05	2.29E-07	6.28E-08	8.35E-09	6.86E-06	9.54E-08	8.73E-07	4.21E-08	1.02E-06	5.40E-08	6.30E-05	7.12E-07
24	83.4	3.37E-05	2.03E-07	7.74E-08	8.72E-09	5.73E-06	8.25E-08	7.16E-07	3.56E-08	9.62E-07	4.94E-08	5.15E-05	5.66E-07
25	95.9	2.94E-05	1.81E-07	5.28E-08	6.69E-09	4.85E-06	7.07E-08	5.66E-07	2.89E-08	6.49E-07	3.80E-08	4.39E-05	4.73E-07
26	110.1	2.48E-05	1.60E-07	4.91E-08	6.10E-09	4.04E-06	6.10E-08	4.73E-07	2.46E-08	5.33E-07	3.28E-08	3.64E-05	3.95E-07
27	126.6	1.92E-05	1.37E-07	5.00E-08	5.77E-09	3.17E-06	5.09E-08	4.09E-07	2.12E-08	4.31E-07	2.82E-08	2.78E-05	3.17E-07
28	145.3	1.36E-05	1.14E-07	3.83E-08	4.83E-09	2.40E-06	4.84E-08	2.83E-07	1.66E-08	2.94E-07	2.42E-08	2.03E-05	2.51E-07
29	166.9	1.01E-05	9.85E-08	3.05E-08	4.15E-09	1.84E-06	4.06E-08	2.44E-07	1.48E-08	2.15E-07	1.76E-08	1.45E-05	1.98E-07
30	191.6	7.00E-06	8.10E-08	1.91E-08	3.10E-09	1.26E-06	3.18E-08	1.68E-07	1.14E-08	1.53E-07	1.46E-08	1.00E-05	1.51E-07
31	220.2	4.60E-06	6.52E-08	2.37E-08	3.26E-09	7.44E-07	2.32E-08	1.10E-07	8.65E-09	7.69E-08	9.28E-09	6.75E-06	1.14E-07

2004-2010 L=12-13 Latitude=-10° to 10°

DPPS	E/Q(keV/e)	H ⁺ n	sigma	He ⁺⁺ n	sigma	H ₂ ⁺ n	sigma	He ⁺ n	sigma	O ⁺⁺ n	sigma	W ⁺ n	sigma
0	2.81	3.79E-03	5.08E-05	0.00E+00	0.00E+00	1.41E-03	4.81E-05	0.00E+00	0.00E+00	0.00E+00	0.00E+00	0.00E+00	0.00E+00
1	3.29	3.13E-03	3.53E-05	0.00E+00	0.00E+00	1.05E-03	3.15E-05	0.00E+00	0.00E+00	0.00E+00	0.00E+00	0.00E+00	0.00E+00
2	3.78	2.13E-03	2.14E-05	0.00E+00	0.00E+00	7.31E-04	1.92E-05	0.00E+00	0.00E+00	0.00E+00	0.00E+00	0.00E+00	0.00E+00
3	4.4	1.52E-03	1.37E-05	0.00E+00	0.00E+00	5.43E-04	1.24E-05	0.00E+00	0.00E+00	0.00E+00	0.00E+00	0.00E+00	0.00E+00
4	5.05	1.20E-03	9.74E-06	0.00E+00	0.00E+00	4.59E-04	9.12E-06	0.00E+00	0.00E+00	0.00E+00	0.00E+00	0.00E+00	0.00E+00
5	5.86	9.32E-04	7.00E-06	0.00E+00	0.00E+00	3.50E-04	6.30E-06	0.00E+00	0.00E+00	0.00E+00	0.00E+00	0.00E+00	0.00E+00
6	6.75	7.31E-04	5.16E-06	0.00E+00	0.00E+00	2.73E-04	4.45E-06	0.00E+00	0.00E+00	0.00E+00	0.00E+00	0.00E+00	0.00E+00
7	7.81	5.69E-04	3.77E-06	0.00E+00	0.00E+00	2.00E-04	2.98E-06	0.00E+00	0.00E+00	0.00E+00	0.00E+00	0.00E+00	0.00E+00
8	8.92	4.47E-04	2.89E-06	0.00E+00	0.00E+00	1.58E-04	2.17E-06	0.00E+00	0.00E+00	1.60E-05	1.08E-06	1.58E-03	3.53E-05
9	10.3	3.73E-04	2.28E-06	0.00E+00	0.00E+00	1.21E-04	1.54E-06	0.00E+00	0.00E+00	1.23E-05	7.93E-07	1.26E-03	2.31E-05
10	11.8	2.88E-04	1.71E-06	0.00E+00	0.00E+00	9.47E-05	1.13E-06	0.00E+00	0.00E+00	9.09E-06	5.86E-07	1.02E-03	1.65E-05
11	13.6	2.25E-04	1.31E-06	0.00E+00	0.00E+00	7.24E-05	8.27E-07	0.00E+00	0.00E+00	7.14E-06	4.58E-07	8.48E-04	1.21E-05
12	15.7	1.81E-04	1.04E-06	1.64E-06	1.78E-07	5.39E-05	5.99E-07	0.00E+00	0.00E+00	5.11E-06	3.35E-07	6.31E-04	8.51E-06
13	18.1	1.43E-04	8.12E-07	1.03E-06	8.73E-08	3.95E-05	4.34E-07	0.00E+00	0.00E+00	4.14E-06	2.62E-07	4.78E-04	6.09E-06
14	20.8	1.17E-04	6.60E-07	8.04E-07	6.03E-08	2.97E-05	3.27E-07	0.00E+00	0.00E+00	4.36E-06	2.37E-07	3.79E-04	4.54E-06
15	23.9	9.46E-05	5.28E-07	1.10E-06	8.58E-08	2.36E-05	2.56E-07	0.00E+00	0.00E+00	3.10E-06	1.96E-07	2.96E-04	3.37E-06
16	27.4	8.09E-05	8.23E-07	3.91E-07	2.97E-08	1.86E-05	9.64E-07	1.29E-06	2.43E-07	2.36E-06	2.47E-07	2.42E-04	2.65E-06
17	31.5	7.15E-05	5.23E-07	3.61E-07	2.64E-08	1.59E-05	4.72E-07	1.52E-06	1.53E-07	1.96E-06	1.50E-07	1.93E-04	2.05E-06
18	36.2	6.16E-05	3.88E-07	2.84E-07	2.19E-08	1.41E-05	2.83E-07	1.21E-06	8.63E-08	1.99E-06	1.42E-07	1.58E-04	1.61E-06
19	41.6	5.26E-05	3.20E-07	2.27E-07	1.84E-08	1.14E-05	1.96E-07	1.11E-06	6.34E-08	1.40E-06	9.18E-08	1.25E-04	1.25E-06
20	47.8	4.68E-05	2.81E-07	1.51E-07	1.41E-08	9.35E-06	1.51E-07	1.09E-06	5.63E-08	1.17E-06	7.35E-08	9.22E-05	2.68E-06
21	54.9	4.11E-05	2.49E-07	1.31E-07	1.27E-08	8.13E-06	1.25E-07	9.41E-07	4.82E-08	9.48E-07	5.94E-08	7.42E-05	1.40E-06
22	63.2	3.60E-05	2.20E-07	1.01E-07	1.06E-08	7.26E-06	1.04E-07	7.59E-07	4.01E-08	8.77E-07	5.63E-08	6.37E-05	8.79E-07
23	72.6	3.10E-05	1.92E-07	8.82E-08	9.40E-09	5.90E-06	8.44E-08	6.60E-07	3.49E-08	7.44E-07	4.79E-08	5.25E-05	6.25E-07
24	83.4	2.58E-05	1.66E-07	6.71E-08	7.79E-09	4.87E-06	7.27E-08	6.08E-07	3.15E-08	6.28E-07	4.08E-08	4.15E-05	4.85E-07
25	95.9	2.08E-05	1.43E-07	4.90E-08	6.30E-09	3.93E-06	6.19E-08	4.90E-07	2.64E-08	5.12E-07	3.56E-08	3.33E-05	3.94E-07
26	110.1	1.68E-05	1.24E-07	3.33E-08	4.97E-09	3.14E-06	5.32E-08	3.86E-07	2.20E-08	4.27E-07	2.98E-08	2.62E-05	3.21E-07
27	126.6	1.35E-05	1.07E-07	3.23E-08	4.67E-09	2.56E-06	4.61E-08	3.04E-07	1.84E-08	3.16E-07	2.49E-08	2.02E-05	2.58E-07
28	145.3	1.04E-05	9.14E-08	2.70E-08	4.12E-09	2.07E-06	4.56E-08	2.62E-07	1.63E-08	2.42E-07	1.96E-08	1.49E-05	2.05E-07
29	166.9	7.74E-06	7.85E-08	2.28E-08	3.60E-09	1.63E-06	3.82E-08	1.85E-07	1.28E-08	1.45E-07	1.36E-08	1.10E-05	1.63E-07
30	191.6	5.13E-06	6.39E-08	1.99E-08	3.19E-09	1.05E-06	2.92E-08	1.37E-07	1.04E-08	1.31E-07	1.34E-08	7.77E-06	1.28E-07
31	220.2	3.63E-06	5.49E-08	1.03E-08	2.21E-09	7.28E-07	2.35E-08	8.60E-08	7.82E-09	7.62E-08	9.36E-09	5.53E-06	1.02E-07

2004-2010 L=13-14 Latitude=-10° to 10°

DPPS	E/Q(keV/e)	H ⁺ n	sigma	He ⁺⁺ n	sigma	H ₂ ⁺ n	sigma	He ⁺ n	sigma	O ⁺⁺ n	sigma	W ⁺ n	sigma
0	2.81	3.19E-03	4.53E-05	0.00E+00	0.00E+00	1.11E-03	4.16E-05	0.00E+00	0.00E+00	0.00E+00	0.00E+00	0.00E+00	0.00E+00
1	3.29	2.70E-03	3.19E-05	0.00E+00	0.00E+00	9.21E-04	2.88E-05	0.00E+00	0.00E+00	0.00E+00	0.00E+00	0.00E+00	0.00E+00
2	3.78	1.77E-03	1.88E-05	0.00E+00	0.00E+00	6.12E-04	1.71E-05	0.00E+00	0.00E+00	0.00E+00	0.00E+00	0.00E+00	0.00E+00
3	4.4	1.28E-03	1.21E-05	0.00E+00	0.00E+00	4.73E-04	1.13E-05	0.00E+00	0.00E+00	0.00E+00	0.00E+00	0.00E+00	0.00E+00
4	5.05	1.00E-03	8.59E-06	0.00E+00	0.00E+00	3.81E-04	8.07E-06	0.00E+00	0.00E+00	0.00E+00	0.00E+00	0.00E+00	0.00E+00
5	5.86	7.96E-04	6.22E-06	0.00E+00	0.00E+00	2.98E-04	5.63E-06	0.00E+00	0.00E+00	0.00E+00	0.00E+00	0.00E+00	0.00E+00
6	6.75	6.25E-04	4.54E-06	0.00E+00	0.00E+00	2.28E-04	3.93E-06	0.00E+00	0.00E+00	0.00E+00	0.00E+00	0.00E+00	0.00E+00
7	7.81	4.72E-04	3.26E-06	0.00E+00	0.00E+00	1.66E-04	2.62E-06	0.00E+00	0.00E+00	0.00E+00	0.00E+00	0.00E+00	0.00E+00
8	8.92	3.73E-04	2.47E-06	0.00E+00	0.00E+00	1.31E-04	1.90E-06	0.00E+00	0.00E+00	1.39E-05	9.60E-07	1.34E-03	3.13E-05
9	10.3	3.08E-04	1.95E-06	0.00E+00	0.00E+00	1.03E-04	1.36E-06	0.00E+00	0.00E+00	9.75E-06	6.80E-07	1.09E-03	2.08E-05
10	11.8	2.33E-04	1.42E-06	0.00E+00	0.00E+00	7.89E-05	9.84E-07	0.00E+00	0.00E+00	7.81E-06	5.20E-07	8.72E-04	1.45E-05
11	13.6	1.79E-04	1.08E-06	0.00E+00	0.00E+00	5.91E-05	7.09E-07	0.00E+00	0.00E+00	5.52E-06	3.80E-07	6.48E-04	1.01E-05
12	15.7	1.44E-04	8.50E-07	1.79E-06	2.07E-07	4.43E-05	5.11E-07	0.00E+00	0.00E+00	3.88E-06	2.75E-07	5.13E-04	7.30E-06
13	18.1	1.14E-04	6.66E-07	1.02E-06	8.22E-08	3.18E-05	3.66E-07	0.00E+00	0.00E+00	3.23E-06	2.17E-07	3.79E-04	5.21E-06
14	20.8	9.22E-05	5.33E-07	8.04E-07	5.65E-08	2.31E-05	2.71E-07	0.00E+00	0.00E+00	2.32E-06	1.61E-07	2.93E-04	3.82E-06
15	23.9	7.51E-05	4.33E-07	9.40E-07	6.99E-08	1.76E-05	2.08E-07	0.00E+00	0.00E+00	2.18E-06	1.57E-07	2.37E-04	2.90E-06
16	27.4	6.42E-05	6.94E-07	4.44E-07	3.11E-08	1.24E-05	7.67E-07	1.09E-06	2.20E-07	1.69E-06	2.12E-07	1.89E-04	2.25E-06
17	31.5	5.31E-05	4.19E-07	3.20E-07	2.43E-08	1.14E-05	3.93E-07	1.26E-06	1.36E-07	1.31E-06	1.27E-07	1.46E-04	1.72E-06
18	36.2	4.50E-05	3.06E-07	2.29E-07	1.89E-08	9.56E-06	2.24E-07	9.59E-07	7.39E-08	1.14E-06	9.45E-08	1.18E-04	1.35E-06
19	41.6	3.87E-05	2.52E-07	1.75E-07	1.55E-08	7.71E-06	1.54E-07	9.95E-07	5.72E-08	9.76E-07	7.36E-08	9.33E-05	1.04E-06
20	47.8	3.41E-05	2.21E-07	1.21E-07	1.21E-08	6.23E-06	1.17E-07	8.89E-07	4.84E-08	1.03E-06	7.40E-08	7.15E-05	2.32E-06
21	54.9	2.95E-05	1.96E-07	1.01E-07	1.05E-08	5.22E-06	9.39E-08	7.74E-07	4.11E-08	6.97E-07	5.25E-08	5.43E-05	1.16E-06
22	63.2	2.51E-05	1.70E-07	7.13E-08	8.35E-09	4.44E-06	7.63E-08	6.51E-07	3.48E-08	6.62E-07	4.85E-08	4.52E-05	7.17E-07
23	72.6	2.14E-05	1.49E-07	6.04E-08	7.24E-09	3.73E-06	6.24E-08	5.68E-07	3.00E-08	4.47E-07	3.25E-08	3.61E-05	4.99E-07
24	83.4	1.81E-05	1.32E-07	5.73E-08	6.71E-09	3.20E-06	5.52E-08	4.58E-07	2.54E-08	3.91E-07	3.10E-08	2.97E-05	3.91E-07
25	95.9	1.53E-05	1.17E-07	4.62E-08	5.64E-09	2.65E-06	4.69E-08	3.85E-07	2.15E-08	3.25E-07	2.58E-08	2.43E-05	3.22E-07
26	110.1	1.26E-05	1.03E-07	4.50E-08	5.34E-09	2.24E-06	4.15E-08	2.99E-07	1.79E-08	2.65E-07	2.23E-08	1.98E-05	2.65E-07
27	126.6	9.58E-06	8.69E-08	2.77E-08	4.00E-09	1.83E-06	3.61E-08	2.07E-07	1.41E-08	2.13E-07	1.86E-08	1.53E-05	2.15E-07
28	145.3	6.79E-06	7.08E-08	2.32E-08	3.49E-09	1.42E-06	3.45E-08	1.86E-07	1.25E-08	1.80E-07	1.66E-08	1.19E-05	1.75E-07
29	166.9	5.13E-06	6.05E-08	1.94E-08	3.07E-09	1.10E-06	2.90E-08	1.37E-07	1.03E-08	1.34E-07	1.33E-08	8.50E-06	1.38E-07
30	191.6	3.80E-06	5.24E-08	1.60E-08	2.67E-09	7.96E-07	2.38E-08	1.08E-07	8.61E-09	8.97E-08	1.04E-08	6.04E-06	1.08E-07
31	220.2	2.73E-06	4.56E-08	9.57E-09	2.00E-09	6.03E-07	2.01E-08	6.19E-08	6.25E-09	6.36E-08	8.51E-09	4.32E-06	8.58E-08

2004-2010 L=14-15 Latitude=-10° to 10°

DPPS	E/Q(keV/e)	H ⁺ n	sigma	He ⁺⁺ n	sigma	H ₂ ⁺ n	sigma	He ⁺ n	sigma	O ⁺⁺ n	sigma	W ⁺ n	sigma
0	2.81	2.71E-03	4.12E-05	0.00E+00	0.00E+00	1.02E-03	3.95E-05	0.00E+00	0.00E+00	0.00E+00	0.00E+00	0.00E+00	0.00E+00
1	3.29	2.26E-03	2.85E-05	0.00E+00	0.00E+00	7.53E-04	2.56E-05	0.00E+00	0.00E+00	0.00E+00	0.00E+00	0.00E+00	0.00E+00
2	3.78	1.52E-03	1.71E-05	0.00E+00	0.00E+00	5.30E-04	1.57E-05	0.00E+00	0.00E+00	0.00E+00	0.00E+00	0.00E+00	0.00E+00
3	4.4	1.07E-03	1.08E-05	0.00E+00	0.00E+00	4.21E-04	1.05E-05	0.00E+00	0.00E+00	0.00E+00	0.00E+00	0.00E+00	0.00E+00
4	5.05	8.53E-04	7.71E-06	0.00E+00	0.00E+00	3.22E-04	7.33E-06	0.00E+00	0.00E+00	0.00E+00	0.00E+00	0.00E+00	0.00E+00
5	5.86	6.60E-04	5.46E-06	0.00E+00	0.00E+00	2.69E-04	5.28E-06	0.00E+00	0.00E+00	0.00E+00	0.00E+00	0.00E+00	0.00E+00
6	6.75	5.35E-04	4.06E-06	0.00E+00	0.00E+00	2.03E-04	3.64E-06	0.00E+00	0.00E+00	0.00E+00	0.00E+00	0.00E+00	0.00E+00
7	7.81	4.06E-04	2.90E-06	0.00E+00	0.00E+00	1.52E-04	2.46E-06	0.00E+00	0.00E+00	0.00E+00	0.00E+00	0.00E+00	0.00E+00
8	8.92	3.27E-04	2.23E-06	0.00E+00	0.00E+00	1.20E-04	1.80E-06	0.00E+00	0.00E+00	1.26E-05	9.07E-07	1.20E-03	2.92E-05
9	10.3	2.69E-04	1.73E-06	0.00E+00	0.00E+00	9.69E-05	1.30E-06	0.00E+00	0.00E+00	9.24E-06	6.51E-07	9.07E-04	1.88E-05
10	11.8	2.08E-04	1.29E-06	0.00E+00	0.00E+00	7.41E-05	9.36E-07	0.00E+00	0.00E+00	6.76E-06	4.74E-07	7.47E-04	1.35E-05
11	13.6	1.62E-04	9.85E-07	0.00E+00	0.00E+00	5.76E-05	6.88E-07	0.00E+00	0.00E+00	4.53E-06	3.40E-07	5.87E-04	9.66E-06
12	15.7	1.30E-04	7.75E-07	1.50E-06	1.71E-07	4.27E-05	4.95E-07	0.00E+00	0.00E+00	3.56E-06	2.59E-07	4.64E-04	7.10E-06
13	18.1	1.03E-04	6.04E-07	1.17E-06	9.02E-08	3.10E-05	3.56E-07	0.00E+00	0.00E+00	2.92E-06	2.04E-07	3.44E-04	4.95E-06
14	20.8	8.38E-05	4.91E-07	7.79E-07	5.59E-08	2.31E-05	2.66E-07	0.00E+00	0.00E+00	2.39E-06	1.62E-07	2.87E-04	3.82E-06
15	23.9	6.77E-05	3.97E-07	9.70E-07	6.85E-08	1.80E-05	2.06E-07	0.00E+00	0.00E+00	1.55E-06	1.25E-07	2.26E-04	2.84E-06
16	27.4	5.57E-05	6.36E-07	4.47E-07	3.06E-08	1.33E-05	7.76E-07	9.31E-07	2.05E-07	1.19E-06	1.64E-07	1.77E-04	2.17E-06
17	31.5	4.87E-05	3.88E-07	3.27E-07	2.43E-08	1.16E-05	3.90E-07	1.26E-06	1.35E-07	1.11E-06	1.27E-07	1.43E-04	1.68E-06
18	36.2	4.04E-05	2.77E-07	3.13E-07	2.18E-08	9.97E-06	2.25E-07	9.02E-07	7.05E-08	7.75E-07	7.41E-08	1.13E-04	1.30E-06
19	41.6	3.43E-05	2.26E-07	2.14E-07	1.69E-08	8.22E-06	1.57E-07	8.15E-07	5.13E-08	7.36E-07	6.08E-08	8.65E-05	9.96E-07
20	47.8	2.89E-05	1.93E-07	1.30E-07	1.23E-08	6.27E-06	1.16E-07	7.73E-07	4.44E-08	5.49E-07	4.64E-08	6.75E-05	2.20E-06
21	54.9	2.42E-05	1.68E-07	9.69E-08	1.00E-08	5.27E-06	9.23E-08	5.84E-07	3.49E-08	4.66E-07	4.19E-08	5.15E-05	1.12E-06
22	63.2	1.99E-05	1.43E-07	9.48E-08	9.34E-09	4.21E-06	7.17E-08	5.10E-07	2.99E-08	4.51E-07	3.83E-08	4.20E-05	6.84E-07
23	72.6	1.59E-05	1.22E-07	6.43E-08	7.24E-09	3.44E-06	5.80E-08	3.79E-07	2.38E-08	2.96E-07	2.66E-08	3.30E-05	4.70E-07
24	83.4	1.30E-05	1.06E-07	4.39E-08	5.68E-09	2.67E-06	4.83E-08	3.15E-07	2.03E-08	3.33E-07	2.95E-08	2.57E-05	3.60E-07
25	95.9	1.02E-05	9.05E-08	4.17E-08	5.25E-09	2.10E-06	4.09E-08	2.68E-07	1.75E-08	2.67E-07	2.54E-08	2.01E-05	2.90E-07
26	110.1	7.71E-06	7.67E-08	2.62E-08	3.95E-09	1.49E-06	3.28E-08	1.97E-07	1.41E-08	1.54E-07	1.64E-08	1.50E-05	2.29E-07
27	126.6	5.60E-06	6.36E-08	2.81E-08	3.94E-09	1.01E-06	2.61E-08	1.44E-07	1.15E-08	9.98E-08	1.27E-08	1.08E-05	1.77E-07
28	145.3	4.06E-06	5.36E-08	1.79E-08	2.99E-09	7.31E-07	2.42E-08	1.32E-07	1.02E-08	9.36E-08	1.15E-08	7.62E-06	1.39E-07
29	166.9	3.09E-06	4.64E-08	2.02E-08	3.05E-09	5.37E-07	1.97E-08	9.12E-08	8.12E-09	8.48E-08	1.01E-08	5.19E-06	1.05E-07
30	191.6	2.00E-06	3.76E-08	1.11E-08	2.18E-09	3.78E-07	1.60E-08	6.26E-08	6.43E-09	3.57E-08	6.43E-09	3.93E-06	8.59E-08
31	220.2	1.36E-06	3.16E-08	7.93E-09	1.77E-09	2.59E-07	1.28E-08	4.44E-08	5.17E-09	3.73E-08	6.15E-09	2.85E-06	6.92E-08

2004-2010 L=15-16 Latitude=-10° to 10°

DPPS	E/Q(keV/e)	H ⁺ n	sigma	He ⁺⁺ n	sigma	H ₂ ⁺ n	sigma	He ⁺ n	sigma	O ⁺⁺ n	sigma	W ⁺ n	sigma
0	2.81	2.23E-03	3.64E-05	0.00E+00	0.00E+00	8.83E-04	3.59E-05	0.00E+00	0.00E+00	0.00E+00	0.00E+00	0.00E+00	0.00E+00
1	3.29	1.83E-03	2.51E-05	0.00E+00	0.00E+00	6.87E-04	2.41E-05	0.00E+00	0.00E+00	0.00E+00	0.00E+00	0.00E+00	0.00E+00
2	3.78	1.24E-03	1.50E-05	0.00E+00	0.00E+00	4.66E-04	1.44E-05	0.00E+00	0.00E+00	0.00E+00	0.00E+00	0.00E+00	0.00E+00
3	4.4	8.71E-04	9.49E-06	0.00E+00	0.00E+00	3.51E-04	9.40E-06	0.00E+00	0.00E+00	0.00E+00	0.00E+00	0.00E+00	0.00E+00
4	5.05	6.87E-04	6.68E-06	0.00E+00	0.00E+00	2.83E-04	6.74E-06	0.00E+00	0.00E+00	0.00E+00	0.00E+00	0.00E+00	0.00E+00
5	5.86	5.25E-04	4.71E-06	0.00E+00	0.00E+00	2.12E-04	4.57E-06	0.00E+00	0.00E+00	0.00E+00	0.00E+00	0.00E+00	0.00E+00
6	6.75	4.23E-04	3.48E-06	0.00E+00	0.00E+00	1.65E-04	3.22E-06	0.00E+00	0.00E+00	0.00E+00	0.00E+00	0.00E+00	0.00E+00
7	7.81	3.22E-04	2.49E-06	0.00E+00	0.00E+00	1.21E-04	2.15E-06	0.00E+00	0.00E+00	0.00E+00	0.00E+00	0.00E+00	0.00E+00
8	8.92	2.54E-04	1.90E-06	0.00E+00	0.00E+00	9.62E-05	1.56E-06	0.00E+00	0.00E+00	0.00E+00	0.00E+00	0.00E+00	0.00E+00
9	10.3	2.05E-04	1.46E-06	0.00E+00	0.00E+00	7.63E-05	1.12E-06	0.00E+00	0.00E+00	0.00E+00	0.00E+00	0.00E+00	0.00E+00
10	11.8	1.61E-04	1.09E-06	0.00E+00	0.00E+00	5.79E-05	8.05E-07	0.00E+00	0.00E+00	0.00E+00	0.00E+00	0.00E+00	0.00E+00
11	13.6	1.23E-04	8.28E-07	0.00E+00	0.00E+00	4.52E-05	5.91E-07	0.00E+00	0.00E+00	0.00E+00	0.00E+00	0.00E+00	0.00E+00
12	15.7	1.03E-04	6.65E-07	7.00E-07	1.18E-07	3.37E-05	4.27E-07	0.00E+00	0.00E+00	0.00E+00	0.00E+00	0.00E+00	0.00E+00
13	18.1	8.12E-05	5.18E-07	7.51E-07	6.57E-08	2.45E-05	3.05E-07	0.00E+00	0.00E+00	0.00E+00	0.00E+00	0.00E+00	0.00E+00
14	20.8	6.71E-05	4.24E-07	6.42E-07	4.80E-08	1.78E-05	2.26E-07	0.00E+00	0.00E+00	0.00E+00	0.00E+00	0.00E+00	0.00E+00
15	23.9	5.44E-05	3.44E-07	7.29E-07	5.54E-08	1.41E-05	1.77E-07	0.00E+00	0.00E+00	0.00E+00	0.00E+00	0.00E+00	0.00E+00
16	27.4	4.55E-05	5.57E-07	3.85E-07	2.81E-08	1.11E-05	7.11E-07	0.00E+00	0.00E+00	0.00E+00	0.00E+00	0.00E+00	0.00E+00
17	31.5	3.90E-05	3.34E-07	3.00E-07	2.25E-08	9.32E-06	3.36E-07	8.57E-07	1.09E-07	1.14E-06	1.24E-07	1.22E-04	1.49E-06
18	36.2	3.25E-05	2.38E-07	2.65E-07	1.96E-08	7.45E-06	1.90E-07	6.52E-07	5.90E-08	5.45E-07	6.13E-08	9.74E-05	1.16E-06
19	41.6	2.73E-05	1.94E-07	1.82E-07	1.51E-08	6.22E-06	1.33E-07	6.39E-07	4.41E-08	4.64E-07	4.93E-08	7.29E-05	8.73E-07
20	47.8	2.28E-05	1.65E-07	1.62E-07	1.34E-08	5.07E-06	1.01E-07	5.44E-07	3.63E-08	4.76E-07	4.35E-08	5.49E-05	1.93E-06
21	54.9	1.91E-05	1.43E-07	1.48E-07	1.21E-08	4.21E-06	8.05E-08	4.31E-07	2.92E-08	3.63E-07	3.59E-08	4.11E-05	9.61E-07
22	63.2	1.50E-05	1.20E-07	1.08E-07	9.79E-09	3.59E-06	6.50E-08	3.32E-07	2.37E-08	2.98E-07	2.93E-08	3.38E-05	5.97E-07
23	72.6	1.21E-05	1.03E-07	1.04E-07	9.02E-09	2.97E-06	5.28E-08	2.93E-07	2.05E-08	2.31E-07	2.43E-08	2.49E-05	3.93E-07
24	83.4	9.89E-06	8.94E-08	9.08E-08	8.00E-09	2.44E-06	4.52E-08	2.28E-07	1.69E-08	2.03E-07	2.30E-08	1.96E-05	3.01E-07
25	95.9	7.73E-06	7.61E-08	6.24E-08	6.30E-09	1.96E-06	3.87E-08	1.93E-07	1.46E-08	1.55E-07	1.84E-08	1.61E-05	2.51E-07
26	110.1	5.95E-06	6.50E-08	6.63E-08	6.21E-09	1.61E-06	3.36E-08	1.53E-07	1.22E-08	1.13E-07	1.39E-08	1.24E-05	1.99E-07
27	126.6	4.46E-06	5.51E-08	4.96E-08	5.11E-09	1.22E-06	2.82E-08	1.45E-07	1.12E-08	9.24E-08	1.32E-08	9.68E-06	1.62E-07
28	145.3	3.11E-06	4.52E-08	3.22E-08	3.91E-09	8.73E-07	2.57E-08	1.01E-07	8.79E-09	5.06E-08	8.58E-09	7.08E-06	1.31E-07
29	166.9	2.11E-06	3.71E-08	2.02E-08	2.98E-09	5.99E-07	2.04E-08	7.67E-08	7.28E-09	3.79E-08	6.92E-09	4.66E-06	9.70E-08
30	191.6	1.28E-06	2.92E-08	1.38E-08	2.36E-09	3.68E-07	1.55E-08	4.25E-08	5.16E-09	2.92E-08	5.65E-09	3.04E-06	7.29E-08
31	220.2	8.77E-07	2.48E-08	5.66E-09	1.46E-09	2.47E-07	1.23E-08	4.17E-08	4.88E-09	9.53E-09	2.91E-09	2.03E-06	5.61E-08

2004-2010 L=16-17 Latitude=-10° to 10°

DPPS	E/Q(keV/e)	H ⁺ n	sigma	He ⁺⁺ n	sigma	H ₂ ⁺ n	sigma	He ⁺ n	sigma	O ⁺⁺ n	sigma	W ⁺ n	sigma
0	2.81	1.72E-03	3.14E-05	0.00E+00	0.00E+00	6.72E-04	3.08E-05	0.00E+00	0.00E+00	0.00E+00	0.00E+00	0.00E+00	0.00E+00
1	3.29	1.42E-03	2.17E-05	0.00E+00	0.00E+00	4.98E-04	2.00E-05	0.00E+00	0.00E+00	0.00E+00	0.00E+00	0.00E+00	0.00E+00
2	3.78	9.70E-04	1.30E-05	0.00E+00	0.00E+00	3.49E-04	1.23E-05	0.00E+00	0.00E+00	0.00E+00	0.00E+00	0.00E+00	0.00E+00
3	4.4	6.84E-04	8.20E-06	0.00E+00	0.00E+00	2.64E-04	7.97E-06	0.00E+00	0.00E+00	0.00E+00	0.00E+00	0.00E+00	0.00E+00
4	5.05	5.35E-04	5.79E-06	0.00E+00	0.00E+00	2.22E-04	5.85E-06	0.00E+00	0.00E+00	0.00E+00	0.00E+00	0.00E+00	0.00E+00
5	5.86	4.06E-04	4.05E-06	0.00E+00	0.00E+00	1.75E-04	4.10E-06	0.00E+00	0.00E+00	0.00E+00	0.00E+00	0.00E+00	0.00E+00
6	6.75	3.22E-04	2.98E-06	0.00E+00	0.00E+00	1.34E-04	2.84E-06	0.00E+00	0.00E+00	0.00E+00	0.00E+00	0.00E+00	0.00E+00
7	7.81	2.49E-04	2.14E-06	0.00E+00	0.00E+00	9.45E-05	1.86E-06	0.00E+00	0.00E+00	0.00E+00	0.00E+00	0.00E+00	0.00E+00
8	8.92	1.95E-04	1.62E-06	0.00E+00	0.00E+00	7.62E-05	1.37E-06	0.00E+00	0.00E+00	9.54E-06	7.55E-07	1.18E-03	2.77E-05
9	10.3	1.59E-04	1.25E-06	0.00E+00	0.00E+00	5.88E-05	9.71E-07	0.00E+00	0.00E+00	7.20E-06	5.49E-07	9.07E-04	1.80E-05
10	11.8	1.26E-04	9.37E-07	0.00E+00	0.00E+00	4.60E-05	7.06E-07	0.00E+00	0.00E+00	5.13E-06	3.96E-07	6.96E-04	1.22E-05
11	13.6	9.98E-05	7.21E-07	0.00E+00	0.00E+00	3.64E-05	5.23E-07	0.00E+00	0.00E+00	3.04E-06	2.64E-07	5.43E-04	8.72E-06
12	15.7	8.17E-05	5.71E-07	8.85E-07	1.21E-07	2.66E-05	3.72E-07	0.00E+00	0.00E+00	2.43E-06	2.04E-07	4.13E-04	6.14E-06
13	18.1	6.55E-05	4.51E-07	6.50E-07	5.96E-08	2.01E-05	2.74E-07	0.00E+00	0.00E+00	2.11E-06	1.66E-07	3.04E-04	4.34E-06
14	20.8	5.51E-05	3.71E-07	4.77E-07	4.18E-08	1.51E-05	2.04E-07	0.00E+00	0.00E+00	1.45E-06	1.19E-07	2.32E-04	3.16E-06
15	23.9	4.56E-05	3.06E-07	4.99E-07	4.11E-08	1.24E-05	1.63E-07	0.00E+00	0.00E+00	1.14E-06	9.62E-08	1.79E-04	2.36E-06
16	27.4	3.82E-05	4.99E-07	2.90E-07	2.37E-08	8.82E-06	6.05E-07	9.73E-07	2.00E-07	9.70E-07	1.62E-07	1.40E-04	1.79E-06
17	31.5	3.32E-05	3.03E-07	2.36E-07	1.97E-08	8.24E-06	3.15E-07	6.95E-07	9.55E-08	6.32E-07	9.90E-08	1.16E-04	1.41E-06
18	36.2	2.82E-05	2.15E-07	2.23E-07	1.77E-08	7.39E-06	1.88E-07	5.42E-07	5.32E-08	4.12E-07	5.19E-08	8.78E-05	1.07E-06
19	41.6	2.40E-05	1.77E-07	1.86E-07	1.51E-08	6.07E-06	1.29E-07	5.41E-07	3.98E-08	5.21E-07	5.85E-08	6.97E-05	8.36E-07
20	47.8	2.05E-05	1.52E-07	1.27E-07	1.16E-08	4.87E-06	9.78E-08	4.68E-07	3.31E-08	4.01E-07	4.24E-08	5.05E-05	1.85E-06
21	54.9	1.70E-05	1.32E-07	9.56E-08	9.56E-09	4.00E-06	7.71E-08	4.11E-07	2.80E-08	3.77E-07	4.00E-08	3.89E-05	9.24E-07
22	63.2	1.38E-05	1.13E-07	9.25E-08	8.89E-09	3.31E-06	6.14E-08	3.16E-07	2.26E-08	2.90E-07	3.26E-08	3.09E-05	5.58E-07
23	72.6	1.08E-05	9.50E-08	6.86E-08	7.19E-09	2.59E-06	4.84E-08	3.04E-07	2.04E-08	2.25E-07	2.61E-08	2.34E-05	3.74E-07
24	83.4	8.72E-06	8.25E-08	6.19E-08	6.50E-09	2.02E-06	4.03E-08	2.38E-07	1.69E-08	1.76E-07	2.02E-08	1.85E-05	2.88E-07
25	95.9	6.79E-06	7.02E-08	4.74E-08	5.37E-09	1.46E-06	3.27E-08	1.88E-07	1.41E-08	1.16E-07	1.52E-08	1.33E-05	2.21E-07
26	110.1	5.11E-06	5.91E-08	3.96E-08	4.70E-09	1.07E-06	2.69E-08	1.46E-07	1.17E-08	1.18E-07	1.46E-08	1.00E-05	1.77E-07
27	126.6	3.69E-06	4.93E-08	3.06E-08	3.95E-09	8.56E-07	2.31E-08	9.96E-08	9.15E-09	6.96E-08	1.03E-08	7.05E-06	1.37E-07
28	145.3	2.55E-06	4.03E-08	2.40E-08	3.34E-09	5.72E-07	2.06E-08	9.07E-08	8.21E-09	4.66E-08	8.78E-09	5.37E-06	1.10E-07
29	166.9	1.77E-06	3.34E-08	1.67E-08	2.67E-09	4.14E-07	1.68E-08	7.29E-08	7.02E-09	2.28E-08	5.40E-09	3.81E-06	8.64E-08
30	191.6	1.17E-06	2.76E-08	1.57E-08	2.51E-09	2.98E-07	1.38E-08	4.48E-08	5.28E-09	2.25E-08	5.17E-09	2.61E-06	6.70E-08
31	220.2	7.17E-07	2.20E-08	8.48E-09	1.77E-09	1.89E-07	1.06E-08	2.96E-08	4.07E-09	1.58E-08	3.85E-09	1.88E-06	5.31E-08

2004-2010 L=17-18 Latitude=-10° to 10°

DPPS	E/Q(keV/e)	H ⁺ n	sigma	He ⁺⁺ n	sigma	H ₂ ⁺ n	sigma	He ⁺ n	sigma	O ⁺⁺ n	sigma	W ⁺ n	sigma
0	2.81	1.54E-03	2.90E-05	0.00E+00	0.00E+00	5.53E-04	2.73E-05	0.00E+00	0.00E+00	0.00E+00	0.00E+00	0.00E+00	0.00E+00
1	3.29	1.22E-03	1.97E-05	0.00E+00	0.00E+00	5.06E-04	1.99E-05	0.00E+00	0.00E+00	0.00E+00	0.00E+00	0.00E+00	0.00E+00
2	3.78	8.31E-04	1.18E-05	0.00E+00	0.00E+00	3.09E-04	1.13E-05	0.00E+00	0.00E+00	0.00E+00	0.00E+00	0.00E+00	0.00E+00
3	4.4	5.94E-04	7.47E-06	0.00E+00	0.00E+00	2.29E-04	7.29E-06	0.00E+00	0.00E+00	0.00E+00	0.00E+00	0.00E+00	0.00E+00
4	5.05	4.61E-04	5.25E-06	0.00E+00	0.00E+00	1.89E-04	5.27E-06	0.00E+00	0.00E+00	0.00E+00	0.00E+00	0.00E+00	0.00E+00
5	5.86	3.62E-04	3.73E-06	0.00E+00	0.00E+00	1.47E-04	3.65E-06	0.00E+00	0.00E+00	0.00E+00	0.00E+00	0.00E+00	0.00E+00
6	6.75	2.87E-04	2.73E-06	0.00E+00	0.00E+00	1.13E-04	2.55E-06	0.00E+00	0.00E+00	0.00E+00	0.00E+00	0.00E+00	0.00E+00
7	7.81	2.13E-04	1.92E-06	0.00E+00	0.00E+00	8.13E-05	1.69E-06	0.00E+00	0.00E+00	0.00E+00	0.00E+00	0.00E+00	0.00E+00
8	8.92	1.70E-04	1.47E-06	0.00E+00	0.00E+00	6.42E-05	1.23E-06	0.00E+00	0.00E+00	7.55E-06	6.54E-07	7.91E-04	2.22E-05
9	10.3	1.42E-04	1.16E-06	0.00E+00	0.00E+00	4.97E-05	8.70E-07	0.00E+00	0.00E+00	4.95E-06	4.44E-07	5.99E-04	1.42E-05
10	11.8	1.08E-04	8.47E-07	0.00E+00	0.00E+00	4.13E-05	6.53E-07	0.00E+00	0.00E+00	4.08E-06	3.45E-07	4.51E-04	9.57E-06
11	13.6	8.42E-05	6.45E-07	0.00E+00	0.00E+00	3.09E-05	4.69E-07	0.00E+00	0.00E+00	2.61E-06	2.39E-07	3.65E-04	6.92E-06
12	15.7	6.80E-05	5.09E-07	6.81E-07	1.06E-07	2.29E-05	3.37E-07	0.00E+00	0.00E+00	1.80E-06	1.72E-07	2.84E-04	4.99E-06
13	18.1	5.42E-05	3.99E-07	5.65E-07	5.82E-08	1.67E-05	2.42E-07	0.00E+00	0.00E+00	2.01E-06	1.57E-07	2.12E-04	3.54E-06
14	20.8	4.53E-05	3.25E-07	4.72E-07	4.00E-08	1.20E-05	1.78E-07	0.00E+00	0.00E+00	1.45E-06	1.16E-07	1.59E-04	2.56E-06
15	23.9	3.62E-05	2.65E-07	4.28E-07	3.84E-08	9.38E-06	1.38E-07	0.00E+00	0.00E+00	7.82E-07	7.98E-08	1.31E-04	1.97E-06
16	27.4	3.12E-05	4.41E-07	2.49E-07	2.19E-08	8.17E-06	5.91E-07	5.75E-07	1.55E-07	4.24E-07	9.23E-08	1.06E-04	1.52E-06
17	31.5	2.62E-05	2.60E-07	1.74E-07	1.65E-08	6.31E-06	2.68E-07	4.71E-07	7.76E-08	6.60E-07	8.76E-08	8.40E-05	1.18E-06
18	36.2	2.16E-05	1.83E-07	1.56E-07	1.45E-08	5.04E-06	1.50E-07	4.29E-07	4.57E-08	4.28E-07	5.27E-08	6.73E-05	9.15E-07
19	41.6	1.83E-05	1.50E-07	1.03E-07	1.09E-08	3.93E-06	1.01E-07	4.26E-07	3.44E-08	3.85E-07	4.80E-08	4.99E-05	6.90E-07
20	47.8	1.52E-05	1.28E-07	9.39E-08	9.78E-09	3.25E-06	7.83E-08	4.32E-07	3.10E-08	3.53E-07	4.18E-08	3.83E-05	1.58E-06
21	54.9	1.27E-05	1.11E-07	6.74E-08	7.84E-09	2.65E-06	6.15E-08	2.83E-07	2.27E-08	2.55E-07	3.14E-08	2.95E-05	7.86E-07
22	63.2	1.03E-05	9.54E-08	5.55E-08	6.72E-09	2.18E-06	4.87E-08	2.81E-07	2.09E-08	2.29E-07	2.80E-08	2.39E-05	4.79E-07
23	72.6	8.35E-06	8.18E-08	4.21E-08	5.47E-09	1.74E-06	3.87E-08	2.19E-07	1.69E-08	1.68E-07	2.00E-08	1.80E-05	3.20E-07
24	83.4	6.61E-06	7.01E-08	4.18E-08	5.21E-09	1.33E-06	3.20E-08	1.78E-07	1.43E-08	1.24E-07	1.78E-08	1.43E-05	2.45E-07
25	95.9	5.00E-06	5.89E-08	2.80E-08	4.04E-09	1.04E-06	2.71E-08	1.30E-07	1.15E-08	6.94E-08	1.15E-08	1.15E-05	2.01E-07
26	110.1	3.60E-06	4.86E-08	2.70E-08	3.78E-09	7.81E-07	2.25E-08	1.07E-07	9.78E-09	1.01E-07	1.41E-08	8.72E-06	1.61E-07
27	126.6	2.68E-06	4.10E-08	2.13E-08	3.21E-09	5.63E-07	1.83E-08	8.84E-08	8.39E-09	5.42E-08	9.74E-09	5.88E-06	1.22E-07
28	145.3	1.92E-06	3.43E-08	1.12E-08	2.24E-09	4.20E-07	1.74E-08	5.19E-08	6.11E-09	4.15E-08	7.23E-09	4.22E-06	9.61E-08
29	166.9	1.39E-06	2.91E-08	1.42E-08	2.39E-09	2.92E-07	1.36E-08	5.59E-08	5.96E-09	3.90E-08	6.43E-09	2.94E-06	7.42E-08
30	191.6	9.48E-07	2.42E-08	8.27E-09	1.76E-09	2.12E-07	1.13E-08	3.36E-08	4.42E-09	1.83E-08	4.10E-09	2.05E-06	5.77E-08
31	220.2	6.34E-07	2.03E-08	5.94E-09	1.44E-09	1.67E-07	9.73E-09	2.44E-08	3.59E-09	1.30E-08	3.52E-09	1.35E-06	4.39E-08

2004-2010 L=18-19 Latitude=-10° to 10°

DPPS	E/Q(keV/e)	H ⁺ n	sigma	He ⁺⁺ n	sigma	H ₂ ⁺ n	sigma	He ⁺ n	sigma	O ⁺⁺ n	sigma	W ⁺ n	sigma
0	2.81	1.42E-03	2.73E-05	0.00E+00	0.00E+00	6.00E-04	2.77E-05	0.00E+00	0.00E+00	0.00E+00	0.00E+00	0.00E+00	0.00E+00
1	3.29	1.18E-03	1.88E-05	0.00E+00	0.00E+00	4.17E-04	1.76E-05	0.00E+00	0.00E+00	0.00E+00	0.00E+00	0.00E+00	0.00E+00
2	3.78	7.69E-04	1.11E-05	0.00E+00	0.00E+00	2.79E-04	1.04E-05	0.00E+00	0.00E+00	0.00E+00	0.00E+00	0.00E+00	0.00E+00
3	4.4	5.44E-04	6.97E-06	0.00E+00	0.00E+00	2.14E-04	6.88E-06	0.00E+00	0.00E+00	0.00E+00	0.00E+00	0.00E+00	0.00E+00
4	5.05	4.39E-04	5.00E-06	0.00E+00	0.00E+00	1.74E-04	4.93E-06	0.00E+00	0.00E+00	0.00E+00	0.00E+00	0.00E+00	0.00E+00
5	5.86	3.35E-04	3.51E-06	0.00E+00	0.00E+00	1.41E-04	3.50E-06	0.00E+00	0.00E+00	0.00E+00	0.00E+00	0.00E+00	0.00E+00
6	6.75	2.68E-04	2.58E-06	0.00E+00	0.00E+00	1.06E-04	2.41E-06	0.00E+00	0.00E+00	0.00E+00	0.00E+00	0.00E+00	0.00E+00
7	7.81	2.01E-04	1.83E-06	0.00E+00	0.00E+00	7.84E-05	1.63E-06	0.00E+00	0.00E+00	0.00E+00	0.00E+00	0.00E+00	0.00E+00
8	8.92	1.57E-04	1.38E-06	0.00E+00	0.00E+00	5.95E-05	1.15E-06	0.00E+00	0.00E+00	6.27E-06	5.83E-07	7.12E-04	2.06E-05
9	10.3	1.31E-04	1.08E-06	0.00E+00	0.00E+00	4.77E-05	8.34E-07	0.00E+00	0.00E+00	4.40E-06	4.11E-07	5.46E-04	1.32E-05
10	11.8	1.01E-04	7.97E-07	0.00E+00	0.00E+00	3.78E-05	6.10E-07	0.00E+00	0.00E+00	3.71E-06	3.21E-07	4.35E-04	9.11E-06
11	13.6	7.92E-05	6.10E-07	0.00E+00	0.00E+00	2.81E-05	4.37E-07	0.00E+00	0.00E+00	2.20E-06	2.14E-07	3.45E-04	6.61E-06
12	15.7	6.39E-05	4.79E-07	9.20E-07	1.15E-07	2.00E-05	3.07E-07	0.00E+00	0.00E+00	1.48E-06	1.51E-07	2.57E-04	4.63E-06
13	18.1	5.07E-05	3.77E-07	5.33E-07	5.33E-08	1.45E-05	2.21E-07	0.00E+00	0.00E+00	1.39E-06	1.27E-07	1.98E-04	3.33E-06
14	20.8	4.14E-05	3.04E-07	4.10E-07	3.58E-08	1.05E-05	1.62E-07	0.00E+00	0.00E+00	1.22E-06	1.04E-07	1.52E-04	2.44E-06
15	23.9	3.35E-05	2.48E-07	4.82E-07	4.03E-08	7.95E-06	1.24E-07	0.00E+00	0.00E+00	5.69E-07	6.84E-08	1.17E-04	1.81E-06
16	27.4	2.72E-05	4.03E-07	2.97E-07	2.31E-08	5.94E-06	4.88E-07	6.42E-07	1.57E-07	4.38E-07	9.52E-08	9.59E-05	1.41E-06
17	31.5	2.33E-05	2.40E-07	2.05E-07	1.75E-08	5.48E-06	2.45E-07	4.89E-07	7.62E-08	4.25E-07	7.05E-08	7.26E-05	1.06E-06
18	36.2	1.95E-05	1.70E-07	1.66E-07	1.46E-08	4.42E-06	1.38E-07	3.33E-07	3.97E-08	3.03E-07	4.87E-08	5.84E-05	8.34E-07
19	41.6	1.59E-05	1.36E-07	1.37E-07	1.23E-08	3.39E-06	9.23E-08	3.75E-07	3.18E-08	2.17E-07	3.41E-08	4.44E-05	6.35E-07
20	47.8	1.31E-05	1.16E-07	1.19E-07	1.08E-08	2.63E-06	6.90E-08	3.33E-07	2.67E-08	2.24E-07	2.91E-08	3.39E-05	1.45E-06
21	54.9	1.09E-05	9.94E-08	8.26E-08	8.47E-09	2.12E-06	5.35E-08	2.39E-07	2.04E-08	1.55E-07	2.17E-08	2.45E-05	7.00E-07
22	63.2	8.13E-06	8.13E-08	8.80E-08	8.21E-09	1.69E-06	4.16E-08	2.08E-07	1.74E-08	1.12E-07	1.68E-08	1.93E-05	4.20E-07
23	72.6	6.45E-06	6.92E-08	5.37E-08	6.04E-09	1.27E-06	3.23E-08	1.81E-07	1.50E-08	9.69E-08	1.67E-08	1.41E-05	2.77E-07
24	83.4	4.78E-06	5.73E-08	4.38E-08	5.21E-09	1.04E-06	2.76E-08	1.28E-07	1.18E-08	9.35E-08	1.38E-08	1.11E-05	2.12E-07
25	95.9	3.62E-06	4.80E-08	4.27E-08	4.86E-09	8.18E-07	2.34E-08	1.28E-07	1.11E-08	8.01E-08	1.20E-08	8.48E-06	1.67E-07
26	110.1	2.74E-06	4.08E-08	2.79E-08	3.76E-09	6.27E-07	1.96E-08	8.70E-08	8.61E-09	7.01E-08	1.14E-08	6.69E-06	1.38E-07
27	126.6	2.02E-06	3.44E-08	2.56E-08	3.46E-09	4.85E-07	1.67E-08	8.00E-08	7.84E-09	4.88E-08	8.28E-09	5.03E-06	1.10E-07
28	145.3	1.39E-06	2.83E-08	2.15E-08	3.01E-09	3.51E-07	1.54E-08	4.81E-08	5.71E-09	3.54E-08	6.56E-09	3.89E-06	9.04E-08
29	166.9	1.03E-06	2.44E-08	1.31E-08	2.26E-09	2.47E-07	1.23E-08	4.33E-08	5.14E-09	2.26E-08	5.36E-09	2.71E-06	6.91E-08
30	191.6	7.05E-07	2.03E-08	8.97E-09	1.79E-09	1.78E-07	1.01E-08	2.43E-08	3.66E-09	1.98E-08	4.59E-09	1.87E-06	5.36E-08
31	220.2	4.76E-07	1.71E-08	4.98E-09	1.28E-09	1.02E-07	7.36E-09	2.42E-08	3.50E-09	1.08E-08	3.13E-09	1.27E-06	4.14E-08

2004-2010 L=19-20 Latitude=-10° to 10°

DPPS	E/Q(keV/e)	H ⁺ n	sigma	He ⁺⁺ n	sigma	H ₂ ⁺ n	sigma	He ⁺ n	sigma	O ⁺⁺ n	sigma	W ⁺ n	sigma
0	2.81	1.23E-03	2.51E-05	0.00E+00	0.00E+00	4.53E-04	2.39E-05	0.00E+00	0.00E+00	0.00E+00	0.00E+00	0.00E+00	0.00E+00
1	3.29	9.38E-04	1.66E-05	0.00E+00	0.00E+00	3.48E-04	1.59E-05	0.00E+00	0.00E+00	0.00E+00	0.00E+00	0.00E+00	0.00E+00
2	3.78	6.56E-04	1.01E-05	0.00E+00	0.00E+00	2.42E-04	9.63E-06	0.00E+00	0.00E+00	0.00E+00	0.00E+00	0.00E+00	0.00E+00
3	4.4	4.61E-04	6.35E-06	0.00E+00	0.00E+00	1.81E-04	6.26E-06	0.00E+00	0.00E+00	0.00E+00	0.00E+00	0.00E+00	0.00E+00
4	5.05	3.54E-04	4.44E-06	0.00E+00	0.00E+00	1.44E-04	4.44E-06	0.00E+00	0.00E+00	0.00E+00	0.00E+00	0.00E+00	0.00E+00
5	5.86	2.76E-04	3.15E-06	0.00E+00	0.00E+00	1.10E-04	3.06E-06	0.00E+00	0.00E+00	0.00E+00	0.00E+00	0.00E+00	0.00E+00
6	6.75	2.17E-04	2.29E-06	0.00E+00	0.00E+00	8.82E-05	2.17E-06	0.00E+00	0.00E+00	0.00E+00	0.00E+00	0.00E+00	0.00E+00
7	7.81	1.63E-04	1.63E-06	0.00E+00	0.00E+00	6.15E-05	1.42E-06	0.00E+00	0.00E+00	0.00E+00	0.00E+00	0.00E+00	0.00E+00
8	8.92	1.31E-04	1.25E-06	0.00E+00	0.00E+00	4.80E-05	1.02E-06	0.00E+00	0.00E+00	5.93E-06	5.99E-07	6.58E-04	1.95E-05
9	10.3	1.08E-04	9.72E-07	0.00E+00	0.00E+00	3.75E-05	7.30E-07	0.00E+00	0.00E+00	3.78E-06	3.75E-07	5.22E-04	1.27E-05
10	11.8	8.39E-05	7.22E-07	0.00E+00	0.00E+00	3.02E-05	5.38E-07	0.00E+00	0.00E+00	3.11E-06	2.90E-07	3.86E-04	8.55E-06
11	13.6	6.57E-05	5.52E-07	0.00E+00	0.00E+00	2.38E-05	3.99E-07	0.00E+00	0.00E+00	2.29E-06	2.16E-07	2.99E-04	6.05E-06
12	15.7	5.51E-05	4.44E-07	6.61E-07	9.75E-08	1.67E-05	2.78E-07	0.00E+00	0.00E+00	1.46E-06	1.49E-07	2.28E-04	4.30E-06
13	18.1	4.42E-05	3.49E-07	5.50E-07	5.31E-08	1.22E-05	1.99E-07	0.00E+00	0.00E+00	1.41E-06	1.27E-07	1.72E-04	3.06E-06
14	20.8	3.65E-05	2.85E-07	3.61E-07	3.30E-08	9.26E-06	1.51E-07	0.00E+00	0.00E+00	1.09E-06	9.73E-08	1.34E-04	2.27E-06
15	23.9	3.00E-05	2.34E-07	4.69E-07	3.89E-08	7.48E-06	1.19E-07	0.00E+00	0.00E+00	4.87E-07	6.12E-08	1.06E-04	1.70E-06
16	27.4	2.58E-05	3.89E-07	2.44E-07	2.05E-08	4.73E-06	4.20E-07	3.93E-07	1.20E-07	3.05E-07	7.35E-08	8.55E-05	1.32E-06
17	31.5	2.16E-05	2.31E-07	1.95E-07	1.67E-08	4.57E-06	2.17E-07	4.39E-07	7.27E-08	2.93E-07	5.29E-08	6.95E-05	1.03E-06
18	36.2	1.85E-05	1.67E-07	1.49E-07	1.37E-08	4.05E-06	1.31E-07	4.32E-07	4.49E-08	2.56E-07	4.05E-08	5.55E-05	8.04E-07
19	41.6	1.52E-05	1.34E-07	1.50E-07	1.28E-08	3.22E-06	8.91E-08	3.45E-07	3.02E-08	2.41E-07	3.13E-08	4.32E-05	6.20E-07
20	47.8	1.24E-05	1.14E-07	1.09E-07	1.02E-08	2.61E-06	6.74E-08	3.46E-07	2.67E-08	1.71E-07	2.75E-08	3.39E-05	1.40E-06
21	54.9	9.80E-06	9.59E-08	1.14E-07	9.86E-09	2.06E-06	5.22E-08	2.48E-07	2.06E-08	1.45E-07	2.11E-08	2.50E-05	7.01E-07
22	63.2	7.69E-06	8.10E-08	6.77E-08	7.13E-09	1.71E-06	4.13E-08	1.95E-07	1.68E-08	1.17E-07	1.81E-08	1.91E-05	4.12E-07
23	72.6	5.97E-06	6.82E-08	4.50E-08	5.52E-09	1.32E-06	3.27E-08	1.98E-07	1.56E-08	1.16E-07	1.62E-08	1.44E-05	2.76E-07
24	83.4	4.56E-06	5.73E-08	4.06E-08	4.96E-09	1.02E-06	2.71E-08	1.46E-07	1.26E-08	8.26E-08	1.46E-08	1.14E-05	2.12E-07
25	95.9	3.45E-06	4.80E-08	2.98E-08	4.01E-09	7.90E-07	2.27E-08	1.07E-07	1.00E-08	5.35E-08	1.01E-08	8.47E-06	1.66E-07
26	110.1	2.49E-06	3.95E-08	2.72E-08	3.67E-09	5.59E-07	1.83E-08	8.27E-08	8.31E-09	4.86E-08	1.07E-08	6.07E-06	1.30E-07
27	126.6	1.70E-06	3.14E-08	1.80E-08	2.84E-09	4.02E-07	1.49E-08	8.00E-08	7.71E-09	3.07E-08	6.70E-09	4.47E-06	1.02E-07
28	145.3	1.18E-06	2.58E-08	1.18E-08	2.21E-09	2.74E-07	1.34E-08	4.95E-08	5.71E-09	2.15E-08	4.96E-09	3.18E-06	7.97E-08
29	166.9	7.64E-07	2.07E-08	7.55E-09	1.69E-09	2.01E-07	1.10E-08	4.40E-08	5.12E-09	1.51E-08	4.21E-09	2.14E-06	6.12E-08
30	191.6	4.83E-07	1.67E-08	3.14E-09	1.05E-09	1.12E-07	7.88E-09	2.54E-08	3.69E-09	7.57E-09	2.70E-09	1.47E-06	4.73E-08
31	220.2	3.16E-07	1.37E-08	9.65E-10	5.58E-10	9.23E-08	6.37E-09	1.48E-08	2.71E-09	6.31E-09	2.48E-09	9.53E-07	3.53E-08

2004-2010 L=20-21 Latitude=-10° to 10°

DPPS	E/Q(keV/e)	H ⁺ n	sigma	He ⁺⁺ n	sigma	H ₂ ⁺ n	sigma	He ⁺ n	sigma	O ⁺⁺ n	sigma	W ⁺ n	sigma
0	2.81	1.16E-03	2.40E-05	0.00E+00	0.00E+00	4.68E-04	2.39E-05	0.00E+00	0.00E+00	0.00E+00	0.00E+00	0.00E+00	0.00E+00
1	3.29	8.85E-04	1.60E-05	0.00E+00	0.00E+00	3.37E-04	1.55E-05	0.00E+00	0.00E+00	0.00E+00	0.00E+00	0.00E+00	0.00E+00
2	3.78	5.77E-04	9.37E-06	0.00E+00	0.00E+00	2.28E-04	9.23E-06	0.00E+00	0.00E+00	0.00E+00	0.00E+00	0.00E+00	0.00E+00
3	4.4	4.05E-04	5.90E-06	0.00E+00	0.00E+00	1.83E-04	6.23E-06	0.00E+00	0.00E+00	0.00E+00	0.00E+00	0.00E+00	0.00E+00
4	5.05	3.05E-04	4.07E-06	0.00E+00	0.00E+00	1.34E-04	4.22E-06	0.00E+00	0.00E+00	0.00E+00	0.00E+00	0.00E+00	0.00E+00
5	5.86	2.26E-04	2.83E-06	0.00E+00	0.00E+00	1.02E-04	2.92E-06	0.00E+00	0.00E+00	0.00E+00	0.00E+00	0.00E+00	0.00E+00
6	6.75	1.80E-04	2.07E-06	0.00E+00	0.00E+00	7.72E-05	2.02E-06	0.00E+00	0.00E+00	0.00E+00	0.00E+00	0.00E+00	0.00E+00
7	7.81	1.36E-04	1.48E-06	0.00E+00	0.00E+00	5.38E-05	1.32E-06	0.00E+00	0.00E+00	0.00E+00	0.00E+00	0.00E+00	0.00E+00
8	8.92	1.06E-04	1.11E-06	0.00E+00	0.00E+00	4.09E-05	9.35E-07	0.00E+00	0.00E+00	4.35E-06	4.72E-07	5.84E-04	1.82E-05
9	10.3	8.76E-05	8.70E-07	0.00E+00	0.00E+00	3.30E-05	6.79E-07	0.00E+00	0.00E+00	3.82E-06	3.75E-07	4.59E-04	1.19E-05
10	11.8	6.61E-05	6.35E-07	0.00E+00	0.00E+00	2.46E-05	4.79E-07	0.00E+00	0.00E+00	2.62E-06	2.64E-07	3.58E-04	8.09E-06
11	13.6	5.34E-05	4.95E-07	0.00E+00	0.00E+00	1.89E-05	3.51E-07	0.00E+00	0.00E+00	1.59E-06	1.79E-07	2.80E-04	5.81E-06
12	15.7	4.27E-05	3.86E-07	5.94E-07	8.99E-08	1.37E-05	2.50E-07	0.00E+00	0.00E+00	1.24E-06	1.36E-07	2.02E-04	4.02E-06
13	18.1	3.44E-05	3.06E-07	4.92E-07	4.82E-08	9.38E-06	1.74E-07	0.00E+00	0.00E+00	1.26E-06	1.20E-07	1.53E-04	2.87E-06
14	20.8	2.82E-05	2.47E-07	3.45E-07	3.30E-08	7.40E-06	1.34E-07	0.00E+00	0.00E+00	9.78E-07	9.17E-08	1.17E-04	2.10E-06
15	23.9	2.30E-05	2.03E-07	3.65E-07	3.48E-08	5.67E-06	1.03E-07	0.00E+00	0.00E+00	5.29E-07	6.51E-08	9.65E-05	1.61E-06
16	27.4	1.91E-05	3.31E-07	1.72E-07	1.77E-08	4.47E-06	4.23E-07	6.29E-07	1.59E-07	2.95E-07	8.46E-08	7.86E-05	1.25E-06
17	31.5	1.60E-05	1.96E-07	1.49E-07	1.46E-08	3.42E-06	1.88E-07	3.93E-07	6.68E-08	2.81E-07	5.93E-08	6.06E-05	9.53E-07
18	36.2	1.33E-05	1.38E-07	1.21E-07	1.23E-08	2.95E-06	1.11E-07	2.75E-07	3.57E-08	2.35E-07	4.14E-08	4.78E-05	7.37E-07
19	41.6	1.07E-05	1.10E-07	9.16E-08	9.74E-09	2.25E-06	7.27E-08	2.52E-07	2.52E-08	1.79E-07	2.83E-08	3.87E-05	5.82E-07
20	47.8	9.14E-06	9.58E-08	6.58E-08	7.83E-09	1.87E-06	5.65E-08	2.05E-07	2.04E-08	1.29E-07	2.28E-08	2.68E-05	1.23E-06
21	54.9	7.59E-06	8.28E-08	5.77E-08	6.95E-09	1.61E-06	4.59E-08	2.05E-07	1.86E-08	1.50E-07	2.39E-08	2.27E-05	6.59E-07
22	63.2	5.74E-06	6.83E-08	3.11E-08	4.78E-09	1.29E-06	3.56E-08	1.57E-07	1.49E-08	1.26E-07	1.99E-08	1.60E-05	3.75E-07
23	72.6	4.58E-06	5.80E-08	2.37E-08	3.96E-09	1.08E-06	2.94E-08	1.16E-07	1.19E-08	7.65E-08	1.27E-08	1.25E-05	2.55E-07
24	83.4	3.50E-06	4.89E-08	2.45E-08	3.82E-09	8.46E-07	2.46E-08	1.14E-07	1.10E-08	5.14E-08	1.10E-08	9.68E-06	1.94E-07
25	95.9	2.70E-06	4.14E-08	1.92E-08	3.20E-09	6.58E-07	2.06E-08	1.19E-07	1.05E-08	5.24E-08	1.11E-08	7.26E-06	1.53E-07
26	110.1	1.95E-06	3.45E-08	1.21E-08	2.41E-09	4.82E-07	1.69E-08	5.80E-08	6.88E-09	3.51E-08	8.34E-09	5.58E-06	1.24E-07
27	126.6	1.36E-06	2.80E-08	1.10E-08	2.21E-09	3.70E-07	1.42E-08	5.90E-08	6.55E-09	3.15E-08	6.96E-09	4.08E-06	9.81E-08
28	145.3	9.09E-07	2.26E-08	1.08E-08	2.07E-09	2.38E-07	1.23E-08	4.23E-08	5.20E-09	1.78E-08	4.62E-09	3.00E-06	7.73E-08
29	166.9	6.10E-07	1.85E-08	8.13E-09	1.73E-09	1.58E-07	9.58E-09	2.73E-08	3.98E-09	1.74E-08	4.53E-09	2.11E-06	6.02E-08
30	191.6	4.11E-07	1.52E-08	6.25E-09	1.47E-09	1.07E-07	7.70E-09	1.76E-08	3.08E-09	1.41E-08	4.09E-09	1.37E-06	4.52E-08
31	220.2	2.69E-07	1.27E-08	5.18E-09	1.29E-09	6.36E-08	5.77E-09	1.12E-08	2.35E-09	2.91E-09	1.46E-09	7.95E-07	3.22E-08

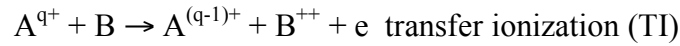
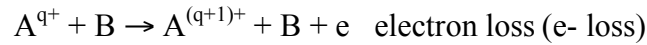
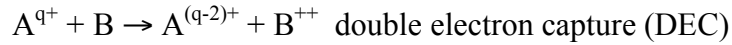
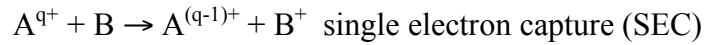
Appendix C

Lifetime Calculations

Here we describe how we calculated the suprathermal ion lifetimes due to ion-neutral collisions, electron impact, and photoionization. We discuss how we determined the collision cross sections at each of the CHEMS energy per charge (E/Q) steps and the assumptions that we made when certain cross sections were not available. A more detailed description of collisions can be found in *Johnson* [1982, 1990], *Hasted* [1972], *Bates* [1962], *Reif* [1965], and *Goldston and Rutherford* [1995]. The introduction to *Lindsay and Stebbings* [2005] also provides a good introduction to charge exchange collisions.

Ion-Neutral Collisions

For ions at suprathermal energies, ion-neutral collisions are the most significant loss process in Saturn's inner magnetosphere. When an ion A^{q+} with charge q collides with a neutral B , several reactions are possible:



The single electron capture (SEC) collision is also called charge exchange or charge transfer and is usually the most likely collision within the CHEMS energy range of 3-220 keV/e.

The ion-neutral collision lifetime of a suprathermal ion depends of the ion velocity v , the neutral density n , and the collision cross section σ :

$$\tau = \frac{1}{nv\sigma} \quad (\text{C.1})$$

Since the neutral velocity is much less than the ion velocity, we can ignore the neutral velocity, so v is determined by equation 2.12. We use the *Cassidy and Johnson* [2010] model to estimate the O, OH, and H₂O neutral densities. Because the suprathermal ion partial number density typically peak between L=9-10, we calculate the lifetimes using the neutral densities at L=9.5 where the neutral density of O, OH, and H₂O are 54 cm⁻³, 14 cm⁻³, and 13 cm⁻³, respectively. Collisions involving neutral OH were not available, so we have to make assumptions about the cross sections involving ion collisions with neutral OH. These assumptions are discussed later in the section. For electron capture collisions between ions and H₂O, the H₂O can be dissociated in addition to being ionized and produce different ion fragments: H⁺, O⁺, OH⁺, and H₂O⁺ [*Gobet et al.*, 2004; *Luna et al.*, 2007]. Some studies (e.g. *Gobet et al.*, [2004]; *Luna et al.*, [2007]) measure the cross sections that produce each of these fragments. We add each of these cross sections when calculating the suprathermal ion lifetime.

Consider the charge exchange reaction $A^+ + B \rightarrow A + B^+ + \Delta E$ where ΔE is the difference between ionization energy. When the particles A and B are the same species (i.e. $\Delta E=0$), the reaction is symmetric or resonant. A near resonant reaction occurs when ΔE is not zero, but very small. For example, the collision between O⁺ and H in their ground states where $\Delta E \sim 0.1$ eV is a near resonant collision. A non-resonant reaction occurs when ΔE is greater than ~ 1 eV.

The cross section σ of a resonant collision decreases with increasing energy E and behaves like

$$\sigma^{1/2} = C - D \ln(E) \quad (\text{C.2})$$

[*Dalgarno* 1958]. The quantities C and D are constants. For non-resonant collisions at low velocities, the cross sections are smaller than the resonant cross section and increase with increasing velocity [*Rapp and Francis* 1962]. The non-resonant cross section maximizes at a velocity that can be approximated by the Massey adiabatic hypothesis [*Massey* 1949]:

$$v_{\max} = \frac{a|\Delta E|}{h} \quad (\text{C.3})$$

In the above equation, $a=7 \times 10^{-8}$ cm and h is Planck's constant. Above this maximum velocity, the non-resonant cross section converges with the cross section of the resonant collision [*Rapp and Francis* 1962]. The collision cross section is predicted to maximize at higher velocities as the difference in ionization energies increase.

The rest of this section focuses on obtaining the cross sections for the various ion-neutral collisions that occur in Saturn's inner magnetosphere. Once we get the cross sections, calculating the ion lifetime is relatively straightforward (see equation C.1). Using the results from various experimental and theoretical studies, we obtain the collision cross sections within the CHEMS energy range and fit the data to get an equation that determines the cross section as a function of energy. We can then calculate the cross sections for each of the 32 E/Q steps of the CHEMS instrument.

We use a few different functional forms. One functional form involves modifying equation C.2 like the fits done by *Lindsay and Stebbings* [2005]. Another functional form is similar to the one used by *Shevelko et al.* [2009] to fit the cross sections of He^+ on various neutral atoms:

$$\log_{10}(\sigma) = \sum_{i=0}^9 A_i (\log_{10}(E))^i \quad (\text{C.4})$$

The quantity A_i is the fitting parameter. While *Shevelko et al.* [2009] using 10 fitting parameters, we typically use only 3 or 4 parameters. We also use polynomial fits for some reactions:

$$\sigma = \sum_{i=0}^4 A_i E^i \quad (\text{C.5})$$

On the next several pages, we will show our cross section fits of the various ion-neutral collisions used in this paper. Some collisions, such as O^+ on O and H^+ on O, have already been fit by prior studies [*Lindsay and Stebbings* 2005], so we use published fits whenever possible.

For all our fits, we put the energy in keV and the cross sections in 10^{16} cm^2 . When we use a functional form like *Lindsay and Stebbings* [2005] or equation C.4, we use the Levenberg-Marquardt fitting method [*Press et al.*, 1989; *Bevington and Robinson* 2003]. We report the uncertainties of the fitting parameters and the reduced χ^2 . The reported parameter uncertainties are determined by taking the square root of the diagonal terms in the covariant matrix (i.e. error matrix) used in the Levenberg-Marquardt fitting method [*Press et al.*, 1989; *Bevington and Robinson* 2003]. When performing a polynomial fit, we use Kaleidagraph and report the R value to test the goodness of our fits. In some

cases, our parameter uncertainties are very large, so these fits can be improved when additional cross section data becomes available.

H⁺ on O

The single electron capture cross sections for H⁺ on O were fit by *Lindsay and Stebbings* [2005]:

$$\sigma = (2.91 - 0.0886 \ln E)^2 (1 - e^{-50.9/E})^2 + (4.73 + 0.862 \ln E) (1 - e^{-0.0306/E})^2 \quad (\text{C.6})$$

Thompson et al. [1996] measured the cross sections for transfer ionization and showed that the transfer ionization cross sections were much smaller than the single electron capture collision. Thus, we did not include transfer ionization in our H⁺ lifetime calculation. Figure C.1a shows the H⁺ on O cross section fit along with data from two experimental studies [*Stebbins et al.*, 1964; *Thompson et al.*, 1996].

H⁺ on H₂O

We fit the experimental data from *Dagnac et al.* [1970], *Rudd et al.* [1985a], *Lindsay et al.* [1997], *Greenwood et al.* [2000], *Gobet et al.* [2004], and *Luna et al.* [2007] to determine the H⁺ on H₂O single electron capture cross sections. We use a functional form similar to the one used in the H⁺ on O electron capture cross section:

$$\begin{aligned} \sigma &= (a_1 - a_2 \ln E)^2 (1 - e^{-a_3/E})^{a_4} + (a_1 - a_5 \ln E)^2 (1 - e^{-a_6/E})^{a_4} \\ a_1 &= 3.03 \pm 0.058 \\ a_2 &= 0.269 \pm 0.04 \\ a_3 &= 208 \pm 0.38 \\ a_4 &= 7.71 \pm 1.79 \\ a_5 &= 0.357 \pm 0.07 \\ a_6 &= 68.7 \pm 18 \\ \text{red. } \chi^2 &= 0.29 \end{aligned} \quad (\text{C.7})$$

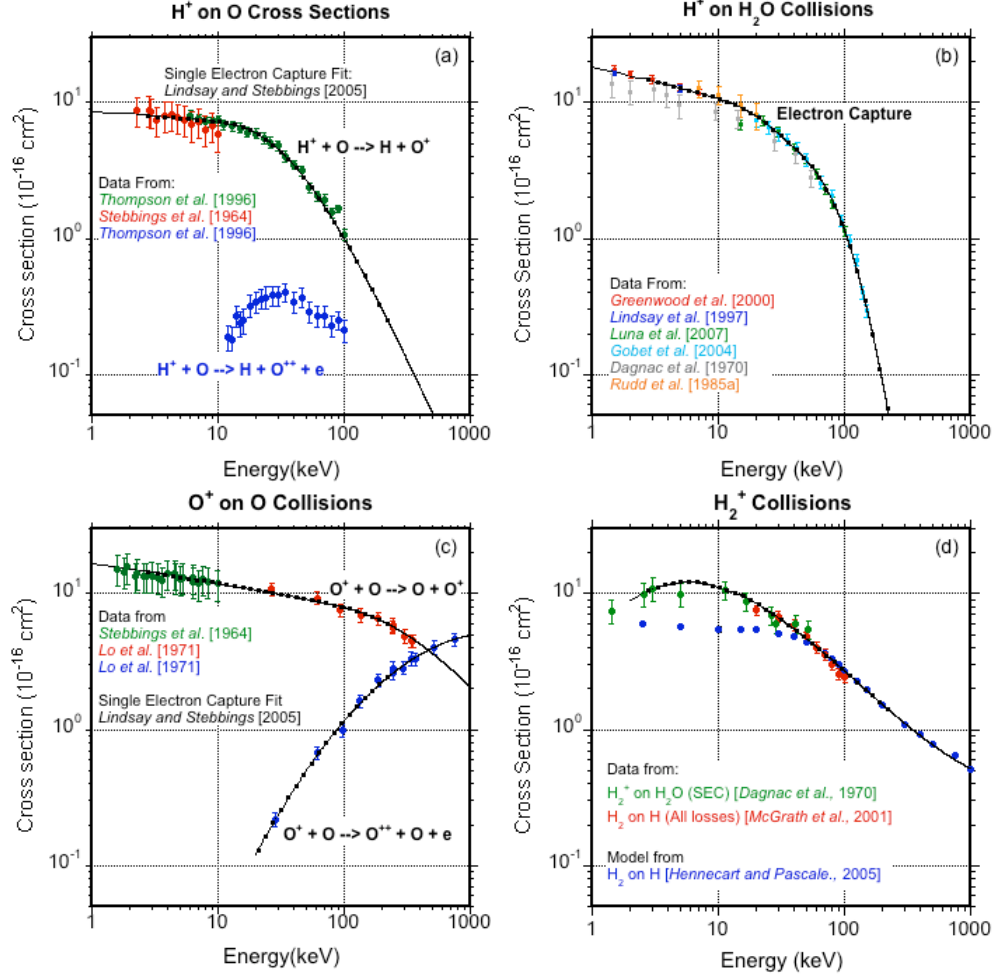


Figure C.1: (a) H^+ on O cross sections as a function of energy. The single electron capture fit is from Lindsay and Stebbings [2005]. The transfer ionization reaction is negligible compared to the electron capture. (b) Electron capture cross sections as a function of energy for the H^+ on H_2O collision. (c) Electron capture and electron loss cross sections for O^+ on O. The single electron capture cross section fit is from Lindsay and Stebbings [2005]. (d) Cross sections for the H_2^+ on H_2O and H. The green points are from the H_2^+ on H_2O electron capture cross section, while the blue and red points are for the H_2^+ on H collisions and include both dissociation and capture. See text for details. The black points in all plots represent the cross sections at the CHEMS E/Q steps.

The fit along with data points is shown in Figure C.1b. Because the cross sections for H^+ on OH are not available, we assume the cross sections for the H^+ on OH is the same as the H^+ on H_2O .

O^+ on O

We use the fit from *Lindsay and Stebbings* [2005] to get the single electron capture cross sections for O^+ on O:

$$(4.07 - 0.269 \ln E)^2 (1 - e^{-415/E})^{0.8} \quad (C.8)$$

At the highest energies observed by the CHEMS instrument, the O^+ on O electron loss collision becomes significant and is an important reaction in the production of suprathermal O^{++} . We fit the O^+ on O electron loss collision cross sections measured by *Lo et al.* [1971] using the functional form of equation C.4:

$$\begin{aligned} \log(\sigma) &= a_0 + a_1 \log_{10}(E) + a_2 (\log_{10}(E))^2 \\ a_0 &= -3.92 \pm 0.24 \\ a_1 &= 2.90 \pm 0.2 \\ a_2 &= -0.454 \pm 0.04 \\ red \chi^2 &= 0.29 \end{aligned} \quad (C.9)$$

Figure C.1c shows the O^+ on O electron capture fit by *Lindsay and Stebbings* [2005] and our O^+ on O electron loss fit. We include the data from the experimental studies *Stebbing et al.* [1964] and *Lo et al.* [1971]. Cross sections for O^+ on OH and O^+ on H_2O were not available within the CHEMS energy range, so we assume that these reactions have the same cross sections as O^+ on O.

H_2^+ on H_2O and H_2^+ on H

Studies involving the H_2^+ on H_2O collision are very limited. *Dagnac et al.* [1970] measured the electron capture cross section of H_2^+ on H_2O for energies ranging from 1-60 keV, but did not include dissociation of H_2^+ . We could not find any cross section data for H_2^+ on O or H_2O for energies greater than 60 keV. We assumed that the cross sections of H_2^+ on the water group neutrals are the same as the cross sections of the H_2^+ on H reaction. We use the H_2^+ on H cross sections from two studies [*McGrath et al.*, 2001;

Hennecart and Pascale 2005] that contain all the H_2^+ loss processes (i.e. capture and dissociation). The cross sections of H_2^+ on H from these studies join smoothly to the H_2^+ on H_2O cross sections measured by *Dagnac et al.* [1970].

We use the functional form from equation C.4 to fit the H_2^+ cross sections:

$$\begin{aligned}\log(\sigma) &= a_0 + a_1 \log_{10}(E) + a_2 (\log_{10}(E))^2 + a_3 (\log_{10}(E))^3 \\ a_0 &= 0.68 \pm 0.073 \\ a_1 &= 1.16 \pm 0.1 \\ a_2 &= -0.938 \pm 0.05 \\ a_3 &= 0.148 \pm 0.008 \\ \text{red } \chi^2 &= 2.66\end{aligned}\tag{C.10}$$

Our fit is shown in Figure C.1d. As shown in Figure C.1d, the low energy points estimated by the *Hennecart and Pascale* [2005] model do not agree with the experimental data and were not included in the fit. The model used by this study (classical trajectory Monte Carlo model) is typically not accurate at lower energies.

O^{++} on H

Cross sections for O^{++} on H_2O or O^{++} on O were not available at the CHEMS energy range, so we assumed that the cross sections for these reactions were the same as the O^{++} on H collision. The O^{++} on H cross sections were fit using Chebychev polynomials at Oak Ridge National Laboratory [*Phaneuf et al.*, 1987]. Figure C.2a shows the O^{++} on H fit along with the experimental data from *Phaneuf et al.* [1978, 1982].

He^+ on H_2O

We obtained cross sections for both the electron capture He^+ on H_2O reaction and the electron loss He^+ on H_2O reaction from *Rudd et al.* [1985b]. We use interpolation to get

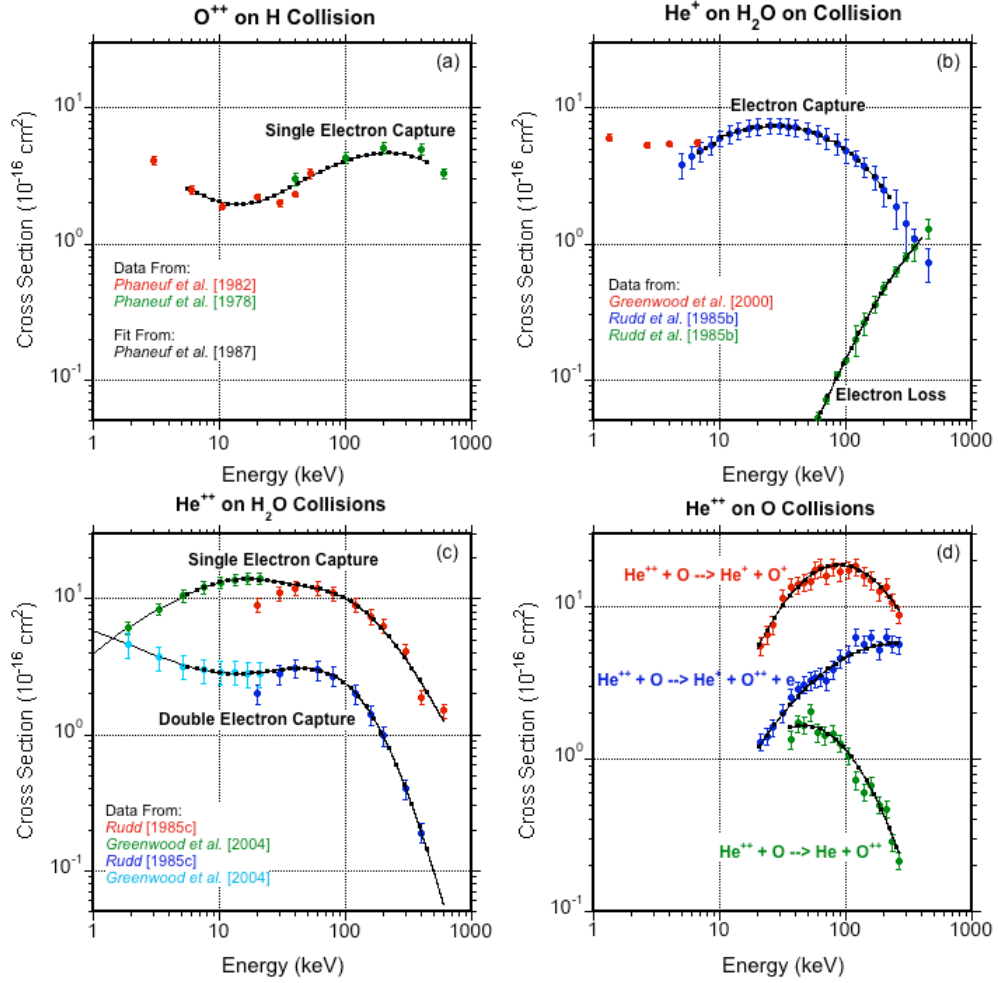


Figure C.2: (a) H^+ on O cross sections as a function of energy. The single electron capture fit is from Lindsay and Stebbings [2005]. The transfer ionization reaction is negligible compared to the electron capture. (b) Electron capture cross sections as a function of energy for the H^+ on H_2O collision. (c) Electron capture and electron loss cross sections for O^+ on O. The single electron capture cross section fit is from Lindsay and Stebbings [2005]. (d) Cross sections for the H_2^+ on H_2O and H. The green points are from the H_2^+ on H_2O electron capture cross section, while the blue and red points are for the H_2^+ on H collisions and include both dissociation and capture. See text for details. The black points in all plots represent the cross sections at the CHEMS E/Q steps.

the single electron capture He^+ on H_2O cross sections at the CHEMS E/Q steps. A fourth order polynomial was used to fit the electron loss collisions:

$$\sigma = 0.00458 - 4.62 \times 10^{-4} E + 2.44 \times 10^{-5} E^2 - 6.54 \times 10^{-8} E^3 + 6.13 \times 10^{-11} E^4 \quad (\text{C.11})$$

$$R = 0.99998$$

The electron loss collision plays a relatively minor role at lower energies. Because cross sections for He^+ on O and OH were not available, we assumed that the cross section for

these collisions were the same as the He^+ on H_2O cross section. Figure C.2b shows a plot of the cross sections versus energy.

He^{++} on H_2O

The experimental studies by *Rudd et al.* [1985c] and *Greenwood* [2004] measured the single electron and double electron cross sections for the reaction He^{++} on H_2O . For both reactions we use a similar functional form as the H^+ on H_2O single electron capture cross section:

$$\begin{aligned}\sigma &= (a_1 - a_2 \ln E)^2 (1 - e^{-a_3/E})^{a_4} + (a_1 - a_5 \ln E)^2 (1 - e^{-a_6/E})^{a_4} \\ a_1 &= -1.41 \pm 0.138 \\ a_2 &= 0.446 \pm 0.0978 \\ a_3 &= 216 \pm 65.8 \\ a_4 &= 2.26 \pm 0.378 \\ a_5 &= 0.623 \pm 0.155 \\ a_6 &= 31.5 \pm 13.3 \\ \text{red. } \chi^2 &= 0.748\end{aligned}\tag{C.12}$$

The double electron capture cross section has a very low reduced χ^2 , and the uncertainties in the fitting parameters are very large:

$$\begin{aligned}\sigma &= (a_1 - a_2 \ln E)^2 (1 - e^{-a_3/E})^{a_4} + (a_1 - a_5 \ln E)^2 (1 - e^{-a_6/E})^{a_4} \\ a_1 &= -1.72 \pm 0.13 \\ a_2 &= -0.0148 \pm 0.062 \\ a_3 &= 294 \pm 88 \\ a_4 &= 4.1 \pm 1.1 \\ a_5 &= -0.662 \pm 0.17 \\ a_6 &= 87.2 \pm 89 \\ \text{red. } \chi^2 &= 0.0069\end{aligned}\tag{C.13}$$

As shown in Figure C.2c, both fits do a good job estimating the cross sections of He^{++} on H_2O . The addition of more data points will improve the uncertainties of the fitting parameters. We assume that the He^{++} on OH cross sections are the same as the He^{++} on OH cross sections.

He⁺⁺ on O

We fit the data from the *Thompson et al.* [1997] experimental study to obtain cross sections for single electron capture, transfer ionization, and double electron capture collisions of He⁺⁺ on O. We use equation C.4 to fit all three reactions. Here is the fit for single electron capture:

$$\begin{aligned}\sigma &= a_0 + a_1 \log(E) + a_2 (\log(E))^2 \\ a_0 &= -3.69 \pm 0.41 \\ a_1 &= 5.10 \pm 0.45 \\ a_2 &= -1.31 \pm 0.12 \\ \text{red } \chi^2 &= 0.30\end{aligned}\tag{C.14}$$

The transfer ionization cross section is

$$\begin{aligned}\sigma &= a_0 + a_1 \log(E) + a_2 (\log(E))^2 \\ a_0 &= -2.52 \pm 0.41 \\ a_1 &= 2.73 \pm 0.45 \\ a_2 &= -0.568 \pm 0.12 \\ \text{red } \chi^2 &= 0.46\end{aligned}\tag{C.15}$$

The double electron capture cross section is determined by the following formula:

$$\begin{aligned}\sigma &= a_0 + a_1 \log(E) + a_2 (\log(E))^2 \\ a_0 &= -3.86 \pm 0.85 \\ a_1 &= 4.90 \pm 0.87 \\ a_2 &= -1.47 \pm 0.22 \\ \text{red } \chi^2 &= 1.08\end{aligned}\tag{C.16}$$

We do not have experimental data points for the entire CHEMS energy range. Because we only have cross section measurements up to 127 keV/e, we do not recommend using these He⁺⁺ on O cross section fits above this energy.

These are all the cross section measurements used in this study. Table C.1 lists the collisions used along with the data references and the fits. As a reminder, the energy for all fits is in units of keV, and the units of the cross sections are in 10^{16} cm^2 . Using

Table C.1: Ion-neutral reactions included in our suprathermal ion lifetime calculations. The cross section references and fits as a function of energy are shown in the table.

Reaction	Experimental and Theoretical References	Fit
$H^+ + O \rightarrow H + O^+$	<ul style="list-style-type: none"> • <i>Thompson et al.</i> [1996] • <i>Stebbins et al.</i> [1964] 	<i>Lindsay and Stebbins</i> [2005]
H^+ on H_2O (SEC)	<ul style="list-style-type: none"> • <i>Dagnac et al.</i> [1970] • <i>Rudd et al.</i> [1985a] • <i>Lindsay et al.</i> [1997] • <i>Greenwood et al.</i> [2000] • <i>Gobet et al.</i> [2004] • <i>Luna et al.</i> [2007] 	Equation C.7
$O^+ + O \rightarrow O + O^+$	<ul style="list-style-type: none"> • <i>Stebbins et al.</i> [1964] • <i>Lo et al.</i> [1971] 	<i>Lindsay and Stebbins</i> [2005]
$O^+ + O \rightarrow O^{++} + O + e$	<ul style="list-style-type: none"> • <i>Lo et al.</i> [1971] 	Equation C.9
H_2^+ on H_2O (SEC)	<ul style="list-style-type: none"> • <i>Dagnac et al.</i> [1970] 	Equation C.10
H_2^+ on H (all loss processes)	<ul style="list-style-type: none"> • <i>McGrath et al.</i> [2001] • <i>Hennecart and Pascale</i> [2005] 	Equation C.10
$O^{++} + H \rightarrow O^+ + H^+$	<ul style="list-style-type: none"> • <i>Phaneuf et al.</i> [1978] • <i>Phaneuf et al.</i> [1982] 	Phaneuf et al. [1987]
He^+ on H_2O (SEC)	<ul style="list-style-type: none"> • <i>Rudd et al.</i> [1985b] 	Interpolation
He^+ on H_2O (e- loss)	<ul style="list-style-type: none"> • <i>Rudd et al.</i> [1985b] 	Equation C.11
He^{++} on H_2O (SEC)	<ul style="list-style-type: none"> • <i>Rudd et al.</i> [1985c] • <i>Greenwood</i> [2004] 	Equation C.12
He^{++} on H_2O (DEC)	<ul style="list-style-type: none"> • <i>Rudd et al.</i> [1985c] • <i>Greenwood</i> [2004] 	Equation C.13
$He^{++} + O \rightarrow He^+ + O^+$	<ul style="list-style-type: none"> • <i>Thompson et al.</i> [1997] 	Equation C.14
$He^{++} + O \rightarrow He^+ + O^{++} + e$	<ul style="list-style-type: none"> • <i>Thompson et al.</i> [1997] 	Equation C.15
$He^{++} + O \rightarrow He + O^{++}$	<ul style="list-style-type: none"> • <i>Thompson et al.</i> [1997] 	Equation C.16

equation C.1, the lifetimes of these species at $L=9.5$ due to the ion-neutral collisions are shown in Figure C.3.

Electron Impact

Electron impact ionization and electron impact dissociation are both potential loss processes for suprathermal ions. Because the suprathermal ion lifetimes due to electron impact depends on the electron velocity, calculating the electron impact lifetimes is more complicated than calculating the ion-neutral collisions. In addition to the electron impact

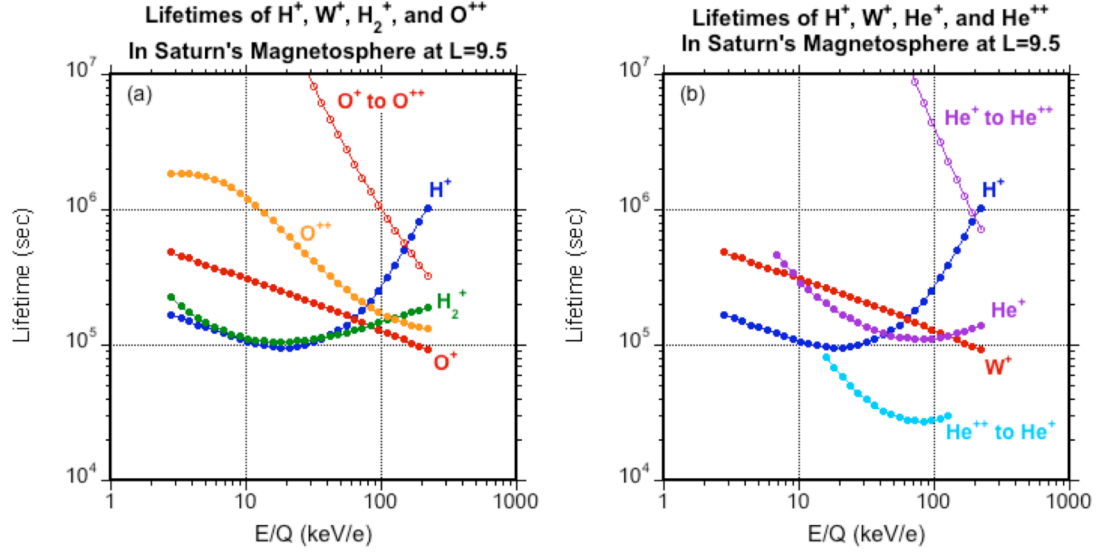


Figure C.3: (a) Lifetimes at L=9.5 due to ion-neutral collisions for the ion species H⁺, H₂⁺, O⁺, and O⁺⁺. (b) Lifetimes at L=9.5 due to ion-neutral collisions for the ion species H⁺, W⁺, He⁺, and He⁺⁺.

cross sections, we must obtain the electron velocity distribution $f(v_e)$ and the electron number density n_e in Saturn's magnetosphere.

Schippers et al. [2008] combined the electron observations from CAPS Electron Spectrometer (ELS) and MIMI LEMMS and fit the electron spectra. Based on these observations, *Schippers et al.* [2008] concluded that the electron velocity distribution for both electron components could be best fit with a kappa distribution:

$$f(v) = \frac{n\Gamma(\kappa+1)}{\omega_0^3 \pi^{3/2} \Gamma(\kappa-1/2)} \left[1 + \frac{v^2}{\kappa\omega_0^2} \right]^{-\kappa-1} \quad (\text{C.17})$$

The quantity ω_0 is the average thermal velocity and depends on the electron mass m and electron temperature T :

$$\omega_0^2 = \frac{2\kappa-3}{m\kappa} T \quad (\text{C.18})$$

Schippers et al. [2008] fit the electron data from Rev 24 in 2006 to determine the electron density n_e , electron temperature T , and kappa as a function of L .

The cold electron parameters can be calculated by using the following equations

$$n_{e,cold}(cm^{-3}) = \begin{cases} (3.8 \times 10^4) L^{-3.9} & L < 9 \\ (3.9 \times 10^4) L^{-3.9} - 0.9 & L = 9 - 14 \end{cases} \quad (C.19)$$

$$T_{e,cold}(eV) = \begin{cases} (6.8 \times 10^{-5}) L^{5.9} & L < 9 \\ (4.245 \times 10^3) L^{-2.3} & L = 9 - 14 \end{cases} \quad (C.20)$$

$$\kappa_{cold} = \begin{cases} (2.4 \times 10^9) L^{-11.4} + 1.9 & L < 9 \\ 0.2 L^{0.6} + 1 & L = 9 - 14 \end{cases} \quad (C.21)$$

[Schippers *et al.*, 2008]. The kappa for the hot component does not show a trend with L and averages about 4 for $L < 14$. Thus, we use $\kappa=4$ for the hot electron component. The density and temperature of the hot component can be calculated using these equations:

$$n_{e,hot} = \begin{cases} (4.8 \times 10^{-6}) L^{5.1} & L < 9 \\ 13.9 L^{-1.9} & L = 9 - 14 \end{cases} \quad (C.22)$$

$$T_{e,hot} = \begin{cases} 0.2 L^{4.3} & L < 9 \\ (1.2 \times 10^6) L^{-2.7} & L = 9 - 14 \end{cases} \quad (C.23)$$

Like the ion-neutral collisions, we will calculate the lifetimes at $L=9.5$ where the suprathermal ion partial number density typically peaks.

We used the electron impact ionization cross section fits from *Mattioli et al.* [2007] to determine the electron impact lifetimes of He^+ , C^+ , N^+ , and O^+ . *Mattioli et al.* [2007] used the following function to determine the electron impact cross sections as a function of energy E:

$$\sigma(E) = \frac{1}{EI} \left[A(1 - I/E) + B(1 - I/E)^2 + C \ln(E/I) + DI \frac{\ln(E/I)}{E} \right] \quad (C.24)$$

Table C.2: Fitting parameters for the electron impact ionization cross sections [See Mattioli et al., 2007]. The units of parameters A, B, C, and D is $10^{-14} \text{ cm}^2 \text{ eV}^2$, while the Ionization energy I is in units of eV.

Species	I	A	B	C	D
H	13.60	13.50	-7.20	2.60	-14.40
O	13.60	-13.40	-18.25	23.05	-7.40
He ⁺	54.52	21.20	-10.60	1.60	-19.70
C ⁺	24.40	-7.55	3.20	11.40	1.95
N ⁺	29.60	31.15	-16.50	12.45	-38.05
O ⁺	35.1	-90.90	36.43	36.07	58.83

The quantities A, B, C, and D are fitting parameters in units of $10^{-14} \text{ cm}^2 \text{ eV}^2$, while E is the collision energy in eV and I is the ionization potential in eV. The parameters are shown in Table C.2 for H, O, He⁺, C⁺, N⁺, and O⁺. A plot of the electron impact ionization cross sections versus electron energy for the four ion species are shown in Figure C.4.

We also consider electron impact dissociation of H₂⁺. *Dunn and Van Zyl* [1967] fit these cross sections at energies greater than 20 eV. At some radial distances, the thermal electrons in Saturn's magnetosphere have energies less than 20 eV, so we fit the cross sections at low energies measured by *Peart and Dolder* [1972] and *Yousif and Mitchell* [1995]. We find that a logarithmic fit of the cross sections fits the data between 0.1 to 20 eV. Here is the equations that we use to fit the e- impact dissociation cross section of H₂⁺:

$$\sigma(\text{cm}^2) = \begin{cases} [126.55 - 60.088 \log_{10}(E)] (10^{-17} \text{ cm}^2) & 0.1 \text{ eV} < E < 20 \text{ eV} \\ \frac{94.3 \ln(E) - 184}{E} \pi a_0^2 & E > 20 \text{ eV} \end{cases} \quad (\text{C.25})$$

The parameter a_0 is the Bohr radius and is equal to $5.29 \times 10^{-9} \text{ cm}^2$. A plot of both fits and the electron impact dissociation cross section data is shown in Figure C.5.

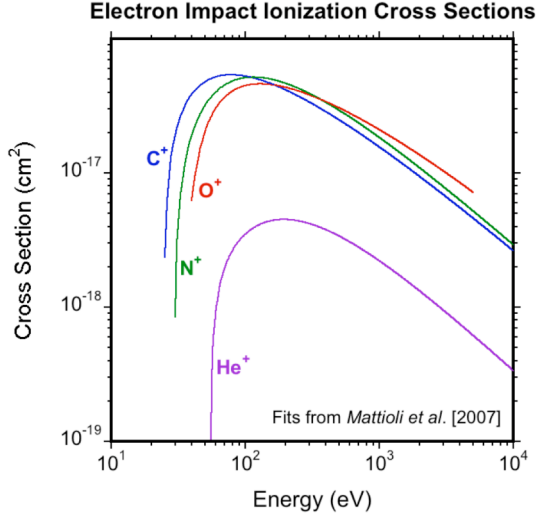


Figure C.4: Electron impact ionization cross sections for C^+ , N^+ , O^+ , and He^+ as a function of energy. Cross sections are from the fits by Mattioli et al. [2007].

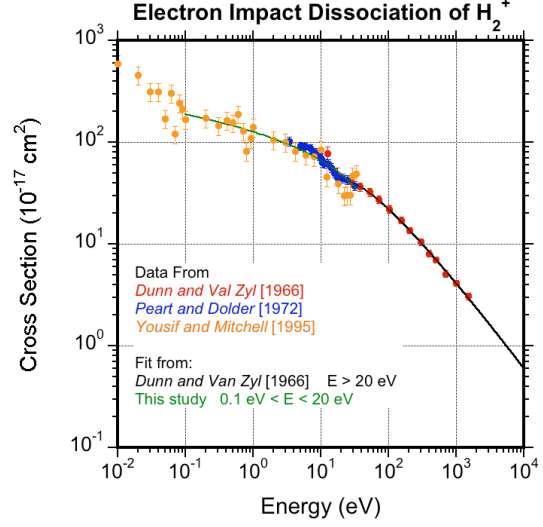


Figure C.5: The electron impact dissociation cross sections of H_2^+ as a function of energy. The black line is the fit done by Dunn and Van Zyl [1966] and accurately fits the cross sections for $E > 20$ eV. The green line is a fit done by this study that fits the cross sections for $0.1 \text{ eV} < E < 20 \text{ eV}$.

We can now calculate the collision lifetime using the following equation:

$$\frac{1}{\tau} = n_e \int V_{rel} \sigma(V_{rel}) f(v_e) d^3 v_e = 4\pi n_e \int_0^\infty v_e^2 V_{rel} \sigma(V_{rel}) f(v_e) dv_e \quad (C.26)$$

The quantity V_{rel} is the relative collision velocity between the electron and ion in the center-of-mass frame. If the electron velocities v_e and the ion velocities v_i are in random directions, the relative collision velocity is

$$V_{rel} = \sqrt{v_e^2 + v_i^2} \quad (C.27)$$

Because the collision cross sections from Mattioli et al. [2007] are given as a function of energy, we convert the electron velocity v_e in equation C.26 to electron energy E_e .

We make the following substitutions to convert the integrating quantity from electron velocity v_e to electron energy E_e :

$$\begin{aligned}
E_e &= \frac{1}{2} m v_e^2 \\
dv_e &= \frac{dE_e}{\sqrt{2mE_e}} \\
E_i &= \frac{1}{2} M v_i^2 \\
W_0 &= \frac{1}{2} m \omega_0^2 = T \left(1 - \frac{3}{2\kappa} \right)
\end{aligned} \tag{C.26}$$

In the above equations, E_i is the ion energy, M is the ion mass, and W_0 is the average thermal energy. Substituting these quantities into our integral, we get

$$\frac{1}{\tau} = \sqrt{\frac{8}{\pi m W_0 \kappa^3}} \frac{\Gamma(\kappa + 1)}{\Gamma(\kappa - 1/2)} \int_0^\infty \sigma(E_{com}) \sqrt{\frac{E_e}{W_0} \left(\frac{E_e}{W_0} + \frac{m}{M} \frac{E_i}{W_0} \right)} \left[1 + \frac{E_e}{W_0 \kappa} \right]^{-\kappa-1} dE_e \tag{C.27}$$

The quantity E_{com} is the center of mass energy of the collision and is calculated by

$$E_{com} = \frac{M}{M + m} \left(E_e + \frac{m}{M} E_i \right) \tag{C.28}$$

When calculating the electron impact lifetime due to the hot electrons, the ion energy is negligible. For electron impact due to the cold electron component, however, the electron impact lifetime depends on the ion energy.

To simplify the integration, we make the substitution $u = E_e/W_0$. After making this substitution, we calculate the electron impact lifetimes using the following equation:

$$\frac{1}{\tau} = \sqrt{\frac{8W_0}{\pi m \kappa^3}} \frac{\Gamma(\kappa + 1)}{\Gamma(\kappa - 1/2)} \int_0^\infty \sigma(E_{com}) \sqrt{u \left(u + \frac{m}{M} \frac{E_i}{W_0} \right)} \left[1 + \frac{u}{\kappa} \right]^{-\kappa-1} du \tag{C.29}$$

The above integral cannot be determined analytically, so we integrate equation C.29 numerically using Romberg integration [Press *et al.*, 1989].

We can now estimate the electron impact lifetimes of the suprathermal ions. The electron impact ionization lifetimes of C^+ , N^+ , and O^+ all range from $\sim 4\text{--}7 \times 10^7$ s due to the cold component and $\sim 1\text{--}3 \times 10^8$ s due to the hot component. The H_2^+ electron impact lifetimes range from $\sim 1.5\text{--}1.7 \times 10^6$ s due to the cold electrons and $\sim 8.5\text{--}8.6 \times 10^7$ due to the hot electrons. Compared to the ion-neutral lifetimes shown in Figure C.3, the electron impact lifetimes are much longer and are negligible.

Photoionization and Photodissociation

Photodissociation and photoionization by solar photons are another potential loss process for suprathermal ions. The solar fluxes $\phi(\lambda)$ at 1 astronomical unit (AU) over several wavelength bins $\Delta\lambda$ can be found in *Huebner et al.* [1992]. To calculate the fluxes at Saturn, we multiply the values in *Huebner et al.* [1992] by $1/r^2$ where r is the average distance between Saturn and the Sun in astronomical units AU ($r=9.6$ AU). *Verner et al.* [1996] fit the photoionization cross sections σ as a function of photon energy ($E=hc/\lambda$) for several ion species. The fitting functions from *Verner et al.* [1996] are complicated and will not be shown here. Using the solar fluxes from Huebner and the cross sections from *Verner et al.* [1996], we can calculate the photoionization lifetimes:

$$\frac{1}{\tau} = \sum_{\lambda=0}^{140000 \text{ \AA}} \Delta\lambda \phi(\lambda) \sigma(\lambda) \quad (C.36)$$

The photoionization lifetimes for O^+ and He^+ are $\sim 7 \times 10^8$ s and 7.9×10^9 s, respectively making this reaction negligible. However, the production of O^{++} due to photoionization of O^+ becomes significant inside of 7 R_S .

The photodissociation lifetimes of H_2^+ in Saturn's magnetosphere were calculated in *Hamilton et al.* [1983]. The H_2^+ lifetimes vary significantly with vibrational state v . For $v \geq 5$, the photodissociation lifetime of H_2^+ is very short and is estimated to be less than 504 seconds [*Hamilton et al.*, 1983]. The lifetimes for vibrational states for $v=2$, $v=3$, and $v=4$ are 8.22×10^4 s, 1.02×10^4 s, and 1.82×10^3 s, respectively [*Hamilton et al.*, 1983] making the H_2^+ photodissociation lifetimes at these states less than the ion-neutral lifetimes. The photodissociation of H_2^+ at the vibrational states $v=0$ and $v=1$ is much longer and is estimated to be 1.75×10^7 s and 1.34×10^6 , respectively [*Hamilton et al.*, 1983].

Production rates

To estimate the source rates of thermal O^{++} in Saturn's magnetosphere, we use the same procedure and cross sections discussed above to calculate the electron impact ionization and photoionization lifetimes of O^+ . Here we are interested in the collisions between the thermal O^+ and electrons. Because the thermal ion velocity is much less than the velocities of both electron components, the electron impact ionization lifetime of thermal O^+ does not depend on the ion energy.

The double ionization of neutral O by electron impact is also an important mechanism in the production of thermal O^{++} . *Taluker et al.* [2009] fit the double electron impact ionization of O cross sections, but their fit does not agree with the experimental observations at energies greater than 200 eV. At high electron energies E , the electron impact cross section is predicted to be proportional to $\ln(E/I)/(E/I)$ [*Lotz 1968; Taluker et*

al., 2009]. The quantity I is called the threshold energy and is determined by adding the first and second ionization potentials of O ($I=48.73$ eV) [Taluker *et al.*, 2009]. To fit the double electron impact ionization cross sections at $E > 200$ eV, we multiplied the cross sections measured by Thompson *et al.* [1995] by the ratio of E/I and performed a logarithmic fit. We use the following equations to calculate the double electron impact ionization cross section of neutral O:

$$\sigma(10^{-17} \text{ cm}^2) = \begin{cases} \frac{8 \times 10^4}{I^3 E} [219.67 \ln(E/I) - 215.57(1 - I/E)] & E < 200 \text{ eV} \\ \frac{1.9 + 0.57 \log_{10}(E/I)}{E} (I) & E > 200 \text{ eV} \end{cases} \quad (\text{C.37})$$

The electron energy is in units of eV, while the cross sections are in units of 10^{-17} cm^2 . A plot of our fit along with the experimental measurements from Thompson *et al.* [1995], Ziegler *et al.*, 1982], and Zipf *et al.* [1985] is shown in Figure C.6.

We calculate the thermal O^{++} source rate separately for each process and then add them to determine the overall source rate. The source rate of thermal O^{++} due to single ionization of O^+ is calculated by dividing the W^+ density observed by Thomsen *et al.* [2010] by each single ionization collision lifetime discussed above. Because W^+ does not consist entirely of O^+ , we are likely overestimating the O^{++} source rate due to the single ionization of O^+ . To calculate the O^{++} source rate due to double ionization of neutral O, we divide the neutral O densities estimated by Cassidy and Johnson [2010] by each double ionization collision lifetime. As shown in Figure C.7, the lifetimes of double ionization of neutral O are much longer than the single ionization lifetimes of O^+ . However, since the neutral O density is much larger than the plasma density, both processes play a significant role. The production rates of thermal O^{++} are shown in Figure 3.7.

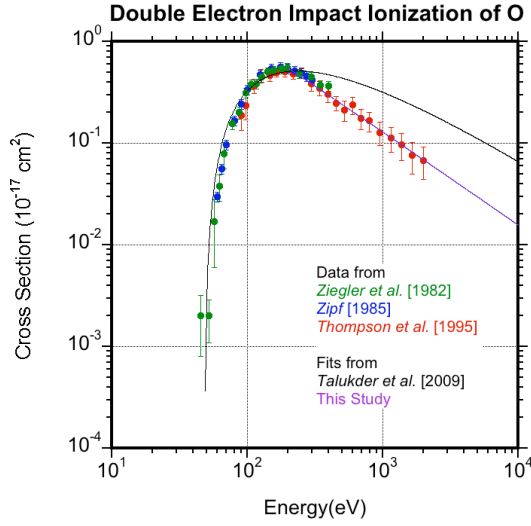


Figure C.6: Cross sections for double electron impact ionization of atomic O. We use the fit from Talukder et al. [2009] for energies less than 200 eV and our fit for energies greater than 200 eV. See text for details.

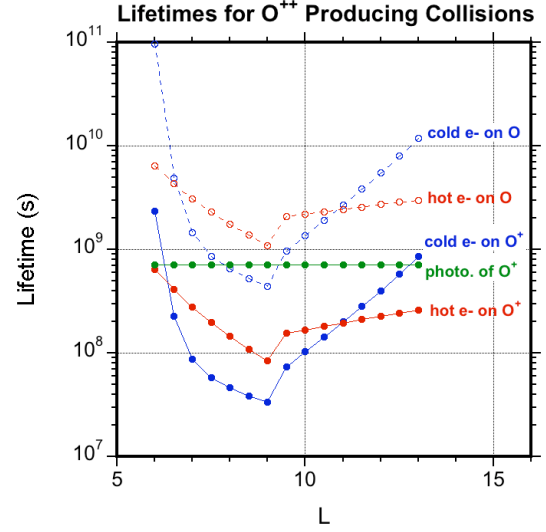


Figure C.7: Lifetimes versus L for the collisions that produce thermal O^{++} . The blue points are collisions involving the cold electrons, while the red points are collisions involving the hot electrons. Solid points are collisions that ionize O^+ and open points are collisions the double ionization collisions of atomic O.

Appendix D

Fitting the 96 keV W^+ Distribution

Here we discuss in more detail how we fit the W^+ time-of-flight (TOF) distribution and separated W^+ into its four major components: O^+ , OH^+ , H_2O^+ , and H_3O^+ . We show the fitting parameters from all three types of fits from the ring current and the fits from each L range. We use the Levenberg-Marquardt method [Press *et al.*, 1989; Bevington and Robinson 2003] to perform all the W^+ fits. The parameter uncertainties are the statistical uncertainties that are determined by taking the square root of the diagonal terms of the covariant matrix (i.e. error matrix) from the fitting routine [Press *et al.*, 1989; Bevington and Robinson 2003]. As discussed in chapter 5, we were only able to fit the W^+ components for the data from telescope 1 at $E/Q=96$ keV/e.

Fitting O^{++} at $E/Q=48$ keV/e

Since the O^{++} data at the $E/Q=48$ keV/e step has approximately same energy as O^+ at the $E/Q=96$ keV/e step, the 48 keV/e O^{++} TOF distribution is nearly identical to 96 keV/e O^+ distribution. We can easily fit the 96 keV O^{++} (i.e. 48 keV/e O^{++}) distribution since there is no overlap from other ion species and use the result in fitting the O^+ . We fit two different functions to the O^{++} distribution. One is an asymmetric Gaussian:

$$f(\tau) = A \left[e^{-\frac{(\tau-\tau_c)^2}{2\sigma_1^2}} P(-\tau + \tau_c) + e^{-\frac{(\tau-\tau_c)^2}{2\sigma_2^2}} P(\tau - \tau_c) \right] \quad (D.1)$$

The sigmoid function $P(x)$ is an approximation to the Heavyside function that is ~ 0 for $x < 0$ and ~ 1 for $x > 0$:

$$P(x) = \frac{1}{1 + e^{-x}} \quad (\text{D.2})$$

Using the sigmoid function allows us to fit a continuous function to the distribution rather than having to perform two separate Gaussian fits on the left and the right side of the distribution. The function $f(\tau)$ maximizes at $\tau = \tau_c$ with an amplitude A . The parameters σ_1 and σ_2 are the Gaussian sigma for the left side and right side of the distribution, respectively.

Gaussian fits performed by *von Steiger et al.* [2000] on ion species distributions from the Ulysses Solar Wind Composition Spectrometer revealed that the sigma to center ratios of the different species is relatively constant. The O^{++} Gaussian sigma to center ratio observed by the CHEMS instrument did not vary significantly with energy. Therefore, we use the σ_1/τ_c and σ_2/τ_c ratios as fitting parameters rather than σ_1 and σ_2 . When fitting the asymmetric Gaussian, we only attempted to fit the TOF channels near the center of the distribution (TOF=183-197), where the distribution behaves like a Gaussian. Our asymmetric Gaussian fit of 96 O^{++} is shown in Figure D.1.

The asymmetric Gaussian fits the center of the distribution, but fails at larger TOF channels where the counts decline more slowly than a Gaussian. We refer to this region of the distribution as the tail. *Allegini et al.* [2006] studied the energy loss of 1-50 keV ions traveling through thin, carbon foils and observed a similar skewed distribution. They fit their energy histograms using a kappa distribution. The kappa distribution did not fit

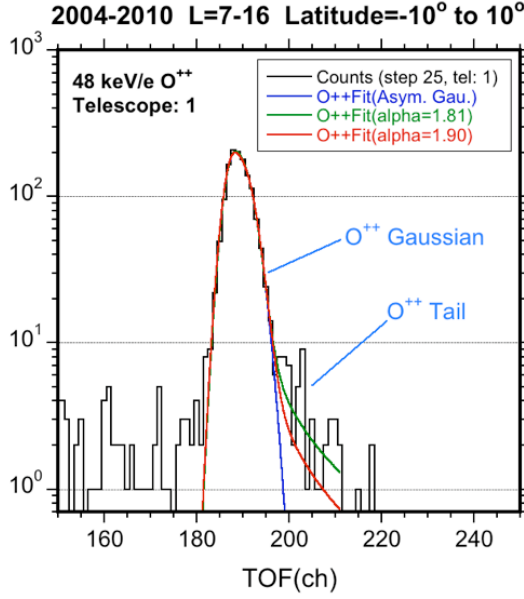


Figure 1: The 96 keV O^{++} TOF distribution with the three types of fits: Asymmetric Gaussian (blue), equation D.4 with $\alpha=1.81$ (green), and equation D.4 with $\alpha=1.90$ (red). Near the center, the fits are similar and overlap.

the tail counts. When trying to fit the TOF distribution observed by CHEMS with a kappa distribution, our best fit had a large kappa value making the fit essentially the same as an asymmetric Gaussian.

To fit the tail counts, we added a small additional term to the Gaussian on the right side of the distribution. Away from the center of the distribution, a kappa distribution behaves like a power law.

Therefore, we define a function $f_{add}(\tau)$ that

is negligible near the center and behaves like a power law for $\tau \gg \tau_c$:

$$f_{add}(\tau) = \frac{(\tau - \tau_c)^2}{100 + [(\tau - \tau_c)^2]^\alpha} \quad (D.3)$$

We add equation D.3 to the Gaussian term on the right side of the distribution to fit the tail counts on the right side of the distribution. Our fitting function becomes

$$f(\tau) = A \left[e^{-\frac{(\tau - \tau_c)^2}{2\sigma_1^2}} P(-\tau + \tau_c) + \left(e^{-\frac{(\tau - \tau_c)^2}{2\sigma_2^2}} + \frac{(\tau - \tau_c)^2}{100 + [(\tau - \tau_c)^2]^\alpha} \right) P(\tau - \tau_c) \right] \quad (D.4)$$

For $\tau \gg \tau_c$ the function declines as $\sim [(\tau - \tau_c)^2]^{(1-\alpha)}$, so the parameter α controls the rate of decline in the tail. We fit the O^{++} distribution using equation D.4 and require that the parameters τ_c and σ_1 are the same as that from the asymmetric Gaussian fit. Because we include the additional term, we can fit a larger range of TOF channels (183-211) and

Table D.1: The parameter values from all three types of fits on the O^{++} distribution along with the Reduced χ^2 to test the goodness of the fit.^a

Parameter	O^{++} Ring Current Asym. Gaussian	O^{++} Ring Current Vary α	O^{++} Ring Current $\alpha=1.90$
TOF fit range	183-197	183-211	183-211
A	203.2 ± 7.1	203.2 ± 6.5	199.9 ± 6.3
τ_c	188.5 ± 0.2	188.5 ± 0.2	188.4
σ_1/τ_c	$(1.12 \pm 0.07) \times 10^{-2}$	1.12×10^{-2}	1.12×10^{-2}
σ_2/τ_c	$(1.67 \pm 0.07) \times 10^{-2}$	(1.52 ± 0.05)	$(1.61 \pm 0.05) \times 10^{-4}$
α	N/A	1.81 ± 0.03	1.90
Reduced χ^2	0.27	0.73	0.51

^a The parameter uncertainties reflect the statistical uncertainties from our fits. When a parameter value in the table above does not have an uncertainty, it was forced to equal that value and not allowed to vary during the fitting routine. See text for details. The TOF fit range refers to the range of TOF channels used to fit the O^{++} .

obtain a better estimate of the O^{++} counts. This fit is plotted in Figure D.1 and shows that using equation D.4 provides a better fit to the O^{++} distribution. The fitting parameters for both types along with the reduced χ^2 are shown in Table D.1.

Fitting W^+ in the main ring current

In order to determine the sensitivity of our results to the form of the fitting function, we have performed three different fits on the W^+ distribution: (1) asymmetric Gaussian ($\alpha=\infty$), (2) requiring α to equal the value from the O^{++} fit ($\alpha=1.81$), and (3) allowing α to vary. For the first two fits, we require the σ_1/τ_c and σ_2/τ_c values for O^+ to equal the results from the O^{++} fits. Since the value of the α constant affects the value of σ_2 , we let both σ_2 and α vary for the third fit. The widths of the molecular ion distributions tend to differ from those of atomic ions, so the σ_1/τ_c and σ_2/τ_c ratios of OH^+ , H_2O^+ , and H_3O^+ are not the same as O^+ . However, we forced these ratios to be the same for all three molecular species. The α parameter is assumed to be the same for all four species.

We first fit the W^+ distribution using the asymmetric Gaussian function. We only include the TOF channels near the center of the peaks (TOF channels=182-212) when performing the fit, so we do not attempt to fit the tails. Our asymmetric Gaussian fit is shown in Figure D.2a, while the fitting parameters and their uncertainties are shown in Table D.2. The parameter τ_c for all four species has a very low uncertainty along with the σ_1/τ_c and σ_2/τ_c parameters for the molecular ions. However, we are clearly leaving out a large number of counts in the tail. While the asymmetric Gaussian fits the centers of the peaks, equation D.4 provides a better fit of the distribution.

Next we attempt to fit the W^+ distribution using equation D.4 and force the α parameter to equal the value from the O^{++} fit ($\alpha=1.81$). We force the τ_c parameter for each species to be the same as that from the Gaussian fits. The σ_1/τ_c and σ_2/τ_c parameters of the O^+ distribution is forced to be the same as the values from the O^{++} fit, and the σ_1/τ_c parameter of the molecular ions is forced to be the same as the asymmetric Gaussian W^+ fit. The results of this fit is shown in Figure D.2b. This function does a better job fitting the tails than the asymmetric Gaussian, but the α parameter appears to be too small. As a result, our function over estimates the tail counts.

In our third fit, we let the α parameter vary. Like the previous fit, we force the parameters τ_c and σ_1/τ_c for all four species to be the same as those from the asymmetric Gaussian fit. We let σ_2/τ_c for O^+ and the molecular ions vary, because the α parameter affects the value of the parameter σ_2/τ_c . The best W^+ fit has a reduced χ^2 of 4.0 and occurs when

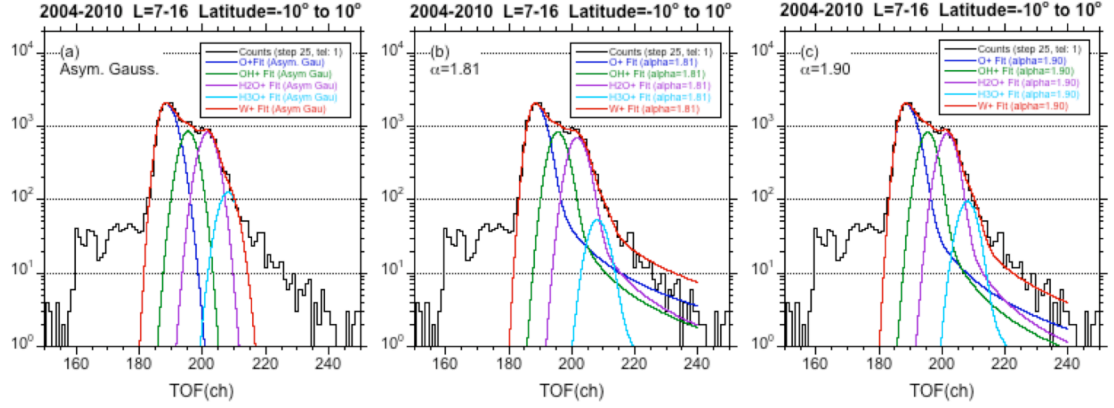


Figure D.2: (a) Asymmetric Gaussian fit of the 96 keV W^+ distribution in the ring current. (b) Fit of the ring current 96 keV W^+ distribution in the ring current using equation D.4 with $\alpha=1.81$. (c) Best fit of the 96 keV W^+ distribution ($\alpha=1.81$). The fits of each individual species are shown along with the sum of the four fits in red.

$\alpha=1.90$. This fit provides the best estimate of the O^+ , OH^+ , H_2O^+ , and H_3O^+ abundances.

We also fit the O^{++} distribution and force α to equal 1.90 to see how well it fits the tail counts. This fit is shown in Figure D.1 and appears to slightly underestimate the O^{++} tail counts. Our estimate of the α parameter will improve as we add more passes to our data set and the statistical uncertainties in the O^{++} distribution improve.

The W^+ TOF channel range at the $E/Q=96$ keV/e step for telescope 1 ranges from 180 to 240. We integrate numerically using the Simpson's method [Press *et al.*, 1989] between these two TOF channels to determine the counts of each ion species. We can then convert these counts to partial number density. Because most of the W^+ counts are between the TOF channels 180-240 and most of the counts are within the asymmetric Gaussian section, we can approximate the species counts by integrating an asymmetric Gaussian function from $-\infty$ to ∞ :

$$Counts = A \sqrt{\frac{\pi}{2}} (\sigma_1 + \sigma_2) \quad (D.5)$$

Table D.2: The fitting parameters for all three types of fits on the W^+ ring current distribution along with the Reduced χ^2 to test the goodness of the fit.^a

Parameter	W^+ Ring Current Asym. Gaussian	W^+ Ring Current $\alpha=1.81$	W^+ Ring Current Vary α
TOF range	182-212	182-240	182-240
$O^+ \sigma_1/\tau_c$	1.12×10^{-2}	1.12×10^{-2}	1.12×10^{-4}
$O^+ \sigma_2/\tau_c$	1.67×10^{-2}	1.52×10^{-2}	$(1.611 \pm 0.04) \times 10^{-2}$
$O^+ A$	2115 ± 35	2098 ± 20	2086 ± 22
$O^+ \tau_c$	188.4 ± 0.04	188.4	188.4
Molecular σ_1/τ_c	$(1.35 \pm 0.09) \times 10^{-2}$	1.35×10^{-2}	1.35×10^{-2}
Molecular σ_2/τ_c	$(1.34 \pm 0.06) \times 10^{-2}$	$(1.39 \pm 0.05) \times 10^{-2}$	$(1.26 \pm 0.04) \times 10^{-2}$
$OH^+ A$	868.0 ± 33	842.9 ± 16	839.0 ± 27
$OH^+ \tau_c$	195.5 ± 0.1	195.5	195.5
$H_2O^+ A$	828.2 ± 23	710.0 ± 23	796.4 ± 21
$H_2O^+ \tau_c$	201.7 ± 0.1	201.7	201.7
$H_3O^+ A$	127.6 ± 17	52.86 ± 7.5	95.34 ± 8.6
$H_3O^+ \tau_c$	208.1 ± 0.3	208.1	208.1
α	N/A	1.81	1.895 ± 0.01

^a The parameter uncertainties reflect the statistical uncertainties from our fits. When a parameter value in the table above does not have an uncertainty (e.g. $O^+ \sigma_1/\tau_c$), it was forced to equal that value and not allowed to vary during the fitting routine. See text for details. The TOF fit range refers to the range of TOF channels used to fit the W^+ .

Although we do not use this equation to determine the counts, we use it to estimate the statistical uncertainties from our fits.

Using the formulas for error propagation [Bevington and Robinson 2003], the statistical uncertainty of the counts is determined by

$$Counts_unc = \sqrt{\Delta A^2 \left(\frac{\pi}{2} \right) (\sigma_1 + \sigma_2)^2 + \frac{\pi}{2} A^2 (\Delta \sigma_1^2 + \Delta \sigma_2^2)} \quad (D.6)$$

The quantities ΔA , $\Delta \sigma_1$, and $\Delta \sigma_2$ are the uncertainties of the parameters A , σ_1 , and σ_2 , respectively. As shown in Table D.2, the uncertainty of the τ_c parameter is very small, so we do not include it when calculating the statistical uncertainties. This formula does not

include the uncertainties in the tail counts, but we estimate that from our three different types of fits. Since the counts in the distribution tails contain only a small percentage of the total counts, our estimates of the O^+ , OH^+ , and H_2O^+ abundances do not vary significantly among the three fits. Therefore, the uncertainty in the abundances of these three species is mostly due to statistical uncertainties from our fits and is estimated using equation D.6.

Because H_3O^+ is much less abundant and the tails from the other three species make up a significant fraction of the counts at the location of the H_3O^+ peak, our estimate of the H_3O^+ counts strongly depends on the α parameter. This introduces a larger systematic error and the quoted H_3O^+ uncertainties reflect the range of values from our three different fits. The asymmetric Gaussian fit with no tails provides an upper limit on the H_3O^+ abundance, while forcing $\alpha=1.81$, which overestimates the tail counts, provides a lower limit.

Fitting the W^+ for different L regions

When fitting the data by L shell, the statistics are worse, and we only let the amplitudes of the peaks vary. We force the τ_c , σ_1 , σ_2 , and α to be the same as the W^+ fits from the ring current. These requirements increase the uncertainties of the fitting parameters σ_1 , σ_2 , and α . To observe how much the O^+ σ_1 might vary in different L ranges, we forced the centers τ_c of each distribution to be the same as those from the ring current fit. We also require that the O^+ σ_2/τ_c to be the same as the O^+ σ_2/τ_c from the asymmetric Gaussian fit of the ring current. We let all other parameters vary and fit the W^+

distribution using asymmetric Gaussians in each L range. We observed that the average $O^+ \sigma_1/\tau_c$ value was the same as the value from the main ring current and showed little variation with L. Therefore, we use the σ_1/τ_c uncertainty from the asymmetric O^{++} fit (7×10^{-4}).

To check the variability of the molecular ion σ_1/τ_c parameter, we force the $O^+ \sigma_1/\tau_c$ value, $O^+ \sigma_2/\tau_c$ value, and the τ_c values for all ion species to be the same as the asymmetric Gaussian fit from the ring current fit. Letting all the other parameters vary, we perform an asymmetric Gaussian fit on the W^+ distribution from each L range. The molecular ion σ_1/τ_c averaged about 1.38×10^{-2} with a standard deviation of 1.92×10^{-3} . This average value was close to the ring current value, so our estimate of the molecular ion σ_2/τ_c provides a good estimate of this parameter. The standard deviation of σ_2/τ_c from these fits was used for the parameter uncertainty.

Finally to determine the uncertainties of $O^+ \sigma_2/\tau_c$, molecular ion σ_2/τ_c , and α , we fit the W^+ distribution from each L range using equation D.4. We force the centers and the σ_1/τ_c values for both O^+ and the molecular ions to be the same as the values from the W^+ ring current fits. We find that the average value for the parameters $O^+ \sigma_2/\tau_c$, molecular ion σ_2/τ_c , and α are 1.62×10^{-2} , 1.28×10^{-2} , and 1.90, respectively. These average values are close to the values obtained by the ring current, so we do not expect the values of these parameters to change significantly with L. We use the standard deviation for the parameter uncertainties, which are 9.75×10^{-4} for $O^+ \sigma_2/\tau_c$, 8.88×10^{-4} for the molecular ion σ_2/τ_c , and 0.03 for α .

Like the fits to the W^+ distribution in the ring current, we perform three types of fits (asymmetric Gaussian, $\alpha=1.81$, and $\alpha=1.90$) to the W^+ distribution in each L range: L=7-8, L=8-9, L=9-10, L=10-11, L=11-13, L=13-15, L=15-18, and L=18-21. The tables on the next four pages contain the fitting parameters for O^+ , OH^+ , H_2O^+ , and H_3O^+ from each L range used in this study. The uncertainties of the parameters are included along with the counts and the partial number densities from each fit. The column labeled sigma1 and sigma2 are the Gaussian sigma on the left and right side of the distribution, respectively and are not the sigma to center ratios. We do not include the uncertainty of τ_c because it is negligible when calculating the statistical error from the fit (See Table D.2).

2004-2010 Latitude=-10° to 10°

O⁺ fit results (alpha=1.90)

Lmin	Lmax	Lmid	Amp	unc	center	sigma1	unc	sigma 2	unc	alpha	unc	Counts	unc	O ⁺ n (cm ⁻³)	unc
7.0	8.0	7.5	187.5	5.8	188.4	2.11	0.13	3.03	0.18	1.90	0.03	1294	65.0	1.89E-05	9.47E-07
8.0	9.0	8.5	328.0	7.7	188.4	2.11	0.13	3.03	0.18	1.90	0.03	2264	105.4	3.79E-05	1.76E-06
9.0	10.0	9.5	316.0	7.6	188.4	2.11	0.13	3.03	0.18	1.90	0.03	2181	102.1	4.78E-05	2.23E-06
10.0	11.0	10.5	303.3	7.3	188.4	2.11	0.13	3.03	0.18	1.90	0.03	2094	98.0	3.81E-05	1.78E-06
11.0	13.0	12.0	421.9	8.7	188.4	2.11	0.13	3.03	0.18	1.90	0.03	2912	132.0	2.02E-05	9.15E-07
13.0	15.0	14.0	295.1	7.3	188.4	2.11	0.13	3.03	0.18	1.90	0.03	2037	95.9	1.25E-05	5.88E-07
15.0	18.0	16.5	310.4	7.5	188.4	2.11	0.13	3.03	0.18	1.90	0.03	2143	100.4	7.47E-06	3.50E-07
18.0	21.0	19.5	206.9	6.1	188.4	2.11	0.13	3.03	0.18	1.90	0.03	1428	70.6	4.37E-06	2.16E-07

O⁺ fit results (Asymmetric Gaussian)

Lmin	Lmax	Lmid	Amp	unc	center	sigma1	unc	sigma 2	unc	alpha	unc	Counts	unc	O ⁺ n (cm ⁻³)	unc
7.0	8.0	7.5	189.9	5.9	188.4	2.11	0.13	3.15	0.18	N/A	N/A	1250	65.6	1.82E-05	9.57E-07
8.0	9.0	8.5	330.7	7.8	188.4	2.11	0.13	3.15	0.18	N/A	N/A	2179	105.4	3.65E-05	1.76E-06
9.0	10.0	9.5	319.2	7.6	188.4	2.11	0.13	3.15	0.18	N/A	N/A	2103	102.0	4.60E-05	2.23E-06
10.0	11.0	10.5	306.0	7.4	188.4	2.11	0.13	3.15	0.18	N/A	N/A	2016	98.1	3.67E-05	1.78E-06
11.0	13.0	12.0	426.0	8.8	188.4	2.11	0.13	3.15	0.18	N/A	N/A	2806	132.0	1.95E-05	9.15E-07
13.0	15.0	14.0	297.9	7.4	188.4	2.11	0.13	3.15	0.18	N/A	N/A	1962	96.2	1.20E-05	5.89E-07
15.0	18.0	16.5	313.9	7.6	188.4	2.11	0.13	3.15	0.18	N/A	N/A	2068	100.7	7.21E-06	3.51E-07
18.0	21.0	19.5	208.9	6.1	188.4	2.11	0.13	3.15	0.18	N/A	N/A	1376	70.7	4.21E-06	2.16E-07

O⁺ fit results (alpha=1.81)

Lmin	Lmax	Lmid	Amp	unc	center	sigma1	unc	sigma 2	unc	alpha	unc	Counts	unc	O ⁺ n (cm ⁻³)	unc
7.0	8.0	7.5	189.0	5.9	188.4	2.11	0.13	2.86	0.18	1.81	0.03	1297	64.2	1.89E-05	9.36E-07
8.0	9.0	8.5	330.7	7.8	188.4	2.11	0.13	2.86	0.18	1.81	0.03	2270	104.1	3.80E-05	1.74E-06
9.0	10.0	9.5	318.4	7.6	188.4	2.11	0.13	2.86	0.18	1.81	0.03	2185	100.5	4.78E-05	2.20E-06
10.0	11.0	10.5	305.3	7.4	188.4	2.11	0.13	2.86	0.18	1.81	0.03	2096	96.7	3.81E-05	1.76E-06
11.0	13.0	12.0	425.2	8.8	188.4	2.11	0.13	2.86	0.18	1.81	0.03	2918	130.4	2.02E-05	9.04E-07
13.0	15.0	14.0	297.1	7.4	188.4	2.11	0.13	2.86	0.18	1.81	0.03	2039	94.7	1.25E-05	5.80E-07
15.0	18.0	16.5	313.1	7.6	188.4	2.11	0.13	2.86	0.18	1.81	0.03	2149	99.2	7.49E-06	3.46E-07
18.0	21.0	19.5	208.8	6.1	188.4	2.11	0.13	2.86	0.18	1.81	0.03	1433	69.4	4.38E-06	2.12E-07

2004-2010 Latitude=-10° to 10°

OH⁺ fit results (alpha=1.90)

Lmin	Lmax	Lmid	Amp	unc	center	sigma1	unc	sigma 2	unc	alpha	unc	Counts	unc	OH ⁺ n (cm ⁻³)	unc
7.0	8.0	7.5	68.4	4.8	195.5	2.64	0.38	2.46	0.17	1.90	0.03	467.9	46.8	7.03E-06	7.04E-07
8.0	9.0	8.5	138.4	6.6	195.5	2.64	0.38	2.46	0.17	1.90	0.03	947.6	83.2	1.64E-05	1.44E-06
9.0	10.0	9.5	138.5	6.6	195.5	2.64	0.38	2.46	0.17	1.90	0.03	948	83.2	2.14E-05	1.88E-06
10.0	11.0	10.5	108.6	6.0	195.5	2.64	0.38	2.46	0.17	1.90	0.03	743.4	68.1	1.39E-05	1.28E-06
11.0	13.0	12.0	164.7	7.4	195.5	2.64	0.38	2.46	0.17	1.90	0.03	1127	97.5	8.05E-06	6.97E-07
13.0	15.0	14.0	119.6	6.2	195.5	2.64	0.38	2.46	0.17	1.90	0.03	819	73.5	5.17E-06	4.64E-07
15.0	18.0	16.5	119.5	6.3	195.5	2.64	0.38	2.46	0.17	1.90	0.03	817.9	73.8	2.94E-06	2.65E-07
18.0	21.0	19.5	75.2	5.0	195.5	2.64	0.38	2.46	0.17	1.90	0.03	514.8	50.4	1.62E-06	1.59E-07

OH⁺ fit results (Asymmetric Gaussian)

Lmin	Lmax	Lmid	Amp	unc	center	sigma1	unc	sigma2	unc	alpha	unc	Counts	unc	OH ⁺ n (cm ⁻³)	unc
7.0	8.0	7.5	71.9	4.8	195.5	2.64	0.38	2.62	0.17	N/A	N/A	473.8	49.1	7.12E-06	7.38E-07
8.0	9.0	8.5	144.2	6.6	195.5	2.64	0.38	2.62	0.17	N/A	N/A	950.3	86.9	1.64E-05	1.50E-06
9.0	10.0	9.5	144.1	6.5	195.5	2.64	0.38	2.62	0.17	N/A	N/A	949.7	86.5	2.14E-05	1.95E-06
10.0	11.0	10.5	113.8	5.9	195.5	2.64	0.38	2.62	0.17	N/A	N/A	750.4	71.0	1.41E-05	1.33E-06
11.0	13.0	12.0	172.1	7.3	195.5	2.64	0.38	2.62	0.17	N/A	N/A	1134	101.9	8.10E-06	7.28E-07
13.0	15.0	14.0	125.1	6.1	195.5	2.64	0.38	2.62	0.17	N/A	N/A	824.6	76.7	5.21E-06	4.84E-07
15.0	18.0	16.5	124.9	6.2	195.5	2.64	0.38	2.62	0.17	N/A	N/A	823.4	76.9	2.96E-06	2.76E-07
18.0	21.0	19.5	79.0	5.0	195.5	2.64	0.38	2.62	0.17	N/A	N/A	520.4	52.8	1.64E-06	1.66E-07

OH⁺ fit results (alpha=1.81)

Lmin	Lmax	Lmid	Amp	unc	center	sigma1	unc	sigma2	unc	alpha	unc	Counts	unc	OH ⁺ n (cm ⁻³)	unc
7.0	8.0	7.5	68.6	4.7	195.5	2.64	0.38	2.72	0.17	1.81	0.03	502.7	47.7	7.56E-06	7.17E-07
8.0	9.0	8.5	138.9	6.5	195.5	2.64	0.38	2.72	0.17	1.81	0.03	1018	84.6	1.76E-05	1.46E-06
9.0	10.0	9.5	138.5	6.4	195.5	2.64	0.38	2.72	0.17	1.81	0.03	1016	84.1	2.29E-05	1.90E-06
10.0	11.0	10.5	109.6	5.8	195.5	2.64	0.38	2.72	0.17	1.81	0.03	803.6	69.2	1.51E-05	1.30E-06
11.0	13.0	12.0	166.0	7.2	195.5	2.64	0.38	2.72	0.17	1.81	0.03	1217	99.2	8.70E-06	7.09E-07
13.0	15.0	14.0	120.6	6.0	195.5	2.64	0.38	2.72	0.17	1.81	0.03	884.3	74.7	5.58E-06	4.72E-07
15.0	18.0	16.5	120.6	6.1	195.5	2.64	0.38	2.72	0.17	1.81	0.03	883.7	75.1	3.17E-06	2.70E-07
18.0	21.0	19.5	75.5	4.9	195.5	2.64	0.38	2.72	0.17	1.81	0.03	553.4	51.3	1.74E-06	1.62E-07

2004-2010 Latitude=-10° to 10°

H₂O⁺ fit results (alpha=1.90)

Lmin	Lmax	Lmid	Amp	unc	center	sigma1	unc	sigma2	unc	alpha	unc	Counts	unc	H ₂ O ⁺ n (cm ⁻³)	unc
7.0	8.0	7.5	70.2	4.1	201.7	2.72	0.39	2.54	0.18	1.90	0.03	493.9	46.2	7.64E-06	7.15E-07
8.0	9.0	8.5	129.7	5.5	201.7	2.72	0.39	2.54	0.18	1.90	0.03	913.1	78.2	1.62E-05	1.39E-06
9.0	10.0	9.5	114.9	5.2	201.7	2.72	0.39	2.54	0.18	1.90	0.03	808.6	70.3	1.88E-05	1.63E-06
10.0	11.0	10.5	112.1	5.0	201.7	2.72	0.39	2.54	0.18	1.90	0.03	789.1	68.4	1.52E-05	1.32E-06
11.0	13.0	12.0	168.0	6.2	201.7	2.72	0.39	2.54	0.18	1.90	0.03	1183	98.6	8.70E-06	7.25E-07
13.0	15.0	14.0	112.4	5.1	201.7	2.72	0.39	2.54	0.18	1.90	0.03	791.2	68.8	5.14E-06	4.47E-07
15.0	18.0	16.5	124.7	5.3	201.7	2.72	0.39	2.54	0.18	1.90	0.03	878.3	75.2	3.25E-06	2.78E-07
18.0	21.0	19.5	76.6	4.2	201.7	2.72	0.39	2.54	0.18	1.90	0.03	539.1	49.4	1.75E-06	1.60E-07

H₂O⁺ fit results (Asymmetric Gaussian)

Lmin	Lmax	Lmid	Amp	unc	center	sigma1	unc	sigma2	unc	alpha	unc	Counts	unc	H ₂ O ⁺ n (cm ⁻³)	unc
7.0	8.0	7.5	72.9	4.1	201.7	2.72	0.39	2.70	0.18	N/A	N/A	495.9	48.1	7.67E-06	7.44E-07
8.0	9.0	8.5	134.1	5.5	201.7	2.72	0.39	2.70	0.18	N/A	N/A	911.7	81.3	1.62E-05	1.44E-06
9.0	10.0	9.5	119.4	5.2	201.7	2.72	0.39	2.70	0.18	N/A	N/A	812.2	73.3	1.89E-05	1.70E-06
10.0	11.0	10.5	116.1	5.0	201.7	2.72	0.39	2.70	0.18	N/A	N/A	789.3	71.1	1.52E-05	1.37E-06
11.0	13.0	12.0	173.5	6.2	201.7	2.72	0.39	2.70	0.18	N/A	N/A	1180	102.5	8.68E-06	7.53E-07
13.0	15.0	14.0	116.4	5.0	201.7	2.72	0.39	2.70	0.18	N/A	N/A	791.2	71.3	5.14E-06	4.63E-07
15.0	18.0	16.5	129.0	5.2	201.7	2.72	0.39	2.70	0.18	N/A	N/A	877.5	77.9	3.24E-06	2.88E-07
18.0	21.0	19.5	79.0	4.2	201.7	2.72	0.39	2.70	0.18	N/A	N/A	537.3	51.2	1.74E-06	1.66E-07

H₂O⁺ fit results (alpha=1.81)

Lmin	Lmax	Lmid	Amp	unc	center	sigma1	unc	sigma2	unc	alpha	unc	Counts	unc	H ₂ O ⁺ n (cm ⁻³)	unc
7.0	8.0	7.5	63.4	4.0	201.7	2.72	0.39	2.80	0.18	1.81	0.03	477.1	43.9	7.38E-06	6.79E-07
8.0	9.0	8.5	116.5	5.4	201.7	2.72	0.39	2.80	0.18	1.81	0.03	876.6	73.0	1.56E-05	1.30E-06
9.0	10.0	9.5	102.2	5.1	201.7	2.72	0.39	2.80	0.18	1.81	0.03	769.2	65.4	1.79E-05	1.52E-06
10.0	11.0	10.5	100.7	4.9	201.7	2.72	0.39	2.80	0.18	1.81	0.03	757.8	63.9	1.46E-05	1.23E-06
11.0	13.0	12.0	150.2	6.1	201.7	2.72	0.39	2.80	0.18	1.81	0.03	1131	91.2	8.32E-06	6.71E-07
13.0	15.0	14.0	100.1	4.9	201.7	2.72	0.39	2.80	0.18	1.81	0.03	753.6	63.7	4.89E-06	4.14E-07
15.0	18.0	16.5	111.8	5.2	201.7	2.72	0.39	2.80	0.18	1.81	0.03	841.4	70.1	3.11E-06	2.59E-07
18.0	21.0	19.5	69.0	4.1	201.7	2.72	0.39	2.80	0.18	1.81	0.03	519.2	46.7	1.68E-06	1.51E-07

2004-2010 Latitude=-10° to 10°

H₃O⁺ fit results (alpha=1.90)

Lmin	Lmax	Lmid	Amp	unc	center	sigma1	unc	sigma2	unc	alpha	unc	Counts	unc	H ₃ O ⁺ n (cm ⁻³)	unc
7.0	8.0	7.5	14.55	2	208.1	2.81	0.40	2.62	0.18	1.90	0.03	105.3	15.8	1.67E-06	2.51E-07
8.0	9.0	8.5	18.24	2.4	208.1	2.81	0.40	2.62	0.18	1.90	0.03	132	19.2	2.41E-06	3.50E-07
9.0	10.0	9.5	14.37	2.2	208.1	2.81	0.40	2.62	0.18	1.90	0.03	104	16.9	2.48E-06	4.04E-07
10.0	11.0	10.5	10.85	2	208.1	2.81	0.40	2.62	0.18	1.90	0.03	78.55	14.9	1.56E-06	2.95E-07
11.0	13.0	12.0	17.8	2.6	208.1	2.81	0.40	2.62	0.18	1.90	0.03	128.9	20.2	9.74E-07	1.53E-07
13.0	15.0	14.0	7.94	1.9	208.1	2.81	0.40	2.62	0.18	1.90	0.03	57.52	45.7	3.84E-07	3.05E-07
15.0	18.0	16.5	8.91	2	208.1	2.81	0.40	2.62	0.18	1.90	0.03	64.51	14.5	2.45E-07	5.50E-08
18.0	21.0	19.5	5.84	1.6	208.1	2.81	0.40	2.62	0.18	1.90	0.03	42.26	11.4	1.41E-07	3.78E-08

H₃O⁺ fit results (Asymmetric Gaussian)

Lmin	Lmax	Lmid	Amp	unc	center	sigma1	unc	sigma2	unc	alpha	unc	Counts	unc	H ₃ O ⁺ n (cm ⁻³)	unc
7.0	8.0	7.5	17.67	2.1	208.1	2.81	0.40	2.79	0.18	N/A	N/A	124	17.7	1.97E-06	2.80E-07
8.0	9.0	8.5	23.41	2.5	208.1	2.81	0.40	2.79	0.18	N/A	N/A	164.3	21.8	3.00E-06	3.97E-07
9.0	10.0	9.5	19.5	2.2	208.1	2.81	0.40	2.79	0.18	N/A	N/A	136.8	18.8	3.26E-06	4.48E-07
10.0	11.0	10.5	15.43	2.0	208.1	2.81	0.40	2.79	0.18	N/A	N/A	108.2	16.4	2.14E-06	3.25E-07
11.0	13.0	12.0	24.28	2.6	208.1	2.81	0.40	2.79	0.18	N/A	N/A	170.4	22.6	1.29E-06	1.71E-07
13.0	15.0	14.0	13.16	2.0	208.1	2.81	0.40	2.79	0.18	N/A	N/A	92.3	15.8	6.16E-07	1.05E-07
15.0	18.0	16.5	13.74	2.0	208.1	2.81	0.40	2.79	0.18	N/A	N/A	96.42	15.9	3.66E-07	6.05E-08
18.0	21.0	19.5	9.5	1.6	208.1	2.81	0.40	2.79	0.18	N/A	N/A	66.62	12.4	2.22E-07	4.13E-08

H₃O⁺ fit results (alpha=1.81)

Lmin	Lmax	Lmid	Amp	unc	center	sigma1	unc	sigma2	unc	alpha	unc	Counts	unc	H ₃ O ⁺ n (cm ⁻³)	unc
7.0	8.0	7.5	9.80	1.9	208.1	2.81	0.40	2.89	0.18	1.81	0.03	75.72	14.6	1.20E-06	2.32E-07
8.0	9.0	8.5	11.20	2.3	208.1	2.81	0.40	2.89	0.18	1.81	0.03	86.52	17.5	1.58E-06	3.20E-07
9.0	10.0	9.5	7.83	2.1	208.1	2.81	0.40	2.89	0.18	1.81	0.03	60.48	15.6	1.44E-06	3.72E-07
10.0	11.0	10.5	5.19	1.9	208.1	2.81	0.40	2.89	0.18	1.81	0.03	40.07	13.9	7.94E-07	2.75E-07
11.0	13.0	12.0	9.13	2.5	208.1	2.81	0.40	2.89	0.18	1.81	0.03	70.52	18.6	5.33E-07	1.40E-07
13.0	15.0	14.0	2.01	1.8	208.1	2.81	0.40	2.89	0.18	1.81	0.03	15.51	12.9	1.04E-07	8.61E-08
15.0	18.0	16.5	2.90	1.9	208.1	2.81	0.40	2.89	0.18	1.81	0.03	22.4	13.7	8.51E-08	5.19E-08
18.0	21.0	19.5	1.86	1.5	208.1	2.81	0.40	2.89	0.18	1.81	0.03	14.4	10.8	4.80E-08	3.59E-08

Appendix E

C^+ and N^+ Partial Number Density Tables

The tables in this appendix contain the C^+ , N^+ , and W^+ partial number densities presented in chapter 6. The partial number densities are in units of cm^{-3} . The C^+ , N^+ , and W^+ partial number densities in the main ring current region ($L=7-16$; Latitude = -10° to 10°) are shown in Table E.1. We were only able to calculate the C^+ and N^+ partial number densities for $E/Q > 96$ keV and $E/Q > 127$ keV, respectively. Table E.2 contains the 118-136 C^+ , N^+ , and W^+ for each L range. The units on all the partial number density values are cm^{-3} . The uncertainties of the W^+ partial number densities are the statistical uncertainties. To determine the uncertainties of C^+ and N^+ , we combine in quadrature their statistical uncertainty with half the difference between their upper and lower limits. See chapter 6 for details.

Table E.1: The partial number densities n of C^+ , N^+ , and W^+ in the main ring current region. Only data from telescope 3 is included.

DPPS	Energy (keV)	C^+ n	sigma	N^+ n	sigma	W^+ n	sigma
25	89-103	2.97E-07	1.94E-08	-	-	4.06E-05	2.61E-07
26	103-118	2.02E-07	1.54E-08	-	-	3.40E-05	2.18E-07
27	118-136	1.70E-07	1.40E-08	2.57E-07	2.40E-08	2.76E-05	1.81E-07
28	136-156	1.36E-07	1.17E-08	1.75E-07	2.27E-08	2.09E-05	1.45E-07
29	156-179	7.50E-08	7.33E-09	1.24E-07	1.45E-08	1.44E-05	1.11E-07
30	179-205	2.98E-08	3.95E-09	2.94E-08	5.37E-09	9.20E-06	8.11E-08
31	205-236	1.88E-08	2.97E-09	2.55E-08	6.48E-09	5.85E-06	6.02E-08

Table 2: 118-136 C⁺, N⁺, and W⁺ partial number densities as a function of L. The partial number densities were determined using the data from all telescopes combined.

L min	L max	C ⁺ n	sigma	N ⁺ n	sigma	W ⁺ n	sigma
6	7	1.53E-07	1.83E-08	1.58E-07	2.02E-08	1.50E-05	2.26E-07
7	8	2.71E-07	2.77E-08	3.15E-07	3.48E-08	3.71E-05	3.71E-07
8	9	2.89E-07	3.06E-08	4.61E-07	4.65E-08	4.84E-05	4.66E-07
9	10	3.45E-07	3.65E-08	5.07E-07	5.75E-08	5.23E-05	5.29E-07
10	11	2.75E-07	2.77E-08	4.44E-07	4.30E-08	4.40E-05	4.43E-07
11	13	1.27E-07	1.37E-08	2.11E-07	2.46E-08	2.37E-05	1.98E-07
13	15	7.50E-08	9.69E-09	1.32E-07	1.62E-08	1.30E-05	1.37E-07
15	18	5.75E-08	5.69E-09	6.67E-08	8.44E-09	7.51E-06	7.94E-08
18	21	3.15E-08	3.99E-09	3.57E-08	5.96E-09	4.53E-06	5.88E-08

References

- Achilleos, N., P. Guio, and C.S. Arridge (2010), A model of force balance in Saturn's magnetodisc, *Mon. Not. R. Astron. Soc.*, 401, 2349, doi:10.1111/j.1365-2966.2009.15865.x.
- Acuna, M.H. and N.F. Ness (1980), The magnetic field of Saturn – Pioneer 11 observations, *Science*, 207, 444, doi:10.1126/science.207.4429.444.
- Aellig, M.R., A.J. Lazarus, and J.T. Steinberg (2001), The solar wind helium abundance: Variation with wind speed and solar cycle, *Geophys. Res. Lett.*, 28, 2767, doi:10.1029/2000GL012771.
- Allegrini, F., D.J. McComas, D.T. Young, J.-J. Berthelier, J. Covinhes, J.-M. Illiano, and J.-F. Riou, H.O. Funsten, and R.W. Harper (2006), Energy loss of 1-50 keV H, He, C, N, O, Ne, and Ar ions transmitted through thin carbon foils, *Rev. Sci. Instrum.*, 77(4), doi:10.1063/1.2185490.
- Armstrong, T.P., M.T. Paonessa, E.V. Bell II, and S.M. Krimigis (1983), Voyager observations of Saturnian ion and electron phase space densities, *J. Geophys. Res.*, 88, 8893-8904, doi:10.1029/JA088iA11p08893.
- Arridge, C.S., et al. (2006), Modeling the size and shape of Saturn's magnetopause with variable dynamic pressure, *J. Geophys. Res.*, 111, A11227, doi:10.1029/2005JA011574.
- Arridge, C.S. C.T. Russell, K.K. Khurana, N. Achilleos, N. Anrdé, A.M. Rymer, M.K. Dougherty, and A.J. Coates (2007), The mass of Saturn's magnetodisc: Cassini observations, *Geophys. Res. Lett.*, 34, L09108, doi:10.1029/2006GL028921.
- Arridge, C.S., K.K. Khurana, C.T. Russell, D.J. Southwood, N. Achilleos, M.K. Dougherty, A.J. Coates, and H.K. Leinweber (2008a), Warping of Saturn's magnetospheric and magnetotail current sheets, *J. Geophys. Res.*, 113, A08217, doi:10.1029/2007JA012963.
- Arridge, C.S., C.T. Russell, K.K. Khurana, N. Achilleos, S.W.H. Cowley, M.K. Dougherty, D.J. Southwood, and E.J. Bunce (2008b), Saturn's magnetodisc current sheet, *J Geophys. Res.*, 113, A04214, doi:10.1029/2007JA012540.
- Arridge, C.S., et al. (2012), Mapping Magnetospheric Equatorial Regions at Saturn from Cassini Prime Mission Observations, *Space Sci. Rev.*, 164, 1, doi:10.1007/s11214-011-9850-4.
- Bagenal, F., and P.A. Delamere (2011), Flow of mass and energy in the magnetospheres of Jupiter and Saturn, *J. Geophys. Res.*, 116, A05209, doi:10.1029/2010JA016294.

- Bame, S.J., J.R. Asbridge, W.C. Feldman and J.T. Gosling (1977), Evidence for structure-free state at high solar wind speeds, *J. Geophys. Res.*, 82, 1487, doi:10.1029/JA082i010p01487.
- Bates, D.R. (1962), *Atomic and Molecular Processes*, Academic Press, New York.
- Bevington, P.R. and D.K. Robinson (2003), *Data Reduction and Error Analysis for the Physical Sciences*, McGraw Hill, Boston.
- Bunce, E.J., S.W.H. Cowley, D.M. Wright, A.J. Coates, M.K. Dougherty, N. Krupp, W.S. Kurth, and A.M. Rymer (2005), In situ observations of a solar wind compression-induced hot plasma injection in Saturn's tail, *Geophys. Res. Lett.*, 32, L20S04, doi:10.1029/2005GL022888.
- Burch, J.L., J. Goldstein, T.W. Hill, D.T. Young, F.J. Crary, A.J. Coates, N. André, W.S. Kurth, and E.C. Sittler Jr. (2005), Properties of local plasma injections in Saturn's magnetosphere, *Geophys. Res. Lett.*, 32, L14S02, doi:10.1029/2005GL022611.
- Burger, M.H., E.C. Sittler Jr., R.E. Johnson, H.T. Smith, O.J. Tucker, and V.I. Shematovich (2007), Understanding the escape of water from Enceladus, *J. Geophys. Res.*, 112, A06219, doi:10.1029/2006JA012086.
- Cassidy, T.A. and Johnson, R.E. (2010), Collisional spreading of Enceladus' neutral cloud, *Icarus*, 209, 696, doi:10.1016/j.icarus.2010.04.010.
- Chen, Y. and T.W. Hill (2008), Statistical analysis of injection/dispersion events in Saturn's inner magnetosphere, *J. Geophys. Res.*, 113, A07215, doi:10.1029/2008JA013166.
- Chen, Y., T.W. Hill, A.M. Rymer, and R.J. Wilson (2010), Rate of radial transport of plasma in Saturn's inner magnetosphere, *J. Geophys. Res.*, 115, A10211, doi:10.1029/2010JA015412.
- Connerney, J.E.P., L. Davis, Jr., and D.L. Chenette (1984), Magnetic field models, in *Saturn*, edited by T. Gehrels and M.S. Matthews, pp. 354-377, Univ. of Ariz., Tucson.
- Cravens, T.E., R.L. McNutt Jr., J.H. Waite Jr., I.P. Robertson, J.G. Luhmann, W. Kasprzak, and W.-H. Ip (2009), Plume ionosphere of Enceladus as seen by Cassini ion and neutral mass spectrometer, *Geophys. Res. Lett.*, 36, L08106, doi:10.1029/2009GL037811.
- CRC Handbook of Chemistry and Physics 49th Edition* (1968-1969), edited by Robert C. Weast, Chemical Rubber CO., Cleveland.

- Cui, J., R.V. Yelle, and K. Volk (2008), Distribution and escape of molecular hydrogen in Titan's thermosphere and exosphere, *J. Geophys. Res.*, 113, E10004, doi:10.1029/2007JE003032.
- Cui, J., R.V. Yelle, I.C.F. Müller-Wodarg, P.P. Lavvas, and M. Galand (2011), The implications of the H₂ variability in Titan's exosphere, *J. Geophys. Res.*, 116, A11324, doi:10.1029/2011JA016808.
- Cuzzi, J., R. Clark, G. Filacchione, R. French, R. Johnson, E. Marouf, and L. Spilker (2009), Ring Particle Composition and Size Distribution, in *Saturn from Cassini-Huygens*, edited by M.K. Dougherty, L.W. Esposito, and S.M. Krimigis, chap. 15, pp. 459-509, Springer, Heidelberg, Ger., doi:10.1007/978-1-4020-9217-6_15.
- Dagnac, R., D. Blanc, and D. Molina (1970), A study on the collision of hydrogen ions H₁⁺, H₂⁺, and H₃⁺ with a water-vapour target, *J. Phys. B: Atom. Molec. Phys.*, 3, 1239, doi:10.1088/0022-3700/3/9/007.
- Dalgarno, A. (1958), The mobilities of ions in their parent gases, *Phil. Trans. R. Soc. London, Ser. A.*, 250, 426, doi:10.1098/rsta.1958.0003.
- De La Haye, V., et al. (2007a), Cassini Ion and Neutral Mass Spectrometer data in Titan's upper atmosphere and exosphere: Observation of a suprathermal corona, *J. Geophys. Res.*, 112, A07309, doi:10.1029/2006JA012222.
- De La Haye, V., J.H. Waite Jr., T.E. Cravens, A.F. Nagy, R.E. Johnson, S. Lebonnois, and I.P. Robertson (2007b), Titan's corona: The contribution of exothermic chemistry, *Icarus*, 191, 236, doi:10.1016/j.icarus.2007.04.031.
- DiFabio, R.D., D.C. Hamilton, S.M. Krimigis, and D.G. Mitchell (2011), Long term time variations of the suprathermal ions in Saturn's magnetosphere, *Geophys. Res. Lett.*, 38, L18103, doi:10.1029/2011GL048841.
- Dong, Y., T.W. Hill, B.D. Teolis, B.A. Magee, and J.H. Waite (2011), The water vapor plumes of Enceladus, *J. Geophys. Res.*, 116, A10204, doi:10.1029/2011JA016693.
- Dougherty, M.K., et al. (2004), The Cassini Magnetic Field Investigation, *Space Sci. Rev.*, 114, 331, doi:10.1007/s11214-004-1432-2.
- Dunn, G.H. and B. Van Zyl (1967), Electron Impact Dissociation of H₂⁺, *Phys. Rev.*, 154, 40, doi:10.1103/PhysRev.154.40.
- Eviatar, A., R.L. McNutt Jr., G.L. Siscoe, and J.D. Sullivan (1983), Heavy ions in the outer Kronian magnetosphere, *J. Geophys. Res.*, 88, 823, doi:10.1029/JA088iA02p00823.

- Farmer, A.J. (2009), Saturn in hot water: Viscous evolution of the Enceladus torus, *Icarus*, 202, 280, doi:10.1016/j.icarus.2009.02.031.
- Fleshman, B.L., P.A. Delamere, and F. Bagenal (2010a), Modeling the Enceladus plume-plasma interaction, *Geophys. Res. Lett.*, 37, L03202, doi:10.1029/2009GL041613.
- Fleshman, B.L., P.A. Delamere, and F. Bagenal (2010b), A sensitivity study of the Enceladus torus, *J. Geophys. Res.*, 115, E04007, doi:10.1029/2009JE003372.
- Glocer, A., A.I. Gombosi, G. Toth, K.C. Hansen, A.J. Ridley, and A. Nagy (2007), Polar wind outflow model: Saturn results, *J. Geophys. Res.*, 112, A01304, doi:10.1029/2006JA011755.
- Gobet, S., et al. (2004), Ionization of water by (20-150)-keV protons: Separation of direct-ionization and electron capture processes, *Phys. Rev. A.*, 70, 062716-1, doi:10.1103/PhysRevA.70.062716.
- Goldston, R.J. and P.H. Rutherford (1995), *Introduction to Plasma Physics*, IOP Publishing, Philadelphia.
- Gombosi, T.I., T.P. Armstrong, C.S. Arridge, K.K. Khurana, S.M. Krimigis, N. Krupp, A.M. Persoon, and M.F. Thomsen (2009), Saturn's Magnetospheric Configuration, in *Saturn from Cassini-Huygens*, edited by M.K. Dougherty, L.W. Esposito, and S.M. Krimigis, 1st ed., chap. 9, pp. 203-255, Springer, Heidelberg, Ger., doi:10.1007/978-1-4020-9217-6_9.
- Greenwood, J.B., A. Chutjian, and S.J. Smith (2000), Measurements of absolute, single charge-exchange cross sections of H^+ , He^+ , and He^{2+} with H_2O and CO_2 , *Astrophys. J.*, 529, 605, doi:10.1086/308254.
- Greenwood, J.B., R.J. Mawhorter, I. Cadez, J. Lorzano, S.J. Smith, and A. Chutjian (2004), The contribution of Charge Exchange to Extreme Ultra-Violet and X-ray Astronomy, *Physica Scripta*, T110, 358, doi:10.1238/Physica.Topical.110a00358.
- Gurnett, D.A., et al. (2004), The Cassini Radio and Plasma Wave Investigation, *Space Sci. Rev.*, 114, 395, doi:10.1007/s11214-004-1434-0.
- Hamilton, D.C., D.C. Brown, G. Gloeckler, and W.I. Axford (1983), Energetic atomic and molecular ions in Saturn's magnetosphere, *J. Geophys. Res.*, 88, 8905, doi:10.1029/JA088iA11p08905.
- Hansen, C.J., et al. (2006), Enceladus' water vapor plume, *Science*, 311, 1422, doi:10.1126/science.1121254.

- Hansen, C.J., L.W. Esposito, A.I.F. Stewart, B. Meinke, B. Wallis, J.E. Colwell, A.R. Hendrix, K. Larsen, W. Pryor, and F. Tian (2008), Water vapour jets inside the plume of gas leaving Enceladus, *Nature*, 456, 477-479, doi:10.1038/nature07542.
- Hansen, C.J., et al. (2011), The composition and structure of the Enceladus plume, *Geophys. Res. Lett.*, 38, L11202, doi:10.1029/2011GL047415.
- Hartogh, P., et al. (2011), Direct detection of the Enceladus water torus with Herschel, *A&A*, 532, L2, doi:10.1051/0004-6361/201117377.
- Hasted, J.B. (1972), *Physics of Atomic Collisions*, 2nd Ed., Elsevier, New York.
- Hennecart, D. and J. Pascale (2005), Classical approach to H_2^+ -H(1s) collisions, *Phys. Rev. A.*, 71, 012710-1, doi:10.1103/PhysRevA.71.012710.
- Hood, L.L. (1985), Radial Diffusion of Low-Energy Ions in Saturn's Radiation Belts: A Combined Analysis of Phase Space Density and Satellite Microsignature Data, *J. Geophys. Res.*, 90, 6295, doi:10.1029/JA090iA07p06295.
- Hood, L.L. (1989), Radial Diffusion and Losses of Energetic Protons in the 5 to 12 R_S Region of Saturn's Magnetosphere, *J. Geophys. Res.*, 94, 8721, doi:10.1029/JA094iA07p08721.
- Hill, M.E., N.A. Schwadron, D.C. Hamilton, R.D. DiFabio, and R.K. Squier (2009), Interplanetary suprathermal He^+ and He^{++} observations during quiet periods from 1 to 9 AU and implications for particle acceleration, *ApJ*, 699, L26, doi:10.1088/0004-637X/699/1/L26.
- Hill, T.W., A.J. Dessler, and C.K. Goertz (1983), Magnetospheric models, in *Physics of the Jovian Magnetosphere*, edited by A.J. Dessler, chap. 10, pp. 353-394, Cambridge University Press, New York.
- Hill, T.W., A.M. Rymer, J.L. Burch, F.J. Crary, D.T. Young, M.F. Thomsen, D. Delapp, N. André, A.J. Coates, and G.R. Lewis (2005), Evidence for rotationally driven plasma transport in Saturn's magnetosphere, *Geophys. Res. Lett.*, 32, L14S10, doi:10.1029/2005GL022620.
- Huebner, W.F., J.J. Keady, and S.P. Lyon (1992), Solar photo rates for planetary atmospheres and atmospheric pollutants, *Astrophys. Space Sci.*, 195, 1-294, doi:10.1007/BF00644558.
- Ip, W.-H. (2000), Thermal plasma composition in Saturn's magnetosphere, *Planet. Space Sci.*, 48, 775, doi: 10.1016/S0032-0633(00)00036-2.
- Jackman, C.M., J.A. Slavin, and S.W.H. Cowley (2011), Cassini observations of plasmoid structure and dynamics: Implications for the role of magnetic reconnection in

- magnetospheric circulation at Saturn, *J. Geophys. Res.*, 116, A10212, doi:10.1029/2011JA016682.
- Jia, Y.-D., C.T. Russell, K.K. Khurana, Y.J. Ma, W. Kurth, and T.I. Gombosi (2010), Interaction of Saturn's magnetosphere and its moon: 3. Time variation of the Enceladus plume, *J. Geophys. Res.*, 115, A12243, doi:10.1029/2010JA015534.
- Johnson, R.E. (1982), *Introduction to Atomic and Molecular Collisions*, Plenum Press, New York.
- Johnson, R.E. (1990), *Energetic Charged Particle Interactions With Atmospheres and Surfaces*, Springer, Berlin (Available at <http://people.virginia.edu/~rej/book.html>).
- Johnson, R.E., et al. (2006a), Production, ionization and redistribution of O₂ in Saturn's ring atmosphere, *Icarus*, 180, 393, doi:10.1016/j.icarus.2005.08.021.
- Johnson, R.E., H.T. Smith, O.J. Tucker, M. Liu, M.H. Burger, E.C. Sittler, and R.L. Tokar (2006b), The Enceladus and OH tori at Saturn, *Astrophys. J.*, 644, L137, doi:10.1086/505750.
- Johnson, R.E., M.R. Combi, J.L. Fox, W.-H. Ip, F. Leblanc, M.A. McGrath, V.I. Shematovich, D.F. Strobel, and J.H. Waite Jr. (2008a), Exospheres and atmospheric escape, *Space Sci. Rev.*, 139, 355, doi:10.1007/s11214-008-94150-3.
- Johnson, R.E., M. Famá, M. Liu, R.A. Baragiola, E.C. Sittler, and H.T. Smith (2008b), Sputtering of ice grains and icy satellites in Saturn's inner magnetosphere, *Planet. Space Sci.*, 56, 1238, doi:10.1016/j.pss.2008.04.003.
- Johnson, R.E., O.J. Tucker, M. Michael, E.C. Sittler, H.T. Smith, D.T. Young, J.H. Waite (2009), Mass loss processes in Titan's upper atmosphere, in *Titan From Cassini-Huygens*, edited by R.H. Brown, J.-P. Lebreton, and J.H. Waite, chap. 15, pp. 373-391, Springer, Dordrecht, Neth.
- Johnson, R.E. (2010), Thermally driven atmospheric escape, *The Astrophysical Journal*, 716, 1573, doi:10.1088/0004-637X/716/2/1573.
- Jurac, S. and J.D. Richardson (2005), A self-consistent model of plasma and neutrals at Saturn: Neutral cloud morphology, *J. Geophys. Res.*, 110, A09220, doi:10.1029/2004JA010635.
- Jurac, S. and J.D. Richardson (2007), Neutral cloud interaction with Saturn's main rings, *Geophys. Res. Lett.*, 34, L08102, doi:10.1029/2007GL029567.
- Kanani, S.J., et al. (2010), A new form of Saturn's magnetopause using a dynamic pressure balance model, based on in situ, multi-instrument Cassini measurements, *J. Geophys. Res.*, 115, A06207, doi:10.1029/2009JA014262.

- Kellett, S., E.J. Bunce, A.J. Coates, and S.W.H. Cowley (2009), Thickness of Saturn's ring current determined from north-south Cassini passes through the current layer, *J. Geophys. Res.*, 114, A04209, doi:10.1029/2008JA013942.
- Kellett, S., C.S. Arridge, E.J. Bunce, A.J. Coates, S.W.H. Cowley, M.K. Dougherty, A.M. Persoon, N. Sergis, and R.J. Wilson (2011), Saturn's ring current: Local time dependence and temporal variability, *J. Geophys. Res.*, 116, A05220, doi:10.1029/2010JA016216.
- Kollmann, P., E. Roussos, C. Paranicas, N. Krupp, C.M. Jackman, E. Kirch, and K.-H. Glassmeier (2011), Energetic particle phase space densities at Saturn: Cassini observations and interpretations, *J. Geophys. Res.*, 116, A05222, doi:10.1029/2010JA016221.
- Krimigis, S.M., et al. (2004), Magnetospheric Imaging Instrument (MIMI) on the Cassini Mission to Saturn/Titan, *Space Sci. Rev.*, 114, 233, doi:10.1007/s11214-004-1410-8.
- Krimigis, S.M., et al. (2005), Dynamics of Saturn's Magnetosphere from MIMI during Cassini's Orbital Insertion, *Science*, 307, 1270, doi: 10.1126/science.1105978.
- Krimigis, S.M., N. Sergis, D.G. Mitchell, D.C. Hamilton and N. Krupp (2007), A dynamic, rotating ring current around Saturn, *Nature*, 450, 1050, doi:10.1038/nature06425.
- Lazarus, A.J. and R.L. McNutt Jr. (1983), Low-Energy Plasma Ion Observations in Saturn's Magnetosphere, *J. Geophys. Res.*, 88, 8831, doi:10.1029/JA088iA11p08831.
- Lebonnois, S., E.L.O. Bakes, and C.P. McKay (2003), Atomic and molecular hydrogen budget in Titan's atmosphere, *Icarus*, 161, 474, doi:10.1016/S0019-1035(02)00039-8.
- Lindsay, B.G., D.R. Sieglaff, K.A. Smith, and R.F. Stebbings (1997), Charge transfer of 0.5-, 1.5-, and 5-keV protons with H₂O: Absolute differential and integral cross sections, *Phys. Rev. A.*, 55, 3945, doi:10.1103/PhysRevA.55.3945.
- Lindsay, B.G. and R.F. Stebbings (2005), Charge transfer cross sections for energetic neutral atom data analysis, *J. Geophys. Res.*, 110, A12213, doi:10.1029/2005JA011298.
- Lo, H.H., L. Kurzweg, R.T. Brackman, and W.L. Fite (1971), Electron capture and loss in collisions of heavy ions with atomic oxygen, *Phys. Rev. A.*, 4, 1462, doi:10.1103/PhysRevA.4.1462.
- Lotz, W. (1968), Electron-impact ionization cross-sections and ionization rate coefficients for atoms and ions from hydrogen to calcium, *Z. Phys.*, 216, 241, doi:10.1007/BF01392963.

- Luna, H., et al. (2007), Water-molecule dissociation by proton and hydrogen impact, *Phys. Rev. A.*, 75, 042711-1, doi:10.1103/PhysRevA.75.042711.
- Massey, H.S.W. (1949), Collisions between atoms and molecules at ordinary temperatures, *Rep. Progr. Phys.*, 12, 248, doi:10.1088/0034-4885/12/1/311.
- Masters, A., N. Achilleos, M.K. Dougherty, J.A. Slavin, G.B. Hospodarsky, C.S. Arridge, and A.J. Coates (2008), An empirical model of Saturn's bow shock: Cassini observations of shock location and shape, *J. Geophys. Res.*, 113, A10210, doi:10.1029/2008JA013276.
- Mattioli, M., G. Mazzitelli, M. Finkenthal, P. Mazzotta, K.B. Fournier, J. Kaastra, and M.E. Puiatti (2007), Updating of ionization data for ionization balance evaluations of atoms and ions for the elements hydrogen to germanium, *J. Phys. B.*, 40, 3569, doi:10.1088/0953-4075/40/18/002.
- Mauk, B.H., et al. (2005), Energetic particle injections in Saturn's magnetosphere, *Geophys. Res. Lett.*, 32, L14S05, doi:10.1029/2005GL022485.
- Mauk, B.H., et al. (2009), Fundamental plasma processes in Saturn's magnetosphere, in *Saturn From Cassini-Huygens*, edited by M.K. Dougherty, L.W. Esposito, and S.M. Krimigis, 1st ed., chap. 11, pp. 281-331, Springer, Heidelberg, Ger., doi:10.1007/978-1-4020-9217-6_11.
- McAndrews, H.J., C.J. Owen, M. Thomsen, B. Lavraud, A. Coates, M. Dougherty, and D.T. Young (2008) Evidence for reconnection at Saturn's magnetopause, *J. Geophys. Res.*, 113, A04210, doi:10.1029/2007JA012581.
- McDonald, F.B., A.W. Schardt, and J.H. Trainor (1980), If you've seen one magnetosphere, you haven't seen them all: Energetic particle observations in the Saturn magnetosphere, *J. Geophys. Res.*, 85, 5813, doi: 10.1029/JA085iA11p05813.
- McGrath, C., M.B. Shah, P.C.E. McCartney, and J.W. McConkey (2001), H_2^+ (20-100-keV) collisions with H: Dissociative and nondissociative capture and ionization and pure-H-target ionization, *Phys. Rev. A.*, 64, 062712-1, doi:10.1103/PhysRevA.64.062712.
- Melin, H., D.E. Shemansky, and X. Liu (2009), The distribution of atomic hydrogen and oxygen in the magnetosphere of Saturn, *Planet. Space Sci.*, 57, 1743-1753, doi:10.1016/j.pss.2009.04.014.
- Melin, J., J.V. Ortiz, I. Martín, A.M. Velasco, C. Lavín (2005), Ground and excited states of the Rydberg radial H_3O : Electron propagator and quantum defect analysis, *J. Chem. Phys.*, 122, 234317, doi:10.1063/1.1926286.

- Mitchell, D.G., et al. (2005), Energetic ion acceleration in Saturn's magnetotail: Substorms at Saturn?, *Geophys. Res. Lett.*, 32, L20S01, doi:10.1029/2005GL022647.
- Mitchell, D.G., J.F. Carbary, S.W.H. Cowley, T.W. Hill, and P. Zarka (2009a), The Dynamics of Saturn's magnetosphere, in *Saturn from Cassini-Huygens*, edited by M.K. Dougherty, L.W. Esposito, and S.M. Krimigis, 1st ed., chap. 10, pp. 257-279, Springer, Heidelberg, Ger., doi:10.1007/978-1-4020-9217-6_10.
- Mitchell, D.G. et al. (2009b), Recurrent energization of plasma in the midnight-to-dawn quadrant of Saturn's magnetosphere and its relationship to auroral UV and radio emissions, *Planet. Space. Sci.*, 57, 1732, doi:10.1016/j.pss.2009.04.002.
- Möbius, E., D. Hovestadt, B. Klecker, M. Scholer, G. Gloeckler, and F.M. Ipavich (1985), Direct observation of He⁺ pickup ions of interstellar origin in the solar wind, *Nature*, 318, 426, doi:10.1038/318426a0.
- Montenegro, E.C., M.B. Shah, H. Luna, S.W.J. Scully, A.L.F. de Barros, J.A. Wyer, and J. Lecointre (2007), Water Fragmentation and Energy Loss by Carbon Ions at the Distal Region of the Bragg Peak, *Phys. Rev. Lett.*, 99, 213201, doi:10.1103/PhysRevLett.99.213210.
- Ogilvie, K.W., M.A. Coplan, P. Bochsler, and J. Geiss (1989), Solar wind observations with the Ion Composition Instrument aboard the ISEE-3/ICE spacecraft, *Sol. Phys.*, 124, 167, doi:10.1007/BF00146526.
- Paonessa, M. and A.F. Cheng (1986), Limits on Ion Radial Diffusion Coefficients in Saturn's Inner Magnetosphere, *J. Geophys. Res.*, 91, 1391, doi:10.1029/JA091iA02p01391.
- Paranicas, C., D.G. Mitchell, E.C. Roelof, B.H. Mauk, S.M. Krimigis, P.C. Brandt, M. Kusterer, F.S. Turner, J. Vande-griff, and N. Krupp (2007), Energetic electrons injected into Saturn's neutral cloud, *Geophys. Res. Lett.*, 34, L02109, doi:10.1029/2006GL028676.
- Paranicas, C., D.G. Mitchell, S.M. Krimigis, D.C. Hamilton, E. Roussos, N. Krupp, G.H. Jones, R.E. Johnson, J.F. Cooper, and T.P. Armstrong (2008), Sources and losses of energetic protons in Saturn's magnetosphere, *Icarus*, 197, 519, doi:10.1016/j.icarus.2008.05.011.
- Peart, B. and K.T. Dolder (1972), Collisions between electrons and H₂⁺ ions III. Measurements of proton production cross sections at low energies, *J. Phys. B.*, 5, 1554, doi:10.1088/0022-3700/5/8/020.
- Phaneuf, R.A., F.W. Meyer, and R.H. McKnight (1978), Single-electron capture by multiply charged ions of carbon, nitrogen, and oxygen in atomic and molecular, *Phys. Rev. A.*, 17, 534, doi:10.1103/PhysRevA.17.534.

- Phaneuf, R.A., I. Alvarez, F.W. Meyer, and D.H. Crandall (1982), Electron capture in low-energy collisions of C^{q+} and O^{q+} with H and H_2 , *Phys. Rev. A.*, 26, 1892, doi:10.1103/PhysRevA.26.1892.
- Phaneuf, R.A., R.K. Janev, and M.S. Pindzola (1987), Collisions of carbon and oxygen ions with electrons, H, H_2 , and He, *Atomic Data for Fusion*, edited by H.T. Hunter, Oak Ridge National Laboratory, Oak Ridge, TN, <http://www-cfadc.phy.ornl.gov/redbooks/history.html>
- Porco, C. et al. (2006), Cassini observes the active south pole of Enceladus, *Science*, 311, 1393, doi:10.1126/science.1123013.
- Press, W.H., B.P. Flannery, S.A. Teukolsky, and W.T. Vetterling (1989), *Numerical Recipes: The Art of Scientific Computing*, Cambridge University Press, New York.
- Rapp, D. and W.E. Francis (1962), Charge exchange between gaseous ions and atoms, *J. Chem. Phys.*, 37, 2631, doi:10.1063/1.1733066.
- Reif, F. (1965), *Fundamentals of statistical and thermal physics*, McGraw-Hill, New York.
- Rucinski, D., M. Bzowski, and H.J. Fahr (2003), Imprints from the solar cycle on the helium atom and helium pickup ion distribution, *Ann. Geophys.*, 21, 1315, doi:10.5194/angeo-21-1315-2003.
- Richardson, J.D., A. Eviatar, M.A. McGrath, and V.M. Vasyliunas (1998), OH in Saturn's magnetosphere: Observations and implications, *J. Geophys. Res.*, 103, 20245, doi: 10.1029/98JE01127.
- Richardson, J.D. (1998), Thermal plasma and neutral gas in Saturn's magnetosphere, *Rev. Geophys.*, 36, 501, doi:10.1029/98RG01691.
- Rudd, M.E., T.V. Goffe, R.D. DuBois, and L.H. Toburen (1985a), Cross sections for ionization of water vapor by 7-4000-keV protons, *Phys. Rev. A.*, 31, 492, doi:10.1103/PhysRevA.31.492.
- Rudd, M.E., A. Itoh, and T.V. Goffe (1985b), Cross sections for ionization, capture, and loss for 5-450-keV He^+ on water vapor, *Phys. Rev. A.*, 32, 2499, doi:10.1103/PhysRevA.32.2499.
- Rudd, M.E., T.V. Goffe, and A. Itoh (1985c), Ionization cross sections for 10-300-keV/u and electron capture cross sections for 5-150-keV/u $^3He^{2+}$ ions in gases, *Phys. Rev. A.*, 32, doi:10.1103/PhysRevA.32.2128.

- Rymer, A.M., et al. (2007), Electron sources in Saturn's magnetosphere, *J. Geophys. Res.*, 112, A02201, doi:10.1029/2006JA012017.
- Rymer, A.M., B.H. Mauk, T.W. Hill, C. Paranicas, D.G. Mitchell, A.J. Coates, and D.T. Young (2008), Electron circulation in Saturn's magnetosphere, *J. Geophys. Res.*, 113, A01201, doi:10.1029/2007JA012589.
- Rymer, A.M., H.T. Smith, A. Wellbrock, A.J. Coates, and D.T. Young (2009a), Discrete classification and electron energy spectra of Titan's varied magnetospheric environment, *Geophys. Res. Lett.*, 36, L15109, doi:10.1029/2009/GL039427.
- Rymer, A.M., et al. (2009b), Cassini evidence for rapid interchange transport at Saturn, *Planet Space Sci.*, 57, 1779, doi:10.1016/j.pss.2009.04.010.
- Saur, J., B.H. Mauk, A. Kaßner, and F.M. Neubauer (2004), A model for the azimuthal plasma velocity in Saturn's magnetosphere, *J. Geophys. Res.*, 109, A05217, doi:10.1029/2003JA010207.
- Saur, J., N. Schilling, F.M. Neubauer, D.F. Strobel, S. Simon, M.K. Dougherty, C.T. Russell, and R.T. Pappalardo (2008), Evidence for temporal variability of Enceladus' gas jets: Modeling of Cassini observations, *Geophys. Res. Lett.*, 35, L20105, doi:10.1029/2008GL035811.
- Schaufelberger, A., P. Wurz, H. Lammer, and Y.N. Kulikov (2012), Is hydrodynamic escape from Titan possible?, 61, 79, doi:10.1016/j.pss.2011.03.011.
- Schippers, P., et al. (2008), Multi-instrument analysis of electron populations in Saturn's magnetosphere, *J. Geophys. Res.*, 113, A07208, doi:10.1029/2008JA013098.
- Sergis, N., S.M. Krimigis, D.G. Mitchell, D.C. Hamilton, N. Krupp, B.H. Mauk, E.C. Roelof, and M. K. Dougherty (2009), Energetic particle pressure in Saturn's magnetosphere, measured with Magnetospheric Imaging Instrument on Cassini, *J. Geophys. Res.*, 114, A02214, doi:10.1029/2008JA013774.
- Shemansky, D.E. and D.T. Hall (1992), The distribution of atomic hydrogen in the magnetosphere of Saturn, *J. Geophys. Res.*, 97, 4143, doi:10.1029/91JA02805.
- Shemansky, D.E., P. Matheson, D.T. Hall, H.-Y. Hu, and T.M. Tripp (1993), Detection of hydroxyl radical in the Saturn magnetosphere, *Nature*, 363, 329, doi:10.1038/363329a0.
- Shemansky, D.E., X. Liu, and H. Melin (2009), The Saturn hydrogen plume, *Planet. Space Sci.*, 57, 1659, doi:10.1016/j.pss.2009.05.002.
- Shematovich, V.I., R.E. Johnson, M. Michael, and J.G. Luhmann (2003), Nitrogen loss from Titan, *J. Geophys. Res.*, 108(E8), 5087, doi:10.1029/2003JE002094.

- Shevelko, V.P., D. Kato, M.-Y. Song, H. Tawara, I.Yu. Tolstikhina, and J.-S. Yoon (2009), One-electron capture and target ionization in He^+ -neutral-atom collisions, *Nucl. Instrum. Meth.*, 267, 3395, doi:10.1016/j.nimb.2009.07.021.
- Sittler, E.C., K.W. Ogilvie, and J.D. Scudder (1983), Survey of low-energy plasma electrons – Voyagers 1 and 2, *J. Geophys. Res.*, 88, 8847, doi:10.1029/JA088iA11p08847.
- Sittler, E.C. et al. (2008), Ion and neutral sources and sinks within Saturn's inner magnetosphere: Cassini results, *Planet. Space. Sci.*, 56, 3, doi:10.1016/j.pss.2007.06.006.
- Smith, E.J., L. Davis, D.E. Jones, P.J. Coleman, D.S. Colburn, P. Dyal, and C.P. Sonett (1980), Saturn's magnetic field and magnetosphere, *Science*, 207, 407, doi:10.1126/science.207.4429.407.
- Smith, H.T., M. Shappirio, E.C. Sittler, D. Reisenfeld, R.E. Johnson, R.A. Baragiola, F.J. Cray, D.J. McComas, and D.T. Young (2005), Discovery of nitrogen in Saturn's inner magnetosphere, *Geophys. Res. Lett.*, 32, L14S03, doi:10.1029/2005GL022654.
- Smith, H.T., R.E. Johnson, E.C. Sittler, M. Shappirio, D. Reisenfeld, O.J. Tucker, M.H. Burger, F.J. Cray, D.J. McComas, and D.T. Young (2007), Enceladus: The likely dominant nitrogen source in Saturn's magnetosphere, *Icarus*, 188(2), 356-366, doi:10.1016/j.icarus.2006.12.007.
- Smith, H.T., R.E. Johnson, M.E. Perry, D.G. Mitchell, R.L. McNutt, and D.T. Young (2010), Enceladus plume variability and the neutral gas densities in Saturn's magnetosphere, *J. Geophys. Res.* 115, A10252, doi:10.1029/2009JA015184.
- Srama, R., et al. (2004), The Cassini Dust Analyzer, *Space Sci. Rev.*, 114, 465, doi:10.1007/s11214-004-1435-z.
- Stebbing, R.F., A.C.H. Smith, and H. Ehrhardt (1964), Charge transfer between oxygen atoms and O^+ and H^+ ions, *J. Geophys. Res.*, 69, 2349, doi:10.1029/JZ069i011p02349.
- Strobel, D.F. (2008), Titan's hydrodynamically escaping atmosphere, *Icarus*, 193, 588-594, doi:10.1016/j.icarus.2007.08.014.
- Strobel, D.F. (2009), Titan's hydrodynamically escaping atmosphere and the structure of the exobase region, *Icarus*, 632-641, doi:10.1016/j.icarus.2009.03.007.
- Strobel, D.F., Atreya, S.K., Bézard, B., Ferri, F., Flasar, F.M., Fulchignoni, M., Lellouch, E., Müller-Wodarg, I.C.F., (2009), Atmospheric structure and composition, in *Titan from Cassini-Huygens*, edited by R.H. Brown, Lebreton, J.-P., Waite, J.H. Jr, pp. 235-257, Springer, Dordrecht, Neth.

- Talukder, M.R., A.K.F. Haque, and M.A. Uddin (2009), Electron impact double ionization cross sections of light elements, *Eur. Phys. J. D.*, 53, 133, doi:10.1140/epjd/e2009-00105-x.
- Teolis, B.D., M.E. Perry, B.A. Magee, J. Westlake, and J.H. Waite (2010), Detection and measurement of ice grains and gas distribution in the Enceladus plume by Cassini's Ion Neutral Mass Spectrometer, *J. Geophys. Res.*, 115, A09222, doi:10.1029/2009JA015192.
- Thompson, W.R., M.B. Shah, and H.B. Gilbody (1995), Single and double ionization of atomic oxygen by electron impact, *J. Phys. B.*, 28, 1321, doi:10.1088/0953-4075/28/7/023.
- Thompson, W.R., M.B. Shah, and H.B. Gilbody (1996), One-electron capture in collisions of 6-100 keV protons with oxygen atoms, *J. Phys. B.*, 29, 725, doi:10.1088/0953-4075/29/4/014.
- Thompson, W.R., M.B. Shah, and H.B. Gilbody (1997), Electron capture in Collisions of He^{2+} Ions with Atomic and Molecular Oxygen, *Physica Scripta*, 73, 214, doi:10.1088/0031-8949/1997/T73/066.
- Thomsen, M.F., D.B. Reisenfeld, D.M. Delapp, R.L. Tokar, D.T. Young, F.J. Crary, E.C. Sittler, M.A. McGraw, and J.D. Williams (2010), Survey of ion plasma parameters in Saturn's magnetosphere, *J. Geophys. Res.*, 115, A10220, doi: 10.1029/2010JA015267.
- Tseng, W.-L., W.-H. Ip, R.E. Johnson, T.A. Cassidy, and M.K. Elrod (2010), The structure and time variability of the ring atmosphere and ionosphere, *Icarus*, 206, 382, doi: 10.1016/j.icarus.2009.05.019.
- Tseng, W.-L., R.E. Johnson, M.F. Thomsen, T.A. Cassidy, and M.K. Elrod (2011a), Neutral H_2 and H_2^+ ions in the Saturnian magnetosphere, *J. Geophys. Res.*, 116, A03209, doi:10.1029/2010JA016145.
- Tseng, W.-L., and W.-H. Ip (2011b), An assessment and test of Enceladus as an important source of Saturn's ring atmosphere and ionosphere, *Icarus*, 212, 294, doi:10.1016/j.icarus.2010.12.003.
- Tucker, O.J. and R.E. Johnson (2009), Thermally driven atmospheric escape: Monte Carlo simulations for Titan's atmosphere, *Planet. Space Sci.*, 57, 1889, doi:10.1016/j.pss.2009.06.003.
- Van Allen, J.A., B.A. Randall, and M.F. Thomsen (1980), Sources and sinks of energetic electrons and protons in Saturn's magnetosphere, *J. Geophys. Res.*, 85, 5679, doi:10.1029/JA085iA11p05679.

- Vandegriff, J., et al. (2012), *Cassini/MIMI Instrument Data User Guide*, (available at http://sd-www.jhuapl.edu/CASSINI/restricted/ftpdata/mimi_user_guide_2012_03_22.pdf).
- Verner, D.A., G.J. Ferland, K.T. Korista, and D.G. Yakovlev (1996), Atomic data for astrophysics. II. New analytic fits for photoionization cross sections of atoms and ions, *ApJ*, 465, 487, doi:10.1086/177435.
- von Steiger, R., N.A. Schwadron, L.A. Fisk, J. Geiss, G. Gloeckler, S. Hefti, B. Wilken, R.F. Wimmer-Schweingruber, and T.H. Zurbuchen (2000), Composition of quasi-stationary solar wind flows from Ulysses/Solar Wind Ion Composition Spectrometer, *J. Geophys. Res.*, 105, 27217, doi:10.1029/1999JA000358.
- Waite, J.H. et al. (2004), The Cassini Ion and Neutral Mass Spectrometer, *Space Sci. Rev.*, 114, 113, doi:10.1007/s11214-004-1408-2.
- Waite, J.H., Jr., et al. (2006), Cassini ion and neutral mass spectrometer: Enceladus plume composition and structure, *Science*, 311, 1419, doi: 10.1126/science.1121290.
- Waite, J.H. et al., (2009), Liquid water on Enceladus from observations of ammonia and ^{40}Ar in the plume, *Nature*, 460, 487-490, doi:10.1038/nature08153.
- Westlake, J.H., J.M. Bell, J.H. Waite Jr., R.E. Johnson, J.G. Luhmann, K.E. Mandt, B.A. Magee, and A.M. Rymer (2011), Titan's thermospheric response to various plasma environments, *J. Geophys. Res.*, 116, A03318, doi:10.1029/2010JA016251.
- Wiedmann, R.T., R.G. Tonkyn, M.G. White, W. Kwanghsi, and V. McKoy (1992), Rotationally resolved threshold photoelectron spectra of OH and OD, *J. Chem. Phys.*, 97, 768, doi:10.1063/1.463179
- Wilson, R.J., R.L. Tokar, M.G. Henderson, T.W. Hill, M.F. Thomsen, and D.H. Pontius Jr. (2008), Cassini plasma spectrometer thermal ion measurements in Saturn's inner magnetosphere, *J. Geophys. Res.*, 113, A12218, doi:10.1029/2008JA013486.
- Yelle, R.V., J. Cui, and I.C.F. Müller-Wodarg (2008), Methane escape from Titan's atmosphere, *J. Geophys. Res.*, 113, E10003, doi:10.1029/2007JE003031.
- Yoder, C.F. (1995), Astrometric and geodetic properties of Earth and the Solar System, in *Global Earth Physics: A Handbook of Physical Constants, Ref. Shelf*, vol. 1, edited by T.J. Ahrens, p. 19, AGU, Washington DC.
- Young, D.T. et al. (2004), Cassini Plasma Spectrometer Investigation, *Space Sci. Rev.*, 114, 1, doi: 10.1007/s11214-004-1406-4.
- Young, D.T. et al., (2005), Composition and Dynamics of Plasma in Saturn's Magnetosphere, *Science*, 307, 1262, doi:10.1126/science.1106151.

- Yousif, F.B. and J.B.A. Mitchell (1995), Electron impact dissociative excitation of H_2^+ : low energy studies, *Z. Phys. D.*, 34, 195, doi:10.1007/BF01437688.
- Ziegler, D.L., J.H. Newman, K.A. Smith, and R.F. Stebbings (1982), Double ionization of atomic oxygen by electron impact, *Planet. Space. Sci.*, 30, 451, doi:10.1016/0032-0633(82)90054-X.
- Zipf, E.C. (1985), The ionization of atomic oxygen by electron impact, *Planet. Space. Sci.*, 33, 1303, doi:10/1016/0032-0633(85)90008-X.